NEVADA NATIONAL SECURITY SITE

Site-Directed Research & Development

Fiscal Year 2011 Annual Report

SDRD
SITE-DIRECTED RESEARCH & DEVELOPMENT

Material Studies and Techniques • Instruments, Detectors, and Sensors • Computational Sciences • Photonics

Disclaimer

This report was prepared as an account of work by an agency of the United States Government. Neither the United States Government nor any agency thereof, nor any of their employees, nor any of their contractors, subcontractors, or their employees, makes any warranty, express or implied, or assumes any legal liability or responsibility for the accuracy, completeness or any third party's use or the results of such use of any information, apparatus, product, or process disclosed, or represents that its use would not infringe privately owned rights. Reference herein to any specific commercial product, process, or service trade name, trademark, manufacturer, or otherwise, does not necessarily constitute or imply its endorsement, recommendation, or favoring by the United States Government or any agency thereof or its contractors or subcontractors. The views and opinions of authors expressed herein do not necessarily state or reflect those of the United States Government or any agency thereof.

Availability Statement

Available for sale to the public from—

U.S. Department of Commerce
National Technical Information Service
5301 Shawnee Road
Alexandria, VA 22312
Telephone: 800.553.6847
Fax: 703.605.6900
E-mail: orders@ntis.gov
Online ordering: http://www.ntis.gov/help/ordermethods.aspx

Available electronically at http://www.osti.gov/bridge

Available for a processing fee to the U.S. Department of Energy and its contractors in paper, from—

U.S. Department of Energy
Office of Scientific and Technical Information
P.O. Box 62
Oak Ridge, TN 37831-0062
Telephone: 865.576.6401
Fax: 865.576.5728
E-mail: reports@adonis.osti.gov
Online ordering: http://www.osti.gov/reportform.html

Nevada National Security Site
Site-Directed Research and Development

Fiscal Year 2011 Annual Report

Computational Sciences

Photonics

10 Years of Innovation

This is the 10th anniversary of Congressional authorization of our Site-Directed Research and Development (SDRD) program. During the last 10 years, the SDRD program has grown and matured, becoming an integral part of our technical base. As the primary source for new discovery and innovation, the program has no equal and provides unparalleled return on investment. Our SDRD program allows us to explore and innovate from the "bottom-up" and, coupled with the strategic vision, to create immensely powerful breakthrough and transformative ideas that have real impact for our mission. Many of the breakthroughs are producing technical capabilities much earlier than expected and are contributing directly to our stockpile, homeland security, and work for others programs in vital and unanticipated ways.

Without the SDRD program, it is difficult to imagine where innovation and breakthroughs would come from for our programs. We see more and more value in the surprising and unexpected successes from pursuing high-risk R&D. The morale of our researchers and the successes of programs are only a few of the benefits. The relatively small amount of funding provides tremendous value for programs, our staff, and the overall site mission.

The first 10 years have been filled with many accomplishments, but we are expecting even more in the years to come by challenging our people to take creativity to new levels, aim high, and stay focused on success to ensure the highest return for our nation's security.

Jim Holt

**Director,
Defense Experimentation
and Stockpile Stewardship**

this page intentionally left blank

SDRD FY 2011 Program Summary

A Milestone Decade

This fiscal year 2011 annual report of the Site-Directed Research and Development program, the 10th anniversary edition, recognizes a full decade of innovative R&D accomplishments in support of the Nevada National Security Site (NNSS). Last year the NNSS itself was renamed to reflect a diversifying mission, and our R&D program has contributed significantly to shape emerging missions that will continue to evolve. New initiatives in stockpile stewardship science, nonproliferation, and treaty verification and monitoring have had substantial successes in FY 2011, and many more accomplishments are expected. SDRD is the cornerstone on which many of these initiatives rest. Historically supporting our main focus areas, SDRD is also building a solid foundation for new, and non-traditional, emerging national security missions. The program continues its charter to advance science and technology for a broad base of agencies including the U.S. Department of Energy (DOE), U.S. Department of Defense (DoD), U.S. Department of Homeland Security (DHS), and many others.

The MPDV team (back row: M. Teel, A. Diaz; front row: C. Gallegos, C. Perez, E. Daykin) pictured with the SDRD breakthrough multiplexed photonic Doppler velocimetry system. The MPDV is being used on experiments at Los Alamos National Laboratory as part of a broad collaboration with Lawrence Livermore National Laboratory and the Nevada National Security Site.

SDRD Paves the Way to Success for Our Programs

SDRD's contribution and impact to our core programs is one way we gauge the effectiveness of our R&D investment. Generally, with advanced R&D some time is required before technologies fully develop and are integrated into our programs. Now, reflecting on a decade of projects, we can claim some major successes; here we highlight three very important contributions that have been born out of SDRD investment.

With the cessation of nuclear testing in the early 1990s and the advent of science-based stockpile stewardship, new diagnostic techniques are constantly being required to assess the safety and performance of the nation's stockpile. The primary methods used to understand materials in extreme conditions are non-nuclear experiments such as subcritical, hydrodynamic, and high-pressure studies. Characterizing materials in these regimes is an

active area of research, and the utilization of advanced modeling and simulation has further driven the need for exceptionally precise diagnostics. It is often said that timing is everything, and in the case of SDRD investments in optical velocimetry this is true literally and figuratively. Optical velocimetry enables the measurement of moving surfaces and as such, directly characterizes fundamentally important shock conditions in materials. Historically, shock wave measurements yielded only a few channels of data. Hydrodynamic tests were even more limited, gathering data with electrical shorting pins at discrete times. SDRD investments over the years resulted in a complete revamping of the traditional velocimetry tool, VISAR (velocity interferometer for any reflector), and greatly improved knowledge of the newer photonic Doppler velocimetry (PDV). Both instruments were improved so much that they began to replace a few of the traditional shorting pins in hydrodynamic tests. In 2010, SDRD breakthroughs in multiplexed PDV (MPDV) achieved by E. Daykin and his team created a new paradigm, allowing experiments to be instrumented with hundreds of velocimetry channels with long time records and yielding an unparalleled amount of information obtained. Key to extracting the full capability of MPDV rests on yet another SDRD-based innovation, the compact fiber-optic probe that was studied extensively in the mid-2000s. These key technologies came together at precisely the right time to provide unprecedented capability and, in fact, are enabling a new class of subcritical experiments to be conducted in 2012–2014.

In addition, recent contributions related to material studies are coming from SDRD projects in dynamic effects conducted at our explosive test facility in Santa Barbara, California. Improved understanding of the equations of state (EOS) of metals under shock conditions is critical to advanced modeling. To fully understand an EOS it is necessary to measure the temperature of the shocked metal, yet obtaining highly accurate measurements has been extremely difficult. SDRD has funded the development of new diagnostics to determine the temperature of a shocked metal sample from its thermal radiation. This work, led by PIs D. Turley and G. Stevens and published in articles in the *Journal of Applied Physics* (110 (2011) 103510 and 110 (2011) 093508), has developed methods for using pyrometry to measure the thermal optical emission and small integrating spheres to determine the emissivity of a shocked sample. In 2 to 3 years these diagnostics will be fielded on specialized gas gun experiments at the NNSS to determine the temperature of shocked plutonium.

D. Turley (right), NSTec PI, describes his dynamic materials properties R&D project at the 2011 LDRD Symposium

An unprecedented and devastating natural disaster occurred on March 11, 2011, when the 9.0 magnitude earthquake off the coast of Japan triggered a massive tsunami. The Fukushima Daiichi nuclear power plant was heavily damaged by the ensuing tsunami wave; ultimately, over the course of many months, radioactive materials were discharged into the surrounding landscape and atmosphere. A rapid response, using both environmental monitoring data and computer simulation, was initiated to deal with the contamination and assess the radiological danger. Cooperating with Japanese authorities, the NNSS radiological emergency response teams were put into action and conducted aerial measuring system (AMS) flights over the areas impacted by release of radioactive materials.

NSTec PI M. Reed (back center) providing aerial measurement data analysis for the Japan reactor accident utilizing techniques developed by prior SDRD projects

Many recent and earlier SDRD projects conducted by our technical staff (many of whom are also members of the response teams) contributed to the ability to deal with the difficult Japan situation. Radiological simulation capabilities used in the absence of live contamination, developed under an FY 2002 SDRD project, have since become integral training tools for the AMS mission and provide a high degree of readiness. An FY 2005 SDRD project resulted in the development of a generation of devices referred to as the Multi-Path Communication Device, or MPCD. The MPCD transmits data in real-time using one of several communication pathways, such as cellular, satellite, and many others. The MPCD technology was embedded in the Search Management Center that was used in the DOE response in Japan. This setup, composed of a small grid of remotely operated detector systems that transmitted sensor data to a remote receiver system, was also first instigated by the SDRD program. Other more recent SDRD projects (FY 2009–2010) sharpened operational expertise and enabled better theoretical understanding and interpretation of the AMS radiological data products. This work allowed DOE's NA-42 Technology Integration Program to develop a suite of tools to quantify aerial radiation data. These tools, in addition to the technical expertise and capabilities developed under these SDRD projects, played a significant role in the Japan response by providing crucial measurements to ensure the safety of citizens and responders and in handling the aftermath consequences.

Program Accomplishments and Return on Investment

The above examples highlight just some of the contributions SDRD has made over the past decade. In this fiscal year alone, over half of our projects have already developed technologies that were adopted by direct program areas in stockpile stewardship, nonproliferation, homeland security, and other applications. Seven new invention disclosures were submitted on activities related to this year's work, multiple peer-reviewed articles were published, and many PIs presented at national technical conferences.

The program generated R&D 100 award entries on high-speed imaging and other technologies relevant to national security issues. Four NNSS projects were highlighted at the annual Laboratory Directed Research and Development (LDRD) Symposium in Washington, D.C., which featured innovations driving new solutions to national security challenges. The LDRD symposium hosted several speakers who addressed contemporary topics in stockpile stewardship and homeland security, and was attended by a diverse audience that included NNSA, the National Weapons Laboratories, DHS, and DoD. The symposium, now in its 4th year, uses a day-long, concentrated, themed format, and has become a well-favored venue for examining national security issues and contributions made by LDRD.

The FY 2011 proposal cycle benefited from the first full year in which funding from non-DOE sources was part of the base SDRD funding. When implemented in FY 2010, we expected this change to greatly enhance the program. This prediction has been realized, as we can now address needs across a broader mission scope and are able to bring solutions to new customers. The 154 proposals submitted for FY 2011 were diverse; they focused on new interest areas such as intelligence, cyber security, treaty verification, and monitoring activities, as well as our traditional stockpile mission. Ultimately 26 projects were selected. This selection rate of about 1 in 6 is comparable to last year's, and ensures good competition, yet maintains proposers' enthusiasm that their ideas have a reasonable probability for acceptance. Our internal and external peer review system for selecting winning proposals relies on key criteria, which has remained essentially unchanged: high technical innovation, probability of success balanced with technical risk, potential for mission benefit, and alignment with our mission goals to achieve the best possible outcomes.

Developing skills and maturing technologies through SDRD have been vital activities in garnering work through external proposal calls. For instance, seed SDRD projects in five cases from FY 2003 to FY 2009 have resulted in newly funded efforts from the NA-22 directorate of DOE. In one of these cases, an extremely small investment for a 2-month feasibility study on nuclear fuel cycle ontology went on to receive funding for a full 3-year life cycle award from DOE—a first for an SDRD feasibility study. Approximately $4.5 million in new funding, equating to a roughly 3X factor return on investment, has been received based on these efforts. In addition, many proposals and ideas unfunded in recent years are being repurposed into proposals targeting specific, directed applications with other agencies.

The *NNSS Technology Needs Assessment* document continues to be a valuable tool for our proposal submitters and reviewers by providing a roadmap and guidance for technology gaps and challenges facing mission areas. Our directed research emphasis areas for FY 2011, which target key investment, included nuclear security, information security/assurance, high-energy density physics, integrated experiments, advanced analysis, and IED threat reduction. The needs assessment is developed from a broad base of input from the national security complex including laboratories, NNSA, and other external agencies. Significant revisions were again made last year by enhancing emerging areas and including new lessons derived from the Japan response. The needs assessment itself is in the 8th year of revision, and its utility and effectiveness has improved year to year, plus many trends have been elucidated by the process of updating the assessment.

Total funds expended for the FY 2011 program were approximately $7 million, a slight increase over last fiscal year. Administrative and management costs, kept to a minimum, are typically less than 10% of the overall budget. Average cost per project for FY 2011 increased slightly over last year to about $250,000. As demonstrated, this relatively small investment yields considerable return based on the achievements and benefit garnered for our mission and programs.

Gauging SDRD Performance

Metrics such as intellectual property and technology transfer are often used to gauge the output and effectiveness of an R&D program. These metrics, along with other factors such as follow-on funding obtained, provide indicators of innovation productivity and are a direct measure of the investment return. SDRD provides our staff with opportunities to explore and allows flexing of the creative motivations that ultimately lead to new knowledge and realized technologies. Traditionally SDRD has generated well over half of all inventions disclosed company-wide since the program began and continues to do so to this day. Patent applications are pending on many of these disclosures, and a new effort was launched this fiscal year to enhance the filing process to improve the NNSS patent portfolio.
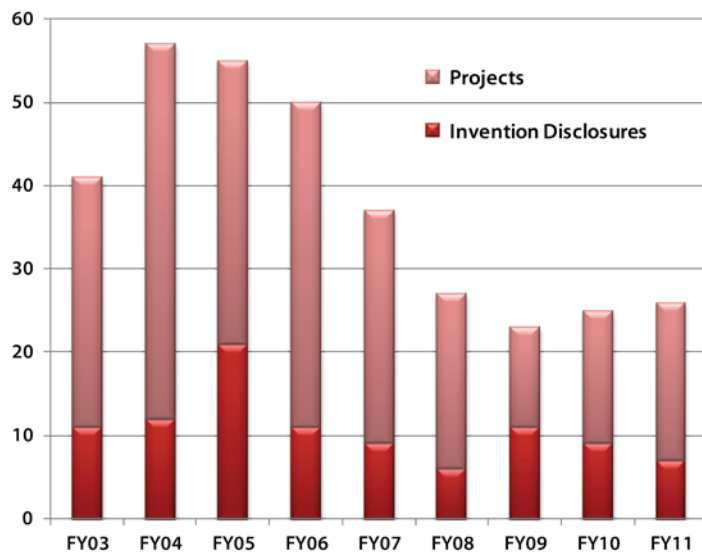
Inventions disclosed (dark red bars) plotted as a function of the total number of SDRD projects (light red bars) in a given fiscal year

Our program areas benefit from a high rate of technology utilization; numerous SDRD projects have developed technologies that were subsequently adopted by an NNSS program. As mentioned earlier, SDRD has become very effective in integrating new technologies into key programmatic efforts on an even timelier basis than expected. Some of this is due to efforts to more effectively include forward-looking needs and "handshake" more efficiently with our NNSS strategic roadmaps to encourage technology transfer. We continue to strive to stay "ahead of our time by design" and push for SDRD-developed technologies to find their way into our future and evolving missions with the highest impact.
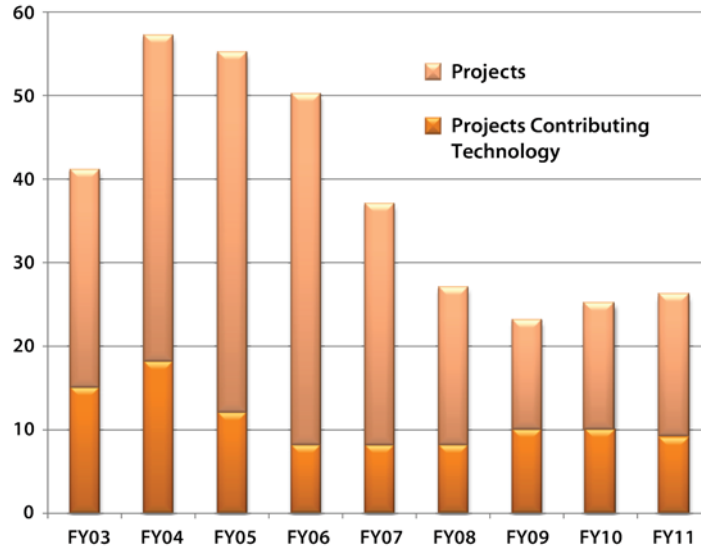
SDRD projects contributing technologies to programs (dark gold bars) compared to total number of projects (light gold bars) in a given fiscal year
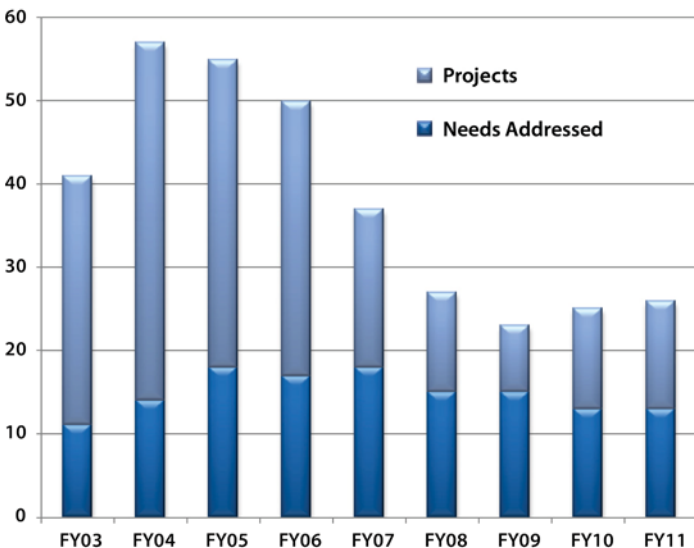
SDRD projects (dark blue bars) that directly address a technology requirement as identified in the yearly *NNSS Technology Needs Assessment*

Another measure of program effectiveness and alignment with missions is how well projects address technology needs as identified in our *NNSS Technology Needs Assessment* annual publication. The percentage of needs addressed to total projects also indicates a trend that aligns efforts strategically with the NNSS mission.

FY 2011 Annual Report Synopsis

The project reports that follow are for activities that occurred from October 2010 through September 2011. The many achievements and challenges described are a testament to the talent

and enthusiasm PIs brought to their individual projects. Many of the reports describe R&D efforts that were "successful" in their pursuits and resulted in a positive discovery or technology realization. However, in some cases the result is a "negative" finding; for instance, a technology is currently impractical or out of reach. This can often be viewed erroneously as a "failure," but is actually a valid outcome in the pursuit of high-risk research that often leads to unforeseen new paths of discovery. As stated before, both types of results advance our knowledge and increase our ability to identify solutions or avoid paths not appropriate for the challenges presented in our pursuits.

In summary, the SDRD program continues to provide the only true unfettered mechanism for innovation and development that returns multifold to the NNSS mission. Overall the program has been strengthened by enhanced mission, resources, and increased competitiveness to yield maximum benefit. The 26 projects described herein exemplify the creativity and ability of a diverse scientific and engineering talent base. The efforts also showcase an impressive capability and resource that can be brought to find solutions to a broad array of technology needs and applications relevant to the NNSS mission and national security.

Finally, as we mark our 10th annual report, I want to gratefully acknowledge the tremendous support by the multiple individuals and teams that make SDRD successful year after year. My sincere gratitude goes out to Michele Vochosky, Sierra Cory, Katharine Kelly Streeton, Bob Watson, and Elizabeth Godfrey for compiling, editing, and publishing this report; to Jaye Oliver and Katina Loo for their graphic design of the cover and dividers; to Linda Flaugher for her valuable efforts in cost accounting of FY 2011 projects and Tom Graves for his significant project management support; to Cathy Cooper and Cindy McIntosh for compiling the financial data for congressionally mandated reporting requirements; to Larry Franks, Rob Hixson, and Lynn Veeser for exceedingly valuable technical guidance; and to SDRD site representatives and review committee, Rob Buckles, Frank Cverna, Paul Guss, Amy Lewis, Eric Machorro, Eric Moore, Mike Mohar, and Jerry Stevens. Again, I offer my sincerest appreciation for your dedication and fortitude to ensure another highly successful year of R&D in support of the NNSS!

Howard A. Bender III
SDRD Program Manager

this page intentionally left blank

Los Alamos Operations (LAO)
P.O. Box 809
Los Alamos, New Mexico 87544-0809

Livermore Operations (LO)
P.O. Box 2710
Livermore, California 94551-2710

North Las Vegas (NLV)
P.O. Box 98521
Las Vegas, Nevada 89193-8521

Nevada National Security Site (NNSS)
P.O. Box 98521
Las Vegas, Nevada 89193-8521

Remote Sensing Laboratory–Andrews Operations (RSL–A)
P.O. Box 380
Suitland, Maryland 20752-0380
(Andrews Air Force Base)

Remote Sensing Laboratory–Nellis Operations (RSL–N)
P.O. Box 98521
Las Vegas, Nevada 89193-8521
(Nellis Air Force Base)

Sandia Operations (SO)
Sandia National Laboratories
P.O. Box 5800
Mail Stop 1193
Albuquerque, New Mexico 87185

Special Technologies Laboratory (STL)
5520 Ekwill Street
Santa Barbara, California 93111-2352

this page intentionally left blank

A

AC	alternating current
ADC	analog-to-digital converter
AFSA	accelerating, focusing, and steering assembly
AGL	above ground level
AlGaN	aluminum gallium nitride
AlInGaN	aluminum indium gallium nitride
AMS	Aerial Measurement System
ANC	accidental neutron counting
Ar	argon
ARM	Acorn RISC Machine
AS	anti-Stokes
ASTM	American Society for Testing and Materials

B

^{10}B	boron-10
Be	beryllium
Bkg	background
BMSB	bis(methylstyryl)benzene
BT	back-thinned

C

CCD	charge-coupled device
CCl_4	carbon tetrachloride
CDA	characterization data acquisition
CdS	cadmium sulfide
CdSe	cadmium selenide
CdSeS	cadmium selenium sulfur
CdTe	cadmium telluride
CMOS	complementary metal oxide semiconductor
CNIBM	Cerenkov non-intercepting beam monitor
CPS	counts per second
CPU	central processing unit
CsI(Tl)	thallium-doped cesium iodide
CUDA	Compute Unified Device Architecture
CW	continuous wave

D

DAC	diamond anvil cell
DARHT	Dual-Axis Radiographic Hydrodynamic Test Facility (LANL)
DC	direct current
D-D	deuterium-deuterium
DDR	double data rate
DHS	U.S. Department of Homeland Security
DNA	deoxyribonucleic acid
DoD	U.S. Department of Defense
DOE	U.S. Department of Energy
DP	diffraction pattern
DPF	dense plasma focus
DR	disperse red
DTRA	Defense Threat Reduction Agency
DU	depleted uranium
D/W	pore diameter to cell width ratio

E

EDM	electrical discharge machining
EM	electron multiplying
EMI	electromagnetic interference
EO	electro-optical
EOS	equation of state

F

FAM	fluorescent aptamer molecule
FIFO	first-in first-out
FPGA	field-programmable gate array
FM	frequency-modulated (system)
FWHM	full-width at half-maximum
FY	fiscal year

G

GaN	gallium nitride
Gd	gadolinium
GPS	global positioning system
GPU	graphics processing units
GUI	graphical user interface

H

^{3}He	helium-3
hcp	hexagonal close-packed
HDPE	high-density polyethylene
HE	high explosive
HeNe	helium-neon
HEU	highly enriched uranium
HFSS	3-D electromagnetic field simulation software from ANSYS, Inc.
HIV	Human immunodeficiency virus

I

IAC	Idaho Accelerator Center
ICCD	intensified charge-coupled device (detector)
IED	improvised explosive device
IF	ion funnel
In_2O_3	indium oxide
I/Q	in-phase/quadrature-phase (detection method)
IR	infrared
IT	ion trap
ITO	tin-doped indium oxide

J

JASPER	Joint Actinide Shock Physics Experimental Research (facility)

K

KCl	potassium chloride
KSU	Kansas State University

L

LANL	Los Alamos National Laboratory
LAO	Los Alamos Operations (NSTec)
LDRD	Laboratory Directed Research and Development
LED	light-emitting diode
^{6}Li	lithium
lidar	light detection and ranging
LiF	lithium fluoride
LIFE	Laser Inertial Fusion Energy Facility

linac	linear accelerator
LLD	lower-level discriminator
LLNL	Lawrence Livermore National Laboratory
LVDS	low-voltage differential signaling

M

MALDI	matrix-assisted laser desorption/ionization
MC	microsecond counter
MCA	multichannel analyzer
MCNP	Monte Carlo n-Particle
MCNPX	Monte Carlo n-Particle Extended
MCP	microchannel plate
MDI	methylene diphenyl diisocyanate
MEF	metal-enhanced fluorescence
MEK	methyl ethyl ketone
MeOH	methanol
MeOH:EtOH	methanol to ethanol (mixture)
MLE	maximum likelihood estimation
MM	multiplet matrix
MMA	methyl methacrylate
MMT	Mini Muon Tracker
MPCD	Multi-Path Communication Device
MPDV	multiplexed photonic Doppler velocimetry
MSM	metal-semiconductor-metal
m/z	mass-to-charge (ratio)

N

NA	neutron search alarm algorithm
NADH	nicotinamide adenine dinucleotide
NaI(Tl), NaI:Tl	sodium iodide
NASA	National Aeronautics and Space Administration
NaTCA	sodium trichloroacetate
ND	neutral density
Nd:YAG	neodymium-doped yttrium aluminum garnet (laser)
NIBM	non-intercepting beam monitor
NIF	National Ignition Facility
NIR	near infrared
NLV	North Las Vegas (NSTec)
NMC	neutron multiplicity counter
NNSA	National Nuclear Security Administration

NNSS	Nevada National Security Site (NSTec)
NSTec	National Security Technologies, LLC
NUV	near ultraviolet

O

OMA	optical multichannel analyzer
OPA	optical parametric amplifier

P

PBM	photonic band gap materials
PC	personal computer
PCB	printed circuit board
PD	photodiode
PDV	photonic Doppler velocimetry
PI	principal investigator
PL	photoluminescence
PLL	phase-locked loop
PMMA	polymethyl methacrylate
PMT	photomultiplier tube
PPO	2,5-diphenyloxazole
PSF	point spread function
PSL	polystyrene latex
PUR	polyurethane
PVA	polyvinyl-alcohol
PVT	polyvinyltoluene

Q

QD	quantum dot
QE	quantum efficiency
QR	quick response

R

R	Rayleigh (scattering)
R&D	research and development
RadHard	radiation-hardened
RDA	real-time data acquisition
RF	radio frequency
RIE	reactive ion etching

RITS	Radiographic Integrated Test Stand (Sandia National Laboratories)
RMD	Radiation Monitoring Devices, Inc.
rms	root mean square
RNA	ribonucleic acid
RPI	Rensselaer Polytechnic Institute

S

S	Stokes
SDK	software development kit
SDRD	Site-Directed Research and Development
SELEX	system evolution of ligands by exponential enrichment
SEM	scanning electron microscope
SI	system initialization
Si	silicon
SND	spiral thermal-neutron detector
SNM	special nuclear material
SNR	signal-to-noise ratio
SSPM	solid-state photomultipliers
START	Strategic Arms Reduction Treaty
STL	Special Technologies Laboratory (NSTec)
SURF	speeded-up robust features
SUV	sport utility vehicle
SWIR	short-wave infrared
SXR	soft x-ray

T

2-D	two-dimensional
3-D	three-dimensional
TCXO	temperature-compensated crystal oscillator
TEM	transverse electromagnetic
THF	tetrahydrofuran
TNT	trinitrotoluene
TOF	time-of-flight
TOPAS	Traveling-Wave Optical Parametric Amplifier Light Source
TOPAS-C	core module of TOPAS product family
TTL	transistor-to-transistor logic

U

UCLA	University of California, Los Angeles
UED	ultrafast electron diffraction
UNLV	University of Nevada, Las Vegas
UTM	universal transverse mercator
UV	ultraviolet
UV-C	ultraviolet light [100–280 nm wavelength]
UV/V	ultraviolet/visible

V

VISAR	velocity interferometer system for any reflector

X

XRD	x-ray diffraction
XUV	extreme ultraviolet

Y

YAG:Ce	cerium-doped yttrium aluminum garnet
Y2F	Feynman variance

Z

ZnO	zinc oxide
ZnS	zinc sulfide
ZnSe:Mn	manganese-doped zinc selenide

this page intentionally left blank

Material Studies and Techniques
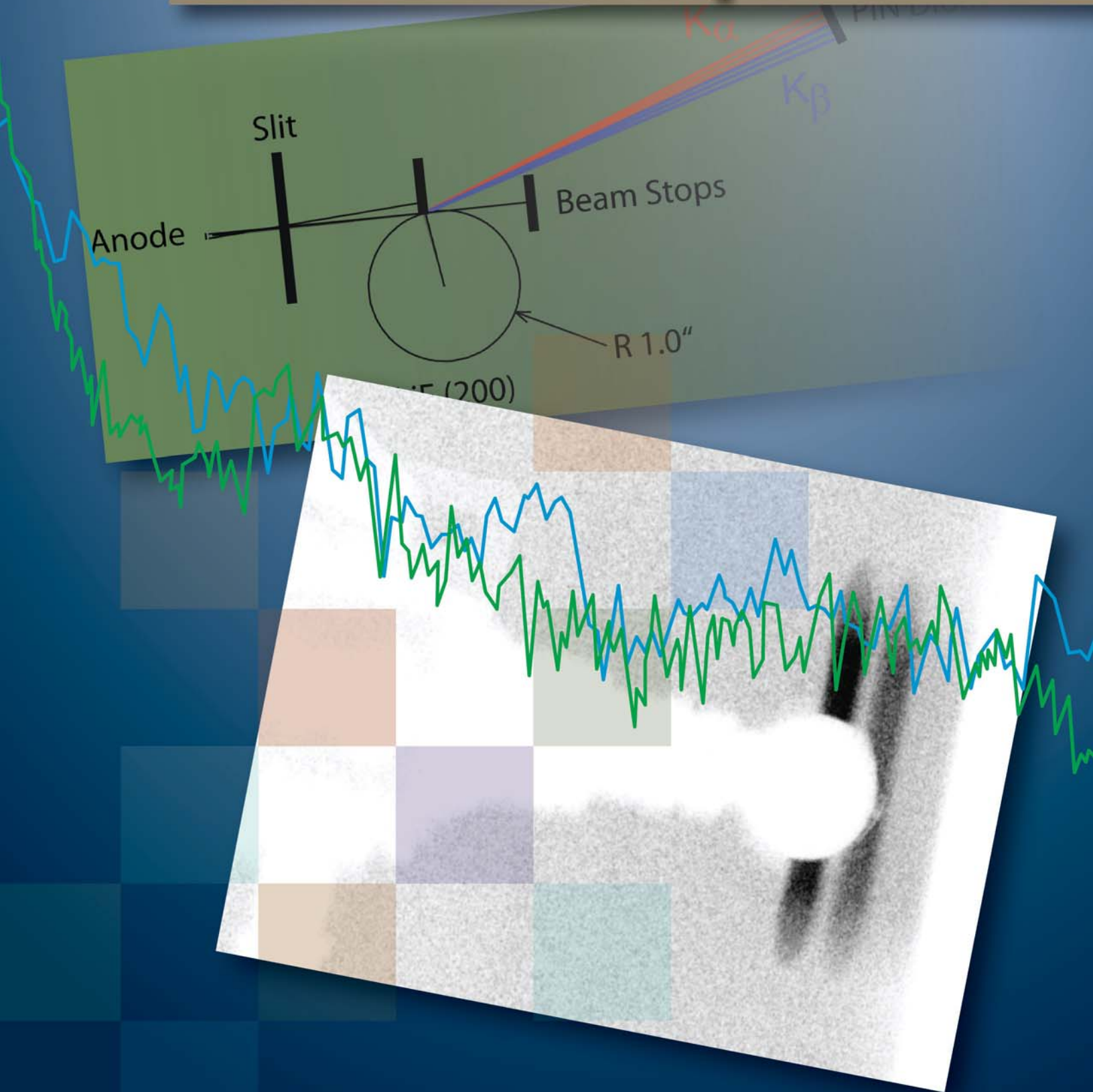
Nanoscale Properties of Shocked Materials

Dane Morgan,[1,a] Mike Grover,[b] Don Macy,[a] and Gerald Stevens[b]

An experimental single-pulse x-ray diffraction diagnostic was used to conduct studies of the material properties of shock-loaded zirconium and single-crystal potassium chloride with both (100) and (111) orientations with respect to the shock direction. The samples under study were 1.0 mm thick, and 0.5 mm thick vitreous carbon back windows were used for shock loading. Reflected pressures ranging from 5.6 to 7.7 GPa were produced with Detasheet high explosives, and a PDV probe measured the vitreous carbon-free surface velocity. The 30 ns, 0.71 Å x-ray pulse produced the diffraction pattern for polycrystalline zirconium, and the broad bremsstrahlung spectrum was used to observe the Laue spot reflections from shocked potassium chloride. A newly devised, fiber-optically reduced imaging system was developed to improve linearity and allow for analytical elimination of vitreous carbon x-ray reflections.

Background

X-ray diffraction (XRD) is a well-established method for determining the arrangement of atoms within a crystal. For the XRD method, the scattering is elastic; the scattered x-rays have the same wavelength as the incoming x-ray. Fundamentally, a beam of x-rays incident on a crystal causes the beam of light to spread into many specific directions. From the angles and intensities of these diffracted beams, it is possible to produce a three-dimensional picture of the density of electrons within the crystal; therefore, the mean positions of the atoms in the crystal can be determined, from which information concerning the structures and chemical bonds can be discerned. X-ray crystallography is still the chief method for characterizing the atomic structure of new materials and materials whose properties appear similar in other types of experiments (Warren 1990).

Over the past few years we have developed a novel single-pulse XRD diagnostic, which is uniquely capable of nanosecond XRD studies of polycrystalline materials. This diagnostic has been used to observe phase transformations, grain size distribution, texture, and the presence of inelastic behavior in both single-crystal and polycrystalline materials. Single-pulse XRD studies of materials that undergo solid-solid phase transitions include explosively driven, shock-loaded experiments with tin (Morgan 2008) and zirconium (Morgan 2010). Solid-solid phase transition experiments consistently have shown the presence of both new solid-state diffraction lines and a single broad diffraction peak, which indicates a lack of repeating structure within the shock-loaded material. Similar high explosives (HE)–driven shock-loaded experiments with aluminum 6061-T6 indicated

---

[1] morgandv@nv.doe.gov, 505-663-2047
[a] Los Alamos Operations; [b] Special Technologies Laboratory

that the sample retained the face-centered cubic phase, and no broad diffraction peak was observed. Single-pulse XRD allows measurement of the shifts of individual diffraction lines; hence, changes in *d*-spacing may be distinguished from systematic effects such as sample translation. Experiments with aluminum 6061-T6 under shock-loaded compression with vitreous carbon back windows to pressures of 6.4 to 7.3 GPa clearly showed angular shift of the XRD lines, and an increase in the shift with scattering angle, consistent with lattice compression. Conversely, increases in *d*-spacings have been observed for sterling silver immediately upon release of the free surface. Similar increases have been interpreted as shock-induced strain hardening in single-crystal copper and aluminum shock-and-release experiments using synchrotron radiation (Turneaure "Real time" 2009).

Project

Two distinct coherent x-ray scattering techniques were employed for the experiments reported here. For polycrystalline samples XRD probes a macroscopic volume; hence, the observed XRD pattern will be composed of microscopic lattice reflections for the grain distribution within the sample probe volume. For this technique, the line emission x-ray wavelength scatters coherently for the Bragg condition,

$$n\lambda = 2d\sin\theta, \tag{1}$$

for grains oriented with inter-plane spacing d, and with reflecting planes at an angle θ with respect to the incoming beam. The scattering angle is given by

$$\varphi = 2\theta, \tag{2}$$

where φ represents the half-angle of the Debye-Scherrer scattering cone. The scattering cones are intercepted at the detection plane by a phosphor or image plate, and the Debye-Scherrer rings' scattering angles are measured with respect to the direct beam. The second dynamic XRD technique utilizes the broad continuum x-ray source spectrum for single-crystal scattering experiments. For this technique, we have obtained 1 mm thick, single-crystal potassium chloride (KCl) discs with both (100) and (111) orientations with respect to the experimental axis. Because of the continuous source spectrum, the appropriate wavelength satisfying Equation 1 will exist naturally, producing a pattern of discrete Laue spots that depend on the rotation of the crystal about the experimental axis (James 1982). Shocked single-crystal KCl solid-solid phase transformation experiments utilizing XRD have been reported by d'Almeida (2000) and Turneaure ("Shock induced" 2009).

For XRD studies of shocked materials, it is important to precisely measure the line shift, line broadening, and changes in line intensity in the dynamic XRD data, because rapid changes in the shocked material properties will affect each of these observable parameters. Hence, our diagnostic development efforts have focused on improvements in signal-to-noise ratio and resolution. New developments implemented for FY 2011 experiments to improve the dynamic XRD measurement capabilities include a new pinhole collimator, an all-tungsten x-ray head for increased x-ray shielding,

and a fiber-optically reduced CCD camera imaging system. A high-energy, transmission-mode XRD setup was tested at 59 keV, and diffraction patterns were obtained for a 1 cm thick aluminum sample. Also, single-pulse XRD patterns were obtained using zirconium anodes, which produce 15.75 keV, 0.80 Å characteristic lines. This wavelength is ideal for obtaining single-pulse XRD patterns from depleted uranium.

The principal goal of this project was to observe the atomic-scale changes on the nanosecond time scale that occur in shocked materials, and the main thrust of experimental efforts was to observe the dynamic XRD patterns from materials that undergo solid-solid phase transitions during shock-loading.

During FY 2011, we made several modifications to the x-ray diode to improve the shielding and collimation of the x-ray beam. Background studies indicated significant hard x-ray penetration of the 1-inch thick brass housing. This observation led to a change in the housing material from brass to copper-tungsten, significantly reducing the scattered background. The cathode material was changed to copper-tungsten as well. These modifications are shown in Figure 1. The new imaging system shown in Figure 1 consists of a mirrored P-43 phosphor from Grant Scientific in intimate contact with a 2:1 fiber-optic reducer. The fiber-optic reducer output is coupled to a 1-inch square, 1024 × 1024 CCD camera by a coherent fiber-optic bundle. This imaging system provides background noise reduction and flat fielding, which improve quantitative analysis. Figure 2 shows XRD images of a KCl (111) target with a vitreous carbon back window and a free-standing vitreous carbon back window. By performing the image subtraction, the resulting final image has flat fielding, fixed pattern noise removal, and removal of the vitreous carbon back window XRD pattern. This imaging system has a signal-to-noise ratio and resolution comparable to the image plates used in previous systems.
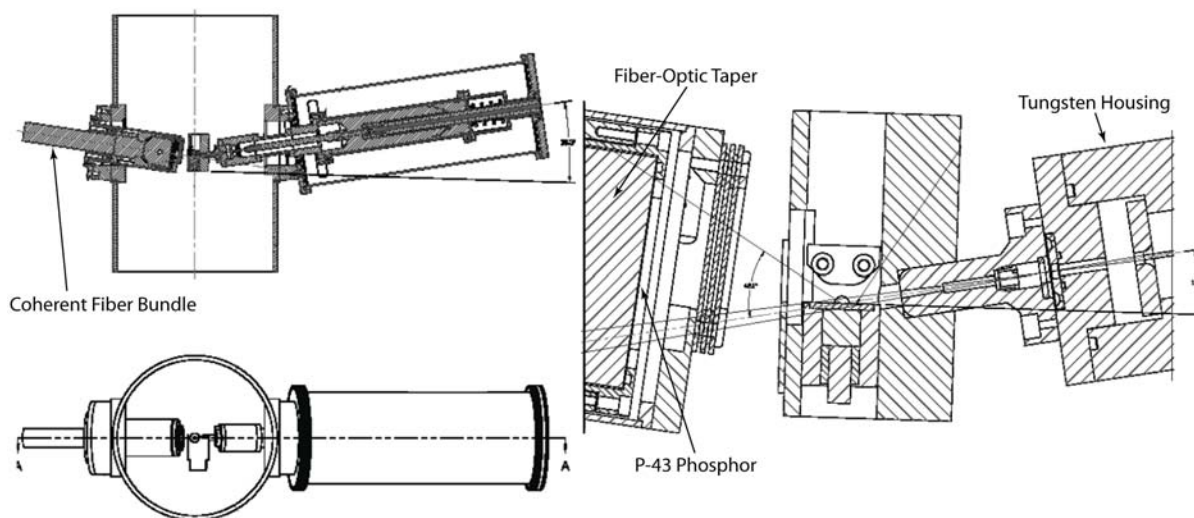
Figure 1. System diagram showing the design changes for FY 2011 XRD system experiments
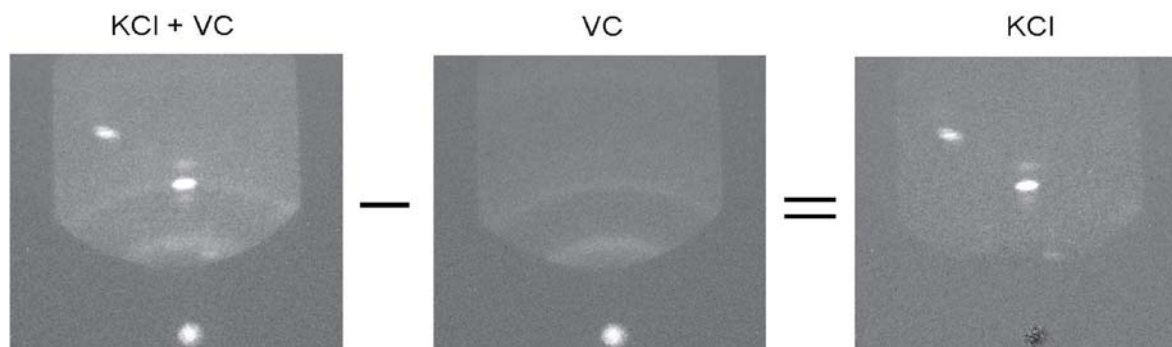
Figure 2. Images showing the subtraction technique for removing the effects of the vitreous carbon back window

Because we are unable to position the x-ray detector in the Special Technologies Laboratory (STL) Boom Box for dynamic experimental pulse timing, an electromagnetic pickup on the diode end of the transmission line outside the containment structure is used to determine the x-ray timing. Figure 3 shows the experimental setup for determining the x-ray pulse width and timing delay with respect to the electromagnetic pickup. A lithium fluoride (LiF) (200) cylindrically bent crystal with a 1-inch convex bend radius disperses the line emission, allowing the 0.71 Å x-ray pulse to be detected and measured in the A-K configuration used in the dynamic experiments. The pulse width was observed to be 30 ns, with peak radiation delayed 32 ns from the leading edge of the electromagnetic timing pulse.

A series of single-pulse XRD experiments for studying HE-driven, shock-loaded 99.9% pure zirconium and KCl single crystals were performed in FY 2011. The KCl single-crystal experiments were performed with both (100) and (111) orientations with respect to the shock direction. The experiments described in this report were conducted at the Boom Box, and the shocks were produced by Detasheet high explosives. Vitreous carbon back windows, 0.5 mm thick, were placed in intimate contact with samples to provide shock loading at the sample-vitreous carbon interface. A total of nine experiment data sets were obtained in FY 2011, as listed in Table 1. For the experiments reported here, molybdenum anodes were used to produce both 0.71 Å line emission and continuum bremsstrahlung x-ray emission.

Figure 4 shows the single-pulse XRD system for the experiments at the STL Boom Box, with the wax target holder set for 10.3° x-ray beam input angle to allow for observation of the low scattering angle expected for the amorphous halo. The 30 ns x-ray pulse was generated by a 350 kV Marx bank electrically coupled to a needle-and-washer diode through a DS-2158 coaxial cable. A pinhole collimator produced a 2 × 5 mm x-ray spot on the target. The x-ray firing time was measured with an electromagnetic pickup on the DS-2158 cable near the x-ray diode, and the x-ray signal timing with respect to the cable electromagnetic pickup time was measured in the laboratory prior to these experiments. PDV was used to measure the vitreous carbon free-surface shock breakout time and the
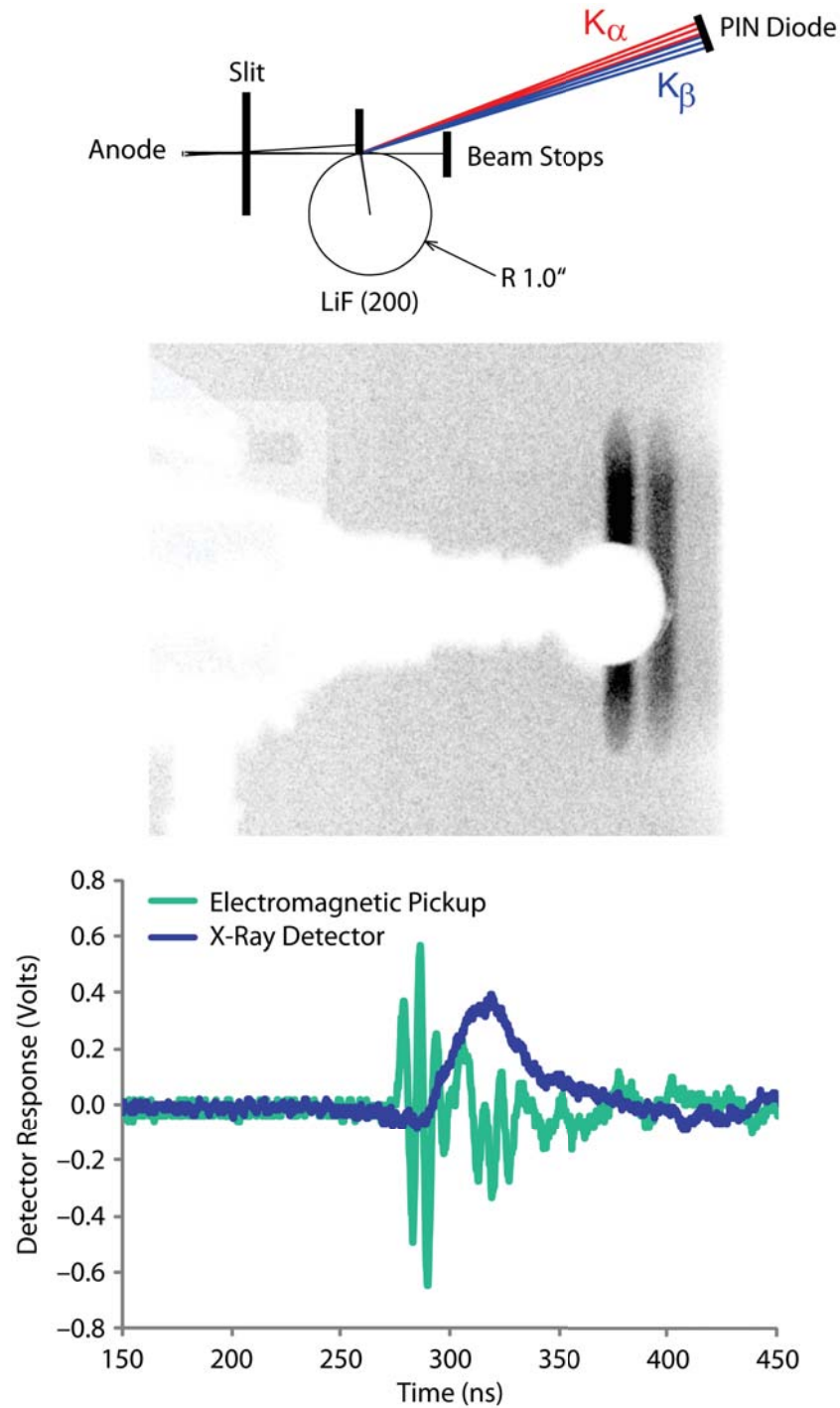
Figure 3. X-ray pulse width and timing delay measurement. (top) The cylindrically bent convex LiF (200) crystal causes sufficient spread of the spectral lines to enable timing measurements of the 0.71 Å line emission. (middle) Image showing the 0.71 Å K_α line centered on the PIN diode. (bottom) PIN diode x-ray detector timing with respect to the electromagnetic pickup.

Table 1. Summary of shock-loaded zirconium and single-crystal KCl experiments at 10.3° input angle and with a molybdenum anode

Experiment No.	Target Material	Reflected Pressure (GPa)	X-Ray Delay (ns)	Interference Motion (µm)
110613-1	Zr	5.6	181	207
110614-1	Zr	5.6	152	170
110614-2	Zr	5.8	369	456
110615-1	KCl (111)	7.8	90	106
110615-2	KCl (111)	7.2	104	117
110616-1	KCl (100)	7.6	−110	0
110616-2	KCl (100)	7.3	568	313
110616-3	KCl (100)	—	—	—
110617-1	KCl (111)	7.7	207	260
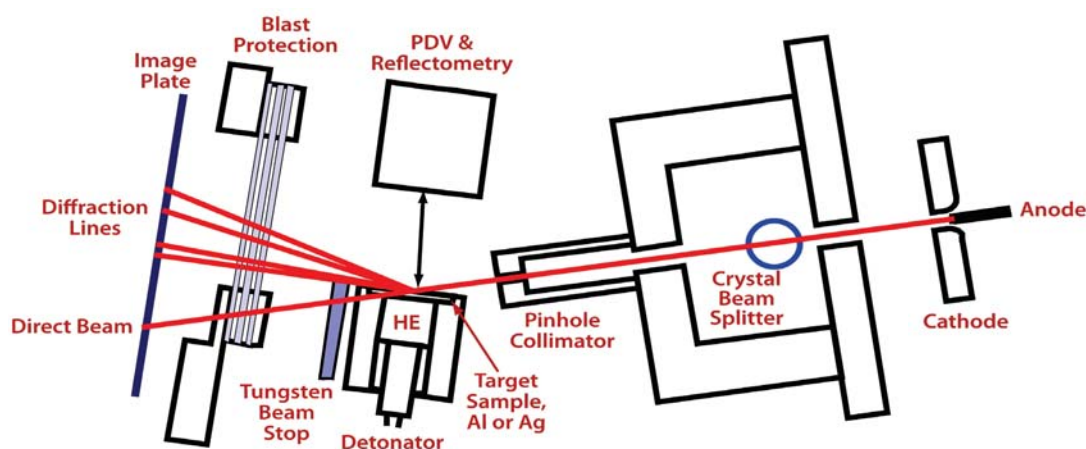
Figure 4. Experimental setup for dynamic single-pulse XRD experiments performed at the STL Boom Box

free-surface velocity, and to determine the surface translation, which was used for the dynamic image corrections. The PDV measurements were included in the WONDY code calculation to determine the reflected pressure at the interface and the interface motion.

Figure 5 shows the results for single-pulse XRD shock-loaded zirconium (Morgan 2010), at a reflected stress of 11.0 GPa, using vitreous carbon as a back window. The dynamic image clearly shows the formation of a new solid phase, as the strong hexagonal close-packed (hcp) (103) line in the static

α-phase is split into two new lines, indicating a new solid phase. This new solid phase is identified as the hexagonal ω-phase in Figure 5. Also, a broad halo is observed at low scattering angles, indicating that some fraction of the zirconium sample exists with no repeating structure, implying that the transformation is diffusive. A repeat experiment generated virtually identical results.

- Shock loaded to ~11.0 GPa
- Amorphous phase present
- New ω-phase

	Zirconium ω-phase *d*-spacing (Å)	
Miller Indices	Shock Experiment (this work)	High-Pressure Cell
(101)	2.51±0.07	2.461
(110)	—	2.436
(111)	1.90±0.05	1.899
(201)	1.72±0.03	1.731
(002)	1.50±0.02	1.516
(121)	1.40±0.02	1.411
(300)	—	1.406
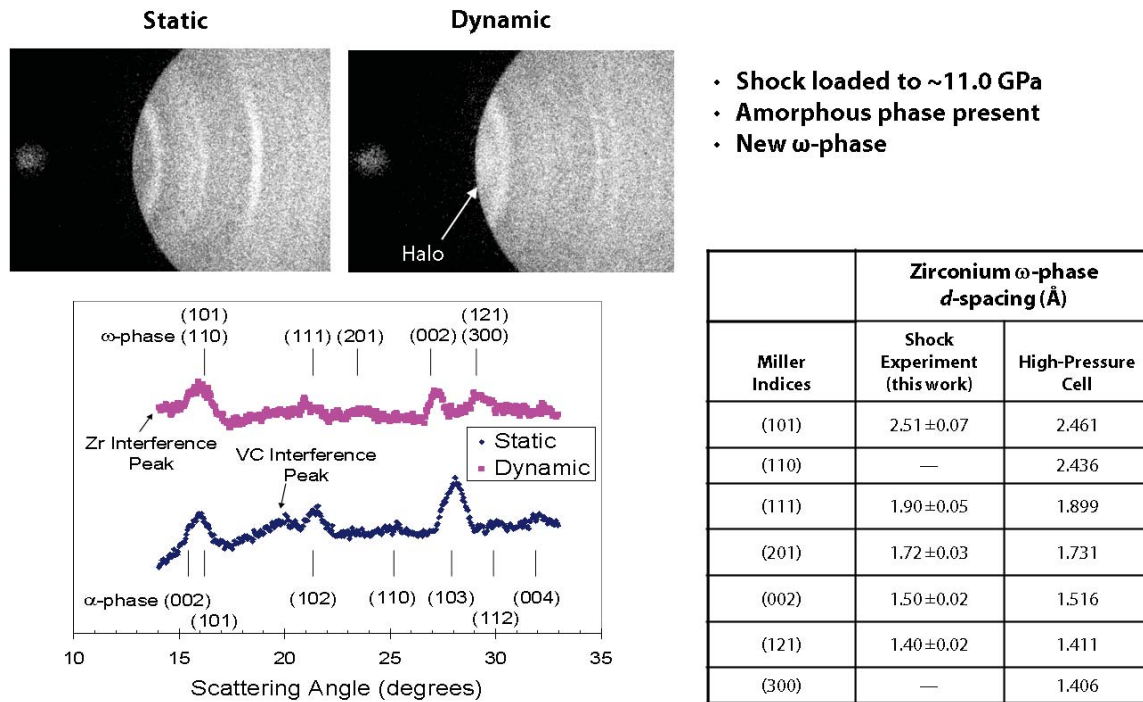
Figure 5. Results of a zirconium XRD experiment with 11.0 GPa shock-loading (Morgan 2010). The new solid ω-phase is clearly present, along with a broad peak associated with zirconium atoms in a disordered state.

Recently, VISAR has been used to observe zirconium shock-loaded interface velocities as a function of stress with projectile-generated, flat-top loading profiles (Rigg 2009). Results from these VISAR experiments indicate that the onset of the dynamic, nanosecond-time-scale α→ω phase transition for pure zirconium occurs at a much higher stress (7–8 GPa) than the transition pressure observed with XRD in static high-pressure cells (~2 GPa). In FY 2011, we performed shock-loaded zirconium single-pulse XRD experiments at stresses between 5.6 and 5.8 GPa, which is above the static transition pressure but below the nanosecond-time-scale transition pressure reported by Rigg (2009).

Because of zirconium's interesting phase change phenomenon, and its suitability for single-pulse XRD experiments, we continued our studies of this material in a shock-loaded state using the new diagnostic developments described previously. Figure 6 shows the PDV vitreous carbon back window free surface velocity data for three separate shock-loaded zirconium experiments (110613-1,
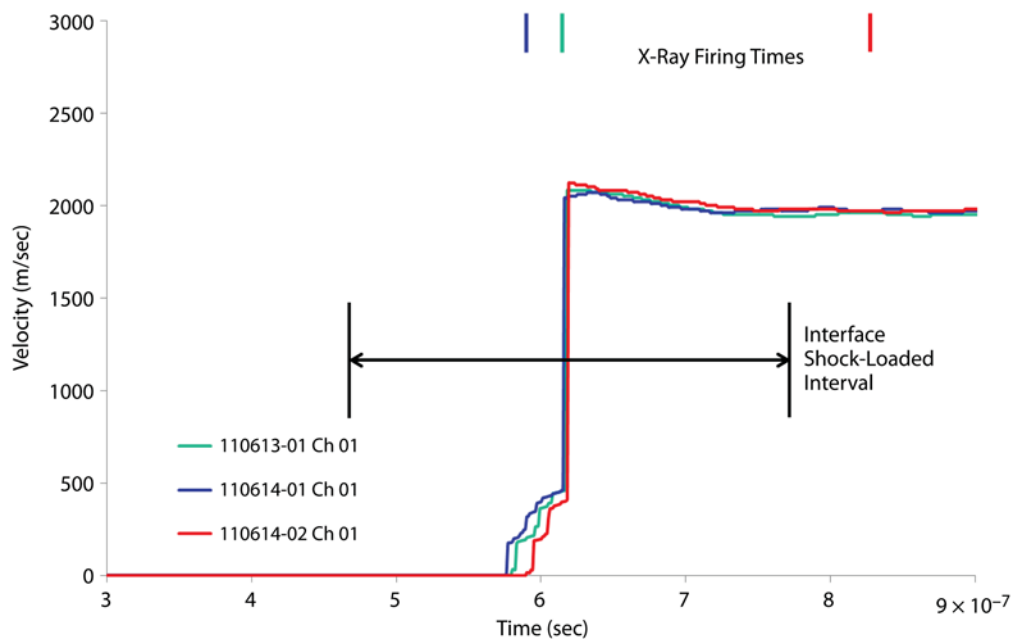
Figure 6. Comparison of PDV data from shock-loaded zirconium experiments 110613-1, 110614-1, and 110614-2. The interface shock-loading time interval and the x-ray firing times are also shown.
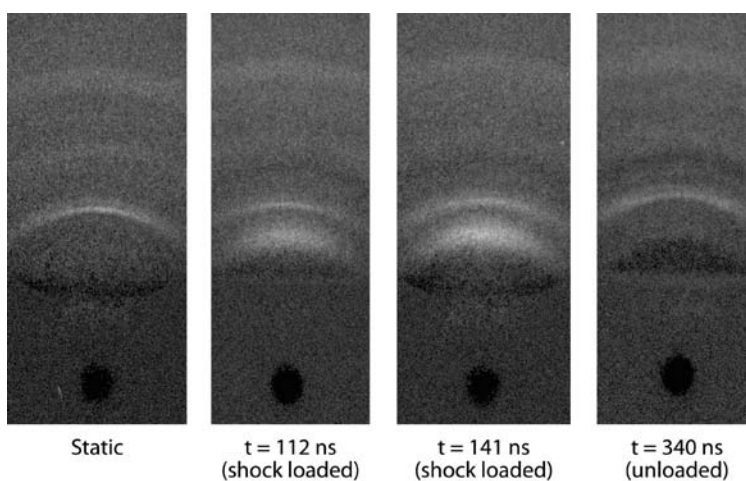
Figure 7. Single-pulse XRD images for shock-loaded zirconium experiments 110613-1, 110614-1, and 110614-2 at interface stresses of 5.6 to 5.8 GPa. The zirconium primarily retains the hcp α-phase, but the broad amorphous peak is also present during shock loading.

110614-1, and 110614-2). All three PDV velocity profiles were shifted to have coincident shock breakout timing. The x-ray firing times are also shown in Figure 6, along with the estimated interface shock-loading interval. For experiments 110613-1 and 110614-1, XRD patterns were obtained during interface shock loading; however, for experiment 110614-2, the XRD image was obtained after interface unloading, at zero pressure. The presence of a broad interference peak at a scattering angle of approximately 12° is observed, similar to the results obtained at 11.0 GPa. However, for the experiments at low pressure, the static hcp solid phase, mixed with the amorphous phase is observed. Upon interface stress unloading, the broad interference peak associated with the amorphous state is no longer present (Figure 7).

Conclusion

New developments to our single-pulse XRD diagnostic include an all-tungsten head and cathode for reduction of x-ray scattering, and a fiber-optically reduced, large-format CCD imaging system. These improvements were implemented for dynamic experiments in FY 2011. Results of the dynamic experiments with zirconium indicated that a dynamic phase transition on the nanosecond time scale requires significantly higher pressure to be observed than for static high pressures. We consistently observe a mix of amorphous and solid phases during shock loading for both zirconium and KCl, as we have previously reported for tin (Morgan 2008). Zirconium experiment 110614-2 indicated that approximately 100 ns after shock unloading the amorphous state is absent, and the material has completely returned to its initial hcp phase.

References

d'Almeida, T., Y. M. Gupta, "Real-time x-ray diffraction measurements of the phase transition in KCl shocked along [100]," *Phys. Rev. Lett.* **83** (2000) 330–333.

James, R. W., *The Optical Principles of the Diffraction of X-rays*, Ox Bow Press, Woodbridge, Connecticut, 1982, 20–25.

Morgan, D. V., D. Macy, G. Stevens, "Real-time x-ray diffraction measurements of shocked polycrystalline tin and aluminum," *Rev. Sci. Instrum.* **79** (2008) 113904.

Morgan, D. V., M. Grover, D. Macy, M. Madlener, G. Stevens, W. D. Turley, "Observations of shock-loaded tin and zirconium surfaces with single-pulse x-ray diffraction," *Powder Diffraction Journal* **25** (2010) 138.

Rigg, P. A., C. W. Greeff, M. D. Knudson, G. T. Gray, R. S. Hixson, "Influence of impurities on the α to ω phase transition in zirconium under dynamic loading conditions," *J. Appl. Phys.* **106** (2009) 123532.

Turneaure, S. J., Y. M. Gupta, "Shock induced phase change in KCl single crystals: Orientation relations between the B1 and B2 lattices," *J. Appl. Phys.* **105** (2009) 013544.

Turneaure, S. J., Y. M. Gupta, "Real time synchrotron x-ray diffraction measurements to determine material strength of shocked single crystals following compression and release," *J. Appl. Phys.* **106** (2009) 033513.

Warren, B. E., *X-ray Diffraction*, Dover Publications Inc., New York, 1990, 189–191.

In Situ Shock-Anvil Thermometry

Gerald Stevens,[1,a] Kevin Kyle,[a] Gene A. Capelle,[a] and Dale Turley[a]

Temperature measurements remain an elusive, high-priority goal for the shock physics community, and despite much recent progress in optical pyrometry (Seifter 2011) the precision of available techniques is still limited. The goal of this SDRD project was to investigate new materials for dynamic Raman spectroscopic temperature measurements. Raman spectroscopy is attractive because it can determine material temperatures based on first principles in an unambiguous manner.

Background

In order to determine material characteristics under extreme conditions, shock physicists historically have relied predominantly on shock and sound-speed velocity measurements and application of the Rankine-Hugoniot jump conditions in order to determine the stress, compression, density, and internal energy of shocked materials. The temperature of the shocked material is typically calculated, and only occasionally measured. Under ramp-loading (shockless) conditions, any deviation from true isentropic loading results in an unknown final thermodynamic state. Further, relating shock or ramp-loading experiments to phase diagrams that are acquired statically in diamond anvil cells requires knowing the material temperature. Optical pyrometry may be used to measure the thermal radiance of a shocked metal sample and infer the temperature if one determines the dynamic emissivity (Seifter 2011). For transparent, dielectric materials with extremely low emissivities, such as windows, an alternate method of determining temperature using Raman spectroscopy has been developed at Washington State University (Pangilinan 1997). This approach has the benefit of measuring an effect that depends directly on the temperature of the sample. Nothing needs to be assumed or inferred because the other parameters required to determine the temperature (the ground-state vibrational energy separation and probe laser wavelengths) are measurable.

Raman scattering is a process by which incident laser light is scattered at frequencies lower (Stokes [S]) and higher (anti-Stokes [AS]) than its original frequency. The difference in energy of the scattered light from that of the incident energy corresponds to the separation between vibrational ground states of the scattering molecules. More importantly, the amplitudes of the scattered S and AS light depend on the population of the ground state. At low temperatures all electrons are found in the ground state (E_0 in Figure 1), and only the Stokes shift (loss of energy from the incident light to the vibrational excitation) is possible. At higher temperatures the population of the excited states of the

---

[1] stevengd@nv.doe.gov, 805-681-2219

[a] Special Technologies Laboratory

molecules follow a Maxwell-Boltzmann distribution as a function of energy separation (ω_V) between the ground state and the first excited vibrational state. The intensity ratio of anti-Stokes (I_{AS,ω_V}) to Stokes scattered (I_{S,ω_V}) light follows the relationship:

$$\frac{I_{AS,\omega_V}}{I_{S,\omega_V}} = \frac{\left(\omega_L + \omega_V\right)^4}{\left(\omega_L - \omega_V\right)^4} \cdot e^{\left(\frac{-\hbar\omega_V}{k_B T}\right)},$$

(1)

where ω_L is the frequency of the laser, ω_V is the frequency between the ground state and the first excited vibrational state, and T is the temperature in Kelvin.
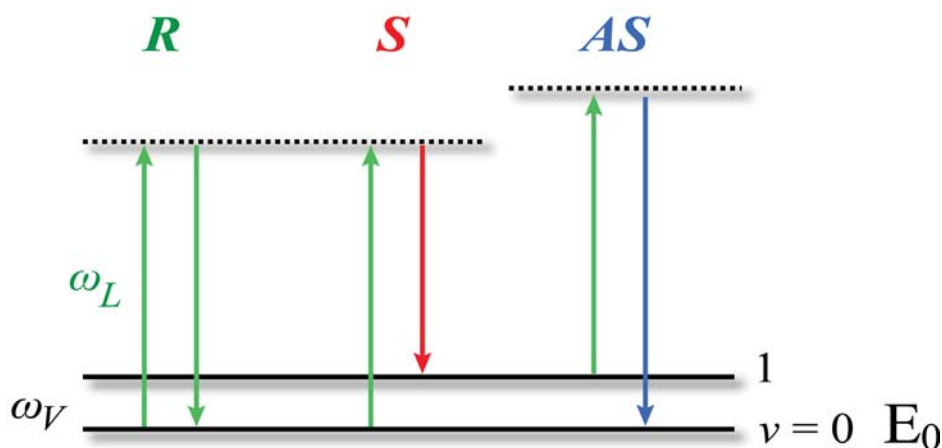
Figure 1. Level diagram showing Rayleigh (R), Stokes (S), and Anti-Stokes (AS) scattering

Raman spectroscopy has been used to determine shock temperatures of carbon tetrachloride (CCl_4) (Pangilinan 1997) and ammonium perchlorate (Winey 2002). In this work, we were interested in extending the technique to provide temperature information of bulk polymethyl methacrylate (PMMA), often used as a shock-anvil sample, or of the glue layer (Loctite 326-polyurethane methacrylate) that we use to bond a metal sample to a lithium fluoride anvil for shock experiments. Some of the earliest dynamic temperature experiments involved thermocouples and thermistors embedded in PMMA (Bloomquist 1980, 1981). There was considerable disagreement between these experiments as well as subsequent attempts by others to refine the technique, with speculation that the thermal diffusivity of PMMA shocked above 2 GPa increases by three orders of magnitude. Because we were ultimately interested in measuring the bulk temperature of shocked metals, such an increase in thermal diffusivity in a glue bond would be of critical importance in estimating the bulk temperature from the measured temperature of a shocked metal-glue interface.

Raman-active dyes were chosen as an attractive candidate for a material-compatible probe layer to be embedded within glue or PMMA. Their strong Raman scattering properties would ideally allow us to use thin layers, significantly thinner than the 0.15 to 1.0 mm CCl_4 and ammonium perchlorate samples used in the previous experiments.

Project

Raman Material Selection

The ideal material for dynamic, in situ temperature measurements of shocked PMMA would have a strong Raman scattering cross section, a small enough Raman shift to observe the anti-Stokes peak at ambient temperature, and the ability to survive at elevated temperatures close to where PMMA pyrolysis begins. Further, the material would need to have shock-impedance properties close to PMMA. It would need to be soluble in a solute that also weakly dissolves PMMA so that the probe layer could be placed between and join two layers of PMMA. It would also be desirable if the material were soluble in Loctite 326.

Our initial list of Raman-active materials included two broad categories: materials with C-Cl bonds and organic dyes. The first class was chosen to leverage against the successful S-AS shock temperature measurements of CCl_4 by Pangilinan (1997). Materials with C-Cl bonds have large polarizability and vibrational modes that give Raman bands at about 280, 430, and 830 cm^{-1}. Sodium trichloroacetate (NaTCA) is an organic salt that has a relatively high melting point (greater than 300°C) and a well-defined and documented Raman spectrum. Our solubility measurements indicated that it dissolves well in tetrahydrofuran (THF), methanol (MeOH), and a 4:1 methanol-to-ethanol mixture (MeOH:EtOH) to be used as a pressure medium in our diamond anvil system. THF is a solvent that dissolves PMMA, and the THF NaTCA mixture was found capable of bonding PMMA samples while producing a thin, slightly hazy, but crystal-free layer of NaTCA.

The second class of materials was organic dyes. These were investigated in terms of Raman signal level, Raman shift, fluorescence, and solubility. Materials we looked at included Bis(methylstyryl) benzene (BMSB); 3,9-Bis(trichloromethyl)-2,4,8,10 tetraoxaspiro-(5.5)-undecane; 5-Chloro-2-(trichloromethyl)benzimidazole; ethyl trichloroacetate (a solvent); 1,1,1-trichloro-2,2-Bis (4hydroxyphenyl)ethane; and (trichloromethyl)benzyl acetate.

Raman spectra were recorded with 50 mW of light from a 300 mW, 532 nm, diode-pumped solid-state continuous wave (CW) laser from Intellite. An f/4 benchtop optical system was configured for both sending and receiving light from pressed-powder samples. Collected light went through a fiber to an Ocean Optics QE65000 spectrometer with a range of 400 to 800 nm. The dominant Rayleigh-scattered 532 nm beam was blocked with a Semrock StopLine notch filter with an optical density >6 at the laser line frequency. 3,9-Bis(trichloromethyl)-2,4,8,10-tetraoxaspiro(5.5)undecane; 5-Chloro-2-(trichloromethyl)benzimidazole; and (trichloromethyl)benzyl acetate all exhibited fluorescence at

longer wavelengths that complicated determination of the Stokes amplitude, making them undesirable. BMSB had strong Stokes lines at 1187 and 1590 cm^{-1}, with the 1187 cm^{-1} AS band having just enough population to observe it just above the noise floor. Of the two remaining candidates, BMSB was very slightly soluble in the solvents we tested (THF, tolulene, MeOH, acetone, water, ethyl trichloroacetate), but 1,1,1-trichloro-2,2-Bis(4hydroxyphenyl)ethane was not soluble. Thus, we narrowed our search for viable Raman-active materials to NaTCA and BMSB.

Various preparation techniques were tested in order to prepare two sample configurations for shock experiments. The first configuration was a 1 mm aluminum target with a 5 mm thick PMMA sample secured by a glue layer impregnated with Raman-active material. The other configuration was an aluminum sample with a 3 mm thick PMMA window glued on with Loctite 326, followed by a thin Raman-active layer and a second 3 mm thick PMMA window. The first sample configuration was designed to give us insight into the temperature of shocked glue at a target/anvil interface. The second configuration was designed to give us an in situ temperature gauge midway through a shocked PMMA sample.

BMSB's poor solubility proved to be problematic, and samples prepared with BMSB were typically heterogeneous with flakes of the material remaining in the solution. This was unfortunate, because the Raman-scattered signal from BMSB was significantly stronger than that of NaTCA (Figure 2).
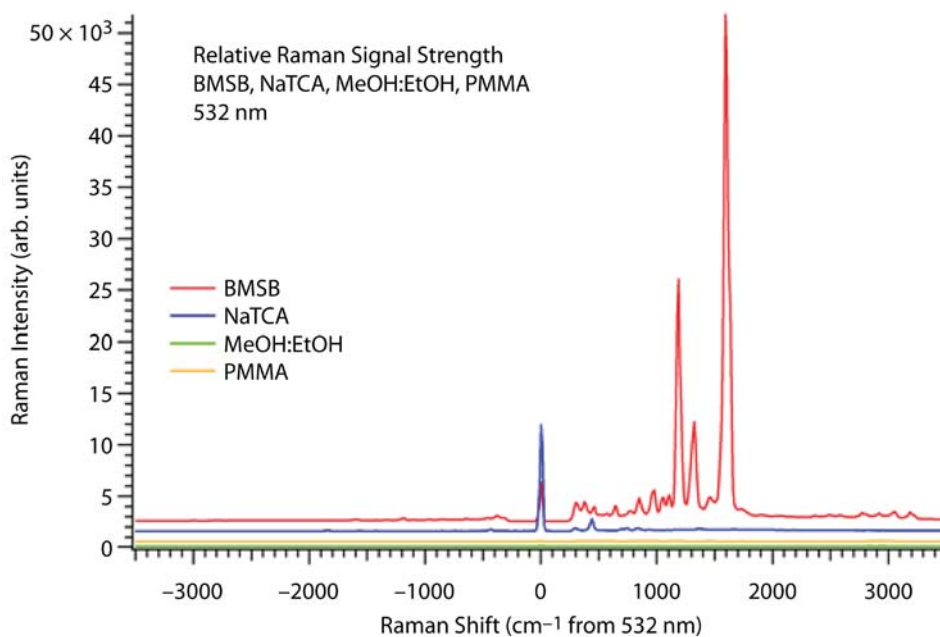
Figure 2. Relative intensities of BMSB and NaTCA Raman lines. Also included for reference are the Raman spectra of MeOH:EtOH and PMMA. The latter two materials are very weak Raman scatterers and are consistent with zero on the scale displayed.

NaTCA, on the other hand, is quite soluble, and samples for both shot configurations were prepared. Further, the Raman spectrum (measured at 785 nm with the handheld unit) from NaTCA in Loctite was stable in time over several days. Unfortunately, the presence of NaTCA hindered the curing process.

Loctite 326 is extremely viscous. In order to make the NaTCA/Loctite solution in a quantitative manner, the weight of each compound was used. For Loctite, 0.800 g was squeezed into a 3 mL vial. Then 0.120 g of NaTCA was directly added to this vial. The mixture was stirred occasionally over a 24-hour period to allow the NaTCA to dissolve in the Loctite. To make the target, a small amount of the solution was placed on the aluminum round. The 3 mm thick PMMA window was carefully placed on the Loctite/NaTCA mixture. The stack was held in a press in the dark overnight.

The BMSB/Loctite 326 solution and the target were created in a similar manner, using 0.007 g of BMSB. Crystals of BMSB remained undissolved in the Loctite/BMSB solution. Fabrication of the target followed the above procedure.

Pressed-powder samples of NaTCA and BMSB were inserted into a heated cell, and spectra were taken in order to test the material's agreement with the theoretical intensity ratio in Equation 1. The AS/S intensity ratio for BMSB's two Raman lines closely matched the predicted value, while NaTCA showed slightly more complicated behavior (Figure 3).
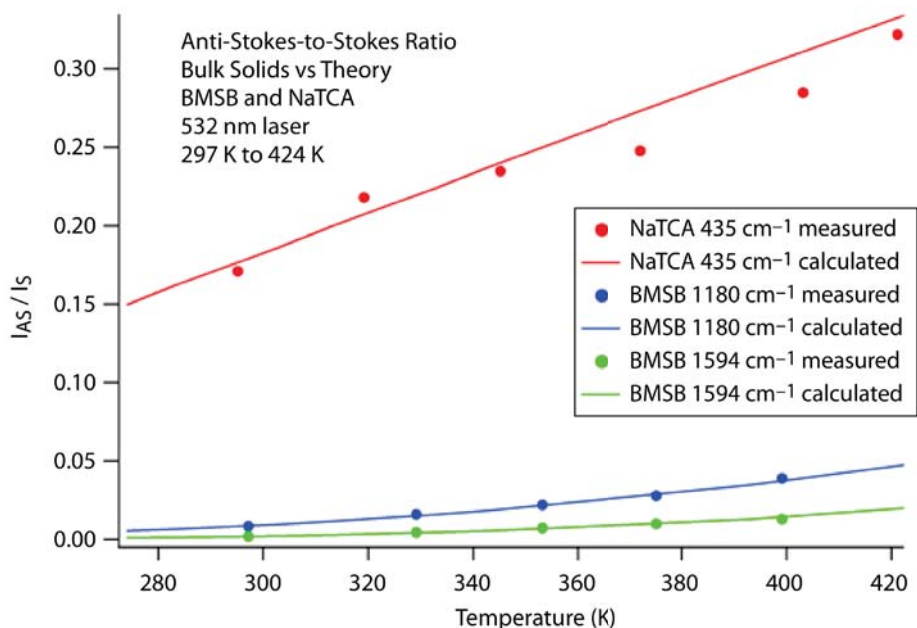
Figure 3. Measured (symbols) ratio of anti-Stokes to Stokes signal levels as a function of temperature for NaTCA and BMSB. Also displayed are the theoretical values for these ratios.

Pulsed–Laser System Results

While a small Intellite 532 nm laser was used for preliminary benchtop measurements on the Raman-active samples, the eventual intended Boom Box application requires a pulsed excitation source for time-resolved measurements. Therefore, for later experiments, the CW laser was replaced with a small pulsed Nd:YAG laser (model CFR400, Big Sky Laser Technologies, Bozeman, Montana) operated at low (~1 mJ) power and with output doubled to 532 nm. After reflection from two beam-cleanup mirrors (to remove residual 1064 nm light), the laser output was launched by means of a 25 mm focal length lens into a 600 μm core fiber. The output end of the fiber was mated to a matched achromatic pair of lenses with 25 and 50 mm focal lengths. This illumination probe was 50 mm from the sample, and the light was incident normal to the sample. The probe magnified the 600 μm fiber by a factor of two. While for these initial experiments it was just as effective to position the unterminated fiber output end close to the sample and let the light spray out onto the sample surface, this would not be a viable option for the Boom Box experiments. The excitation pulse reaching the sample was nominally 15 ns wide (FWHM) with an energy of 0.75 mJ per pulse; the pulse rate was single shot to 5 Hz.

Light from the target was collected with another matched 25 mm and 50 mm focal-length achromatic pair placed 25 mm from the target at approximately 45° off-normal. Scattered light was collected from a 300 μm spot and launched into another 600 μm fiber. Output of this fiber was sent into a set of matched relay lenses to provide nearly parallel light into a 532 nm notch filter (NF01-532U, Semrock Inc., Rochester, New York). Output of the relay continued into a 29-fiber, close-packed, stripped bundle of 100 μm core fibers that converted the shape from a circle to a line, and relayed the collected light onto the slit of a CP200 imaging spectrograph. The spectrograph gives a resolution near 3.5 nm in the region of interest, which is enough to see the spectral features of interest. Higher resolution would have been desirable, but such equipment was not available. An intensified CCD at the focal plane collected the light. The microchannel plate intensifier allowed fast shuttering of the detector, which would be needed at the Boom Box to eliminate high-explosive light shortly after the data. A gate width of 200 ns, starting 50 ns before the laser pulse, was used. Data were first collected using 50 accumulations (data from 50 laser pulses, added together), but once the system was aligned properly, a reasonable Raman signal could be collected with one laser pulse.

Because there was concern of spurious Raman signals being generated in the silica fiber of the measurement system, a second set of measurements was made after eliminating as much of the fiber in the system as possible. The lens and fiber were removed, and the 532 nm laser excitation beam was sent directly onto the target; in this case the beam was about 6 mm in diameter with an energy near 5 mJ. For detection, the 532 nm notch filter was placed directly in front of the spectrograph input slit, and the spectrograph was positioned about 15 cm from the sample and normal to the line of sight from it, with no other intervening optics. This distance was sufficiently long that the light entering the notch filter was essentially parallel (necessary for the notch filter to function correctly), but still allowed the signal to be measured with a reasonable signal-to-noise ratio.

Three issues became evident from the initial measurements made with the pulsed-laser system. First, in our measurements of NaTCA powder, the large S and AS peaks at ±434 cm^{-1} were present even when we removed the sample powder, indicating that they were generated in the fibers used to send and receive probe and scattered light. Figure 4 shows signals from a powder sample and from light scattered from an aluminum block (black and blue curves), both of which contain lines from silica fibers at about 440 cm^{-1}.
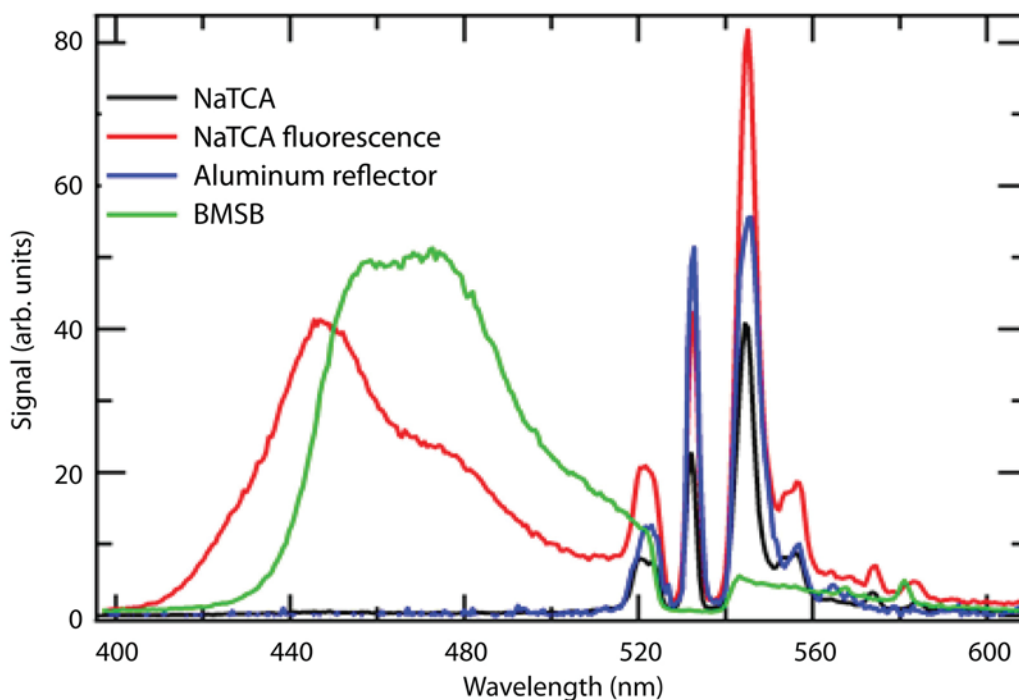
Figure 4. Raman signal from pressed powder NaTCA (black) and the same material positioned differently, exhibiting fluorescence (red). Light reflected from an aluminum sample (blue) shows that the 440 cm^{-1} S and AS peaks are likely silicon oxide peaks generated within the laser coupling fiber, not from the NaTCA. BMSB has severe fluorescence issues, with the large green peak washing out any hints of the AS peaks for that material.

Next, for certain configurations of pure NaTCA powdered samples and all configurations with BMSB, a large fluorescence signature was present. This fluorescence completely overwhelms the tiny AS peaks required for temperature measurements. The materials are both fluorescent, but their absorption peaks are significantly lower than 532 nm, which leads us to believe that a two-photon excitation is responsible for the observed fluorescence. Two-photon excitation is a process that is nonlinear in excitation intensity, and when our pulsed-laser system is focused to a 1 mm^2 spot, its intensity averages about 15 MW/cm^2 during a pulse. Reducing the laser intensity by moving the sample away from

focus reduces the fluorescence for NaTCA (Figure 4, black trace). BMSB is unfortunately an efficient two-photon material (Nag 2010), and we could not reduce the amplitude of the fluorescence peak significantly.

Last, the signal amplitudes for the Stokes lines for both materials were fairly small, even for the *neat pressed-powder samples*. Thin layers embedded within PMMA samples scatter orders of magnitude less light than the pressed-powder samples. Because of this, we did not implement improvements to the pulsed-laser system setup such as open-air light coupling or laser-line passband filtering to remove the silica Raman lines.

Diamond Anvil Cell (DAC) Measurements

In addition to testing the pulsed system, we were concerned with the behavior of the Raman-active dyes at high pressure in a dynamic experiment. Pressure-induced line-shifts, broadening, and intensity changes could all affect the interpretation of dynamic Raman spectra. We set up an easyLab Diacell HeliosDAC to observe the behavior of the selected Raman lines at elevated pressures and temperatures. We used ~10 μm ruby microspheres as a pressure manometer, and we measured the Raman spectrum up to 16.0 GPa for a NaTCA sample. Unfortunately, system Raman lines from the coupling fiber at 440 cm^{-1}, and from the diamond itself at 1330 cm^{-1}, obscured the very weak signal from a 25 μm thick by 100 μm diameter saturated NaTCA in a 4:1 MeOH:EtOH pressure medium. Air-coupling the laser and spectrometer would help, but the ruby sample bridged the diamonds and cracked them at 16 GPa.

Conclusion

Raman-active materials can be used to make in situ temperature probe layers in shock experiments. After rejecting a half-dozen other candidates, we focused primarily on two materials: NaTCA and BMSB. BMSB gave excellent signal levels in static measurements. However, under the pulsed-laser conditions (tens of ns, tens of MW/cm^2) required to make a measurement during a shock experiment, the material is fluorescent. Further, no reasonable solvent was found that could dissolve BMSB while preserving the integrity of PMMA. NaTCA did not suffer from this problem, and samples were successfully fabricated with Raman-active probe layers of the material. The Raman scattering cross section for this material was significantly lower than BMSB, and other artifacts, such as silica Raman peaks from fiber-coupling and two-photon fluorescence, easily overwhelmed the signal in a dynamic experimental mockup.

The need to demonstrate a temperature measurement technique that characterizes transparent material such as glue or shock anvils remains. We hope to find alternate materials or preparation techniques to continue this investigation in the future.

Acknowledgments

References

Bloomquist, D. D., S. A. Sheffield, "Thermocouple temperature measurements in shock-compressed solids," *J. Appl. Phys.* **51**, 10 (1980) 5260–5266.

Bloomquist, D. D., S. A. Sheffield, "Shock-compression temperature rise in polymethyl methacrylate determined from resistivity of embedded copper foils," *Appl. Phys. Lett.* **38**, 3 (1981) 185–187.

Nag, O. K., R. R. Nayak, C. S. Lim, I. H. Kim, K. Kyhm, B. R. Cho, H. Y. Woo, "Two-photon absorption properties of cationic 1,4-Bis(styryl)benzene derivative and its inclusion complexes with cyclodextrins," *J. Phys. Chem. B* **114**, 29 (2010) 9684–9690.

Pangilinan, G. I., Y. M. Gupta, "Use of time-resolved Raman scattering to determine temperatures in shocked carbon tetrachloride," *J. Appl. Phys.* **81**, 10 (1997) 6662–6669.

Seifter, A., M. Grover, D. B. Holtkamp, A. J. Iverson, G. D. Stevens, W. D. Turley, L. R. Veeser, M. D. Wilke, J. A. Young, "Emissivity measurements of shocked tin using a multi-wavelength integrating sphere," *J. Appl. Phys.* **110** (2011) 093508.

Winey, J. M., Y. A. Gruzdkov, Z. A. Dreger, B. J. Jensen, Y. M. Gupta, "Thermomechanical model and temperature measurements for shocked ammonium perchlorate single crystals," *J. Appl. Phys.* **91**, 9 (2002) 5650–5656.

this page intentionally left blank

Improved Understanding of Windows for Optical Shock-Wave Diagnostics[†]

Dale Turley,[1,a] David Holtkamp,[b] Gene A. Capelle,[a] Gerald Stevens,[a] and Lynn Veeser[c]

In shock wave equation-of-state experiments, a lack of understanding of the physical and thermodynamic behavior of optical windows and sample-to-window attachment methods can limit the accuracy and precision of dynamic pyrometry, radiance, and reflectivity measurements. In an attempt to understand some of the temperature differences between a gap or a thin glue layer separating the sample and window, we modeled results from recent experiments that measured the time-dependent radiance of shocked tin samples in both configurations. It appears that much of the extra heating caused by a gap can be explained by shock compression of the surface irregularities (20 nm perturbations) of the diamond-turned samples. For samples attached by glue, the glue fills in the space and reduces the compression heating. We also captured high-speed images and measured the spectral output (350–750 nm) of light generated by a lithium fluoride (LiF) window during a dynamic experiment. The light appears to originate from the outer edge of the LiF window, and the optical signature is characterized by sharp spectral lines and is a strong function of the surrounding gas atmosphere. We completed two manuscripts summarizing experimental campaigns in which we measured the change in emissivity in the infrared spectral range (1.2–5.4 μm) of the free surface of a tin sample releasing to a liquid state (Seifter 2011) and at its interface with a LiF window upon release of a 25 GPa shock wave from the tin into the window (Turley "IR" 2011). For the free-surface study, emissivity increases nearly 10-fold upon release to a liquid state. For a polished sample beneath a LiF window, emissivity changes were small for all but the longest wavelength band, where uncertainties were high because of poor signal-to-noise ratio at that wavelength.

Background

Optical reflectivity and radiance diagnostics for equation-of-state (EOS) temperature measurements and detection of phase transitions typically are used under a transparent window. This prevents the sample from expanding when the shock decays, keeping the sample near its shocked condition long enough to perform a measurement. Presently, such measurements suffer from problems related to the window attachment. A gap or glue surface between the optically emitting or reflecting surface and the window can affect the optical transmission and apparent emissivity, and unwanted light generated in the attached window can interfere with reflectivity and pyrometry measurements. These issues can raise uncertainty in absolute temperature measurements to greater than 10%, a value well outside the

1% uncertainty desired for EOS measurements. Although radiance is still viewed as the preferred diagnostic for dynamic temperature measurements, these uncertainties have limited confidence in this method.

Last year we demonstrated the use of integrating spheres to illuminate a sample and measure its emissivity from the change in sample reflectance upon shock arrival at the sample-window interface, and we have now published the results (Turley "IR" 2011). We also measured radiance emissions for several window attachment methods, including thick and thin layers of transparent epoxy, mechanical (with a small gap), and glued with thin chromium layers sputtered onto the sample before gluing to the window (Turley "Improved" 2011). In this study we investigated a number of other issues to determine the scientific basis of their effects and to quantify their contributions to radiance-based temperature measurements. In particular we modeled the heating of a sample with its surface attached mechanically to a window. We compared the model with measurements of such a system in a vacuum and measurements of a sample glued to a window. We measured the spectra from LiF windows of various configurations to further understand the source of unwanted, non-thermal light, which constitutes a background for pyrometer measurements and must be eliminated or corrected for. Finally, based on this work, we have been asked to modify our technique so that it can be fielded on the Joint Actinide Shock Physics Experimental Research (JASPER) shots beginning in FY 2013.

Project

Estimated Shock Heating of a Thin Layer of Diamond–Turned Tin in the Window–Target Gap

In FY 2010 we performed pyrometric temperature measurements on tin samples attached to LiF windows to study the effects of the attachment method, both glued and mechanically pressed together with a small gap (Turley "Improved" 2011). For samples held together mechanically (micron-sized gaps) and fielded in a vacuum, the temperature immediately after shock release shows a spike, which is not present when the window is glued to the sample. After about 30 ns the temperatures are similar in both experiments (Figure 1).

With a Zygo optical surface profilometer, we measured the surface roughness of our diamond-turned samples. A typical surface has a sawtooth profile with peaks and distance between peaks both around 20–25 nm. In addition, there may sometimes be micron-scale features, which were not part of this work. To predict the physical state of material at the interface between a window and a shocked tin surface, we assume (Urtiew 1974) that between the window and sample there is a uniform layer of tin with half-normal density and thickness comparable to the measured surface roughness. We used the hydrodynamic codes CTH and WONDY to calculate the internal energy from shock heating, and in the case of WONDY, compression heating as well, to estimate the temperature of this thin layer of shock-compressed porous tin. We then used heat conduction models (Grover 1974) to estimate the rate at which this hot layer will equilibrate with the adjacent shock-compressed, initially solid

tin sample. Because optical emissions originate within an optical skin depth (~30 nm) of the sample surface,[2] the temperature of most interest is about 15 nm from the window, i.e., about 5 nm into the compressed solid tin and behind the low-density tin layer, which is now compressed to ~10 nm.
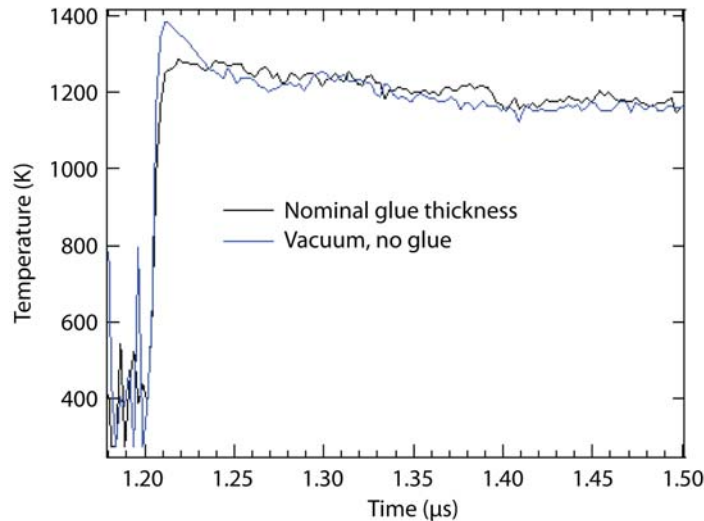
Figure 1. Shock-induced interface temperature vs time measured for the nominal glue and vacuum configurations. Shock arrival is at approximately 1.2 µs.

Using WONDY and CTH we calculated one-dimensional shock waves propagating at 2.2 km/sec into porous tin to estimate its shock heating. The velocity was chosen to obtain a shock temperature of about 1100–1200 K and pressure before release of 33 GPa in the solid tin, typical of our previously reported (Turley "Improved" 2011) explosive experiments. Only the first shock was considered. In general, there will be some following ring-up as the gap closes, but we neglected the heating from the subsequent shocks in an effort to get a first-order estimate. There are some differences between CTH and WONDY, but the results, shown in Table 1, are in rough agreement. CTH shows a lower temperature for the porous tin, likely because it does not include thermal heating effects. Both codes are thought to overestimate the heating slightly because latent heat from phase changes is neglected. (For WONDY we have a three-phase tin EOS subroutine available, but we did not use its results here because it does not calculate temperatures, only internal energies.) We assume that the WONDY

---

[2] The skin depth for tin at ambient conditions is $\delta_0 = \sqrt{(2\rho/\omega\mu_0\mu_R)}$, where ρ is the electrical resistivity and the μ's are the magnetic permeability constant and the relative magnetic permeability. For tin, the resistivity is $\rho = 115$ nΩ m and μ_R is of order 1. For 2 µm IR light, the frequency is $\omega = 2\pi c/\lambda \sim 1 \times 10^{15}$, giving $\delta_0 \sim 15$ nm. At higher temperatures the skin depth is larger, $\delta/\delta_0 \sim T/T_0 \exp[2\gamma_0(\rho_0/\rho - 1)])$. For shocked tin at 250 kbar, typical of our conditions, $\gamma_0 \sim 1.5$, $\rho_0/\rho \sim 0.78$, $T/T_0 \sim 4$, giving $\delta \sim 2\delta_0 = 30$ nm. If we have 20 nm of initially 50% porous tin (compressed to 10 nm between the window and the sample), the detectors will see this layer plus about 20 nm of colder, initially solid tin adjacent to it.

calculation is more realistic because it includes the compression heating. To account for latent heat, we rounded off to 6000 K. This temperature is perhaps still somewhat high because of ionization, but it should give a realistic rough estimate of the amount of energy in the compressed porous tin layer.

Table 1. Specific energy and temperature calculations for porous tin and polymethyl methacrylate (PMMA)

Code	WONDY	CTH	WONDY	CTH
Material	Porous Tin	Porous Tin	PMMA	PMMA
ρ_0 **(gm/cm^3)**	3.6435	3.6435	1.186	1.186
ρ **(compressed)**	6.88	7.28	1.77	1.772
P (Gdy/cm^2)	218	173	108	102
½ P (V$_0$ − V) (J/g)	1400	1180	1510	1500
ΔE from code (J/g)	1400	—	1490	—
C$_p$ (J/g K)	0.227	0.227	2.1	2.1
½ P (V$_0$ − V)/C$_p$ (K)	6200	5200	720	750
ΔT from code (K)	—	5400	—	340

For comparison we also calculated the case of a 5 μm glue layer between the sample and window, the configuration for the glue shot of Figure 1. Here, we used the EOS of polymethyl methacrylate (PMMA) since EOS parameters do not exist for the glue. (PMMA is likely to have comparable density, heat capacity, and thermal conductivity to the glue.) For compressed glue or PMMA, the shock temperature is a little over 700 K using either code. The change in specific energy is not greatly different for porous tin and PMMA. However, the heat capacity of PMMA is ten times larger, so PMMA remains relatively much cooler. Results from the calculations are shown in Table 1.

Next, using the one-dimensional heat conduction equations, we modeled a 10 nm hot layer positioned between two thick tin samples to calculate the rate of heat change. This is solved by Grover's heat conduction equation, Equation 6 (Grover 1974), for a thin source of thickness λ and temperature T_1 = 6000 K between two samples of the same (initially solid) material at temperature T_0 = 1000 K. The solution is:

$$T(x, t) = T_0 + T_1/2 \ \{\mathrm{erf}\,[(x + \lambda/2)/2\sqrt{\kappa t}] - \mathrm{erf}\,[(x - \lambda/2)/2\sqrt{\kappa t}]\}, \tag{1}$$

where x is the distance from the hot layer, t is the duration of the heat conduction, and κ is the thermal diffusivity of tin, assumed to be 0.235 cm^2/sec. Because one side of our experiment has a LiF window, for which the thermal conductivity is only about 10% as large as for tin, we slowed the conduction rate to half by using κ = 0.12 cm^2/sec.

The results are shown in Figure 2 for *x* = 5, 100, and 500 nm. On a time scale of interest in the case of a detector with a resolution of 2–5 ns, the first two calculations at 5 and 100 nm (bracketing the optical skin depth) are nearly identical. They show a quickly cooling temperature spike that levels off within the time scale of a pyrometric measurement to 20–30 K above the temperature when there is no hot layer. At 500 nm from the hot layer, the spike is greatly reduced because little heating occurs as the conduction is fast and the amount of thermal energy in the hot layer is small. For the tin in the shocked bulk sample, the temperature within 100 nm of the window is relatively uniform after the first couple of nanoseconds. One consequence of this rapid heat conduction is that the porous tin cools to equilibrium with the tin sample in time <10 ns.
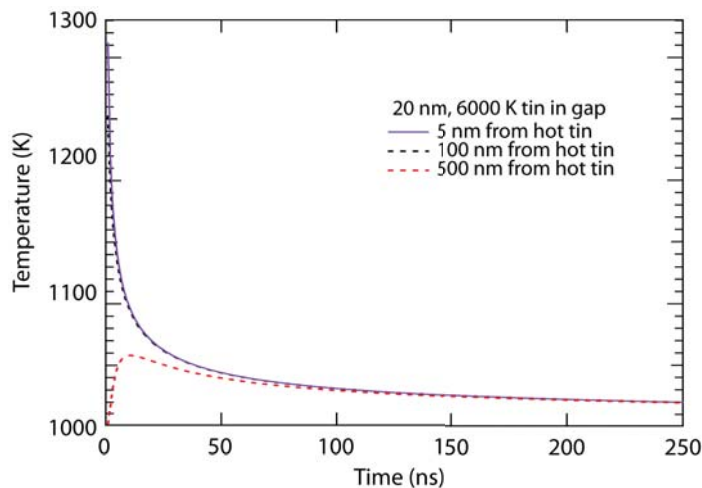
Figure 2. Estimated tin temperature at three positions near the surface of a diamond-turned sample adjacent to a LiF window after compression and shock heating. Grover's (1974) heat-conduction equations were used for a layer of 6000 K tin placed between a tin sample at 1000 K and a LiF window. The temperature equilibrates throughout the first 100 nm of tin within a few nanoseconds. A detector beyond the window will view a temperature characterized by the purple curve. Farther from the interface (red curve) it takes about 10 ns for the tin to heat up, and after that time that region cools as the heat conducts away into the bulk tin faster than it arrives from the (formerly) hot layer at the interface.

Figure 3 shows a comparison between the glue shot data of Figure 1 added to the calculated heating from compressing the porous tin (blue) and the measured gap shot (green). From this it appears that the calculated heating is roughly correct, although, after the first 20–30 ns, the measured vacuum-gap

temperature drops off a little faster than the calculated one. Note that the vacuum-gap shot (green curve) indicates a small temperature jump at 1.35 μs, about 100 ns after shock arrival. This jump does not appear in the glue shot, and we have not been able to model or understand it. Similar temperature jumps often occur when the shock stress releases for some reason.
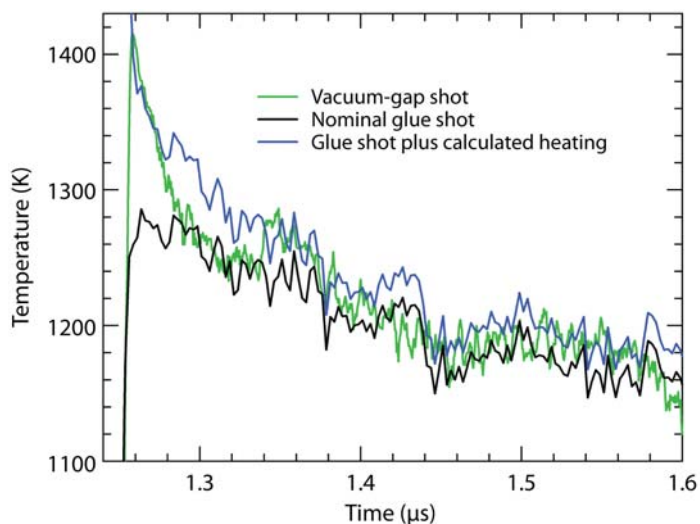
Figure 3. Comparison between measured vacuum-gap shot (green) and glue shot with calculated heating (blue). The glue shot without heating is shown in black. The calculated heating from the porous tin equals the purple curve of Figure 2 minus 1000 K, the temperature of the shocked, solid tin. The green and black curves are the same as shown in Figure 1 on different temperature and time scales.

Knowing that the tin equilibrates quickly allows us to speculate somewhat on what might happen if there is a thin film of some other material, such as chromium, on the sample. Compared to tin, chromium has higher emissivity but similar thermal conductivity and diffusivity. Its value in this case would be to increase the detected radiance because of its higher emissivity. This work indicates that it should equilibrate very quickly to the tin temperature, even in the presence of a glue layer. If the chromium were to be deposited onto the window directly and then glued to the sample, the results might be different.

For much higher shock temperatures, such as might appear in high-pressure JASPER experiments, it is possible that the glue will disintegrate and may cause problems, such as partial absorption of light intended for the detectors. Consequently, it will be important to learn the upper limit of the glue transparency. Certainly we will also need improved understanding of the thermal conductivities of the metal sample, window, and glue under shock conditions.

Shock–Induced Light Production in a LiF Window

As described in the **Background** section, shock-induced light emitted from a LiF window is a key noise source for various optical diagnostics. Understanding the nature of this signal is an important step to designing methods to mitigate the problem. In FY 2010 we performed experiments to determine the spectral content of this light and its physical origin. In these experiments, we selected a package from previous studies known to generate significant light when shocked. This package (Figure 4) was composed of a 40 mm diameter and 1 mm thick aluminum cylinder. A LiF window (25 mm diameter and 10 mm thick) was attached to the top of the aluminum target. This package was shock loaded using a 25 mm diameter by 8.8 mm thick cylinder of PBX-9501 explosive.
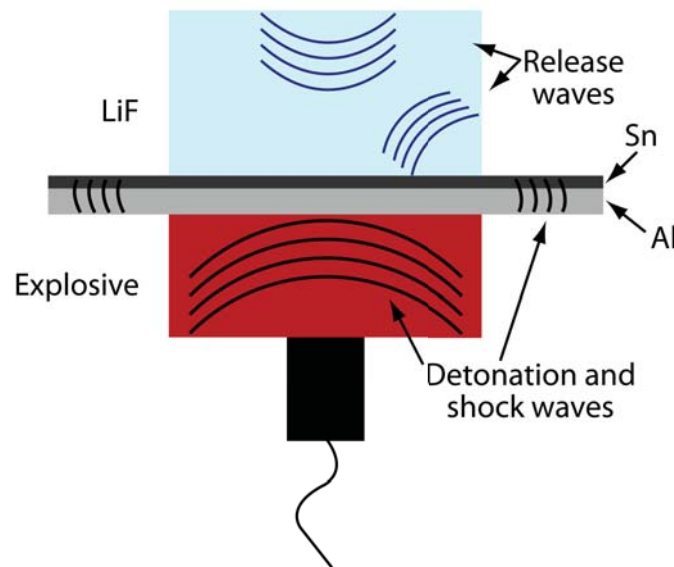
Figure 4. Sketch of explosive package used for the study of shock-induced light from a LiF window 25 mm in diameter and 10 mm thick. The aluminum target is 40 mm in diameter and 1 mm thick. The explosive is a 25 mm diameter, 8.8 mm thick PBX-9501 cylinder.

In FY 2011 we performed additional spectral and high-speed imaging experiments. The results of the spectral experiments differ significantly from the FY 2010 study. In FY 2011 we modified the explosive package by increasing the internal diameter of the plastic housing encasing the experiment. Using this configuration, the shock wave strikes the package wall after the experiment is complete, and light emitted from the shocked plastic does not contaminate the measurements. With this new

configuration a very different spectral character was measured. In the previous work we measured a broad structureless emission; however, with the new package configuration, the measured spectrum was characterized by a number of sharp spectral lines between 350 and 800 nm.

Figure 5 shows typical experimental signals recorded using this new configuration. All signals were relayed from the experiment to the recording systems using a compact fiber-optic probe developed from previous shock experiments. Photomultiplier tube (PMT) data were collected simultaneously with the optical multichannel analyzer (OMA) microchannel plate (MCP) gate monitor and PDV data. The input to the PMT was filtered through a 600 × 40 nm band-pass filter, and the PMT output of a typical experiment is shown in Figure 5.
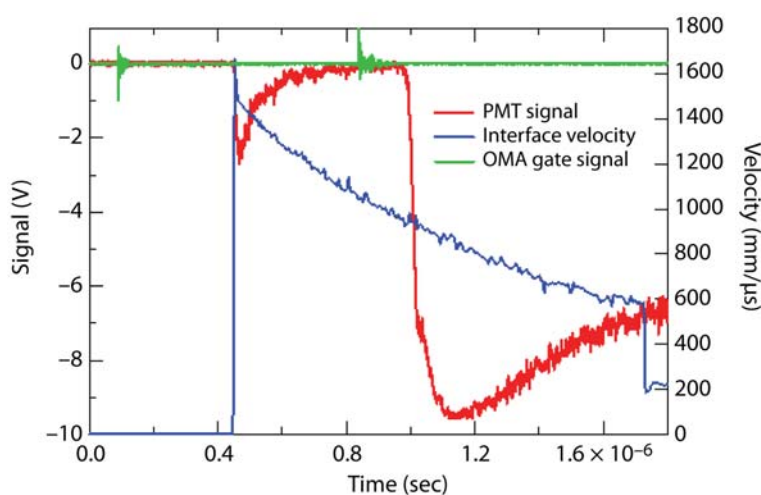
Figure 5. Velocity profile of the aluminum/LiF interface (blue) measured using PDV. Also shown is the signal indicating the OMA MCP gate width (800 ns width marked by two green spikes). The signal from the PMT (red) filtered at 600 nm shows the time history of light production.

The first 500 ns after breakout show a typical PMT signal. This signal likely results from the stress-induced radiance that tracks the rise and fall of the explosively driven shock wave. At 500 ns after breakout, a sharp rise in the PMT signal occurs and may indicate fracturing of the LiF outer edge or the interaction of LiF fragments with the surrounding atmosphere. The velocity profile of the aluminum/LiF interface was measured using PDV. Also shown is the signal indicating the gate time and width (~800 ns width) for the MCP fitted to the optical spectrometer. Figure 6 shows spectra collected with the new configuration.

The key spectral lines are summarized in Table 2. From prior imaging experiments it appears much of the light generated in these experiments originates from the outer edge of the LiF window. As

this light may result from an interaction with the surrounding gas, a number of experiments were conducted in various atmospheres (air, helium, vacuum). When the experiment was purged with helium, emission lines between 434 and 671 nm were significantly reduced or eliminated. When the experiment pressure was reduced to 1 torr (rough vacuum), the emission lines from 390 to 470 nm increased significantly, relative to the 670 nm emission.
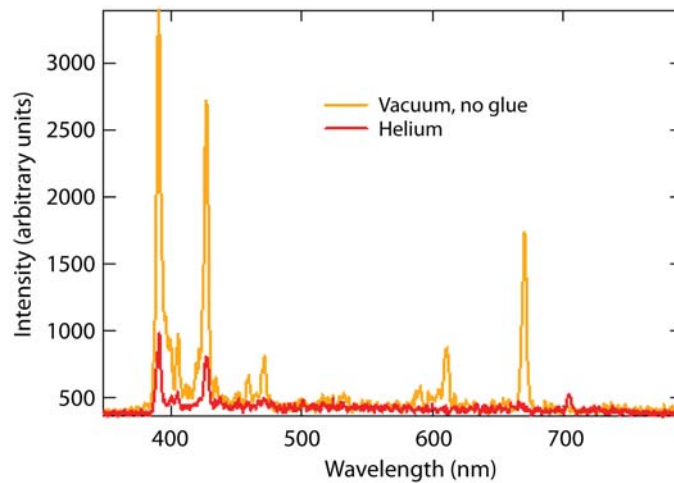
Figure 6. Optical emission from LiF light generated during a dynamic experiment. In both experiments the intensifier gate was opened before the shock wave arrived at the tin surface, and then closed just prior to shock arrival at the top surface of the LiF window. Spectra were collected for samples immersed in a vacuum or helium atmosphere.

Table 2. Peak location (nm) of spectral lines measured from shocked LiF in different atmospheres

Vacuum	390	405	426	434	452	459	471	591	597	611	671
Helium	390	405	427	706	—	—	—	—	—	—	—

In addition to changing the experiment atmosphere, we also varied the gate width and adjusted the acquisition time of the OMA sensor. Figure 7 shows the spectrum collected between shock breakout and 500 ns after breakout. The emission spectrum is broad and structureless and is probably associated with the intrinsic radiance of the shock-heated aluminum sample. When the gate was opened from shock breakout to 1.5 μs after breakout, the sharp lines dominated the emission.
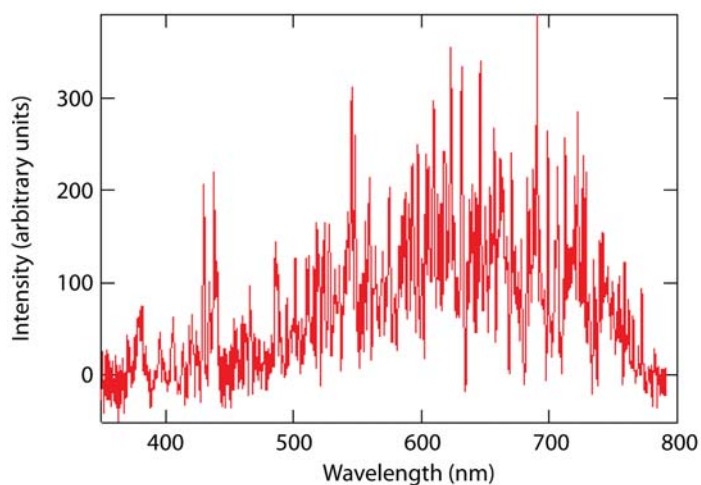
Figure 7. Optical emission generated at early time during a dynamic experiment. The OMA gate width opens before shock arrival and closes 500 ns after. This broad emission is probably associated with shock-induced radiance from the aluminum target.
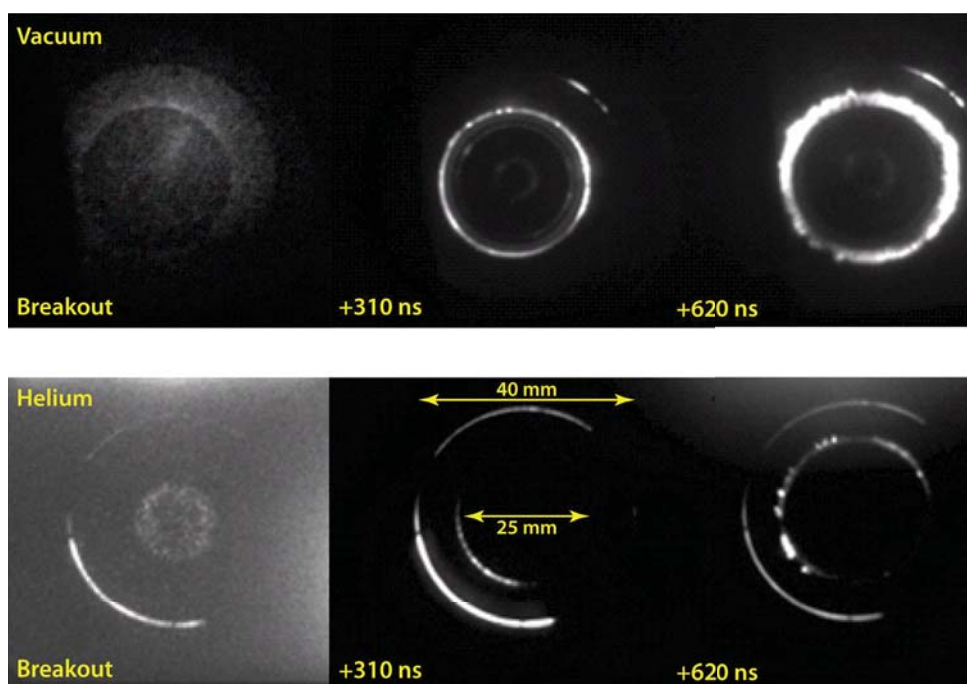
Figure 8. Framing camera images captured during dynamic experiments showing origin and development of light emitted from a shocked LiF window. The experimental package in Figure 4 is viewed from the top, and time increases from left to right. The window and target diameters marked with yellow arrows are 25 and 40 mm in diameter, respectively. The integration time per frame is 90 ns and the interframe time is 310 ns. The top images are for a 1 torr atmosphere and the bottom are for helium.

High-speed framing camera experiments were also conducted to further characterize the nature of this light signature. In Figure 8 (top and bottom), three frames are shown for each of two experiments where the surrounding atmosphere was reduced to 1 torr or switched to helium. The camera MCP gate width was set to 90 ns and the interframe time to 310 ns. The first frame is timed to occur at shock breakout, and the characteristic radiance emission from the aluminum target is present. The image scale was stretched significantly in order to view this signal. In frame 2 the edge of the LiF exhibits increased emission, and in frame 3 the emission increases further. When the LiF window edges are polished and the experiment package was purged with helium (Figure 8, bottom), light at the outer edge of the LiF is present, but nearly ten-fold lower in amplitude. Again, scales have been stretched to allow visual comparison between the vacuum and helium experiment images. When the experiment is executed in 1 atmosphere of air, the light emission is relatively intense but still dominated by light originating at the outer diameter of the LiF.
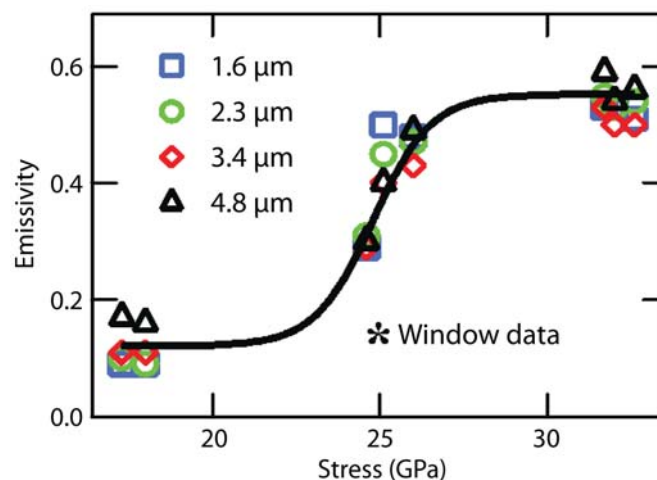
Figure 9. Emissivity at four wavelengths for an initially nearly specular sample after shock release into either air (curve and points along curve) or a LiF window (∗), where it is similar for the three shortest wavelengths. Uncertainty was high for the 5 μm LiF channel, and it is not shown. The emissivity before shock was around 0.05.

Publication of Emissivity Measurements

Figure 9 shows the emissivity immediately after shock release as a function of shock stress just before release into vacuum or LiF. For the free-surface case, the emissivity becomes large when the release causes the tin to melt. Partial melt begins around 19 GPa and is complete above 33 GPa. With a LiF window the sample is tamped and does not roughen. We do not have sufficient shock strength to melt tin under a LiF window, so we do not yet know what will happen when a metal melts on release

under a window. This project consisted of data analysis and write-up of work done previously (Turley "Improved" 2011). The results were published in the *Journal of Applied Physics* (Seifter 2011; Turley "IR" 2011).

Conclusion

By increasing our understanding of emissivity changes upon shock release, background light generation, and other shock effects, we are continuing to improve our ability to make high-quality radiance temperature measurements. We have been asked by Lawrence Livermore National Laboratory to modify our emissivity diagnostic to make it suitable for use on JASPER gas gun shots beginning in FY 2013. This will require smaller integrating spheres and shorter wavelength detectors, and work has begun at NSTec's Los Alamos Operations on the latter.

The LiF light measurements establish a baseline for understanding the nature of optical noise generated in shocked LiF windows. The optical signal appears to be dominated by light generated at the edges of the LiF and has a strong dependence upon the atmosphere surrounding the window. Polishing the surface of the LiF windows as well as purging the experiment with helium was found to significantly reduce this emission.

References

Grover, R., P. A. Urtiew, "Thermal relaxation at interfaces following shock compression," *J. Appl. Phys.* **45**, 1 (1974) 146–152.

Seifter, A., A. J. Iverson, W. D. Turley, J. A. Young, M. Grover, D. B. Holtkamp, G. D. Stevens, L. R. Veeser, "Emissivity measurements of shocked tin using a multi-wavelength integrating-sphere," *J. Appl. Phys.* **110** (2011) 093508.

Turley, W. D., D. B. Holtkamp, L. R. Veeser, G. D. Stevens, B. R. Marshall, A. Seifter, R. B. Corrow, J. B. Stone, J. A. Young, M. Grover, "IR emissivity change of a tin surface upon release of a 26-GPa shock into a LiF window," *J. Appl. Phys.* **110** (2011) 103510.

Turley, D., D. Holtkamp, G. D. Stevens, L. Veeser, "Improved understanding of windows for optical shock-wave diagnostics," *Nevada National Security Site–Directed Research and Development*, FY 2010, National Security Technologies, LLC, Las Vegas, Nevada, 2011, 11–20.

Urtiew, P. A., R. Grover, "Temperature deposition caused by shock interactions with material interfaces," *J. Appl. Phys.* **45**, 1 (1974) 140–145.

Ultrafast Electron Diffraction for Shock Physics Phase Transition Studies

Ming Wu,[1,a] Brian Cox,[b] Wendi Dreesen,[b] Aric Tibbitts,[b] Nicholas Wilcox,[b] Renkai Lee,[c] and Pietro Musumeci[c]

A single electron imaging capability was established by this SDRD. Incoherent electron scattering was observed in reflection mode due to the surface roughness of the samples. A useful platform has been built to study phase transition of metal foils and to explore a new method for temperature measurement of thin metal foils. A preheated pump-probe scheme is proposed for picosecond phase transition dynamics of thin metal foils.

Background

One of the great experimental challenges in understanding the dynamic behavior of phase transitions is to obtain a real-time view of structural changes in the lattice at the atomic level. Pump-probe time-resolved x-ray and electron diffraction methods with ultrafast time resolution have made it possible to directly observe ultrafast surface and bulk structural dynamics and follow restructuring and diffusion at longer times during the melt and phase transitions of solids induced by laser excitation (Siwick 2004, King 2005, Zewail 2006, Nie 2009). One advantage of electron diffraction is that the cross section for electron scattering is about six orders of magnitude larger than that of x-ray scattering. Due to their strong interaction with matter, electrons can reveal the transient structures of surfaces and thin crystals; the coexistence of crystalline and polycrystalline structures can be clearly identified in the diffraction pattern (DP). The penetration depth of electrons should be similar to the depth of heat deposition by the pump laser and on the order of the mean free path for elastic scattering of electrons. Electrons are also less damaging to specimens per useful elastic scattering event. Key components for performing these experiments are the electron source, detection systems, and specimen preparation.

The main technical obstacle to ultrafast electron diffraction is associated with the production of the requisite electron pulse. Electron pulse broadening is dominated by space-charge effects. An electron pulse of ~100 fs keV can contain no more than a few hundred electrons (Gahlmann 2008, Wang 2009). For ultrafast electron diffraction (UED) in a single shot, it is necessary to increase the charge density in each pulse. Overcoming the limitation on the temporal resolution of UED due to the space-charge effects, the University of California, Los Angeles (UCLA) Pegasus photoinjector laboratory and a few others have demonstrated that it is possible to encompass up to 10^7 electrons in a single 100 fs pulse (Musumeci "Relativistic" 2008, Yang 2009, Li 2010), showing that a single-shot

---

[1] minwu@sandia.gov, 505-844-5647

[a] Formerly Los Alamos Operations, now Sandia National Laboratories; [b] Los Alamos Operations; [c] Department of Physics and Astronomy, University of California, Los Angeles

UED with 100 fs temporal resolution can be done. And recently, UED of a single crystal and thin metal foil was done in the transmission mode (Musumeci "Relativistic" 2008, Yang 2009, Li 2010, Musumeci "Laser-induced" 2010, Musumeci "High quality" 2010).

In this project we aimed to take UED to the next level by exploring reflection mode geometry using the UCLA photoinjector linear accelerator (linac) to enable actual shock physics–type configurations to examine phase transitions in materials under high pressures. To date, a penetrating technique is not available to directly interrogate crystal structure deep within the bulk material. With relativistic UED we expected to probe a few hundred nanometers into samples and thus obtain a two-dimensional look into the material of interest.

Project

Experimental Apparatus

The UCLA photoinjector linac has been described in detail previously (Musumeci "Relativistic" 2008, Musumeci "Experimental" 2008, Musumeci "High quality" 2010). A schematic of the beam line is displayed in Figure 1.
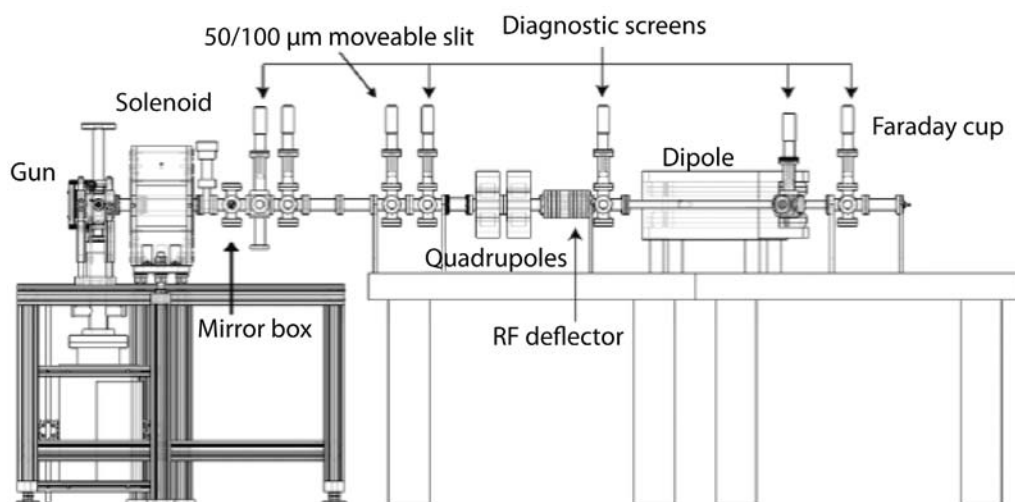
Figure 1. Schematic of the Pegasus photoinjector beam line

Briefly, a state-of-the-art laser system from Coherent provides a short laser pulse (<50 fs) to illuminate a metallic Mg cathode inside a standard 2.856 GHz, 1.6-cell RF gun (co-owned and operated by the SLAC National Accelerator Laboratory [Stanford University], Brookhaven National Laboratory, and UCLA). The RF gun in these experiments is operated at a 1 Hz repetition rate with a peak field of 80 MV/m to reduce arcing and maximize beam stability. Using a 9.599 GHz, 9-cell standing-wave cavity with a maximum deflecting voltage of V_0 = 500 kV located 1.7 m downstream from

the cathode, we characterized the time profile and the time-space beam distribution. A doublet of quadrupole lenses serves to control the electron transverse sizes along the beam line. A screen located after the 45° exit port of the dipole is used for energy and energy spread measurements, and a Faraday cup in the straight-through beam line allows the measurement of the beam charge. A list of the typical operating parameters of the Pegasus photoinjector linac is given in Table 1.

Table 1. Operational parameters of the Pegasus photoinjector linac for electron diffraction experiments

Parameter	Value
Laser pulse length	35 fs (rms)
Laser spot size on cathode	400 μm (rms)
Peak field on the cathode	80 MV/m
Beam energy	3.75 MeV
Beam energy spread	0.5% (rms)
Beam charge	1–10 pc
Injection phase	25°

Under such operation conditions, in principle, the RF photoinjectors can deliver up to 10^7–10^8 electrons packed in bunches of 100 fs lengths, allowing unprecedented time resolution and enabling the study of irreversible phenomena by single-shot diffraction patterns.

Single Electron Imaging for Relativistic Beams

For nonrelativistic UED there are well-established methods and instruments to image keV electrons with high detection efficiency. The microchannel plate (MCP) detects and amplifies either the keV electrons or the low-energy electrons inside an image intensifier. The amplified electron flux is then converted by a scintillator to visible photons, which are subsequently fiber-optically coupled to a high-efficiency CCD camera. It is relatively straightforward to achieve single-electron detection capability due to the large gain of the MCP and the high light-collection efficiency of the fiber-optical coupling.

The MCP has also been tested for MeV electrons, and high-quality single-shot DPs were obtained (Musumeci "High quality" 2010). Blurring of the DP was observed due to the large penetration depth of MeV electrons and the resulting excitation of secondary electrons in many surrounding microchannels. It was also found that, due to the active amplification process, the signal from the MCP has larger fluctuations, which may be a concern in single-shot measurements where very small changes in the DP are to be detected. Performance degradation of the MCP and fiber optics after long-term exposure to MeV electrons was not tested.

An effective alternative for the detection of MeV electrons is the use of optimized passive scintillator screens, which are low cost and provide high electron-to-photon conversion efficiency and improved spatial resolution. A phosphor screen could yield as many as a few thousand photons for each MeV electron due to the large penetration depth of MeV electrons. As an example, two recent papers reported calibration measurements showing greater than 10^3 photons per MeV electron from a Lanex fine screen (Glinec 2006, Buck 2010). Considering an energy loss rate of 1.2 to 1.5 MeV cm^2/g for 1 to 4 MeV electrons and a screen density of 34 mg/cm^2, the total energy deposition by each electron is, in fact, approximately E_{loss} = 50 keV. For an optimal choice of phosphor material and screen composition, the efficiency in the conversion of this energy into output visible photons is on the order of η = 15% to 20%. Approximately half of these photons will exit from the screen side facing the CCD camera, while roughly equal amounts exit from the back side. Because the photon spectrum is narrowly peaked at $h\nu$ = 2.27 eV (545 nm), we have n_{scr} = (½)$E_{loss}\eta/h\nu$ = 1.7 – 2.8 × 10^3 as an estimate of the number of photons emitted per incident electron. With a properly designed lens coupling system whose collection efficiency is higher than 1% and a state-of-the-art CCD camera capable of single-photon detection, single-electron imaging is possible. To test this hypothesis, we performed experiments to quantitatively study the levels of signal at the conversion, coupling, and detection stages in the system.

The schematic of the detection system is shown in Figure 2. A Lanex fine phosphor screen is placed 3 m from the cathode and perpendicular to the beam path. The converted photons are reflected by a 45° mirror and imaged onto an Andor iXon+ 897 electron-multiplying (EM) CCD camera. The optical-coupling system consists of a Canon 50 mm f/0.95 lens and an extension tube to adjust the magnification ratio. The extension tube reduces the effective f-number of the system to n = 1.4.
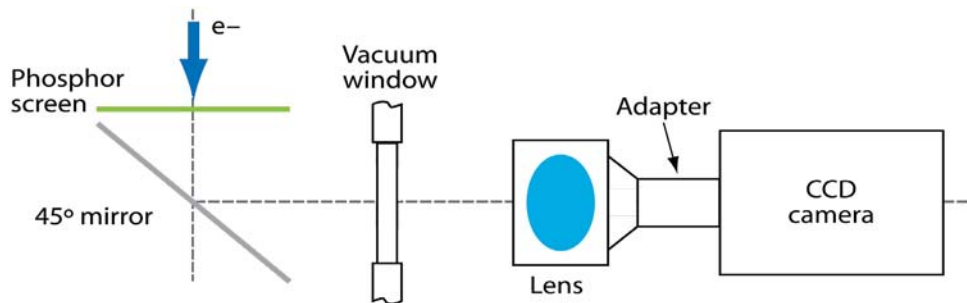
Figure 2. A schematic of the phosphor screen, lens-coupling optics, and CCD camera configuration

The light collection efficiency (Liu 1994) of the lens-coupling system is g = $T/[kn^2 (1 + M)^2]$, where T = 0.85 is the transmission of all the optical elements, M = 2.0 is the magnification ratio, and k is a parameter depending on the angular distribution of the light source. For an ideal Lambertian emission source k = 4, and, hence, g = 1.2%. A thin (<20 μm) aluminum foil that blocks stray light from the beam pipe (including pump and cathode driver laser photons) covers the front surface of the

phosphor screen and increases the collection efficiency by 40% due to its reflectivity in the relevant photon spectrum. The number of photons per single MeV electron reaching the CCD can then be estimated as $n_{ccd} = n_{scr} \times g \times 1.4 = 28 - 47$.

Even if a single electron essentially appears as a point source at the screen, the collected photons are distributed on the CCD chip due to the finite point spread function (PSF) of the detection system. The PSF is, due to the thickness of the phosphor screen, effectively increased by the reflective aluminum foil, and to the depth-of-view and aberrations of the optical system. The PSF was estimated to be a two-dimensional Gaussian distribution with an rms width of $\sigma_{psf} = 2.1$ pixels on the CCD chip (pixel size = 16 μm). Taking into account the magnification ratio of the optical system M = 2.0, this corresponds to an object size of 64.

The average digital counts per pixel of the PSF on the CCD can be written as

$$S_0 = n_{ccd} \times \varepsilon_{ccd} / A_{psf}$$ (1)

where

$$A_{psf} = 2\pi\sigma_{psf}^2$$ (2)

is the area of the PSF in pixel size, and ε_{ccd} represents the conversion factor from the number of incident photons to digital counts output, which depends on the detailed electronic design and settings of the camera as well as the quantum efficiency of the CCD chip. A single electron can be detected if S_0 is clearly above the noise N_0 or, equivalently, if the signal-to-noise ratio (SNR) of each electron in the acquired image, $SNR_0 = S_0/N_0$, is notably larger than 1. N_0 is dominated by the rms fluctuation of the CCD readout level, which can be measured by operating the camera normally, but closing its built-in shutter.

The detector system was calibrated with a relativistic beam of 1.6 MeV and a relatively high charge (~10^6 electrons per pulse). The charge was measured independently using a Faraday cup, and the calibration value was obtained by dividing the total number of counts within the beam spot by the number of electrons. The result is 43 counts per MeV electron at an EM gain level of $G_{EM} = 4$. Similar values for the calibration (within 15%) were found when varying the beam energy up to 3.5 MeV. Using the factory calibration data for the EM CCD, this corresponds to 45 photons per MeV electron, which is in good agreement with our estimate.

The EM CCD's unique ability to multiply electrons improves SNR. S_0 is basically linearly proportional to the EM level G_{EM}. Unfortunately, it is found that N_0 also depends on G_{EM}. We plotted the SNR_0 as a function of G_{EM} (Figure 3). Before turning on the EM gain, the SNR_0 is much less than 1, hence the signal from a single MeV electron is indistinguishable from the large fluctuating noise. As the EM gain increases, S_0 first increases much faster than N_0, leading to a rapid improvement of SNR_0. However, when G_{EM} is >200, SNR reaches a plateau, because at such high gain the noise N_0 also starts to grow linearly with G_{EM}. Data with $G_{EM} = 300$ in the plateau region yielded the highest SNR.
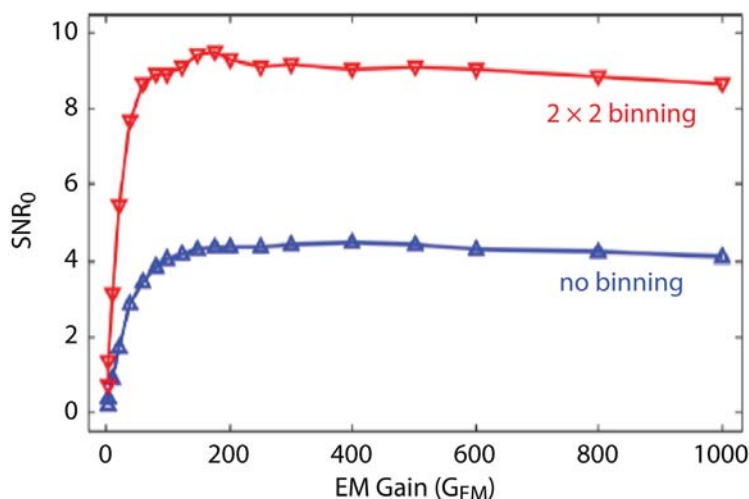
Figure 3. The SNR of a single MeV electron, SNR_0, as a function of the EM gain level G_{EM} for no binning and 2×2 pixels binning cases

An effective way to further increase the SNR is by binning the CCD pixels to match the PSF. For instance, if we bin by 2×2 pixels, the output value per pixel will be four times as large as that without binning. At the same time, the noise only increases as the square root of the binned area, i.e., by a factor of 2. In other words, 2×2 binning immediately improves the SNR_0 by a factor of 2, shown as the red curve in Figure 3. The values of N_0, S_0, and SNR_0 at EM gain level 300 for the no binning and 2×2 binning cases are listed in Table 2. The mean values of the readout level N are also shown, but they do not affect the SNR, as an average background can easily be subtracted off.

Table 2. At $G_{EM} = 300$ and for the no binning and 2×2 binning cases, the rms fluctuation of the readout level N_0, the height of the PSF S_0, and the SNR of a single MeV electron SNR_0

Binning	N_0	S_0	SNR_0
None (1×1)	29.3	128	4.4
2×2	55.8	514	9.2

Figure 4 is a plot of the PSFs and their superpositions with the camera noises to further illustrate the detection of a single MeV electron and the effects of camera noise and pixel binning. The noise follows normal distributions with the mean and rms values as listed in Table 2. At $G_{EM} = 300$ each relativistic electron generates a total integrated over the PSF of 3.3×10^3 counts. In the 2×2 binning case, S_0 is nine times as large as the noise N_0, allowing a clear threshold for single-electron detection.
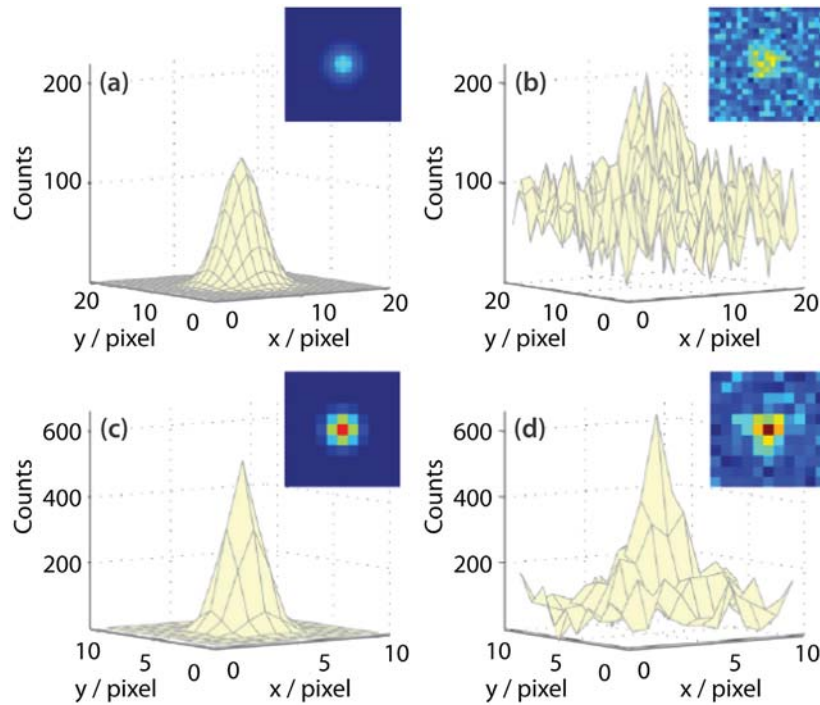
Figure 4. The ideal PSFs (left column) and their superpositions with the simulated camera readout noise (right column). The noise follows a normal distribution with an rms value as listed in Table 2. (a) and (b) are for the no binning cases, and (c) and (d) are for the 2 × 2 binning cases.

As an additional confirmation of the single-electron detection capability, we also acquired images with a strongly attenuated flux of electrons on the screen obtained by blocking the photocathode driver laser and reducing the RF gradient and the focusing solenoid strength. With these settings, the field-emitted electrons (dark current) have a wide energy spectrum, from 1.2 MeV to 500 keV, and a large angular distribution. The probability of more than one electron ending up in the same spot on the screen is statistically unlikely. We took 200 consecutive images (Figure 5a is representative) and identified a total of 2.4×10^3 spots with a peak-finder computer algorithm. All the spots have transverse dimensions similar to our estimated PSF, confirming that they originate from single particles impinging on the phosphor screen. Figure 5b shows the histogram of the total number of digital counts in each of the spots. The total number of counts per spot mainly spans from 4 to 10 $\times 10^3$ counts, i.e., 1.3 to 3 times the calibration value for 1.6 MeV electrons. The spread in CCD counts (number of photons) per electron results because the wide energy spectrum of dark current electrons of different energies are depositing different amounts of energies in the phosphor layer. This observation agrees very well with the Monte Carlo simulation results reported in Glinec (2006).

Figure 5. (a) A typical image of field-emitted electrons in which each isolated spot is an electron, and (b) the histogram of the total counts of each spot; 2.4×10^3 spots in 200 images are identified and counted

As an example of the improved detection capabilities, we show in Figure 6 the single-shot DPs of a 20 nm thick single-crystal gold sample. The sample was located 80 cm from the cathode, and a 1 mm diameter collimation hole was placed 1 cm before the sample. There were 50 fC ($3 \times 10^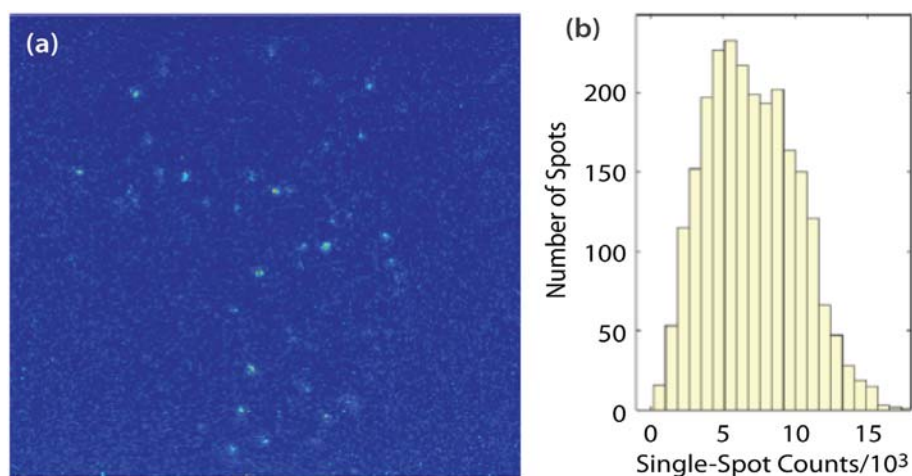5$) electrons that went through the collimator and arrived at the sample. A steering coil was used to move the DP horizontally on the screen. Two DP images were taken at different EM gain levels to avoid camera saturation. The peak intensities of the (200) and (220) spots in Figure 6a and the (400) and (420) spots in Figure 6b range between 4.6×10^2 and 1.3×10^2 times the rms fluctuation of the camera readout levels, allowing the tracking of the changes of diffraction features with high precision.

Another issue in the detection of diffracted electrons in MeV photocathode RF gun setup is the signal contamination due to the field-emitted electrons. A small portion of these low-quality electrons can copropagate along the beam line with the ultrashort photoelectron beams, go through the collimation hole located before the sample, arrive at the screen, and generate a spurious signal. The actual spatial distribution of these field-emitted electrons on the screen depends on the focusing setting. In the DP taken with a gun field gradient of 45 MV/m, at the (200) spot the intensity ratio between field-emitted electrons and photoelectrons is less than 1% (Figure 6). This ratio can reach 10% as the gun field gradient increases to 75 MV/m. However, because a static background can be recorded and subtracted off, the limit on the detection capabilities is only set by the fluctuation of the distribution of the field-emitted electrons. Such fluctuations are typically more than one order of magnitude smaller, especially when the RF system is operated with a feedback stabilization loop.

With state-of-the-art techniques for the surface processing of RF structures, the dark current can be limited to negligible levels compared to the photoelectron beam density, but for field gradients greater than 100 MV/m, this is a potential problem due to the exponential increase in field-emitted charge.
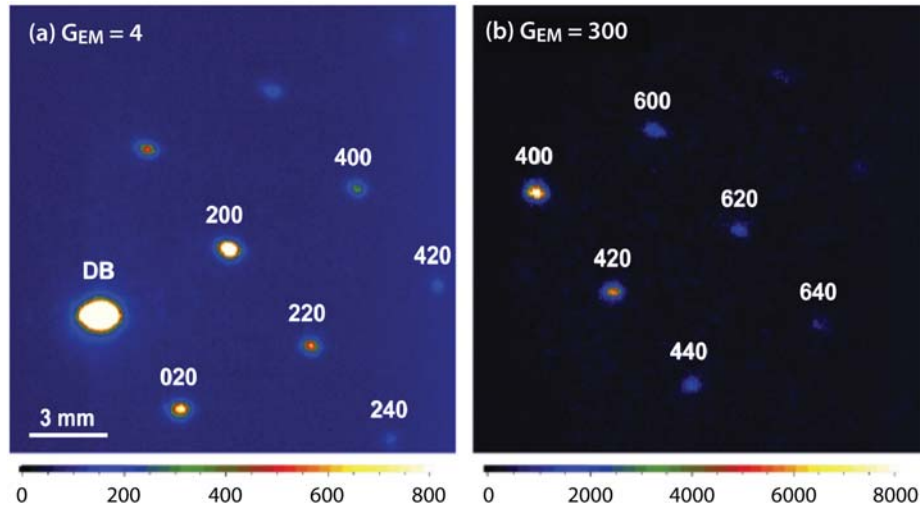
Figure 6. Single-shot DPs of a 20 nm single-crystal gold sample at an EM gain level of (a) $G_{EM} = 4$ and (b) $G_{EM} = 300$. Both DPs were taken with the same electron beam settings except steered horizontally by a dipole coil. Each electron pulse entering the sample contained 3×10^5 electrons. There are 3.2×10^2 electrons in the (420) spot.

In this case, one would consider using a fast scintillator screen and a gated intensified CCD (ICCD) camera to capture all the photoelectrons but remove most of the signal from the field-emitted ones. For example, a 200 μm thick YAG:Ce [cerium-doped yttrium aluminum garnet] screen (decay time of YAG ~70 ns), whose brightness is 40%–50% of the Lanex fine screen (decay time 1 ms), coupled with an ICCD (quantum efficiency 50%, gating tuned to match the YAG:Ce screen) camera can still provide single-electron detection capability but reduces the noise from dark current (which has a characteristic time scale of τ_{dark} ~1 μs) by a factor of $\tau_{dark}/\tau_{YAG} \approx 14$.

The spatial resolution and dynamic range are important figures of merit for a DP detector as well. In our current prototype the spatial resolution, i.e., the size of the PSF, is much smaller than the beam spot size itself (defined by a 1 mm diameter collimation hole located before the diffraction sample); thus, it is not the limiting factor in achievable reciprocal space resolution. In this case, phosphor screens with even larger phosphor density (higher electron-to-photon conversion efficiency) and still reasonably small PSF sizes, such as the DRZ standard phosphor panel for digital radiography, could be used. Finally, as the G_{EM} is set at a high level to achieve high detection efficiency, but the camera well depth is a fixed value, one should note that the effective dynamic range is actually suppressed. To cover the large intensity ratio between the direct beam and high order spots, an effective solution is to coat a radially symmetrical, variable neutral-density apodizing optical filter on the output side of the phosphor screen, extending the dynamic range over seven orders of magnitude (Harb 2008).

Ultrafast Electron Diffraction in Reflection Mode

UED in reflection mode has been demonstrated using electron beams in the tens of keV range (Carbone 2008). Conducting UED with an MeV electron beam is challenging, as it requires that the glancing angle of incidence be only a few degrees in order to observe the DP with a reasonable SNR. The depth of interaction is less than 100 nm, with most of the metal of the MeV e-beam under the glancing angle. But the interaction area between the 0.1×1 mm^2 e-beam and the sample can be 10×1 mm^2 under the glancing angle. This implies that incoherent electron scattering can be dominated if the sample does not have atomic flat terraces in a relative larger area. Experimentally, the sample is mounted on a computer-controlled goniometer for high-precision (0.005°) angular rotation. Ideally, the sample should be prepared and characterized in situ. In other words, a preparation chamber needs to have sputtering and cleaning tools and also be equipped with low-energy electron and Auger spectroscopy.

Our initial experiment setup is shown in Figure 7 without the preparation chamber. Si(100) and Au(100) single crystals were purchased from Marketech International. The samples were used in the experiments without further processing. For these experiments, the e-beam energy was set to 1.5 MeV and the pulse width to 100 fs. The e-beam intensity was measured to be 10^6 electrons per pulse and its beam size was 0.1×1.0 mm. Our recording system had the sensitivity to observe single
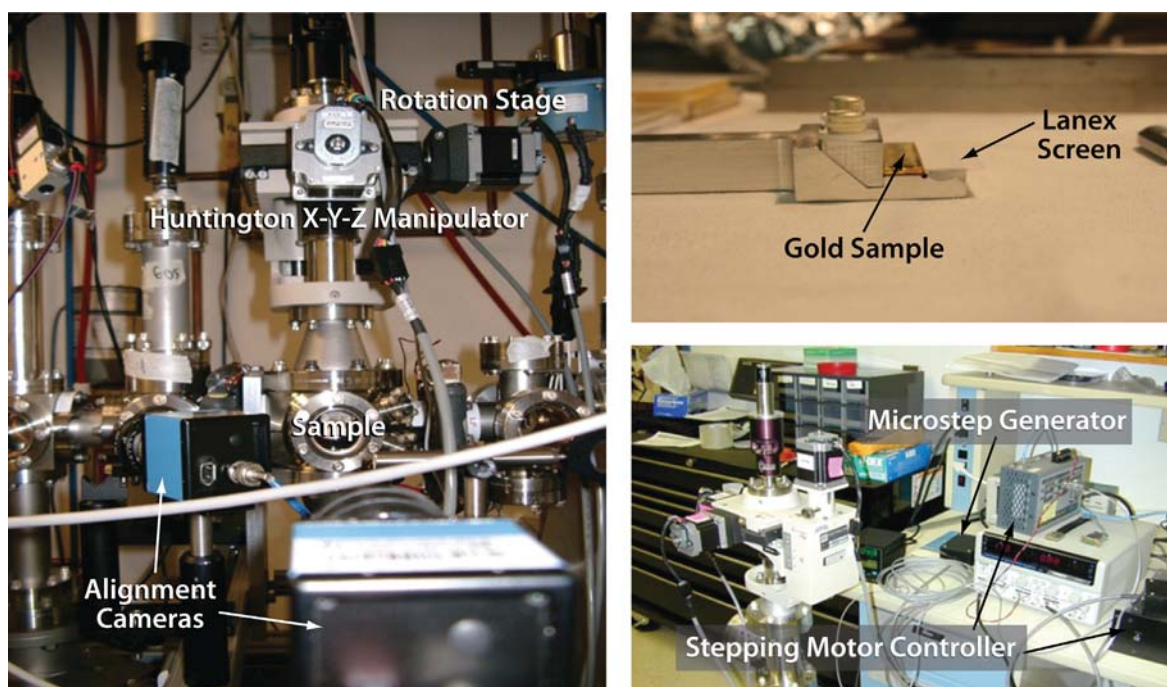
Figure 7. Experiment setup for UED in reflection mode at UCLA Pegasus photoinjector beam line

MeV electrons. Unfortunately, only incoherent scattering was recorded from these samples. A careful examination of surface finishes of Si(100) and Au(100) showed that the incoherent scattering was indeed due to surface roughness. The in situ sample preparation approach could be a reasonable choice, but it was beyond the scope of this initial research effort.

Preheated Pump–Probe Scheme for Picosecond Phase Transition Studies of Thin Foils

A special stage (Figure 8), which operates in an ultra-high vacuum environment (10^{-8} torr or lower) for sample transfer and manipulation, and in which samples can be heated up to at least 1000°C and cooled down to −160°C or lower, was procured for this project. The unit is fitted with a Eurotherm 2408 temperature controller with 25% control accuracy ±1°C. The manipulator has x-y travel ±25 mm, and the z travel is 150 mm. Resolution of the x, y, and z modules is ±0.5 microns with the encoders. The polar rotational range can be ±100° with rotational resolution of 0.01°. The x-y-z and rotation manipulations are controlled remotely by stepper motors operated with a computer.
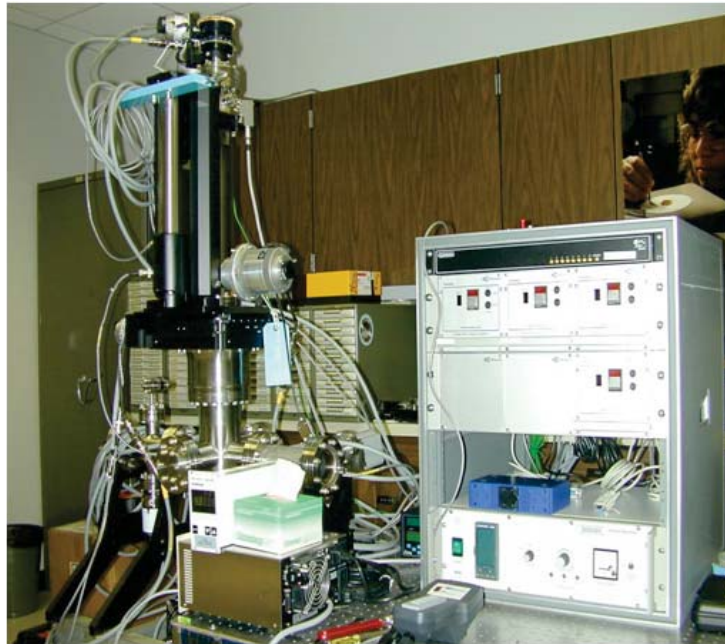
Figure 8. The heating/cooling stage with its control system

This heating/cooling stage can provide a useful tool to study UED of metal foils at different phases and the Debye-Waller temperature effect, which may open a new method for temperature measurement for shocked metal foils. But the foil thickness can be a limiting issue in actual applications. Figure 9 shows the UED patterns of cobalt foils at different thicknesses. It is evident that no 2.8 MeV electrons were observed with 1 μm thick cobalt foils. The 100 nm sample gives a high SNR diffraction pattern. Radiation heating can be a more dominated effect than thermoconductivity for a 100 nm

foil. A sample holder assembly was designed, and temperature distribution on the 100 nm cobalt foil was simulated by ANSYS software. The result indicates that it is possible to heat the 100 nm cobalt foil to 890°C. The homogeneous temperature can be obtained on about a 3 mm sample area, which is about three times larger than the e-beam diameter currently used. Our current design can be used to study metal foils such as cobalt, titanium, zirconium, uranium, and plutonium.
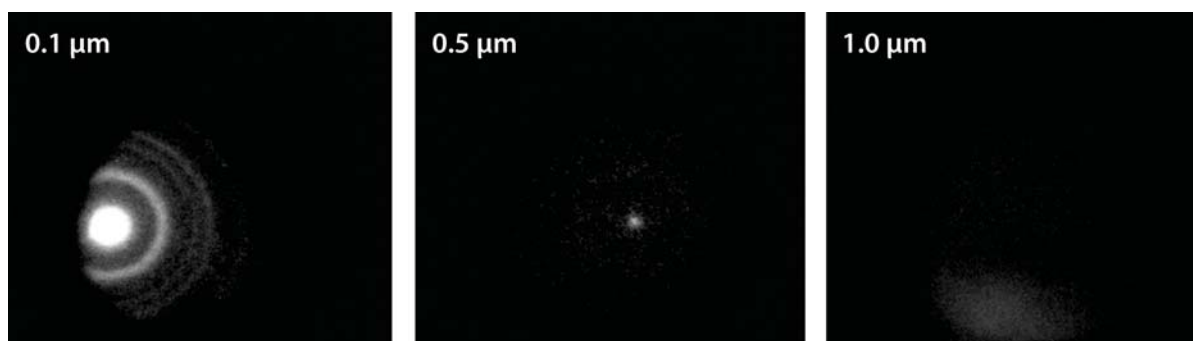
Figure 9. UED patterns of cobalt foils with a 2.8 MeV beam in transmission mode at different foil thicknesses; no 2.8 MeV electrons were observed in the 1 μm foils
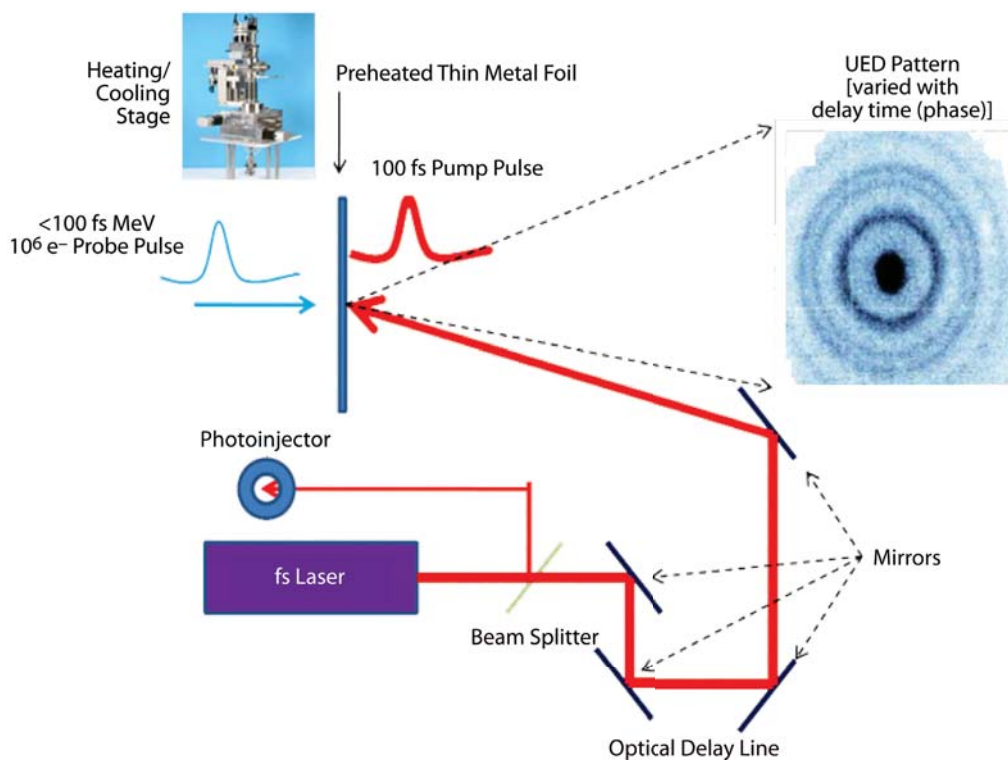
Figure 10. Schematic of preheated pump-probe scheme for picosecond phase transition dynamics studies

This heating/cooling stage also has potential as an application to study phase transition dynamics in femtosecond or picosecond time scales with the current available laser source at UCLA. A proposed preheated pump-probe scheme is illustrated in Figure 10.

Conclusion

A single electron imaging capability has been developed and demonstrated to support relativistic UED. Reflection mode operation was explored for the potential to enhance experimental schemes and options. Unfortunately, only incoherent scattering was observed due to the surface roughness of the samples. In situ sample preparation is needed to achieve atomic flatness on a relatively larger area of the sample surface to successfully conduct UED in reflection mode for MeV e-beams. A useful platform has been built to study phase transition of metal foils and to explore a new method for temperature measurements. A preheated pump-probe scheme has also been proposed for picosecond phase transition dynamics of thin metal foils and will be the subject of future studies.

References

Buck, A., K. Zeil, A. Popp, K. Schmid, A. Jochmann, S. D. Kraft, B. Hidding, T. Kudyakov, C. M. S. Sears, L. Veisz, S. Karsch, J. Pawelke, R. Sauerbrey, T. Cowan, F. Krausz, U. Schramm, "Absolute charge calibration of scintillating screens for relativistic electron detection," *Rev. Sci. Instrum.* **81** (2010) 033301.

Carbone, F., D.-Y. Yang, E. Giannini, A. H. Zewail, "Direct role of structural dynamics in electron-lattice coupling of superconducting cuprates," *Proc. Natl. Acad. Soc. USA* **105** (2008) 20161–20166.

Gahlmann, A., S. T. Park, A. H. Zewail, "Ultrashort electron pulses for diffraction, crystallography and microscopy: theoretical and experimental resolutions," *Phys. Chem. Chem. Phys.* **10** (2008) 2894–2909.

Glinec, Y., J. Faure, A. Guemnie-Tafo, V. Malka, H. Monard, J. P. Larbre, V. De Waele, J. L. Marignier, M. Mostafavi, "Absolute calibration for a broad range single shot electron spectrometer," *Rev. Sci. Instrum.* **77** (2006) 103301.

Harb, M., R. Ernstorfer, C. T. Hebeisen, G. Sciaini, W. Peng, T. Dartigalongue, M. A. Eriksson, M. G. Lagally, S. G. Kruglik, R. J. D. Miller, "Electronically driven structure changes of Si captured by femtosecond electron diffraction," *Phys. Rev. Lett.* **100** (2008) 155504/1–4.

King, W. E., G. H. Campbell, A. Frank, B. Reed, J. F. Schmerge, B. J. Siwick, B. C. Stuart, P. M. Weber, "Ultrafast electron microscopy in materials science, biology, and chemistry," *J. Appl. Phys.* **97** (2005) 111101.

Li, R. K., W. H. Huang, Y. C. Du, L. X. Yan, Q. Du, J. R. Shi, J. F. Hua, H. B. Chen, T. B. Du, H. S. Xu, C. X. Tang, "Single-shot continuously time-resolved MeV ultrafast electron diffraction," *Rev. Sci. Instrum.* **81** (2010) 036110.

Liu, H., A. Karellas, L. J. Harris, C. J. D'Orsi, "Methods to calculate the lens efficiency in optically coupled CCD x-ray imaging systems," *Med. Phys.* **21** (1994) 1193.

Musumeci, P., J. T. Moody, M. S. Gutierrez, C. M. Scoby, "Relativistic electron diffraction at the UCLA Pegasus Laboratory," *Ultramicroscopy* **108** (2008) 1450.

Musumeci, P., J. T. Moody, R. J. England, J. B. Rosenzweig, T. Tran, "Experimental generation and characterization of uniformly filled ellipsoidal electron-beam distributions," *Phys. Rev. Lett.* **100** (2008) 244801.

Musumeci, P., J. T. Moody, C. M. Scoby, M. S. Gutierrez, H. A. Bender, N. S. Wilcox, "High quality single shot diffraction patterns using ultrashort megaelectron volt electron beams from a radio frequency photoinjector," *Rev. Sci. Instrum.* **81** (2010) 013306.

Musumeci, P., J. T. Moody, C. M. Scoby, M. S. Gutierrez, M. Westfall, "Laser-induced melting of a single crystal gold sample by time-resolved ultrafast relativistic electron diffraction," *Appl. Phys. Lett.* **97** (2010) 063502.

Nie, S., X. Wang, J. Li, R. Clinite, J. Cao, "Femtosecond electron diffraction: Direct probe of ultrafast structural dynamics in metal films," *Microscopy Res. & Tech.* **72** (2009) 131.

Siwick, B. J., J. R. Dwyer, R. E. Jordan, R. J. D. Miller, "Femtosecond electron diffraction studies of strongly driven structural phase transitions," *Chem. Phys.* **299** (2004) 285–305.

Wang, X., S. Nie, H. Park, J. Li, R. Clinite, R. K. Li, X. J. Wang, J. Cao, "Measurement of femtosecond electron pulse length and the temporal broadening due to space charge," *Rev. Sci. Instrum.* **80** (2009) 013902.

Yang, J., K. Kan, N. Naruse, Y. Yoshida, K. Tanimura, J. Urakawa, "100-femtosecond MeV electron source for ultrafast electron diffraction," *Rad. Phys. Chem.* **78** (2009) 1106–1111.

Zewail, A. H., "4D ultrafast electron diffraction, crystallography, and microscopy," *Annu. Rev. Phys. Chem.* **57** (2006) 65–103.

Instruments, Detectors, and Sensors

Incoming
Signal

$\sin(\omega$

Quadrature
Phase

Low-Pass
Filter

$I := A \cdot \cos(\phi)$

Low-Pass
Filter

$Q := A \cdot \sin(\phi)$
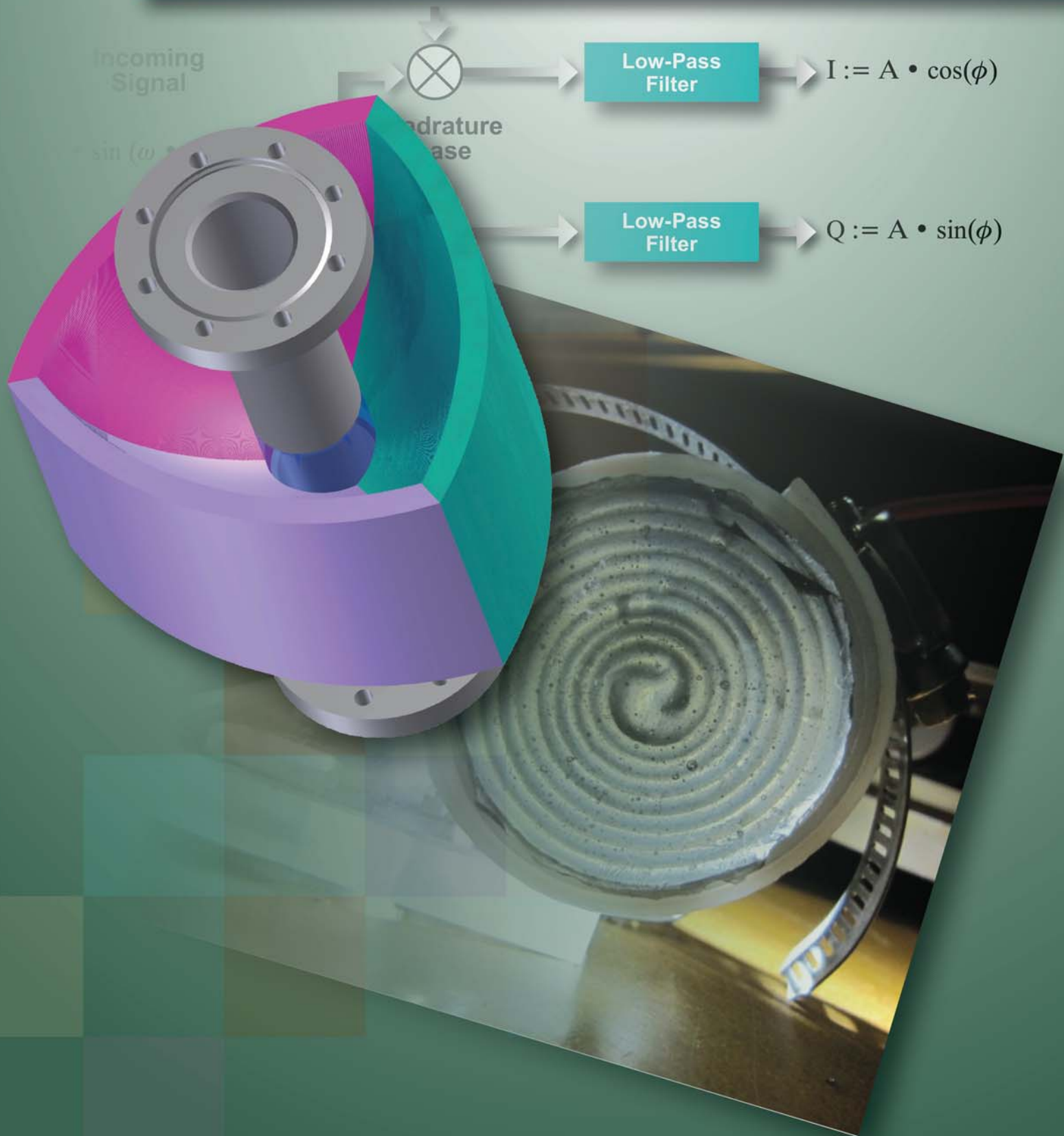
Back-Thinned Silicon Radiation Detector Readout

Stuart Baker,[1,a] Christopher Stapels,[b] Larry Franks,[c] J. Andrew Green,[d] Ronald Guise,[d] and Jason Young[a]

We have researched and evaluated techniques to improve gamma radiation detection capabilities for homeland security applications. Our goals were to improve radiation detection sensitivity and energy resolution as well as system portability. Our initial concept was to adapt recent developments in hybrid CMOS image sensors to replace the historic photomultiplier tube-based/scintillator technologies. Subsequent connections into solid-state photomultiplier development along with a high level of community interest in scintillator studies formed the focus of our effort. We have pursued research into custom design and fabrication of back-thinned solid-state silicon photomultiplier devices with industry partner Radiation Monitoring Devices, Inc. Prototype device fabrication was carried out in FY 2011. Evaluation of prototype radiation detectors is planned for FY 2012.

Background

Past experience with hybrid CMOS imagers applied to radiographic imaging led to the investigation of back-illuminated hybrid CMOS detectors for radiation detection (Douence 2005, Suntharalingam 2007). The concept is to develop a solid-state detector readout that will modernize optical and radiation detectors. Photomultiplier tubes (PMTs) coupled to sodium iodide [NaI(Tl)] have been the gamma radiation detection standard for over 50 years (Knoll 2010), are available in a variety of sizes, and can accommodate large-area radiation detecting scintillators. However, solid-state radiation detection has the potential to improve detection sensitivity and reduce the footprint and power requirements for portable and remote monitoring systems.

Project

We collaborated with industrial partner Radiation Monitoring Devices, Inc. (RMD) to contract for custom CMOS design and fabrication. We investigated detection characteristics of standard solid-state photomultipliers (SSPM) while RMD developed a back-illuminated CMOS design and carried out fabrication. Preliminary optically initiated electron mobility tests were made on semiconductor material to identify a path forward for scintillator tests.

[1] bakersa@nv.doe.gov, 505-663-2040
[a] Los Alamos Operations; [b] Radiation Monitoring Devices, Inc.; [c] Keystone, Inc.; [d] Remote Sensing Laboratory–Nellis

Detector Readout SSPM Concept

Our general requirements were to (1) match detector spectral sensitivity to the scintillator emission spectrum, (2) achieve detector electron multiplication gain comparable to PMTs (on the order of 10^4), (3) incorporate a solid-state silicon detector with simple power requirements, and (4) reduce the overall system footprint.

For the proposed layout we chose back-illuminated silicon, which has detection quantum efficiency (QE) well matched to the scintillator emission of thallium-doped cesium iodide [CsI(Tl)]. CsI(Tl) is a better spectral match to silicon detectors than traditional NaI(Tl) for improved radiation detection sensitivity and scintillation light collection efficiency. The SSPM Geiger mode operation will provide gain comparable to traditional PMTs. SSPMs will operate at low voltage with the potential to reduce power requirements and support remote operation or extended surveillance periods.

Figure 1 (left) illustrates the back-illuminated silicon detection concept relative to standard front illumination and PMT detection. A back-illuminated pixel (upper left) allows 100% fill factor, a large improvement over the front-illuminated pixel configuration (lower left), which has only an ~40% fill factor due to pixel gating and bias structures. The back-illuminated substrate is thinned to optimize sensitivity to green light. The photo on the right in Figure 1 shows the SSPM sensors' volume relative to two different-sized PMTs. Large scintillators are relatively more efficient at absorbing radiation and converting that energy to optical photons because relatively fewer electrons are lost out the sides; they also exhibit better energy resolution discrimination when mated with a large-area PMT. Large-area SSPMs are not currently available. Tiling smaller SSPMs is one way to achieve larger surface area. This performance trade-off will be considered during radiation tests on prototypes.
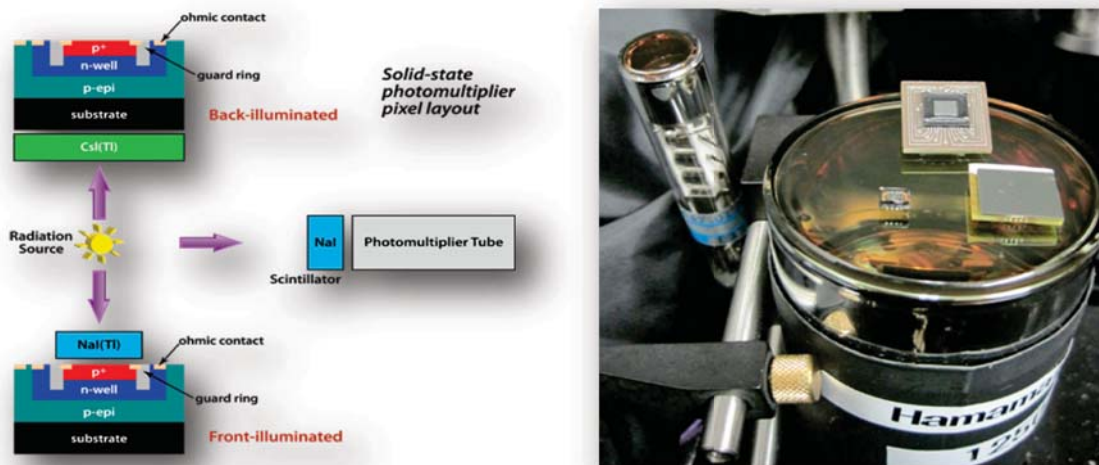

Figure 1. (left) SSPM detector pixel layout compared to PMT detection scheme and (right) a PMT (large tube) with three SSPMs resting on its top and a smaller PMT (upper left corner)
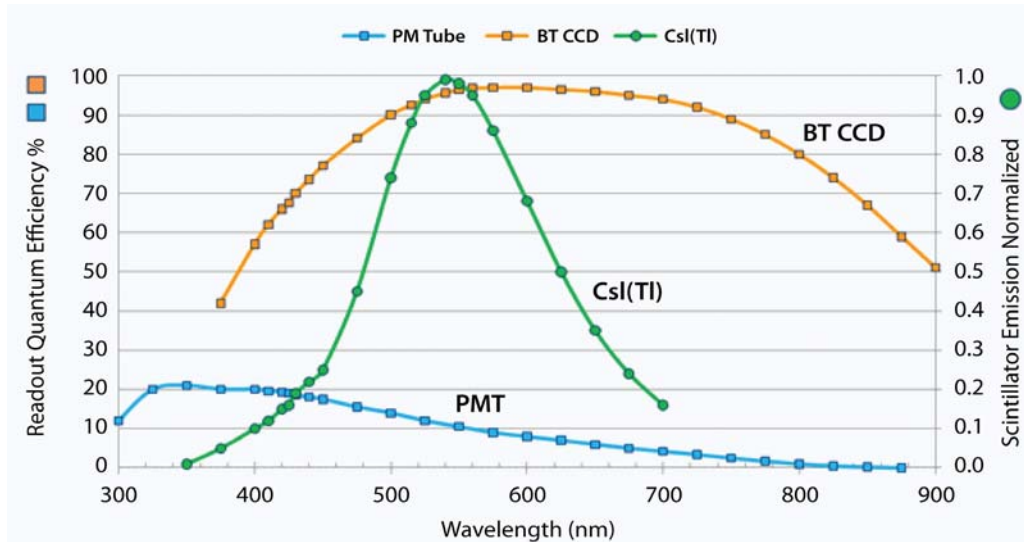
Figure 2. A comparison of detector spectral response (squares) to scintillator spectral emission (circles) shows that back-thinned (BT) CCD efficiency is far superior to current PMT photocathode response for detection of typical blue or green scintillators. The standard SSPM detection efficiency is front-illumination QE × fill factor.

Detector Performance Model

In Figure 2 (Baker 2011) typical detector spectral response (squares) is compared to scintillator spectral emission (circles). The graph shows that back-thinned (BT) CCD efficiency is far superior to current PMT photocathode response for detection of typical blue or green scintillators.

The BT readout spectral sensitivity is very well matched to CsI(Tl) scintillator output to provide high scintillation detection. Detector QE of 95% in the 540 nm scintillator emission range can significantly improve energy resolution. Scintillator collection efficiency estimation indicates BT silicon with CsI(Tl) to be potentially eight times that of a PMT with NaI. Absorption efficiency of CsI is indicated to be 83% vs 78% for NaI. The radiation-to-light yield of CsI(Tl) is 54 photons/keV$_\gamma$ vs 38 for NaI(Tl) (Saint-Gobain Crystals 2008).

Visible Light Measurements

We compared a BT CCD to a standard PMT used in radiometry applications. The sensitivity of the CCD was similar to the PMT, with 16 × 16 binning on 24-micron BT pixels (Figure 3). We collected a sampling of SSPMs and PMTs and compared them using visible light. The PMTs, loaned from the NSTec Remote Sensing Laboratory, were representative of typical field detectors. Small test SSPMs were purchased from SensL of Ireland and RMD.
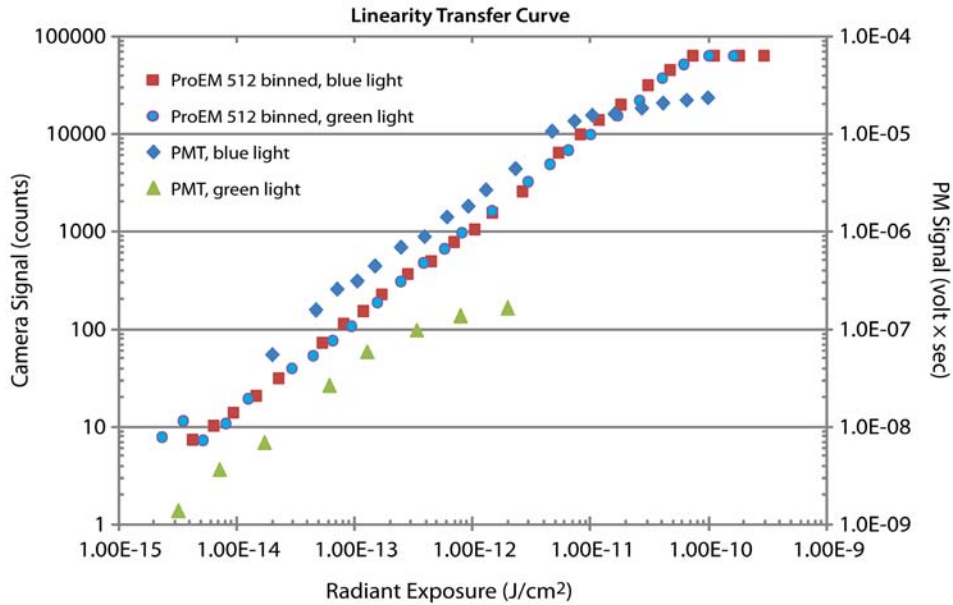
Figure 3. Comparison of a BT CCD to a PMT. The CCD is binned 16 × 16 to increase charge collection area. The PMT signal (V × sec) shows total energy collected.

Figure 4 shows the configuration for light measurements on SSPMs and PMTs. The detectors were compared by measuring the same pulsed blue (460 nm) light source. A 40 ns pulsed blue LED array optically simulated NaI(Tl) scintillation and mimicked the spectral emission and decay time. Neutral density (ND) filters were used to test detector recording range.

Figure 4. LED array positioned in front of sample detector. The LED array was a 1-inch-square area of surface-mount LEDs. Opal glass diffused the output of the LED array. Pulsed signals were measured on each detector.

Measurement results are shown in Figures 5 and 6. Figure 5 is a plot of the detected signal versus the input photon fluence (photons/cm^2). Note the units of photons directly relate to the scintillator radiation-to-light conversion efficiency (photons/keV$_\gamma$). In this situation the larger PMT tubes collected more photons and showed more signal per energy density. The smaller PMT, of comparable size to the SSPM, showed similar signal levels based on energy density. Figure 6 folds in the optically sensitive photon collection area of the detector in this plot of signal versus photons collected. The front-illuminated SSPMs exhibit more signal volts per photon collected than some of the PMTs.
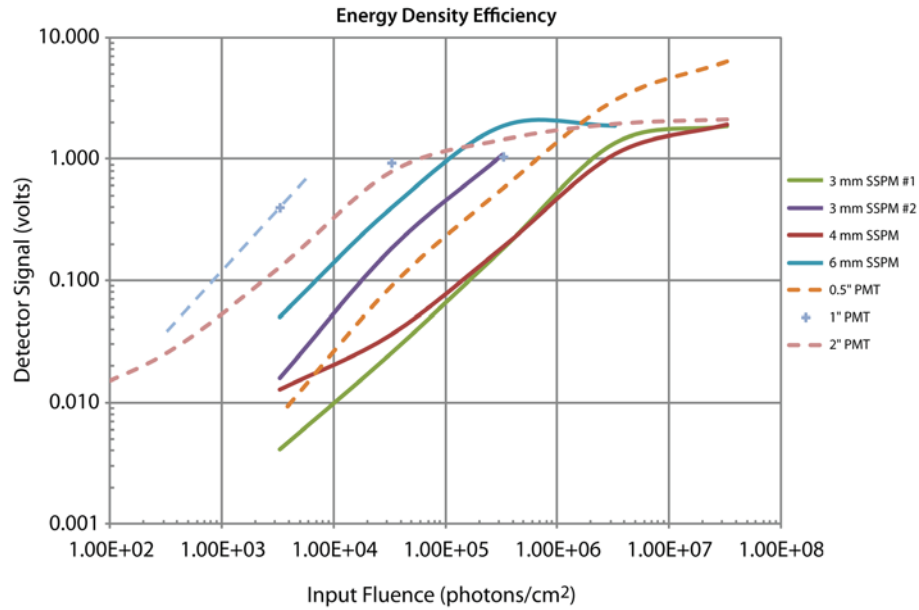
Figure 5. Detected signal versus the input photon energy density. Larger PMT tubes collected more photons and showed more signal per energy density. The smaller PMT, of comparable size to the SSPM, showed similar signal levels based on energy density.

Figure 6. Plot of signal versus photons collected. The signal input is photons collected in the detector area. High-gain, low-noise SSPMs show advantage over larger-area PMTs. The front-illuminated SSPMs exhibit more signal volts per photon collected than some of the PMTs used for this comparison.

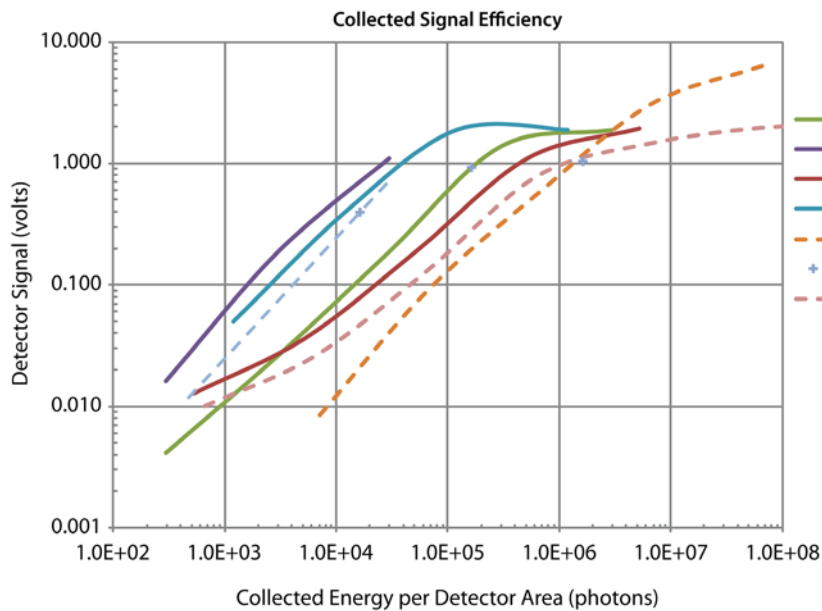Table 1 summarizes the detection sensitivities for the PMTs and SSPMs we compared. The detector sensitivity metric used is detected collected millivolts per photons of signal generated. The photon density input for this detection level was approximately 3000 photons/cm^2. The SSPMs were set for medium gain operation. The reported results are for the SSPM with no signal amplifier. The 2-inch PMT collected many more photons for a given photon energy density, but the small-area SSPM produced much more signal for the number of photons collected.

Table 1. Summary of SSPM and PMT sensitivity

Detector	Detected Collected (mV/photon)	Detector Area (cm)
2" PMT	0.002	19.6
1" PMT	0.025	4.9
0.5" PMT	0.001	2.0
SSPM #1 (3 mm)	0.014	0.09
SSPM #2 (3 mm)	0.056	0.09
SSPM (4 mm)	0.024	0.16
SSPM (6 mm)	0.042	0.36

Sensor Development

Pixel design for efficient collected charge transfer and fabrication of the back-thinning process are two challenges facing the design and manufacture of back-illuminated SSPM devices. Pixel design for back-illuminated charge collection requires modification from front-illuminated designs.

RMD has incorporated some design/process modifications to improve front surface QE. Post-processing to reduce the oxide thickness over the Geiger photodiode elements has produced what appears to be measurable improvement in the QE of the SSPM, in preliminary measurements. This QE improvement shows the largest gain in the blue wavelengths.

Earlier back-illumination experiments indicate that a near 100% fill factor is possible (Stapels 2010). Back-thinning silicon can allow appropriate surface treatments to achieve high QE; green wavelengths can reach 90% QE. Back-thinned devices thus far have shown improved spatial collection, but have not shown improved charge collection from back illumination.

RMD and NSTec developed a series of prototype pixel array designs and evaluated their performance. Twenty-four small test arrays per chip (Figure 7) are in wafer fabrication. Forty chips were produced for evaluation. Fabrication of BT components in small quantities requires a thinning process on the sensor die after the wafer process. The prototype devices in Figure 7 will be evaluated under a continuation of this SDRD project in FY 2012.
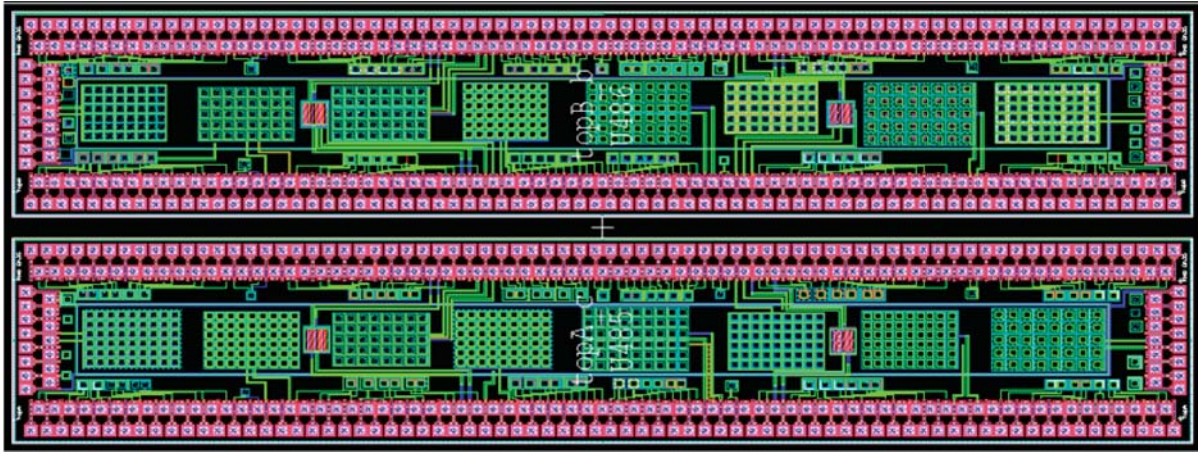
Figure 7. CMOS layout of test structures of 24 Geiger photodiodes and photodiode arrays (green), some large and some small. The die is 2 mm × 5 mm and is surrounded by 50-micron contact pads. Wire bond contacts are shown in pink. The rectangular shape of the chip allows the maximum number of contact pads and, thus, the maximum number of test structures.

Conclusion

The SSPM detector shows potential to improve scintillator detection efficiency over the typical PMT. Front-illuminated SSPMs show similar gain performance to PMTs in terms of volts of signal generated per photon detected. Successful back-illumination techniques for improved detection pixel fill factor and QE can provide ~4 times gain to detection efficiency; results will be evaluated in FY 2012. The SSPM most certainly will provide a sensitive detection system to enhance the capabilities in remote radiation detection as well as provide a more compact detection module for field deployment teams. SSPMs also have a promising role in support of high-energy density physics experiment radiation-detection applications. Our SSPM research was published in SPIE conference proceedings for Penetrating Radiation Systems and Applications XII (Baker 2011).

References

Baker, S., J. A. Green, R. E. Guise, J. A. Young, B. Stokes, E. Wendelberger, C. Stapels, L. Franks, "SSPM scintillator readout for gamma radiation detection," *Proc. SPIE* **8144** (2011) 81440O.

Douence, V. M., Y. Bai, H. Durmus, A. B. Joshi, P.-O. Pettersson, D. Sahoo, K. Kwiatkowski, N. S. P. King, C. Morris, M. D. Wilke, "Hybrid image sensor with multiple on-chip frame storage for ultrahigh-speed imaging," *Proc. SPIE* **5580** (2005) 226–234.

Knoll, G. F., *Radiation Detection and Measurement*, 4th edition, Wiley & Sons, New York, 2010, 321.

Saint-Gobain Crystals, "Efficiency calculations for selected scintillators," http://www.detectors. saintgobain.com/uploadedFiles/SGdetectors/Documents/Technical_Information_Notes/ Efficiency-Calculations.pdf (2008) 7, 9, accessed on April 4, 2010.

Stapels, C. J., X. J. Chen, E. B. Johnson, J. F. Christian, "Performance specifications for large-area CMOS SSPM devices," IEEE Nuclear Science Symposium, poster, 2010.

Suntharalingam, V., R. Berger, J. A., Burns, C. K. Chen, C. L. Keast, J. M. Knecht, R. D. Lambert, K. L. Newcomb, D. M. O'Mara, D. D. Rathman, D. C. Shaver, A. M. Soares, C. N. Stevenson, B. M. Tyrrell, K. Warner, B. D. Wheeler, D. R. W. Yost, D. J. Young, "Back-illuminated three-dimensional integrated CMOS image sensors for scientific applications," *Proc. SPIE* **6690** (2007) 669009.

Spiral Thermal-Neutron Detector

Michael Berninger,[1,a] Aric Tibbitts,[a] Brian Cox,[a] Lorynne Kennel,[a] Michael Jones,[a] Matthew Martin,[a] Tim Meehan,[b] and Robert O'Brien[c]

The scope of the project was to design, build, and test a compact thermal neutron detector. The detector was constructed with two spiraled foils in a strip-transmission line where a 500 nm layer of high-purity ^{10}B on one of the foils was used to capture thermalized neutrons. The detector was exposed with a ^{239}PuBe source where the neutrons were thermalized with various thicknesses of high-density polyethylene plastic. The detector has a 27:1 signal to background ratio in scaler mode. The detector's gamma-ray discrimination is excellent. The spiral detector has good energy resolution (R = 0.2) and estimated 25.2% (measured 12.1 ±2.8%) intrinsic efficiency.

Background

The spiral thermal-neutron detector (SND) project was motivated by the need to detect neutrons with a material alternative to ^{3}He, of which there is a dwindling supply. Candidates for a replacement material were lithium-6 (^{6}Li), ^{10}B, and Gd. ^{6}Li and Gd are typically used in powder form and doped into scintillators that have trouble discriminating gamma rays. Although it is not as efficient as ^{6}Li and Gd for capturing neutrons, ^{10}B was chosen because it is readily available from suppliers and can be coated onto surfaces with different geometries and porosities.

In a ^{10}B(n,α) reaction, a thermal neutron is captured (cross section of 3840 barns) (Sutton 1947, Garber 1976) by the ^{10}B nucleus exciting it to ^{11}B. The excited nucleus is unstable and quickly decays with the following process: ^{10}B + ^{1}n → (^{7}Li + γ) + α. The alpha particle has energy E_α = 1.47 MeV, the ^{7}Li atom has 840 keV kinetic energy, and the gamma has 480 keV of energy (McGregor 2000). We detect the neutron capture when the alpha (and possibly the ^{7}Li) particle ionizes a gas such as argon (Ar). It takes 25.4 eV of energy to ionize an Ar atom (Fermi 1949). The number of electrons liberated in the ionization process is directly proportional to the energy of the α-particle. A 1.47 MeV α-particle will generate about 58,000 electrons if all of its energy goes into ionizing a volume of Ar gas. The pulse occurs in less than a microsecond and will produce a current of about 1 nA, which is low enough that a low-noise electrode must be designed and a charge-collecting pre-amplifier is necessary to measure each pulse.

[1] berninmj@nv.doe.gov, 505-663-2032
[a] Los Alamos Operations; [b] North Las Vegas; [c] University of Nevada, Las Vegas

When using ^{10}B to detect neutrons, it must be applied in layers less than 1 micron thick so that the escaping α-particles have high enough energy to distinguish their alpha peaks from the ^{7}Li and the gamma rays in a pulse height spectrum. This thickness requirement limits the thermal neutron capture efficiency of ^{10}B to ~6% per layer. To build up the efficiency of the detector to something comparable to ^{3}He, a ^{10}B-based detector must have a very large area comprising a significant solid angle with the thermal neutron source, or the boron layers must somehow be stacked. Neither of these solutions is very efficient from the standpoint of detector design. Inspired by early fission chambers (Bright 1945), we conceptualized a double foil assembly in a concentric spiral. This practical compact geometry makes efficient use of space by enclosing a relatively large surface area within a small volume. In the spiral detector, thin layers, multiple windings, and large surface contact areas combine to enhance the overall detection sensitivity. The SND spiral design (Figure 1) was scaled to offset the material limitations of ^{10}B. The single transmission line reduces the complexity of the electrical measurement circuit.
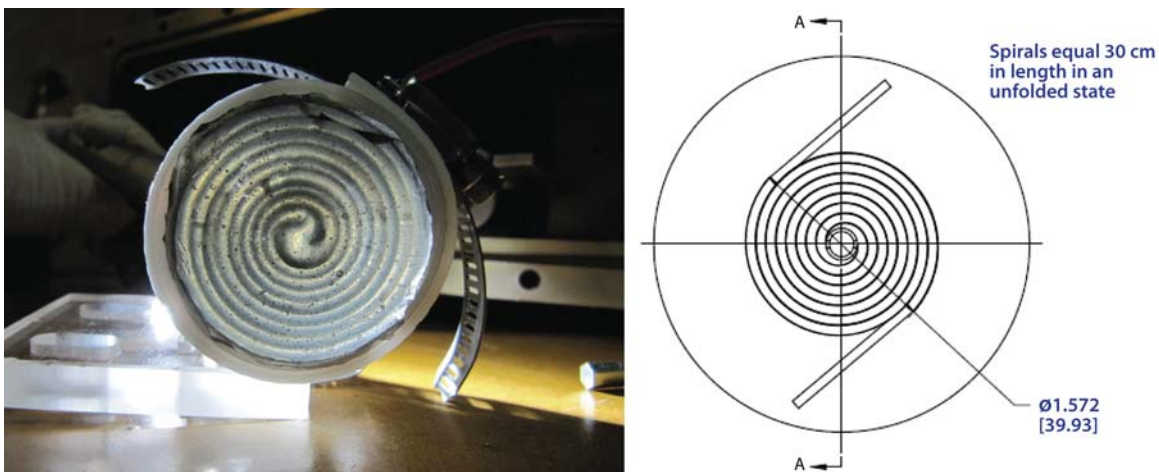
Figure 1. (left) An end view of the SND whose thin layers, multiple windings, and large surface contact areas enhance neutron detection; (right) the detector is 1.6 inches in diameter and 2 inches long

Project

The SND is made of two pieces of a 0.002-inch thick titanium foil (5 cm × 33 cm). An e-beam deposition technique was used to coat one of the foils on both sides with a 500 nm ±15% thick layer of ^{10}B where the ^{10}B was enriched to 97% purity. The coated films had a blue-grey appearance, indicating a successful coating (Figure 2). The coatings contained contaminants that amounted to perhaps 10% atomic replacement of the boron. At most this would produce 2% reduction in the neutron capture efficiency of the boron film.

The coatings were exceedingly durable, as demonstrated when they were subjected to standard bend tests (Figure 3): ASTM E290-09 Section 3.75, where the coated foil was bent over the edge of a
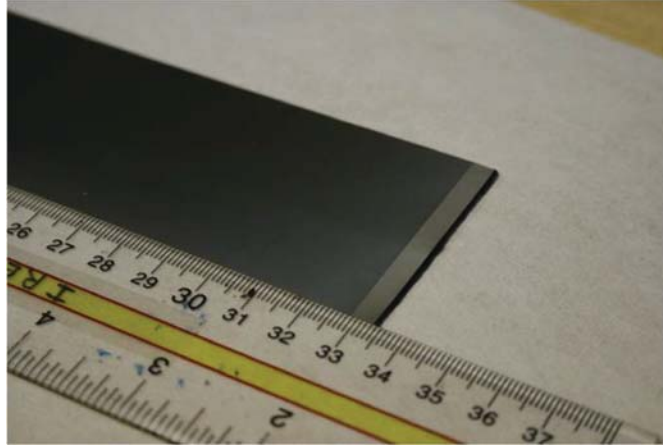
Figure 2. Coated foils had a blue-grey contrast with the silvery grey titanium substrate

0.0625-inch plate and ASTM E290-09 Section 3.8, where the coated foil was bent around a 0.0625-inch gauge pin. A check for cracks and fissures with an imaging microscope showed no signs of damage to the coatings. The coatings did not flake or crack when the foils were spiraled, and the films did not break off when subjected to vigorous cleaning with 200-proof ethyl alcohol. The boron coating stained easily if contacted with grease from fingers or vacuum seals, but n-heptane cleaned off this oil without obviously diminishing the performance of the detector.
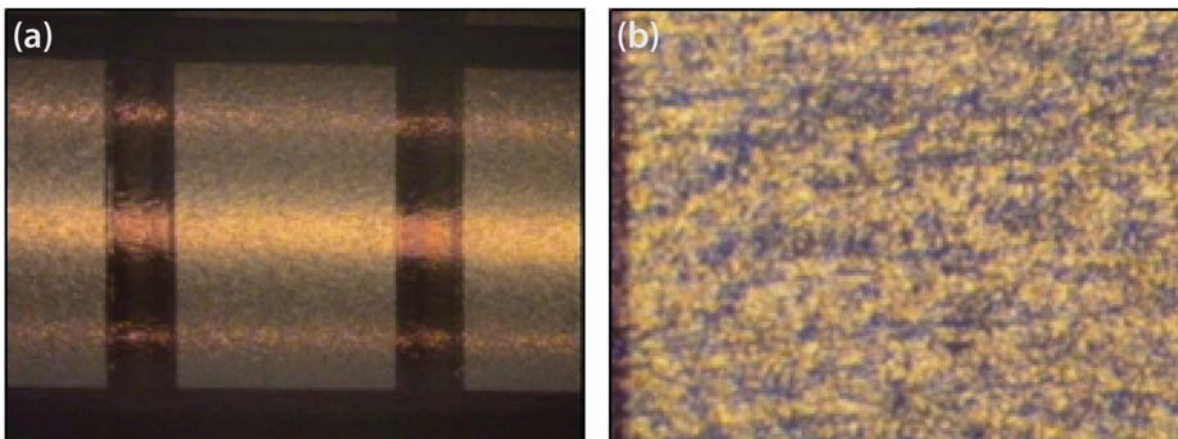
Figure 3. ASTM E290-09 Section 3.8 bend test results show no cracks or fissures at (a) 1X and (b) 100X zooms

The foils were wound into concentric spirals on a winding jig (Figure 4a) where the spacing was maintained with a 2 mm thick ribbon. The jig was composed of a bracket that suspended a spool that could rotate freely on an axle. The axle contained a center slot into which the foils and ribbon were

inserted prior to winding. The spiral was completed by turning the jig about five times while maintaining tension on the foils and ribbon. Care was taken to prevent the assembly from wandering and binding with the sides of the spool. The tension on the assembly had a tendency to compress the ribbon, and this compression limited the gap spacing between the foils to 1.7 mm. Once the foils were completely wound, they were secured with tape. A third of the ribbon was removed from one side of the spiral assembly and then that exposed side was permanently fixed in place with a strong high-resistance epoxy (Delcro 4461). After curing overnight, the remainder of the ribbon was removed from the spiral and then epoxy was applied to add mechanical support to the open end of the spiral. Once completed, the spiral was installed in an ion chamber for measurements (Figure 4c).
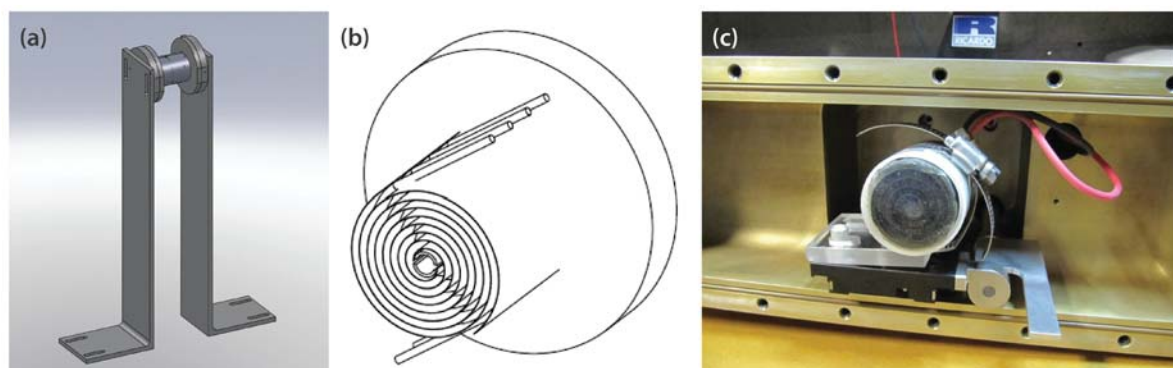
Figure 4. (a) View of the winding-jig mechanism, (b) a schematic of the spiraled foils with ribbons sticking out the ends of the spiral assembly, and (c) the spiral detector installed inside an ion chamber

Data were collected using a Canberra DSA1000 spectrum analyzer and Canberra Genie2000 software. We used the following pulse shaping parameters: 5.6 μs rise, 0.8 μs flat top, and nominal 1 ms long decay. In scaler mode, the dwell time was 20 ms. A gross gain of 40X and fine gain of 1.4X were used. The detector had a signal-to-noise ratio of 27:1. For the pulse height measurements, the gain was reset to 80X. The lower level discriminator was varied between 1% and 2% to reject the lowest noise levels. Dead time varied between 0.56% and 3.2%. Pulse height spectra were typically measured with an average "live" time period of 6 minutes.

Results and Discussion

The SND was tested with a ^{239}PuBe neutron source at the University of Nevada, Las Vegas. The ^{239}PuBe source was uncalibrated. The spectrum and flux were determined with a calculation using the "SOURCES4C" code (Wilson 1999). The PuBe flux calculation was normalized with the mass of the ^{239}PuBe source. Calculations indicated that the ^{239}PuBe source had an activity of 2 Ci and generated ~2 × 10^6 neutrons/sec. The source produced neutrons with a range of energies up to 10 MeV and a central peak at 3 MeV.

Pulse Height Spectrum and Gamma Discrimination

A typical pulse height spectrum (Figure 5) contains two well-defined peaks. The alpha peak is centered on 1.47 MeV and the ^{7}Li peak was peaked at about 600 keV, which is well below the 840 keV energy of the ^{7}Li decay product. This lower apparent peak energy shows that the massive ^{7}Li isotope loses much of its energy escaping the thin layer of ^{10}B on the foil. These two peaks are superimposed on a steeply sloping background that is produced by dark current in the detector, shot noise on the electrical circuitry, and fractional gamma-ray interactions. The 480 keV gamma-ray peak is not seen in the pulse height spectrum. The blue curve (Figure 5a) is a Gaussian fit with the alpha peak where the FWHM = 294 keV. The energy resolution is FWHM/E_α = 0.2. This resolution is good enough that neutron particles can easily be discriminated from the lithium peak, low-energy background, and gamma rays.

In addition to producing a broad band of neutron energies, the ^{239}PuBe source produces a rich gamma-ray spectrum (Figure 5b). This spectrum contains a 4.4 MeV gamma-ray peak from the ^{9}Be neutron capture. This peak and associated escape peaks are not seen in the SND pulse height spectrum. The fact that the SND pulse height spectrum lacks the 480 keV peak from the ^{10}B capture and the 4.4 MeV peak from the ^{9}Be capture demonstrates that the SND is insensitive to gamma rays.
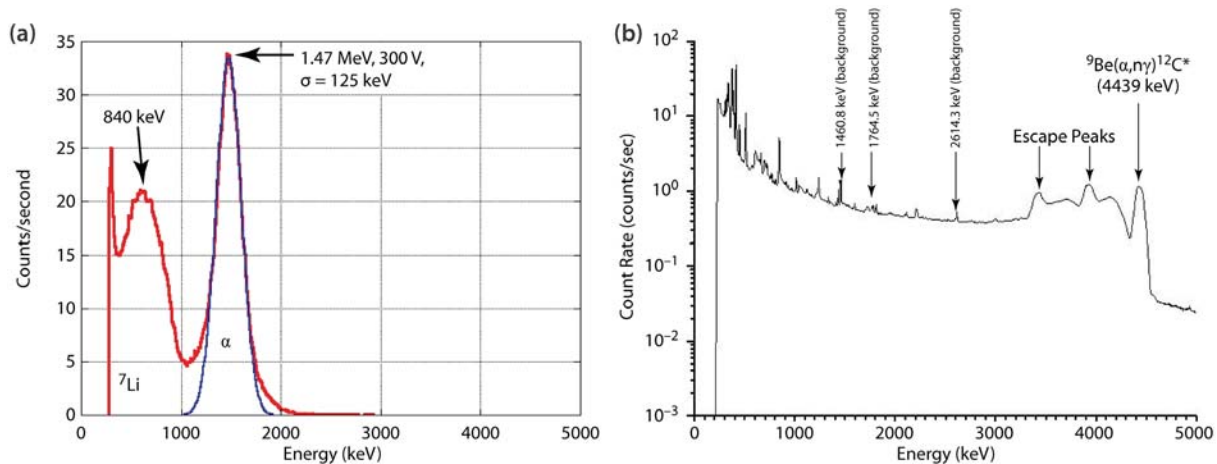
Figure 5. (a) A pulse height spectrum from the spiral detector shows two well-resolved peaks; (b) the ^{239}PuBe gamma-ray spectrum shows a rich spectrum with a prominent neutron capture peak at 4.4 keV

This observation, that the SND is insensitive to gamma rays, was reinforced by measuring (for 1 hour) two ^{60}Co sources totaling about 1 mCi of activity taped to the front face of the ion chamber. ^{60}Co has two strong peaks at 1.17 MeV and 1.33 MeV (Figure 6). These peaks are also not seen in the SND pulse height measurement. The observed peaks are actually due to background-neutron flux from the ^{239}PuBe source in its shielded container about 3 feet away!
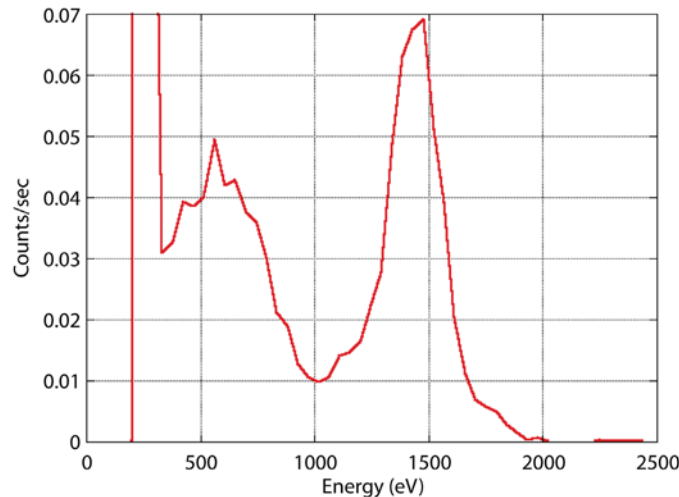
Figure 6. We would expect to see two strong peaks at 1.17 and 1.33 MeV from a pulse height measurement of ^{60}Co sources, but they were not present in the SND spectra

All detectors experience voltage drifts over time, and it is important to demonstrate that the ion chamber is insensitive to these drifts. Therefore, the ion chamber must be operated on a voltage plateau. The amplitude of the pulse (in units of channel #) from the SND versus bias voltage is plotted in Figure 7. The plot shows the detector operates in the ionization regime where the detector reaches a point of ion saturation with biases above about 150 V. At very low values of the bias voltage, the detector does not produce enough field strength to overcome the effects of recombination and diffusion of the ions out of the active volume of the detector. The amount of charge collected per neutron capture is less than the total amount of ionization. As the voltage is raised, the recombination is suppressed and saturation is achieved. This is the normal mode of operation for ionization chambers.

Data collected with the detector in two normal orientations (end on to the source and sideways with respect to the source) produced identical pulse height spectra; the detector does not appear to be directionally dependent.

Detector Efficiency

It is difficult to analytically determine the efficiency of the spiral detector because the thermal neutron trajectories through the detector are randomly distributed and intersect the boron coatings at all angles. Rather than attempting to devise a complicated analytical model, we used the MCNP code to calculate the efficiency of the detector. In the MCNP model, the spiral detector was represented three-dimensionally with a set of nested cylinders surrounded by a uniform cylindrical shell of high-density polyethylene (HDPE). Cylinders more efficiently modeled the spirals in MCNP. The plastic acts as a kind of neutron-energy filter: neutrons are thermalized over a large range of energies, but the
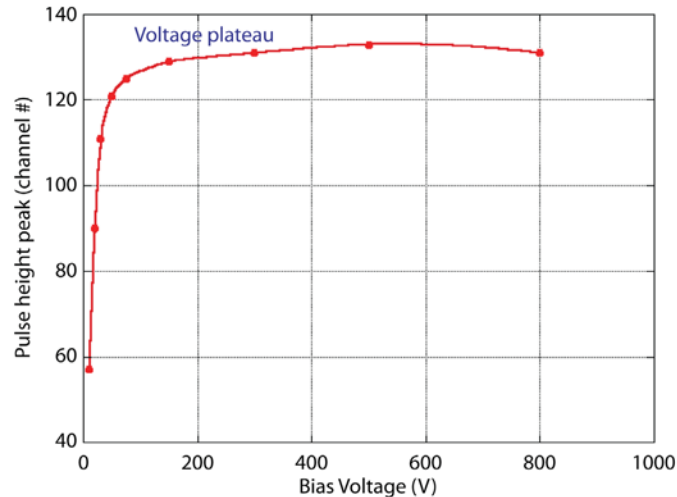
Figure 7. A plot of the alpha peak versus applied bias voltage shows a plateau that represents ion saturation

thicker the plastic, the higher in neutron energy is the peak response with thermalized neutrons. The neutron source was defined with the broad PuBe spectrum as a parallel beam of particles incident on the front face of the HDPE.

Separate calculations were run with 2- and 4-inch thick layers of HDPE. The peak response of the 2-inch moderator was in a range of neutron energies around 0.6 MeV (Bramblett 1960). The 4-inch layer of HDPE caused neutrons with a broad band of energies peaked at 2 MeV to be thermalized. MCNP calculations show that the 2-inch layer of HDPE converts 2.8% of the flux of energetic neutrons from the ^{239}PuBe source into thermal neutrons, and the 4-inch layer of HDPE thermalizes 6.5% of the flux from the PuBe, a factor of 2.4 increase. After scaling between the cylindrical geometry and the spiral geometry, regardless of the magnitude of the flux entering the detector, the calculations showed that the spiral detector's intrinsic efficiency for detecting *thermalized* neutrons is 25.2%. Thus, the combined moderator and spiral-HDPE system should have 0.7% efficiency with the 2-inch moderator and 1.6% efficiency with the 4-inch moderator.

To verify this model, the efficiency of the detector was measured with an HDPE plastic moderator. It was not possible to exactly recreate the conditions in the calculation because it was necessary to install the spiral in the center of the ion chamber (Figure 4c) that had been designed for detecting neutrons with foils in a planar geometry. The HDPE bricks, also intended for use with the ion chamber, were of 2-inch and 4-inch thicknesses and were stacked around the chamber. The large lateral dimensions of the ion chamber caused bricks on the sides and rear of the box to be 6 inches or more from the spiral detector. Additionally, the moderator placed near the front face of the detector, about 1 inch away from the spiral, was cut into a hyperbolic-wedge shape to ensure neutrons from the source would

be thermalized by the same thickness (2 and 4 inches, respectively) of HDPE in all radial directions from the source. This geometry allowed the relatively weak ^{239}PuBe source to be placed inches away from the detector, in the detector's "near field," where the close size relation of the source with the detector (the source is a 2.5-inch high × 1-inch diameter cylinder, and the detector is 1.6 inches in diameter and 2 inches long) produced an inverse-radius, 1/R, flux dependence rather than 1/R^2 that is typically observed with more distant point-like sources.

To check the radial dependency of the flux, the ^{239}PuBe source was then placed at different distances from the front face of the detector. The plot in Figure 8 shows the detector count rate for the 2-inch wedge and the 4-inch wedge. Curve fitting with the data shows that the flux had a dependence on radius of approximately 1/R. The flux of the thermalized neutrons with the 4-inch wedge was a factor of 2 greater than with the 2-inch wedge, in good agreement with the MCNP calculations.
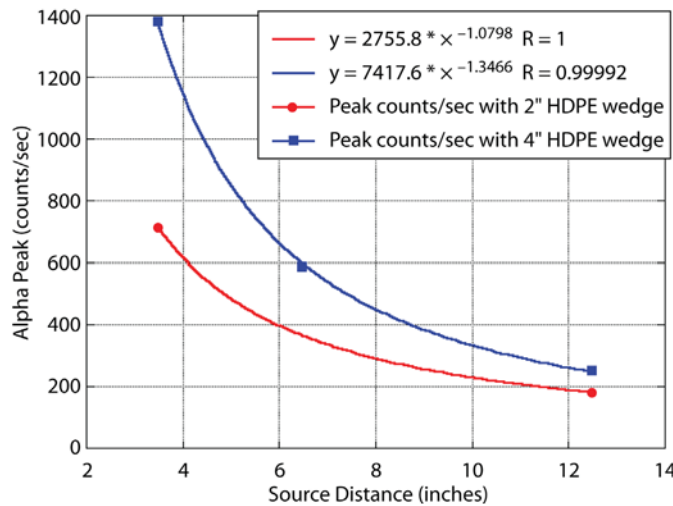
Figure 8. A plot of peak area versus source distance for two different moderator schemes shows a 1/R flux dependence

With the current experiment setup, the effective solid angle of the detector with the source is not clearly defined. If a solid angle consistent with area of the front face of the HDPE in the calcula-tions were used, then the spiral detector's measured intrinsic efficiency equals 12.1 ±2.8% [neutrons counted/(source neutrons emitted into 4π × solid angle fraction × thermal conversion efficiency)]. The factor of 0.5 discrepancy between the measured intrinsic efficiency and the calculation indicates the existence of systematic errors in the measurement. The systematic errors can be attributed to the poorly controlled usage of the moderating plastic in the experiment and the difficulty this presents for calculating the solid angle of the detector with the source, and the fact that an uncalibrated source was used.

Conclusion

We fabricated and tested a thermal neutron detector. Thermal neutrons were captured with a 500 nm layer of ^{10}B that emits a 1.47 MeV α-particle. In scaler mode with a 20 ms dwell, the detector has a 27:1 signal-to-noise ratio. The detector showed little or no sensitivity to gamma rays. The pulse height spectrum showed multiple distinct peaks where the alpha peak had an energy resolution of 20%. The efficiency has been measured at 12.1 ±2.8%; however, this quantity is likely to be underestimated.

This project will continue in FY 2012. We will investigate increasing the detector sensitivity with a mesh grid (Frisch grid). The mesh grid will distinguish the electron signal from other sources of signal in the detector by lowering noise and improving the timing of the measuring circuit. For the next set of efficiency measurements, an ion chamber and HDPE moderator will be fabricated with a cylindrical geometry fitting closer to the dimensions of the spiral detector and a calibrated neutron source will be used.

Acknowledgments

We would like to thank Lynn Veeser and Patrick O'Gara for their discussions and advice with this work.

References

Bramblett, R. L., R. J. Ewing, T. W. Bonner, "A new type of neutron spectrometer," *Nucl. Instrum. Methods* **9** (1960) 1–12.

Bright, W. C., "Spiral fission chambers," Los Alamos National Laboratory, Report 420, Los Alamos, New Mexico, April 4, 1945.

Fermi, E., *Nuclear Physics: A Course Given by Enrico Fermi at the University of Chicago*, University of Chicago Press, Chicago, Illinois, 1949, 34.

Garber, D. I., R. R. Kinsey, "Neutron cross sections," Vol. 2, 3rd ed. Curves, National Neutron Cross Section Center, Brookhaven National Laboratory, BNL-325, Upton, New York, 1976.

McGregor, D. S., S. M. Vernon, H. K. Gersch, S. M. Markham, S. J. Wojtczuk, D. K. Wehe, "Self-biased boron-10 coated high purity epitaxial GaAs thermal neutron detectors," *IEEE Trans. Nuclear Science* **47**, 4 (2000) 1364–1370.

Sutton, R. B., B. D. McDaniel, E. E. Anderson, L. S. Lavetelli, "The capture cross section of boron for neutrons of energies from 0.01 eV to 1000 eV," *Phys. Rev.* **71** (1947) 272.

Wilson, W. B., R. T. Perry, V. S. Charlton, T. A. Parish, G. P. Estes, T. H. Brown, E. D. Arthur, M. Bozoian, T. R. England, D. G. Madland, J. E. Stewart, "SOURCES 4A: A Code for Calculating (alpha,n) Spontaneous Fission, and Delayed Neutron Sources and Spectra," LA-13639 (September 1999).

this page intentionally left blank

RITS Non-Invasive Energy/Angle Diagnostic

Cindy Christensen[1,a] and Daniel Frayer[a]

Inverse Compton scattering was investigated as a time-dependent, non-invasive beam diagnostic for RITS, the Radiographic Integrated Test Stand at Sandia National Laboratories. It was found that a modest-sized source laser will give adequate signal for the RITS machine, that different electron distribution profiles give very distinctive responses as a function of detector position and detected frequency, and that signals gathered at a reasonable number of positions allow simultaneous deconvolution of electron source amplitude, average energy, energy spread, average angle between the beam and the machine axis, and the angular width of the beam. The time-dependent beam evolution is observed by using a pulsed laser. This technique opens the way to deconvolution of more detailed beam profiles in energy and angle, both for RITS and other high-current discharges.

Background

There is a great need for non-invasive diagnostics for charged particle beams such as those found at many universities and research institutions. Examples include DARHT and RITS. Presently, most beam diagnostics are either one of two types: intercepting measurements, or coils that surround the beam and pick up magnetic signals. Intercepting diagnostics, such as bending magnets, require costly and time-consuming reconfiguration, do not give information on the same shots that are used for experiments, and can produce debris that must later be cleaned out of the vacuum chamber. Magnetic coil diagnostics give information on total charge, but no information on energy or the angular distribution of the beam with respect to the axis. Compton scattering has been used mainly to produce tunable x-ray beams but can be used for diagnostic purposes (Chouffani 2006). Unlike previous work, this SDRD effort is based on an *ab initio* theoretical treatment, and does not make any assumptions about the beam parameters.

The inverse Compton scattering technique relies on a laser beam introduced at some angle into the electron beam. Interactions between the photons and electrons scatter the photons in direction and change their energy in an angle-dependent manner. The electrons also suffer a change in momentum, but for relativistic electrons and IR or visible photons, the change in electron momentum is utterly negligible, and thus inverse Compton scattering is considered non-invasive. The differential cross section in the rest frame of the electron has a certain angular dependence, which must be Lorentz transformed into the laboratory frame, giving a different angular dependence in laboratory coordinates.

---

[1] christcr@nv.doe.gov, 505-663-2079
[a] Los Alamos Operations

Lorentz transformations are determined by the velocities of the particles, so the spectrum of scattered radiation is a function of electron velocity (energy and angle), and inverse Compton scattering has the potential to reveal the distribution of velocity in an electron beam. This report describes the inference of electron density, average energy, energy spread, average polar angle, and spread in polar angle from signals gathered at several positions around the interaction point. A technique that could be used to deconvolve the energy/angle distribution, using no prior assumptions, is described.

It should be noted that the polar angles of electron velocities with respect to the machine axis should be very small for linear accelerators, but in many high-current discharges, it cannot be assumed that this angle is small. In either case, the treatment must be performed in its full generality, *even if one is not interested in measuring the angular spread*, because the energy and angular dependence are intertwined, and the angular dependence must be understood in order to confirm inferences of energy spread.

Project

Jackson (1975) gives the Compton scattered photon frequency. The formula is not reproduced here, because in this regime (relativistic electron beam and IR or visible photons), the frequency shift on scattering is negligible in the electron rest frame. The appreciable frequency shifts that are observed are due to Lorentz transformations between the laboratory and electron reference frames. The incoming laser beam must be transformed into the electron rest frame, where Compton scattering occurs

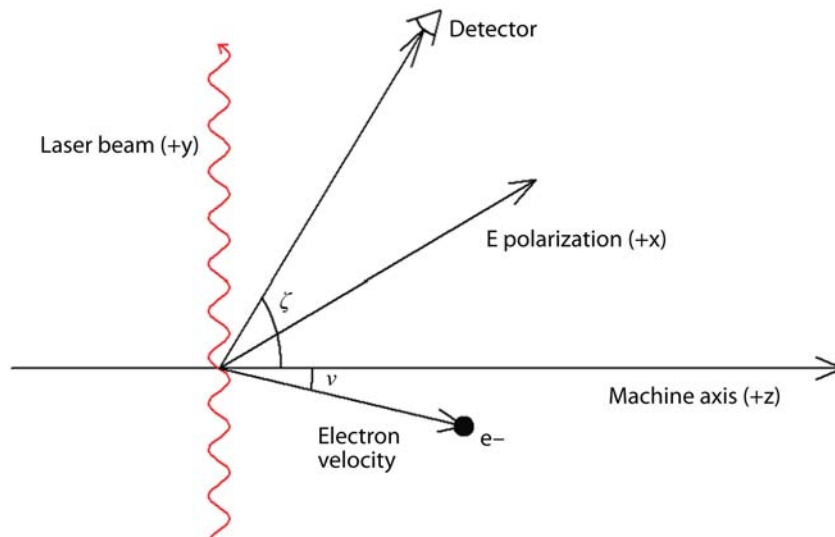**Figure 1. The machine axis is in the +z direction, the laser beam is in the +y direction, and the electric polarization is in the +x direction. The direction of velocity of each individual electron is at a separate polar angle ν and azimuthal angle μ. The +x axis defines the zero of azimuthal angle. Each detector has a unique value of ζ, the polar angle, and ξ, the azimuthal angle.**

with a cross section appropriate to the rest frame, and then the scattered photon direction and frequency must be Lorentz transformed back into the laboratory reference frame, giving two Doppler shifts. Only the results of this derivation are presented below.

In what follows, the laser beam is in the +y direction, the machine axis is in the +z direction, and the electric field polarization is in the +x direction (Figure 1). γ is the relativistic energy divided by the rest energy of the electron m_0c^2, ζ is the polar angle of the detector with respect to the machine axis, ξ is the detector azimuthal angle, ν is the polar angle of any given electron, and μ is the electron azimuthal angle. ω_0 is the angular frequency (2π times the number of cycles per second) of the laser, and ω is the detected frequency. The differential cross section for each individual electron must be calculated, and then the scattering patterns for all electrons of the beam are superimposed to obtain N_p $(\omega; \zeta, \xi)$, the number of photons as a function of frequency, with the detector angles as parameters.

The twice Doppler–shifted frequency is given by

$$\omega_D = \gamma^2 \omega_0 (1 + \beta \hat{n}' \cdot \hat{\beta})(1 - \beta \hat{k} \cdot \hat{\beta}),$$ (1)

where β = v/c for an individual electron, and $\hat{\beta}$ is a unit vector in the direction of velocity, so that $\vec{v} = \beta c \hat{\beta}$. $\hat{k}$ is the unit vector in the +y direction, which is the direction of the laser beam in the lab frame. $\hat{n}'$ is the unit position vector of the detector in the electron rest frame and, as such, depends on the Lorentz transformation.

The differential cross section in the center of mass frame is

$$\frac{d\sigma}{d\Omega} \equiv r_0^2 S = r_0^2 (\cos^2 \theta \cos^2 \phi + \sin^2 \phi),$$ (2)

where θ is the polar angle between the incoming and outgoing photon directions and ϕ is the azimuthal angle, with ϕ = 0 being the electric field polarization direction. Both θ and ϕ are measured in the electron rest frame. r_0 = 2.82×10^{-13} cm is the classical electron radius. This makes the cross section extremely small, but, as we shall see, the total number of scattered photons involves this factor multiplied by the number of laser photons and the density of electrons in the beam, which are both very large numbers, making their product adequate to obtain good photon statistics.

Another factor that enters into the calculation is $d\Omega'/d\Omega$, which is the Jacobian of the Lorentz transformation. It is the change of variables multiplier that is needed when transforming between the two frames. It is this factor that causes the well-known effect of funneling the scattered radiation into the forward direction (with respect to the electron beam).

$$\frac{d\Omega'}{d\Omega} = \frac{1}{\gamma^2 (1 - \beta \cos \alpha)^2}$$ (3)

α is the angle between the velocity and the detector direction. Notice that this expression reduces to 1 as $\beta \to 0$. Also, $\int d\Omega \, d\Omega' / d\Omega = 4\pi$, independent of β. The final expression we must evaluate is

$$N_p(\omega; \xi, \zeta) = \Delta\Omega \, N n_e \, \overline{\ell} \, r_0^2 \iiint d\gamma \sin\nu \, d\nu \, d\mu \, \frac{d\Omega'}{d\Omega} S(\theta, \phi) \, f(\gamma, \nu) \, \delta(\omega - \omega_D). \tag{4}$$

$\Delta\Omega$ is the solid angle subtended by the detector at the interaction point, N is the number of laser photons, n_e is the electron density in cm^{-3}, and $\overline{\ell}$ is the calculated average distance that a photon travels through the electron beam. The product of the five multipliers of the integral can be substantial, even though r_0^2 is a very small number. This will be illustrated for the case of RITS.

The expression for S was given in Equation 2, but remember that θ and ϕ must be measured in the electron rest frame. They are functions of ζ, ξ, ν, and μ, but also γ, because the Lorentz transformation depends on γ. f is the distribution function of the electrons. It is assumed that f is independent of μ, but that does *not* make μ an ignorable coordinate! The laser beam comes in from the bottom (–y direction) of the machine, which breaks the azimuthal symmetry around the z axis. Also, each electron has an angle with respect to the transformed laser direction that depends on μ. The total photon scattering pattern is a linear superposition of the scattering patterns produced by the individual electrons, but the dependence of these patterns on the angles of the problem, including μ, is very complex, and certainly not linear. As we shall see, the integrand can have a very sensitive dependence on μ. The expression for ω_D is given by Equation 1. The inclusion of the Dirac delta function picks out only those angles and values of γ for which the twice Doppler–shifted frequency is equal to a particular detector frequency under consideration. The units of both f and S must be taken to be ster^{-1} in order to make this equation dimensionally correct.

To infer f, the electron distribution function, from measurements of N_p, we express f as a sum of basis functions, which are rectangular functions of γ and ν,

$$f(\gamma, \nu) = \sum_{i,j} c_{ij} f_{ij}$$

$$\text{where} \quad f_{ij} = \begin{cases} 1 \text{ for } \gamma_i \leq \gamma \leq \gamma_{i+1}, \, \nu_j \leq \nu \leq \nu_{j+1} \\ 0 \text{ otherwise} \end{cases}. \tag{5}$$

In other words, each f_{ij} represents a group of electrons whose energies and angles are uniformly distributed over narrow ranges of γ and ν, and uniformly over $0 \leq \mu < 2\pi$. The total response is the sum of responses to the rectangular functions. With f expressed this way, N_p is now a linear functional of the coefficients $\{c_{ij}\}$. The integral of Equation 4 can now be evaluated for f equal to each basis function in turn, and the deconvolution reduces to finding the coefficients $\{c_{ij}\}$ that give the best match of N_p to the data, taken as a function of ω, at several different positions ξ and ζ. The problem is now in the realm of linear algebra, and amounts to a matrix inversion. The question of whether these coefficients can be found uniquely with a reasonable number of detectors must be determined empirically. We shall see that the answer is yes.

We now reconsider the integral. For some general function g(x),

$$\delta(g(x) - g_0) = \sum_i \delta(x - x_i) \Big/ \left|\frac{dg}{dx}\right|_{g(x_i)=g_0} , \tag{6}$$

where the sum is taken over all values of x_i for which $g(x_i) = g_0$. It would be desirable to use this identity to perform the integration over μ, because the deconvolution of f is over γ and ν, so one would want to get the μ integration out of the way. Unfortunately, μ is a cyclical variable, so $d\omega/d\mu$ is zero twice per cycle. It is not known how to deal with a zero in the denominator. The solution is to write

$$\delta(\omega - \omega_D) = \delta(\gamma - \gamma_D) \Big/ \left|\frac{d\omega}{d\gamma}\right|_{\omega(\gamma_D)=\omega_D} . \tag{7}$$

For given values of ξ, ζ, ω, and ν, γ_D is calculated as a function of μ. The interval of μ for which $\gamma_i \leq \gamma_D \leq \gamma_{i+1}$ is integrated over, and then ν is integrated over the interval $\nu_j \leq \nu \leq \nu_{j+1}$. The integrand was first calculated on a grid of 1163 values of ν (from 0 to $\pi/6$) and 1093 values of μ (from 0 to 2π). The calculations were done on an ω grid of 427 points. This was found to be not nearly precise enough, because it turns out that a given value of γ is found in only a narrow strip (see Figures 2–4). These very narrow strips are precisely where the integrand takes on its maximum values, so it is important to calculate this region very precisely. This calculation was very time-consuming, sometimes taking 30 to 40 hours for each solution running on four computers.

Figure 2 (left) shows the value of γ_D, as a function of ν and μ, needed to make $\omega = 2.9 \times 10^{16}$ sec^{-1} equal to the Doppler-shifted frequency. This calculation was done for $\zeta = 5.7°$ and $\xi = 0$. The black regions in Figures 2–4 are values of ν and μ for which no value of γ less than the maximum considered ($\gamma = 18$) would cause radiation of this frequency to be scattered into this detector. The maximum value for all plots of γ is 18, which is red, and occupies a region too small to see on Figures 2 and 3. The plots on the right in Figures 2–4 show the values of the expression sin ν dΩ'/dΩ S(θ', ϕ') from the integrand of Equation 4. For these plots, f(γ, ν) = f_{ij} = 1, and the δ function instructs us how to use the information for $\gamma(\nu, \mu, \omega = \omega_D)$ to pick out the proper regions of the integrand and integrate over μ in such a way that $\gamma_i \leq \gamma \leq \gamma_{i+1}$ and $\nu_j \leq \nu \leq \nu_{j+1}$, corresponding to a single basis function f_{ij}.

The integration is performed by delineating the region between two successive values of the γ grid (a single color on the left) and two successive values on the ν grid such that $\nu_j \leq \nu \leq \nu_{j+1}$ (which would be shown by vertical segments on the plots), and integrating the integrand over μ. This gives the response to one basis function f_{ij}, which, after multiplication by the factors shown in Equation 4, will be the number of photons scattered into a given detector at a given frequency by the (i, j) component of the electron distribution.
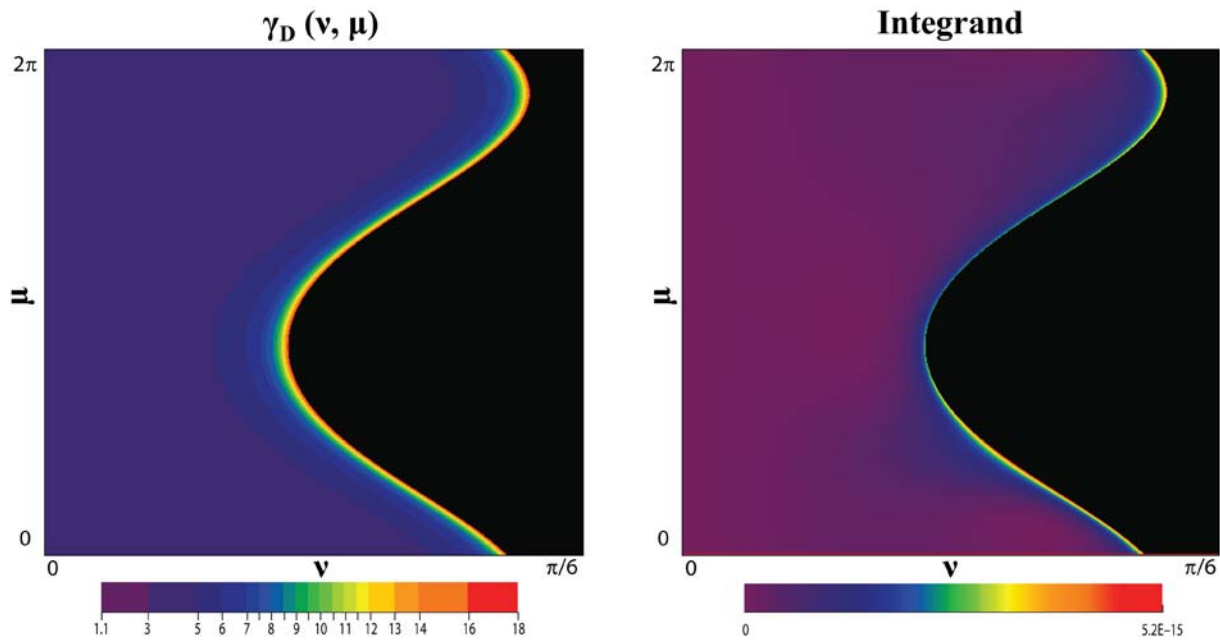
Figure 2. For a given ω (2.9 × 10^{16} sec^{-1}) ⇒ 19 eV and a given detector position (ζ = 5.7°, ξ = 0), (left) the value of γ$_D$(ν, μ) that is required to make ω = ω$_D$ for the specified value of ω, and (right) the integrand of Equation 4. For the areas shown in black, no value of γ less than the maximum considered will cause an electron with ν and μ in these areas to scatter photons of frequency ω into the given detector.

Figure 3. γ$_D$ and integrand as in Figure 2, but for ω = 1.02 × 10^{16} ⇒ 6.7 eV. The areas highlighted by boxes are shown enlarged in Figure 4.

Figure 4. These magnifications of the areas indicated by boxes in Figure 3 illustrate how a region between two successive values of the gamma grid (a single color on the left plot) is used to select a region of integration for the integrand of Equation 4

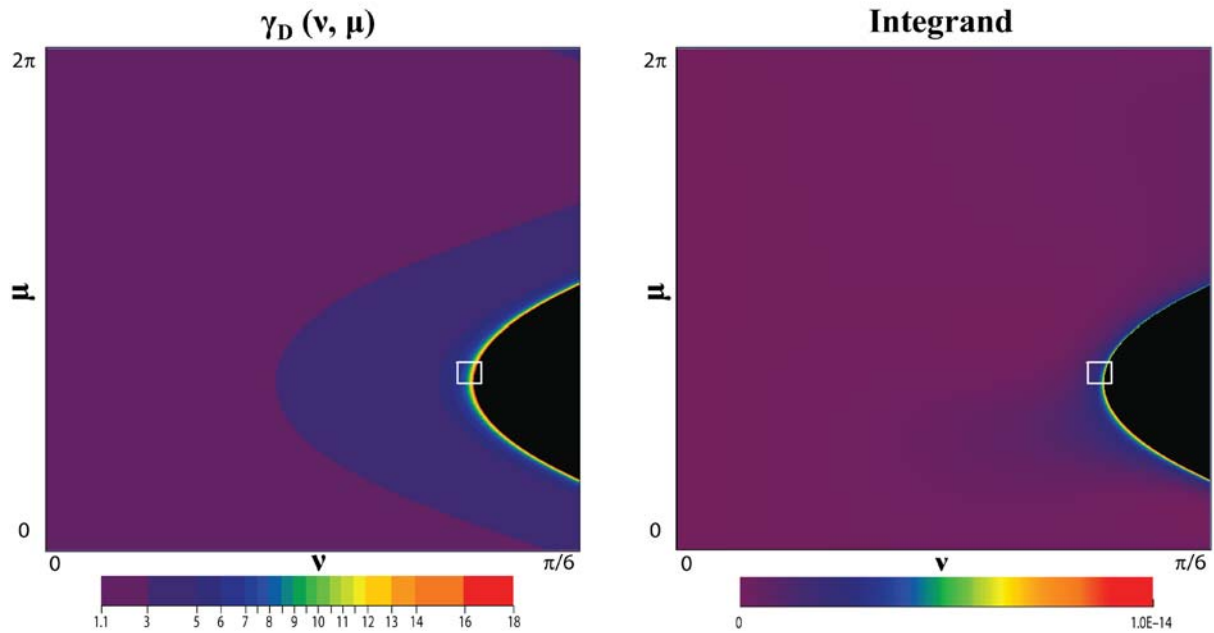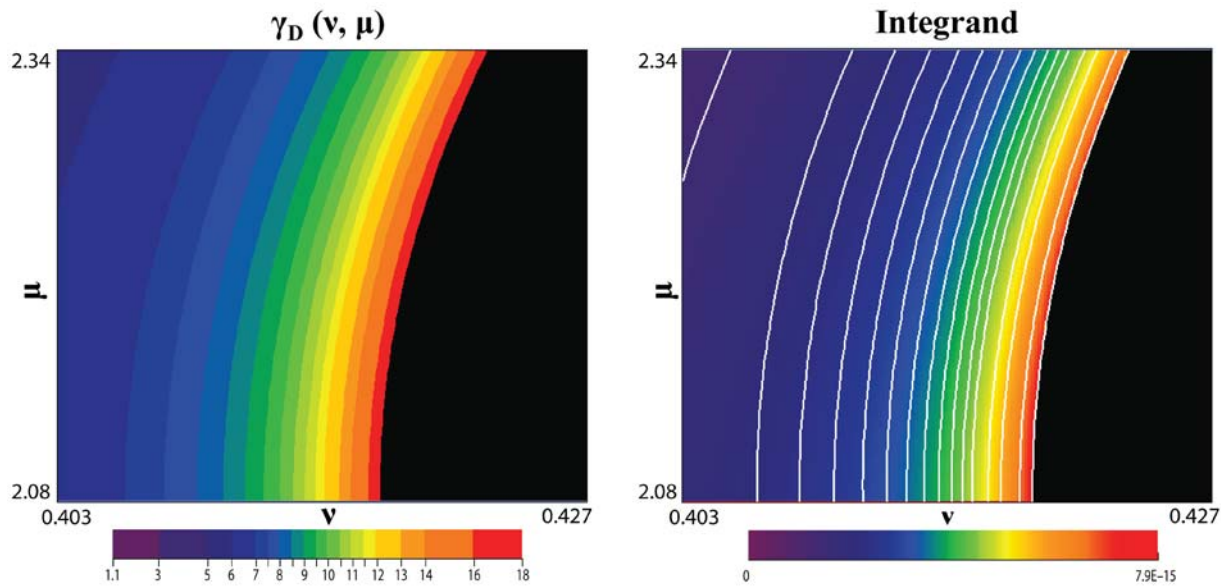Figure 5 shows responses versus ω of a detector at $\zeta = 5.7°$ and $\xi = 0°$ to three different basis functions. Each of these plots is the result of integration of Equation 4 over γ, ν, and μ and given fixed values of γ_i, ν_j, ζ, ξ, and ω, as in the examples of Figures 2–4. For (a), $13 \leq \gamma \leq 14$ and $24.7° \leq \nu \leq 26.5°$. For (b), $1.1 \leq \gamma \leq 3$ and $28.2° \leq \nu \leq 30°$. For (c), $13 \leq \gamma \leq 14$ and $7.1° \leq \nu \leq 8.8°$. Because the responses to the basis functions f_{ij} are very different and distinctive, deconvolution should be possible. Only three randomly chosen examples are shown out of many, but, in general, the responses are very distinctive.

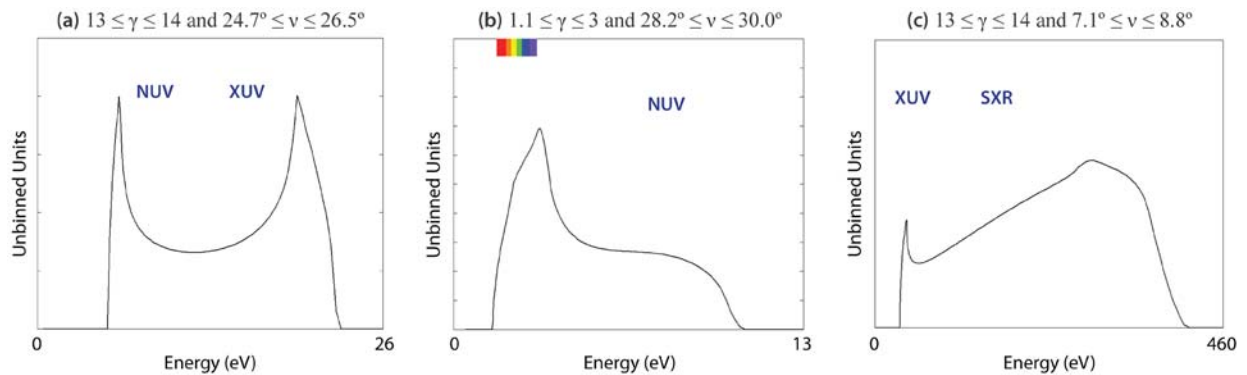**Figure 5. Responses to three different basis functions. The frequency ranges (near UV [NUV], extreme UV [XUV], and soft x-ray [SXR]) are denoted. The visible range is shown in color. The amplitudes must be multiplied by several factors and binned in ω in order to have units of number of photons. The responses to the various basis functions are seen to be very distinctive, indicating that deconvolution should be possible.**

All the responses shown so far were calculated for a Nd:YAG laser (λ = 1.064 µm). It is unfortunate that much of the response is in the x-ray region. This situation is undesirable because working with x-rays is difficult, and hardware such as lenses, fibers, and filters are unavailable or have undesirable properties. The original approach was to use high-dispersion optical fibers to disperse the wavelengths in time, so that a time signal could give information on the response versus frequency. This is not attainable in the x-ray region, so the calculations were repeated with a CO_2 laser (λ = 10.6 µm) and with ω restricted to give a wavelength from 400 to 700 nm. It was found that in this narrow wavelength range, the responses to different basis functions were not distinguishable enough, and the deconvolution properties were not favorable. This is easily understood, because if the responses to the different source functions were all basically similar, the information necessary to separate the various contributions would not be contained in the data. It was found that there was no fine structure in this wavelength range, so that dispersing the signals according to wavelength is not particularly useful in this range. Note that Figure 5 shows that there definitely *is* defining information in the spectra, but only when the entire range is considered. The next approach would be to recalculate the responses over the full wavelength range for a CO_2 laser, bringing the responses down to lower energies than the original Nd:YAG calculations. Then filters would be used to bin the signals according to frequency in the IR, visible, and UV regions, and insofar as possible, in the x-ray. This third round of calculations was not completed, but an illustrative deconvolution was performed with the results of the Nd:YAG calculations.

In general, a parametric fit is the easiest form of deconvolution; it involves the assumption that the source function is of a given functional form involving parameters. For example, a linear fit y = ax + b involves the parameters a and b. In what follows, it is assumed that the source is of the form a_0 exp $(-(\gamma - a_2)^2 / a_1)$ exp $(-(\nu - a_4)^2 / a_3)$, dependent on the parameters a_0 through a_4. Deconvolution then becomes a determination of the parameters by a search routine. A generalized deconvolution, making no assumptions about the source function, is possible, but was not performed because the CO_2 calculations were not completed. Instead, a quick parametric fit is presented for illustration using the Nd:YAG calculations. Much of the response of these calculations is seen in the x-ray range, where filter performance is unfavorable, so they do not give a fair prediction of the results possible with data binned according to filter response in the CO_2 wavelength range. Thus, the fit was made to the results of the Nd:YAG calculations without binning.

The first step is to posit values for a_0 through a_4 and simulate the signals that would be gathered by an array of detectors. Ideally, the positions of the detectors should be optimized in order to give the maximum amount of information with the fewest detectors. This optimization was not done in the example shown; rather, the positions were chosen at the outset when no prior information was available. The polar angles were 5.7°, 11.5°, 28.6°, 51.6°, 77.3°, 108.9°, 143.2°, and the azimuthal angle was 72° for all seven detectors. (Other azimuthal angles were calculated but found to be less favorable.)

The coefficients obtained by averaging the test function over intervals in γ and ν were multiplied by the calculated response functions to predict the amplitudes at the detectors as functions of ω. Then,

the amplitudes were multiplied by the solid angles of the lenses used, and the quantum efficiency of the detectors. Suitable lenses are available in the IR, visible, and UV ranges, so the solid angle was calculated for a 5 cm diameter lens placed 25 cm from the interaction point for the last four of the seven detectors. The first three detectors receive x-ray signals, so their solid angle was calculated for a 63 mm^2 bare detector at the same distance. The quantum efficiency is taken to be 100% in the visible through the x-ray, and 70% in the IR. (These numbers come from a casual scan of detector manu-facturer catalogs.) The overall normalization is dictated by the 125 kA total current on RITS. Figure 6 shows the seven predicted signals. The label on the y axis is labeled "unbinned units" because the signal must be operated on by multiplicative factors and binned to arrive at the number of photons. The widely different number of total photons received at the various detectors points to the need for optimization of detector placement, which has not been done.
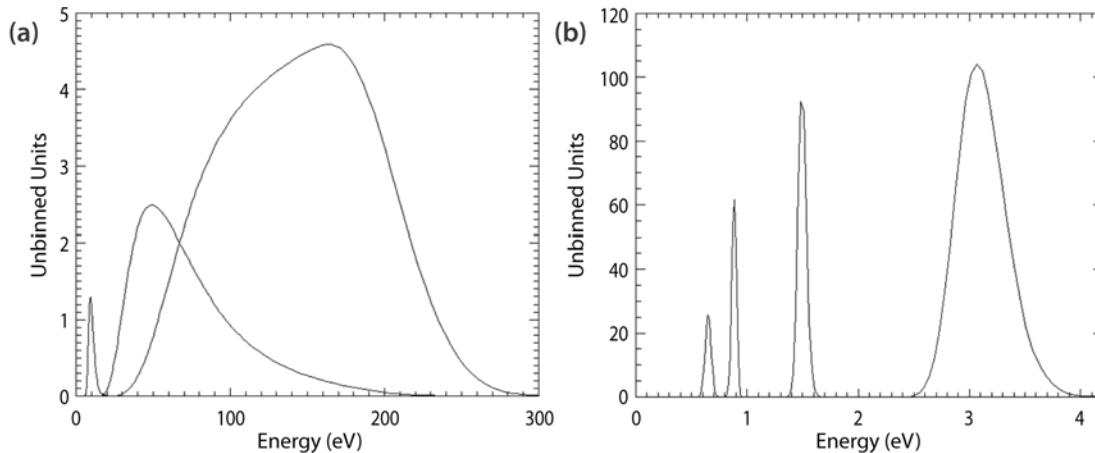

Figure 6. (a) Seven predicted signals as a function of energy; (b) the low-energy region is expanded

The next step is to add noise. Photon statistic noise is the first concern. Calculation of the square roots of numbers of photons integrated over frequency (one big bin) gives resulting signal-to-noise ratios that are more than adequate for all detectors. However, noise from various sources is present on all real signals, and the noise environment of RITS might be particularly challenging. For the purposes of the simulation, an amount of noise that was considered "reasonable" was added (Figure 7). The photon statistics must be checked again after the eventual binning by frequency in order to make sure that the signal-to-noise ratio limited by photon statistics is still adequate. (Other sources of noise must be considered later.)

Fifty different noisy data sets were generated from the same simulated signals. The parameters are searched for by the IDL routine CURVEFIT. The results are shown in Table 1. The error bars show the deviation of the inferred parameters over the 50 searches.
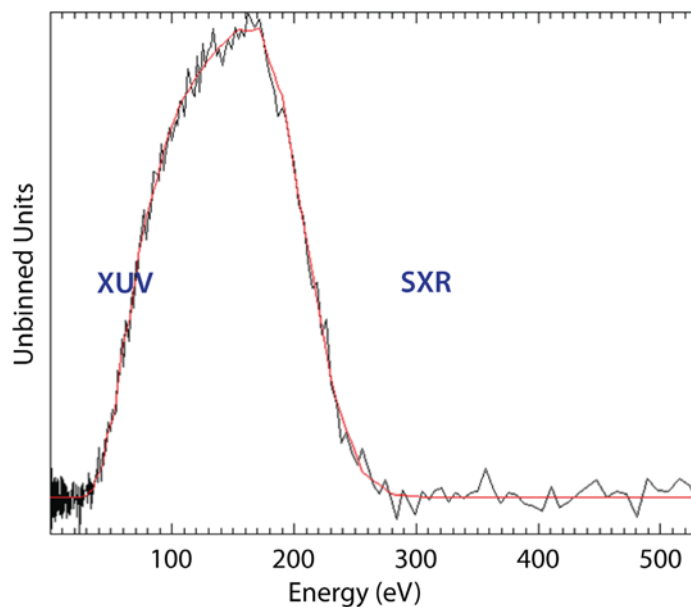
Figure 7. A "reasonable" amount of random noise is added to the simulated signals. The energy grid is finer at lower energies, which explains the frequency characteristics of the noise.

Table 1. Results of parameter search

Parameter	Initial Value	Inferred Values	$(a_{true} - a_{search}) / a_{true}$
a_0 (amplitude)	1.12×10^{10}	$1.1047 \times 10^{10} \pm 3\%$	1.3%
a_1 (width in γ)	0.8	$0.8037 \pm 2\%$	−0.5%
a_2 (average γ)	10	$9.995 \pm 0.3\%$	0.05%
a_3 (width in v)	0.0068	$0.0067 \pm 2\%$	1.5%
a_4 (average v)	0	$1 \times 10^{-3} \pm 2\%$	∞

This exercise was very successful, and shows that the needed information indeed exists in the data. The next step would be to use a test function that is not Gaussian, and make sure that the inferred parameters of the Gaussian fit are still good matches to the average energy, energy spread, etc. However, the parametric approach is limited in the amount of information it gives, and the real goal is to use linear algebra to carry out a completely general deconvolution, using binned simulations of scattering of a CO_2 beam.

Conclusion

Inverse Compton scattering of a laser beam by an electron beam can be useful as a simultaneous diagnostic of beam amplitude, energy, and angular spread from the axis. Detection across the full energy spectrum of the scattered radiation is necessary. Even though Compton scattering is inherently a weak process, adequate scattering amplitude can be afforded by a high-current discharge and a laser of moderate energy. This approach is very promising and should be pursued further. Further work would involve repeating the calculation for a CO_2 laser over the full scattered wavelength range, binning the data according to the wavelength ranges of available filters, and performing a full 2-D deconvolution (rather than the illustrative deconvolution by parameter search shown herein). Measured sources of noise on RITS should be added to simulations to demonstrate that this method will lead to a practical diagnostic for that machine. If RITS were judged to be too noisy an environment, this scheme could also be suitable for a huge number of charged particle beam machines worldwide.

References

Chouffani, K., F. Harmon, D. Wells, J. Jones, G. Lancaster, "Laser-Compton scattering as a tool for electron beam diagnostics," *Laser and Particle Beams* **24** (2006) 411–419.

Jackson, J. D., *Classical Electrodynamics*, John Wiley & Sons, 1975, Section 14-7.

this page intentionally left blank

Cerenkov Non-Intercepting Beam Monitor (CNIBM) for Relativistic Charged Particles

Brent A. Davis[1,a] and David D. Schwellenbach[b]

A Cerenkov non-intercepting beam monitor (CNIBM) designed to passively provide signals that are directly related in real time to charged particle beam characteristics was studied. The CNIBM concept relies on the production of Cerenkov radiation by relativistic charged particles traveling near a dielectric. CNIBM signals are practically immune to EMI distortion and electrical ringing. These attributes allow beam temporal structure to be measured that is necessary to optimize accelerator performance.

Background

The common explanation for the production of Cerenkov radiation implies that the charged relativistic particle must pass through an optically transparent dielectric to produce Cerenkov radiation. It is true that a charged, relativistic particle's electromagnetic field will cause Cerenkov radiation if the particle's velocity exceeds the phase velocity of light within the dielectric media. However, it is not necessary for the charged particle to propagate through that same media (Jelley 1958). Jelley considers the effect of a single charged particle passing near the surface of a transparent dielectric. The expression for induced Cerenkov radiation within the dielectric by a near-grazing, single, relativistic particle is

$$W_\omega = \frac{2e^2\omega}{c^2} \upsilon \left(1 - \frac{1}{\beta n}\right) exp\left[-2\frac{\omega z_0}{c}(\varepsilon - 1)^{\frac{1}{2}}\right] ergs/sec, \tag{1}$$

where ω is the mid-band frequency of radiation, ε is the dielectric constant of the material, n is the index of refraction, and z_0 is the distance between the particle's track and the surface. Since the optical output is expected to scale linearly with the number of particles, the Cerenkov non-intercepting beam monitor (CNIBM) performance will additionally depend on the current in the accelerated pulse. Jelley also points out that the wavelength of peak optical yield is a function of distance of the charged particles from the dielectric surface

$$\lambda_{max} \approx 4\pi(\varepsilon - 1)^{\frac{1}{2}} z_0. \tag{2}$$

For λ_{max} = 420 nm, the approximate mid-range of typical photo detectors, $z_0 \approx 10^{-5}$ mm, indicating that controlling beam position is an important variable in this study.

---

[1] davisba@nv.doe.gov, 702-295-2563
[a] North Las Vegas; [b] Los Alamos Operations

Applying these principles, Cerenkov radiation production from a charged particle beam with relativistic velocities is expected without particle interception of a transparent dielectric. By measuring the temporal and intensity characteristics of the Cerenkov radiation, it should be possible to design a CNIBM that has important applications associated with high-energy, charged particle accelerators; it may be possible to improve particle beam steering and provide more accurate temporal characterization of the beam. If correctly designed, a CNIBM could measure in real time (1) beam current (charge/sec) and (2) beam radial location within the accelerator's vacuum beam line.

The traditional non-intercepting beam monitor (NIBM) only provides differential signals. In contrast, the signal from the CNIBM would characterize the actual transitory particle beam with an improved signal-to-noise ratio. CNIBM signals are expected to be less sensitive to innate beam electromagnetic noise because the detection media is light emission rather than a direct measurement of the particle beam's electric field. This innate signal fidelity may even allow the temporal response of the particle beam to be deconvolved from a test detector's signal output—a unique and important possibility for radiation detector development.

Project

The simplest CNIBM geometry is a thick-walled cylinder of optically clear material on axis within an accelerator's vacuum beam line. This configuration would allow a particle beam (with outer boundary limits smaller than the inner diameter of the dielectric cylinder) to propagate within a vacuum environment concentric to the cylindrical axis. Simultaneously the associated electromagnetic field would penetrate the volume of the cylindrical dielectric. Based upon this general configuration, a prototype CNIBM was designed, fabricated, and subsequently tested. Figure 1 depicts the general features of the first prototype CNIBM that was used for the experiments described in this paper.
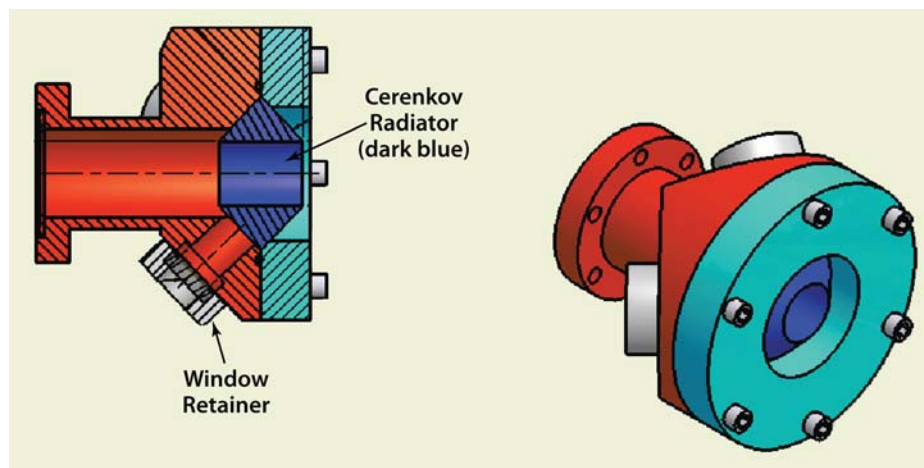

Figure 1. Configuration of the prototype CNIBM (particle beam enters from the right). The optical detectors (not shown) would be mounted at the three small flanges at the window retainer.

The Cerenkov radiator is made from optically clear (polished) Plexiglas. Cerenkov radiation produced within the Plexiglas propagates at a Cerenkov angle (Ø) to the particle beam's velocity described by

$$\text{Ø} = \text{Cos}^{-1}(c/nv), \tag{3}$$

where *c* is the velocity of light in a vacuum. This specified angle dictates the mandatory position of the optical sensor (detector).

Plexiglas was chosen for the prototype's Cerenkov radiator because of its common availability. Figure 2 shows the Cerenkov angle as a function of electron energy for a Cerenkov radiator made from Plexiglas. The best Cerenkov radiator design would use Suprasil (synthetic quartz) to ensure immunity to radiation damage should the particle beam accidentally strike the material due to imperfections in beam tuning.
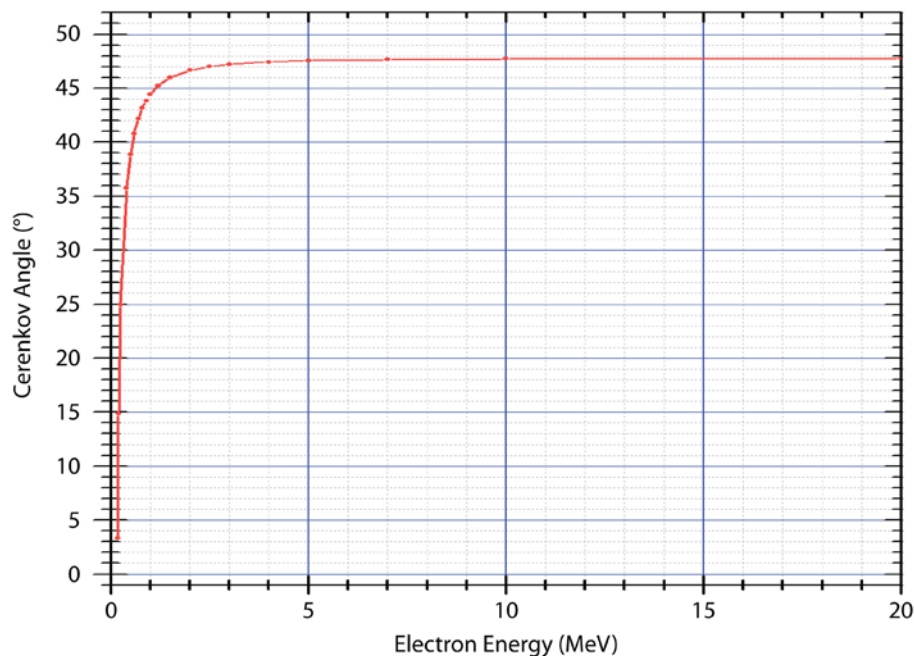
Figure 2. The Cerenkov angle in Plexiglas as a function of electron energy. The nearly constant angle above a few MeV implies that for typical electron accelerator energies a single design of the Cerenkov radiator could be possible (rather than requiring a specific design for each electron energy).

Linac Experiments at the Idaho Accelerator Center (IAC)

As discussed earlier, the intensity of Cerenkov radiation depends upon (1) the charged particle's beam current, (2) the particle's velocity (*v*), (3) the optical media's refractive index (*n*), and (4) the distance

between the charged particles and the Cerenkov radiator's surface. With this in mind, the linear accelerator (linac) at the IAC was chosen for a first series of experiments. The IAC linac provides the highly relativistic electron beam required with beam energies up to 40 MeV. A 70 ps FWHM, 20 MeV bunched electron beam provided an impulse with about 4×10^9 electrons in each Gaussian envelope.

Detectors for the CNIBM must be sensitive to light wavelengths near 400 nm. Although the prototype CNIBM has three ports available for detectors (for beam position measurements), the experimental setup was simplified by using a single microchannel plate (MCP) detector. The ensuing measurements were therefore dedicated to demonstrate that Cerenkov radiation can be produced without direct interference of the linac beam's relativistic electrons.

To avoid intruding into the IAC linac's vacuum beam line, the CNIBM was mounted immediately outside the accelerator's beam line exit port, which includes a 0.001-inch thick steel vacuum barrier (exit window). Immediately upstream from that exit window was an 18-inch long, traditional NIBM that was used for beam characterization. A small quadrupole magnet was located several inches upstream from the linac's NIBM to provide a final electron beam focus onto the center of the exit window.

Figure 3 shows a typical signal acquired from the prototype CNIBM using an MCP detector (PMT210 made by Photek Ltd.) to measure the Cerenkov radiation. This signal was induced by a Gaussian, 70 ps (FWHM), 20 MeV, 10 A (peak) electron impulse. The transient beam was focused to ~0.395-inch in diameter at the accelerator's exit window to help ensure that the 1-inch diameter clearance hole in the Cerenkov radiator would not intercept beam electrons.

There was concern that the Cerenkov radiation detected from the CNIBM could possibly have been caused by electron beam scatter at the exit window, or from natural electron beam divergence wherein electrons were intercepted by the Cerenkov radiator. To address this concern, the linac's NIBM was removed so that the CNIBM would be positioned closer to the quadrupole magnet and thereby improve beam focus onto the exit window. Multiple beam exposures were made on several glass slides at various positions relative to the beam's axis and CNIBM position. Figure 4 shows two simultaneous electron beam exposures onto glass slides. These slides were placed at both the entrance and exit ends of the CNIBM's former position (the CNIBM was removed to avoid its interaction with the electron beam). The exposure duration of the 10 A, 60 Hz beam was 15 minutes (~54,000 impulses), which ensured that the energy deposition would detect possible electron beam penumbra and beam position jitter.

Both exposures are compared to the diameter of a U.S. nickel (0.8125-inch diameter). In order to estimate the rms spot size of the electron beam, it was assumed that radiation damage is proportional to dose at a given point. Image J (image analysis software from nih.gov) was used to find the relative darkening of the slide shown in Figure 4a. The results, shown in Figure 5, give an rms (1σ) full width of ≈50 pixels. From the same image the width of the U.S. nickel is estimated to be 140 pixels, giving
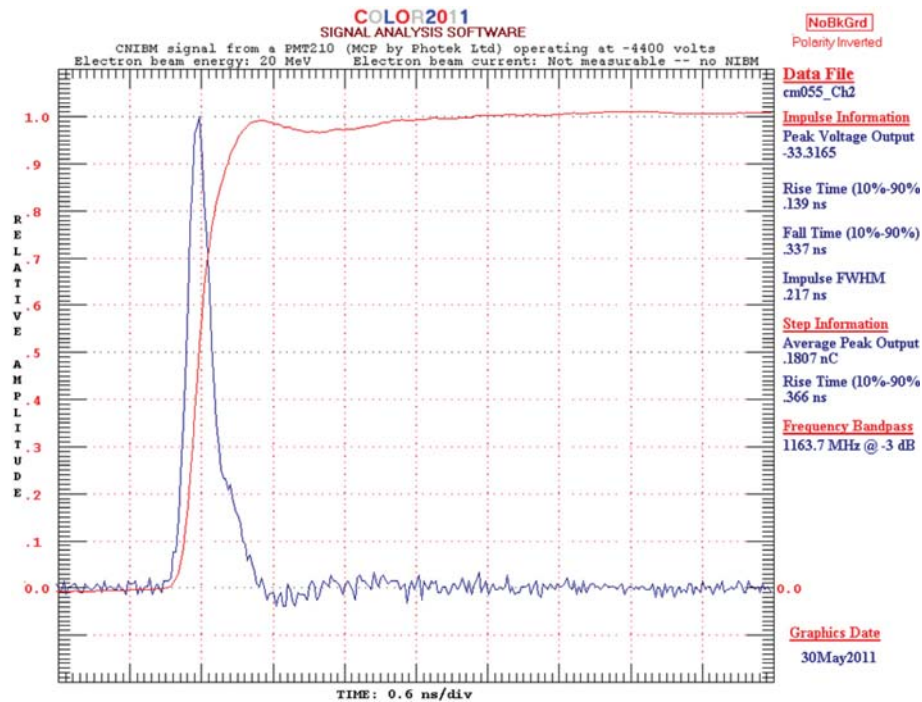
Figure 3. The CNIBM signal as measured by an MCP detector
(PMT210) operated at −4400 V. The linac electron beam was
20 MeV. No peak beam current measurements were possible
because the linac's NIBM had been removed for these particular
measurements, but (based on previous measurements) were
presumed to be about 10 A.

Figure 4. Electron simultaneous exposures onto glass slides located at the (a) entrance and
(b) exit locations of the CNIBM (the CNIBM was removed) show that it is unlikely the CNIBM
would have intercepted the main electron beam. A related intensity plot of Figure 4a is
shown in Figure 5.

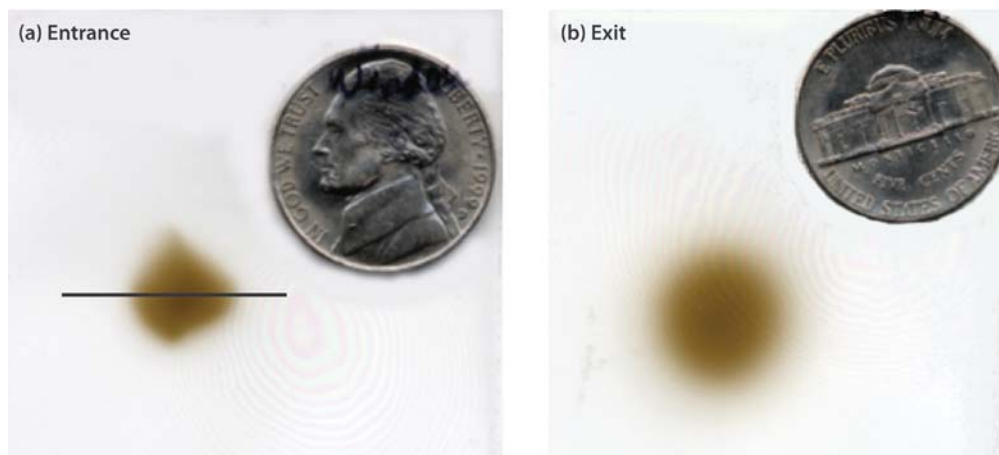an rms beam diameter of ≈0.3 inches. Based on these comparisons, it appears that the 1-inch inner diameter of the prototype CNIBM (with proper alignment) does not intercept the main electron beam. Further analysis was performed to determine if relativistic electrons were expected within ~λ of the inner wall of the CNIBM. Typical values (Wrangler 1998) for maximum to rms ratios range from 5 for very compact beams to as high as 10 to 12 when observing the beam halo of mismatched beams. This gives an expected maximum diameter of the electron pulse from 1.5 to 3.6 inches, greater than the 1-inch inner diameter of the Cerenkov radiator. Even though the electron density at the 1.5–3.6-inch diameter of a 0.3-inch diameter beam from beam center is expected to be quite low, Cerenkov radiation from electrons in proximity to the radiator and from electrons penetrating the dielectric is possible. Further studies to measure parameters such as charge buildup on the Cerenkov radiator are needed to resolve the ultimate source of the observed light emission.
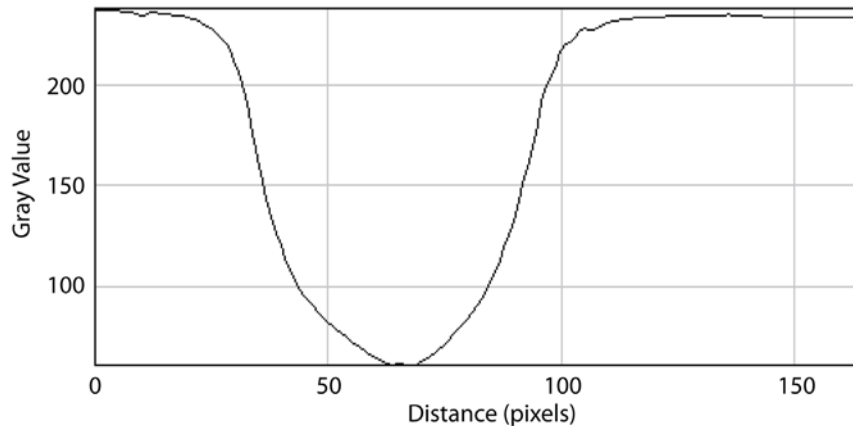

Figure 5. Intensity plot of line through slide shown in Figure 4a created using Image J software. The horizontal line indicates the rms width of the distribution.

Cerenkov radiation using the prototype CNIBM equipped with a simple bi-planar photodiode (PD) was not possible even with a 10 A linac peak beam current. The PD was simply too insensitive for the weak intensity of the emitted Cerenkov radiation. The PMT210 used for the initial tests yielded a peak signal near 33 V because of its inherent 1×10^6 gain. The PMT210 signal data acquired for the described test conditions imply that detector replacement for the PMT210 would require a gain not less than about 300. This estimate is based upon the presumption that both detector photocathodes would have the same quantum efficiency (~12% at 400 nm), and that a minimum of 10 mV is an acceptable peak signal output. The PMT113 (another MCP) has about a 2000 gain. However, its temporal response is limited to measuring impulses not less than about 150 ps (FWHM). To be useful for the nominal capabilities of the IAC linac (for example), the detector's temporal response must be able to measure at least 70 ps (FWHM) transients.

A simple bi-planar phototube could be designed to make such a measurement, but it would have no gain. Consequently, it would be useful if the CNIBM Cerenkov radiation could be enhanced or more of the radiation could be collected at the detector's photocathode.

Design studies show that Cerenkov radiation from a modified CNIBM is possible. The existing CNIBM collects only a very small portion of the available Cerenkov radiation (less than 10° of a possible 120° arc of a three-detector array). By using a compound parabolic mirror (or lens), almost all of the light within the 120° arc could be focused to a common point where the detector's photocathode would be positioned. Figure 6 is a concept drawing of such a mirror. The axis of the CNIBM would be positioned at the center of the semicircle located at the bottom of the figure with the particle beam propagating toward the top of the figure. The focal spot would be offset from the axis; for this particular mirror design, that offset would be 3 inches vertical from the CNIBM axis.
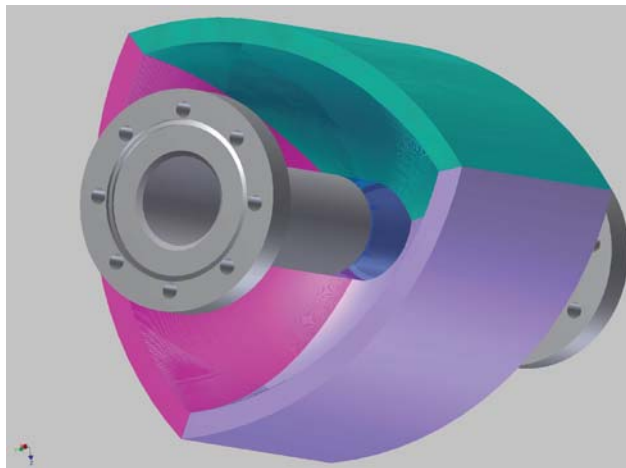
Figure 6. The CNIBM with three compound parabolic mirrors enveloping the Cerenkov radiator (item in blue). Each mirror has an independent focal point to the left of each mirror. The flanged gray item is the beam line.

In addition, if the length of the prototype's Cerenkov radiator were increased from 0.600 inch to 6 inches, the light measured from the CNIBM would be augmented by a factor of ten. With an increase of the accelerator's peak electron beam current from 10 to 30 A, it would be possible to replace the PMT210 with a special, high-bandwidth bi-planar phototube and thereby successfully measure charged particle beam transients of 50 to 70 ps.

To deploy mirrors (or lenses) would require careful and sophisticated ray tracing analysis and subsequent mirror/lens design to ensure propagation time of each ray throughout the CNIBM's collection zone arrives at the intended focal spot within about a 10 ps time frame. Otherwise, a high bandwidth signal from the CNIBM will be unacceptably compromised.

Another option for enhancing the collection of Cerenkov radiation from the CNIBM is depicted in Figure 7. This method uses large gallium-nitride crystals as detectors (in development stages by Kevin Sun of NSTec). Three or more of these detectors simply collect the Cerenkov radiation ring that is produced by using a simple hyperbolic mirror. Although the gallium-nitride detector is still in development, these detectors are projected to have sensitivities near the 400 nm range, theoretically have sufficient gain for CNIBM applications, and would measure 50 ps (FWHM) input transients. As with the compound parabolic mirror approach, the optics would have to be adjusted so that the multiple optical paths of the Cerenkov radiation are essentially equal.
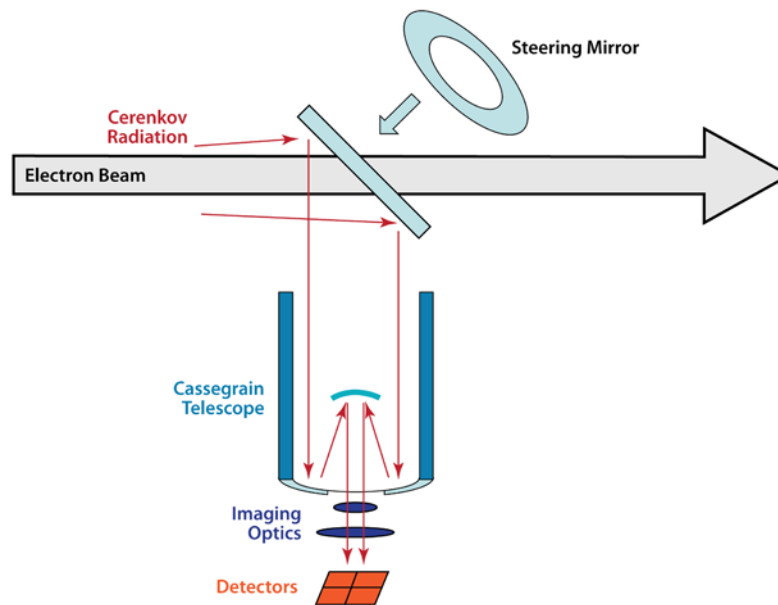

Figure 7. This CNIBM concept uses inexpensive optic lenses and mirrors, plus gallium-nitride detectors to measure a focal ring

Conclusion

Tests with relativistic electrons (20 MeV) have demonstrated that the CNIBM has potential as a charged particle beam monitor for relativistic electrons. Since beam halo can have a much larger spatial distribution than the primary beam, the use of this device for beam steering and to determine spot size will require further studies. However, the experimental demonstrations indicate that temporal characterization of a relativistic electron beam is possible even if the Cerenkov production is from the beam's penumbra. This demonstration opens up new opportunities to improve measurement of temporal characteristics of the beam in high-energy particle accelerators as well as the potential to measure amplitude and spatial characteristics.

Acknowledgments

References

Jelley, J. V., *Cerenkov Radiation and its Applications*, Pergamon Press, New York, 1958, 46–48.

Wrangler, T., *RF Linear Accelerators*, John Wiley & Sons, New York, 1998, 289.

this page intentionally left blank

Time-Resolved Hyperspectral Fluorescence Spectroscopy Using Frequency-Modulated Excitation

John Di Benedetto,[1,a] Gene A. Capelle,[a] and Mary D. O'Neill[a]

The use of modulated light sources and synchronous detection was demonstrated as an alternative to the use of pulsed-laser systems for time-resolved hyperspectral applications. An intensity-modulated excitation light source was used together with a microchannel plate–intensified CCD detector gated at a slightly different frequency to generate a beat frequency. The addition of a spectrograph produced a hyperspectral data product where the resulting beat frequency can be detected with the low frame–rate CCD camera. Both experimental and analysis techniques are discussed, and data are presented from the spectrograph system and from the photodetectors used for diagnostics. Measuring the phase shift of the beat wave at any particular wavelength gives not only spectral data, but also the emission lifetime. The technique described herein investigates a new way to hyperspectrally and temporally resolve emissions without lock-in amplifiers or other forms of digital phase-locked loops.

Background

Time-resolved systems are used for trace detection and/or identification of materials in a multitude of applications. Time-resolved fluorescence spectroscopy techniques can generally be categorized as either time domain or frequency domain. For most remote sensing applications, pulsed-laser time-domain systems are used. These systems require high peak–power lasers and short integration times to detect weak return signals in high ambient light–level backgrounds. The second general approach towards fluorescence detection is based on frequency-domain techniques (Lakowicz 2006). Sine or square-wave intensity modulation of the excitation light causes a corresponding modulation of the returned fluorescence light that can be phase shifted and intensity demodulated relative to the excitation wave. Advantages of this technique over pulsed laser systems include greatly decreased non-linear effects due to lower peak excitation power; smaller size, weight, and power requirements; and excellent optical background rejection. Standard (and now commercially available) methods exist to detect frequency-modulated (FM) fluorescence spectra using a single detector. These systems can operate over a large frequency range, obtaining lifetimes down to picoseconds. However, they require a scanning monochromator and acquisition times unsuitable for remote sensing applications. In this work, the beat pattern for an entire spectrum was recorded over multiple CCD camera acquisitions, and the lifetime of the spectrally dispersed emission was calculated both from the phase shift and (independently) from the demodulation of the beat wave. The absolute phase shift was determined by measuring the phase shift of the emission spectrum relative to the unshifted excitation peak, which was also recorded through the spectrograph.

[1] dibeneja@nv.doe.gov, 805-681-2240
[a] Special Technologies Laboratory

In 2006–2007, the Special Technologies Laboratory developed a single-color, single spatial–pixel, FM system (Di Benedetto 2008). This project demonstrated that phosphorescent signals could be measured in high background light conditions. Compact LEDs were used as an excitation source. These were modulated at various discrete frequencies, and signals were recorded using high dynamic range photodiode detectors. Using commercially available digital lock-in amplifiers and techniques (Gardner 2005), the resulting phosphorescence wave phase shift and modulation depth were measured. When these measurements are extended to a number of modulation frequencies, the frequency response of the material is mapped out in the frequency versus phase-shift response much like one does with an electrical circuit. Multiple lifetimes can be elucidated when this response is fitted using Laplace transform analysis. The single-color measurement demonstrated that phosphorescent signals could readily discriminate against ambient light such as sunlight, against facility lights, and against prompt fluorescence emissions.

The FM method described in this report records the modulation as a beat pattern generated when an excitation source and a spectral detector gate are operated at slightly different frequencies. As the excitation source and the detector gate slowly pass out of phase and then back into phase again, a beat wave is produced within multiple (wavelength versus intensity) images collected by the spectrograph/ intensified CCD (ICCD). The beat pattern for the entire spectrum is recorded over multiple CCD camera acquisitions, and the lifetime of the spectrally dispersed emission can be calculated both from the phase shift and (independently) from the demodulation of the beat wave.

Project

Theory

In most optical frequency domain systems, the primary method for determining the lifetime of a fluorescent material is based on determining the phase shift and/or modulation of the fluorescence return with respect to the laser excitation. Figure 1 shows the change in depth of modulation and the phase shift of fluorescence relative to the excitation, where ϕ is the phase shift of fluorescence return relative to the excitation signal, ω is the modulation frequency in radians/second, τ is the lifetime in seconds, and m is the modulation, with signals as defined in the figure.

The equations used in determination of fluorescence lifetime from modulation and phase shift are

$$m = \frac{B/A}{b/a} = \frac{1}{\sqrt{1+\omega^2\tau^2}} \tag{1}$$

and

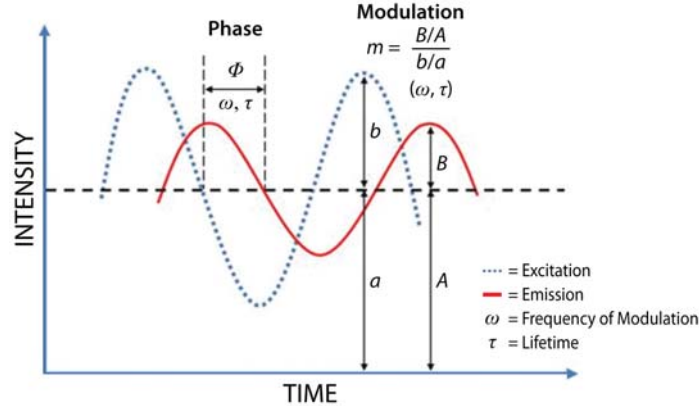$$\tan(\phi) = \omega\,\tau. \tag{2}$$

Figure 1. Phase shift and change in modulation depth of the fluorescence return relative to the excitation

For our hyperspectral data, the phase shift of the beat wave at the fluorescence wavelength of interest was measured relative to the unshifted beat waveform at the excitation wavelength, which was 405 nm for the experiments to be described. We created a simple model for simulating the expected beat frequency output from a sample excited by a square wave–modulated source and measured with a gated detector, where the gating frequency is shifted by frequency F from the excitation frequency. This model includes noise and can provide a means to determine the limitations of this approach with added electronic and atmospheric noise. The present model includes only a single lifetime, but it will later be modified to add multiple lifetimes. The adjustable parameters of this model are excitation and detector frequencies, number of samples per cycle, fluorescence lifetime, duration of the data collection in seconds, and the standard deviation of the noise level. The model generates the excitation source (called "*Laser*" in the equations below) and detector gate square waves with added noise, x_{Laser}, and x_{DET}. It then computes the fluorescence decay signal as

$$g(t) = e^{-t/\tau}, \tag{3}$$

where t is the time in the sequence, and τ is the lifetime of an arbitrary fluorescent material. The laser diode (or LED) return into the detector is modeled as the convolution of the excitation with the fluorescence decay

$$y_{Laser}(t) = x_{Laser}(t) * g(t). \tag{4}$$

The detector output is modeled as the dot product of the laser diode return and the detector response

$$y_{DET}(t) = y_{Laser}(t) \cdot x_{DET}(t). \tag{5}$$

Finally, the beat signal is the integrated detector output computed as

$$x_{Beat}(t_{Beat}) = \sum_{t=t_{Beat}}^{t_{Beat}+1/f_{Laser}} y_{DET}(t) \cdot \Delta t, \tag{6}$$

where Δt is related to the laser frequency and the number of samples by $\Delta t = 1/(f_{Laser} * n_{Samps})$. Results from this model are compared directly to measured data in the ***Results and Analysis*** section of this report. The measured hyperspectral data include data at multiple wavelengths.

Experiment

Initial experiments were carried out with a square wave–modulated LED, a gated photomultiplier, a synthetic ruby sample, and an oscilloscope with long record length for data collection. This initial setup provided experimental confirmation of the concept, as well as preliminary data on which to begin testing analysis algorithms. Subsequent experiments were performed with a full hyperspectral system.

Excitation

The experimental setup is shown in Figure 2. An LED with nominal 405 nm output was used as the excitation source, with a cleanup filter (60 nm wide band pass centered at 417 nm) to eliminate other emissions from the LED. The square-wave rise and fall time of the LED was near 5 μsec, so measurements were limited to frequencies of 4 kHz and below. For measurements at higher frequencies, the LED was replaced with a 405 nm laser diode capable of giving a fairly clean square-wave output at frequencies up to 100 kHz. Average power on target was near 50 mW over an area of several square centimeters. Square-wave excitation was used for two reasons: (1) this made it easy to see any artifacts (deviation from square wave) in the excitation source output at various output powers and frequencies, and (2) it was compatible with the square-wave nature of the detector response (i.e., the gated photomultiplier or microchannel plate [MCP] could only be on or off).
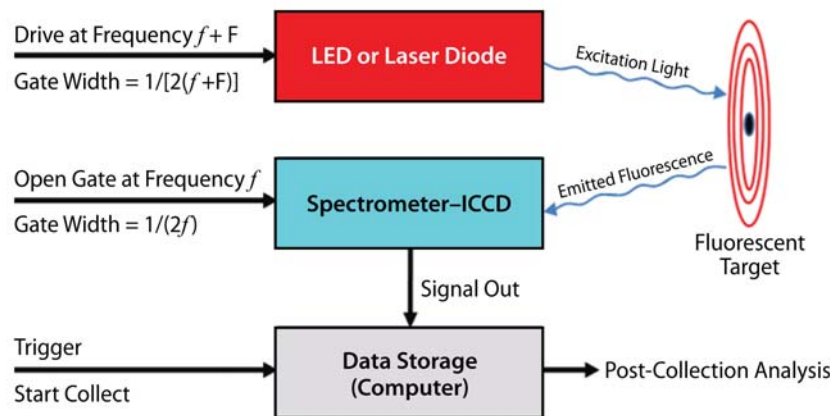

Figure 2. Experimental setup

Targets

The first experiments were conducted using a synthetic ruby crystal target, which was chosen because it has a relatively long lifetime (near 4 msec), can be excited at 405 nm, and has a strong emission peak near 694 nm. Later, a second, fluorescent green target material was used; the green target also absorbs well at 405 nm, emits quite strongly in the 500 to 550 nm region, and has a considerably shorter lifetime than the ruby target (in the hundreds of microseconds region [with multiple component decay times]).

Detection

Fluorescence from the target was collected by a 600-micron core fiber, bare except for a filter to attenuate the 405 nm excitation light, positioned 8 to 12 cm from the target. The illumination collected by this fiber was sent to the input slit of a small imaging spectrograph with the ICCD detector mounted at its focal plane. The ICCD's MCP gate was always operated at a frequency f that was slightly less than the frequency of the excitation source, and with a 50% duty factor (equal on and off times). The difference in frequencies gives the observed beat frequency, F. Various values of F between 0.1 and 1 Hz were used in these experiments. For all experiments, F << f (i.e., the beat frequency was always much less than the modulation and detection frequencies). To monitor how a gated MCP interacts with the excitation pulse and the CCD exposure cycle, a diagnostic system was set up to analyze behavior. An oscilloscope with a long record length (10 M points) was used to collect four supplemental channels of data, but ultimately this information was not used in the data analysis. These channels included the MCP intensifier gate monitor, a photodiode monitor of the excitation source output light, an optically filtered photodiode monitor of the target fluorescence, and a CCD exposure interval monitor.

Timing

A square-wave generator gates the detector at frequency f, and another square-wave generator controls the LED or laser diode output at frequency f + F. Both generators are operated with a 50% duty factor and the two signal generators are free-running with respect to each other. A start pulse arms the ICCD system, which initiates data collection by the ICCD system at the next gate pulse; it also initiates the diagnostic oscilloscope scan. The data collection system typically is set to collect up to 1024 frames of data, each frame consisting of a wavelength-intensity waveform (1024 channels × 16 bits) at a particular window in time. Full vertical binning was used on the CCD, effectively converting the 1024 × 256 array to a 1024 × 1 (linear) array.

Results and Analysis

As the 405 nm excitation source and the MCP gate slowly pass out of phase and then back into phase again, a beat wave is produced. At the 405 nm readout wavelength of the detected excitation source, the beat wave is a triangle wave (the convolution of the two square waves passing over one

another), which serves as a built-in zero phase–shift reference wave. An experimental data set for a particular target material is collected at a number of different frequencies f, ranging from well below up to roughly at the frequency given by $f' = 1/\tau$, where τ is the radiative lifetime of the sample. As f becomes much less than f', the phase shift becomes very small and difficult to measure, while as f increases above f', the modulation depth becomes increasingly shallow, eventually making the beat wave unmeasurable; in either extreme, satisfactory measurements cannot be made. In the experiments presented here, some values of f well above f' were used for demonstration, but the accuracy of the lifetime values produced at these frequencies is poor, as expected.

Parameters were normally adjusted to achieve near 40 frames ("snapshots") per cycle of the beat wave to ensure a reasonable representation of the wave, and data were collected for multiple cycles of the beat wave. With our system constrained to a frame rate of 20 to 40 frames per second, we were limited to beat frequencies of 1 Hz or less, and collection times were tens of seconds. The results of applying this beat frequency technique to a synthetic ruby crystal sample are shown in Figure 3, taken at a frequency f = 32 Hz and a beat frequency F = ½ Hz. Figure 3a is the first CCD frame of the data collection, obtained when the LED and the detector gate opened simultaneously. Both the excitation pulse around 405 nm and the ruby emission at 694 nm are clearly visible. Figure 3b shows frames 15 through 39, where the effects of the ruby lifetime are evident at this frequency. While the excitation light peak shows the fully modulated triangle-wave pattern as the frames advance, the fluorescence light signal has become more rounded, its modulation depth has decreased, and there is a clear delay or phase shift with respect to the excitation wave. Figure 3c is the same data set, but showing the first 120 frames. Here the beat waves are clearly visible. These three-dimensional data are reduced to two dimensions by taking a slice through multiple successive CCD frames at a single wavelength.
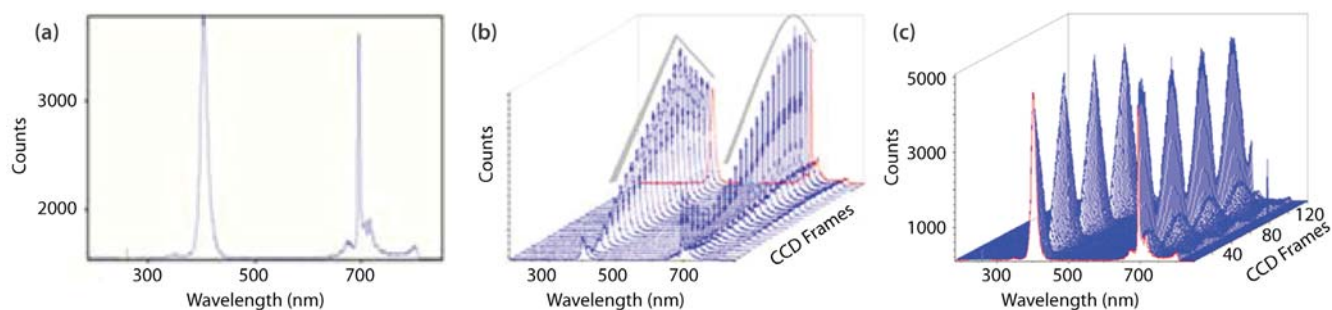

Figure 3. (a) Single CCD frame showing 405 nm excitation light (left peak) and ruby fluorescence signal (right peak); (b) frames 15–39 of same data collection; (c) 120 frames of the same collection

Examples of intensity at a single wavelength versus frame number are plotted in Figure 4 for both the excitation light at 405 nm (the triangle wave) and for several wavelengths around the maximum ruby emission. Data at this wavelength are shown at four different excitation frequencies. Note that the phase shift increases and the modulation depth decreases as frequency increases. The lifetime of
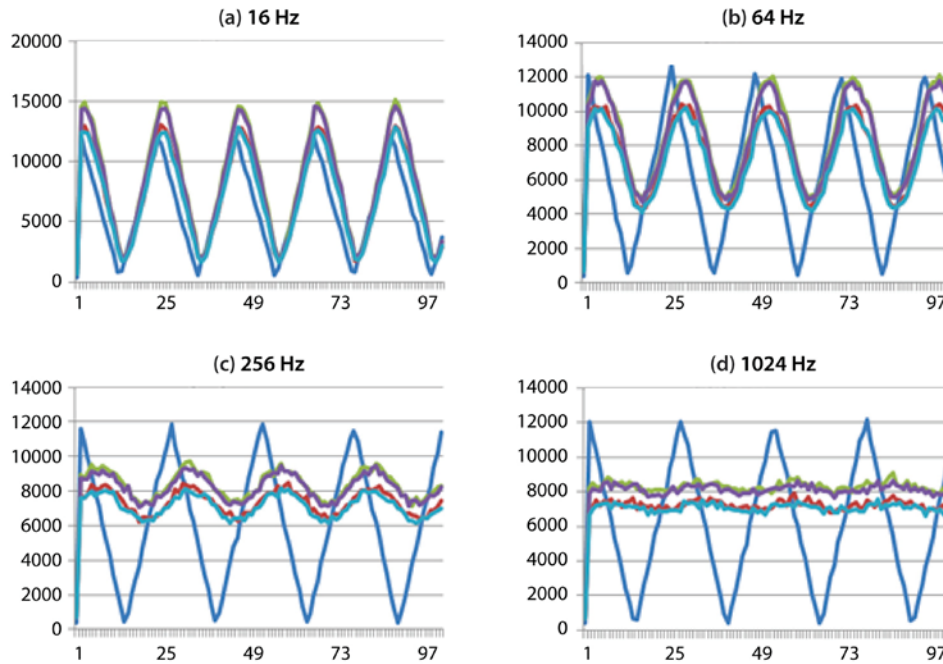
Figure 4. Superposition of signal collected at 405 nm (unshifted sawtooth) and as several wavelengths around the maximum ruby emission for four frequencies

the sample was calculated both from the phase shift and independently from the modulation depth, as discussed in the previous section. The beat waveform from the model was compared directly to the measured beat waveforms, and the result is shown in Figure 5.
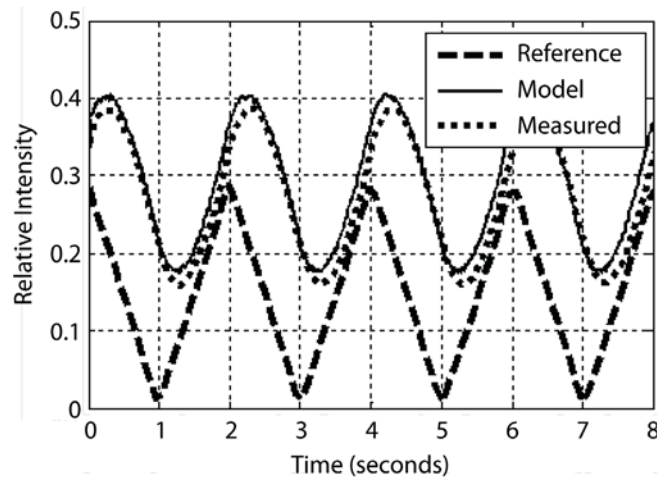

Figure 5. Model versus measured beat waveform for ruby sample (64 Hz excitation, 0.5 Hz beat frequency); note that DC offsets of the model and measurement agree. The prompt return from the reference (excitation) is also shown.

Figure 5 shows data taken from the synthetic ruby material target with a 100 Hz excitation signal and a 0.5 Hz beat frequency. Note the good agreement between the phase and the modulation levels.

Reduction of these waveforms into target material lifetimes was done using a digital implementation of the common in-phase and quadrature-phase (I/Q) phase detection method as shown in Figure 6. The incoming signal (in our case, the fluorescence return with phase shift, ϕ, relative to the excitation-wavelength beat wave) is mixed with both in-phase reference (excitation return) and quadrature-phase reference (excitation return shifted by 90°) signals. The low-pass filter removes the high-frequency components such that the DC levels of I and Q are measured. The ratio of Q to I is directly related to the phase shift ϕ and the lifetime τ by

$$\tan(\phi) = \frac{Q}{I} = \omega\tau \tag{7}$$

and

$$\tau = \frac{Q}{I \cdot \omega} = \frac{\tan(\phi)}{\omega}. \tag{8}$$

This analysis requires knowledge of the excitation wavelength and the beat frequency. The data analysis method results in a single lifetime even if multiple lifetimes are present. Note that for I/Q calculations, the AC coupling of the signals removes offsets that would skew the phase calculation. Also, data must contain full cycles or there will be a skew in the I or Q value, resulting in an incorrect phase calculation. In addition to using phase to compute lifetime, the lifetime from the modulation was computed from the demodulation as

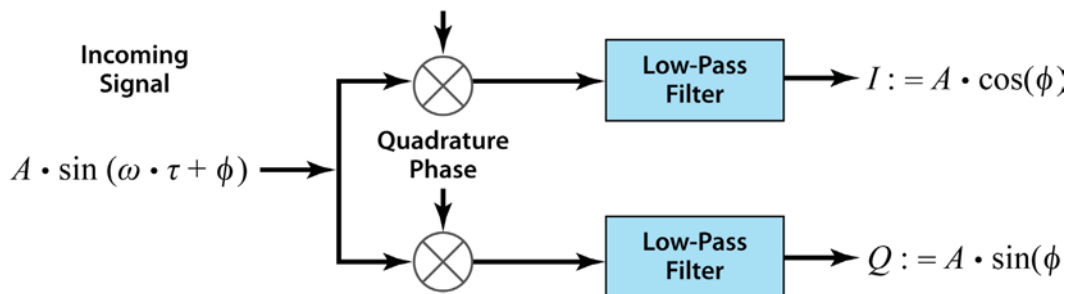$$\tau_m = \frac{\sqrt{1-m^2}}{\omega \cdot m}. \tag{9}$$

Figure 6. *I/Q* block diagram. The incoming signal with a phase shift (ϕ) is mixed (multiplied) by in-phase and quadrature-phase reference signals resulting in I and Q, respectively. By definition, $\tan(\phi) = Q/I = \omega\tau$, where ω is the frequency in radians/second and τ is the lifetime.

For each target material, measurements were made near the optimum frequency (phase shift near 45˚) as well as at a number of frequencies above and below this value. The computed lifetime of the ruby sample from phase (solid line) and modulation (dashed line) is shown in Figure 7a. The lifetime calculated using the I/Q method (solid line) agrees fairly well with the decay time of 4 msec. This decay time was measured independently by pulse excitation of the ruby sample followed by measurement of the 1/e decay time of the fluorescence intensity, using a photomultiplier detector and an oscilloscope and cross-checked using a silicon photodiode detector. As can be seen from Figure 7a, the accuracy suffers as the frequency increases beyond the optimum (about 40 Hz for the ruby sample).

A second fluorescent sample, called the "green target," was also measured with this technique. It had a shorter lifetime and an emission band in the green. As measured by 1/e decay time on an oscilloscope, the lifetime is roughly 220 µsec, with a second, longer decay time that was weakly apparent. Analyzed data for this sample are shown in Figure 7b. With two or more lifetimes, the lifetimes computed from phase and modulation techniques are systematically perturbed from the dominant single-lifetime value. In fact, the I/Q lifetime tends to be shorter than the average lifetime. The modulation-derived lifetime is longer than the average lifetime and decreases with frequency as the modulation depth decreases (Lakowicz 2006). This is clearly seen in Figure 7b. By measuring the phase and modulation values for a wide range of frequencies, the actual lifetime can be derived using a least squares procedure (Lakowicz 2006). Both techniques give a reasonable estimate of decay time. Accuracy of the analysis methods is discussed further below.
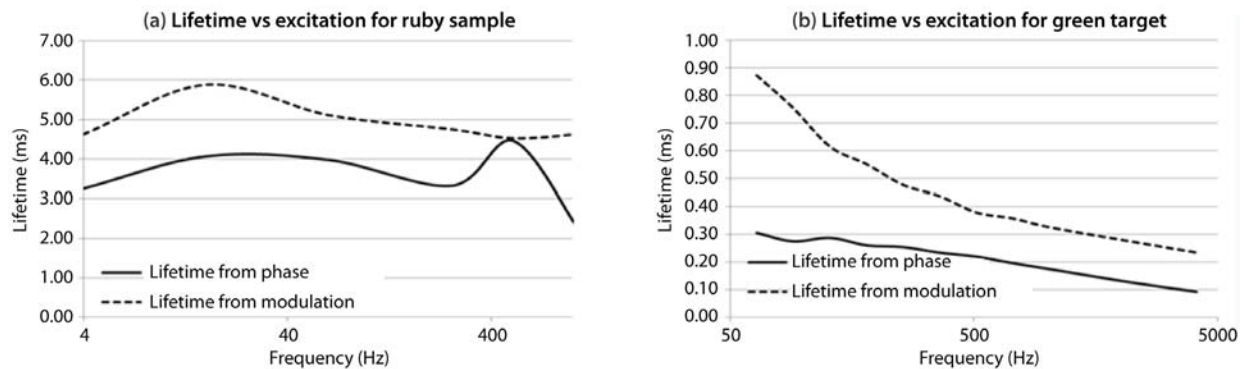

Figure 7. (a) Sample lifetime as a function of frequency, calculated by both methods for a ruby sample (single decay time); (b) same as (a) except using the green target, which has multiple decay times

Conclusion

The technique we have demonstrated will have direct applications in time-resolved fluorescence microscopic analysis (where high peak power must be avoided) and also for fluorescence lidar [light detection and ranging]. Because the light sources can be modulated over a wide frequency range, FM measurements may be made from tens of hertz to hundreds of megahertz, depending

on the exciter and detector bandwidth, even when using relatively low frame–rate CCD cameras. If ultrafast lasers and detectors are used, the same technique may also find application in Raman and transient resonance Raman applications. For remote sensing (outdoor) measurements, a much faster CCD would also permit increasing the beat frequency to mitigate the effects of some noise, since background noise (solar, atmospheric fluctuations, etc.) is worst at lowest frequencies. A lock-in amplifier could also be used to recover weak signals (Harper 2004). The optimum frequency region for the phase-shift determinations of the lifetime is at or slightly below the value given by $\tan (45) = 2\pi f\tau$, so f is about = $0.1592/\tau$, the frequency where the phase shift is 45° and changing most rapidly with frequency. For the ~4 msec lifetime, this frequency is 40 Hz, and for 220 μsec it is slightly over 700 Hz. For each target material, measurements were made near the optimum frequency, as well as at frequencies above and below this value. As the frequency increases beyond this ideal value, the accuracy suffers, though in some cases the drift downward in apparent lifetime is due in part to faster lifetime components having more effect at higher frequencies where demodulation begins to wash out the slower components. The same loss of accuracy occurs at frequencies far below the ideal, because at this point both the phase shift and demodulation are very small. This method gives a reasonable measurement of radiative lifetime; the accuracy is sufficient to provide discrimination between fluorescent targets of reasonably different lifetimes. The main point here, however, is not just to make a reasonable lifetime measurement of a sample, but, more generally, to demonstrate a new detection technique that provides another method for looking at fluorescent targets of interest. By collecting data at multiple frequencies, target materials can be analyzed not only by their spectral output, but also simultaneously by their radiative lifetimes.

References

Di Benedetto, J., G. Capelle, L. Chandos, J. Herning, I. McKenna, P. Ryan, R. Trainham, "Frequency modulated detection of phosphorescence on surfaces," *Nevada Test Site–Directed Research and Development*, FY 2007, National Security Technologies, LLC, Las Vegas, Nevada, 2008, 83–91.

Gardner, F. M., *Phaselock Techniques*, 3rd edition, Wiley Interscience, John Wiley & Sons, Hoboken, New Jersey, 2005.

Harper, W. W., J. D. Strasburg, "Remote chemical sensing with quantum cascade lasers," *Proc. SPIE* **5403** (2004) 378–386.

Lakowicz, J. R., *Principles of Fluorescence Spectroscopy*, 3rd edition, Springer Science+Business Media, LLC, New York, 2006, 160–163.

Nanostructured Nuclear Radiation Detector[†]

Paul P. Guss,[1,a] Ronald Guise,[a] Ding Yuan,[b] and Sanjoy Mukhopadhyay[c]

Composite scintillators consisting of nanosized inorganic crystals embedded in an organic matrix have been actively pursued in recent years. Nanostructure detectors may provide a way to engineer very large detectors that have flexible form factors at an extremely low cost. These detectors would have a broad energy range and a sufficient energy resolution to perform isotopic identification. Nanocomposites are easy to prepare; it is much less costly to use nanocomposites than to grow large, whole crystals. The material can also be fabricated on an industrial scale, further reducing cost. In this work, nanoparticles with sizes <10 nm were fabricated, embedded in a polystyrene matrix, and the resultant scintillators' radiation detector properties were characterized as a follow-up to studies performed under SDRD in FY 2010 (Guss "Nanostructured" 2011).

Background

Scintillators play an important role in many applications involving radiation detection, in areas such as laboratory experiments, medical imaging, and nuclear material safeguards. Traditionally, the most widely used scintillators are one of two types: organic and inorganic. In addition, composite scintillators seeking to combine the advantages of both organic and inorganic scintillators are being actively developed (Dai 2002, McKigney 2007, Osinski 2008). Composite scintillators are radiation detectors consisting of small inorganic crystals embedded in an organic matrix. Ideally, a composite scintillator would have efficiency and resolution similar to those of an inorganic scintillator, while retaining the low cost and manufacturability of the organics (Guss "Investigation" 2011, "Nanostructured" 2011). In order to produce these composite scintillators, small inorganic crystals suitable for incorporation in the organic matrix must be made. Historically, the first composite scintillators consisted of microsized (~10 μm diameter) inorganic crystals in an organic matrix, but they suffered from optical opacity caused by refractive index mismatch between the matrix and the crystals (Vasil'chenko 2003). It was reported by McKigney (2007) that transparent composite scintillators may be made using nanosized crystals.

The use of commercially available inorganic semiconductors (bulk particle size range: μm) as scintillators has been limited by their low solubilities in organic and polymeric matrices. Likewise, their preparation in inorganic matrices, such as sol-gel, results in optically opaque gels with the lowering of

[1] gusspp@nv.doe.gov, 702-295-8095
[a] Remote Sensing Laboratory–Nellis; [b] Los Alamos Operations; [c] Remote Sensing Laboratory–Andrews
[†] Project continued from FY 2010

photoluminescence quantum yields. During the past two decades, there have been extensive investigations of semiconductor nanocrystals or quantum dots (QDs). When the sizes of these QDs become comparable to or smaller than the bulk exciton Bohr radius, unique optical and electronic properties occur (Henglein 1989, Schmid 1992, Alivisatos 1996, Nirmal 1999). These effects arising from the spatial confinement of electronic excitations to the physical dimensions of the nanocrystals are referred to as quantum confinement effects. One such effect is the quantization of the bulk valence and conduction bands that result in discrete atomic-like transitions that shift to higher energies as the size of the nanocrystal decreases. With the size-dependent optical properties of QDs (especially the photoluminescence property), QDs with specific sizes can be made for specific detection wavelengths over the whole UV/V range.

In 1993, Bawendi and coworkers (Murray 1993) were the first group to synthesize highly luminescent cadmium selenide (CdSe) QDs by using high-temperature organometallic procedures. Later, the deposition of a surface-capping layer such as zinc sulfide (ZnS) or cadmium sulfide (CdS) in the core/shell QD structure was also found to dramatically increase the quantum yields of CdSe nanocrystals up to 40% to 50% at room temperature (Hines 1996, Dabbousi 1997, Peng 1997). Another key advancement in this area was the synthesis of highly luminescent cadmium telluride (CdTe), CdSe, and CdS QDs in large quantities (Peng 2001, Qu 2001).

Several metal chalcogenides (e.g., ZnS, CdSe/ZnS) are known to be highly efficient scintillators. Their preparation in inorganic matrices results in nontransparent gels, thus lowering their efficiency as scintillating devices. By reducing their particle sizes from commonly used micrometer into nanometer-sized regimes, their optical properties and solubilities in both polar and nonpolar solvents can be controlled (Dai 2002).

An objective of this project was to develop QD scintillators for high brightness and efficiency x-ray, γ-ray, and α-particle detection. The initial effort focused on CdSe/ZnS, and CdTe/ZnS core/shell QDs, and manganese-doped zinc selenide (ZnSe:Mn) nanocrystals incorporated into the polymer at various concentrations. The solid polymer matrix is an advancement over the nanoparticle loading of an organic liquid (Del Sesto 2007), wherein the nanoparticles may aggregate. Another objective was to determine what leads to observation of photopeaks in energy spectra of isotopes using the QD scintillators (Létant 2006, McKigney 2007).

Project

Detectors

Radiation Monitoring Devices, Inc. (RMD) prepared a set of detector samples. Fourteen are core/shell and four are QD detectors, but all have the basic consistency of a mixture of nanoparticles in a polymer matrix with different densities of nanoparticles. The detector set includes two samples of CdSe with a ZnS shell (CdSe/ZnS). The two samples of CdSe/ZnS employ a polystyrene matrix.

The QD sample of cadmium selenium sulfur (CdSeS) had a volume greater than 1 cc. The physical form of the CdSeS sample was a 2 cm wide flat disk. This sample had 0.2% CdSeS by weight uniformly distributed in an epoxide-amine polymer. There were six samples of CdTe with a ZnS shell (CdTe/ZnS). There were three samples with ZnSe:Mn in a polystyrene matrix. The three samples were roughly 1 cc and contained 1%, 2%, and 5% QD loading. The 5% sample, however, was formed with many voids and defects. RMD also provided the six surfactant detectors that resulted from their process of forming the CdTe/ZnS detectors, though these surfactant detectors are of smaller dimension, uniformity, and quality. A BC400 detector from the Remote Sensing Laboratory was used as a reference.

Figures 1a and 1b show photographs of the nanoparticle (or nanocomposite) detectors, and Table 1 lists all the sample compositions, material matrixes, and characteristics with different radioactive sources for the detectors used in this work.
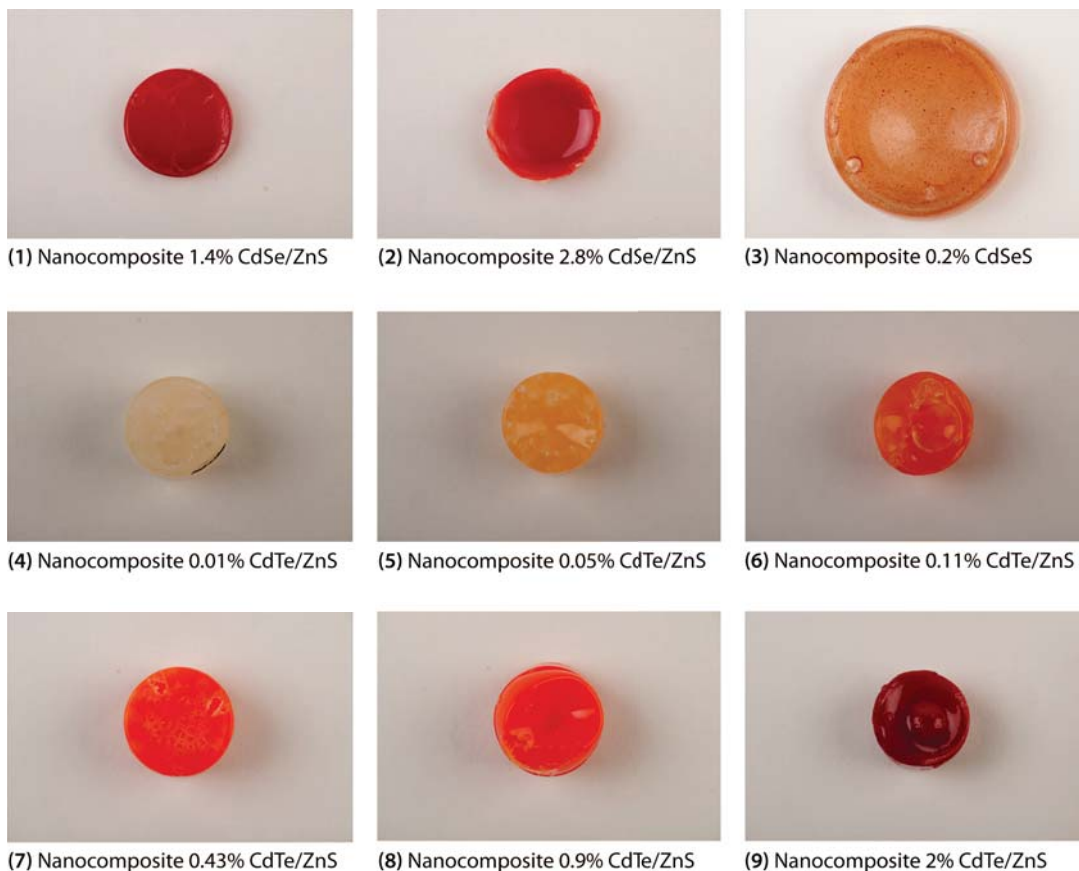

(1) Nanocomposite 1.4% CdSe/ZnS   (2) Nanocomposite 2.8% CdSe/ZnS   (3) Nanocomposite 0.2% CdSeS

(4) Nanocomposite 0.01% CdTe/ZnS   (5) Nanocomposite 0.05% CdTe/ZnS   (6) Nanocomposite 0.11% CdTe/ZnS

(7) Nanocomposite 0.43% CdTe/ZnS   (8) Nanocomposite 0.9% CdTe/ZnS   (9) Nanocomposite 2% CdTe/ZnS

Figure 1a. Nanocomposite detectors (1–9) used in this project; see Table 1 for details
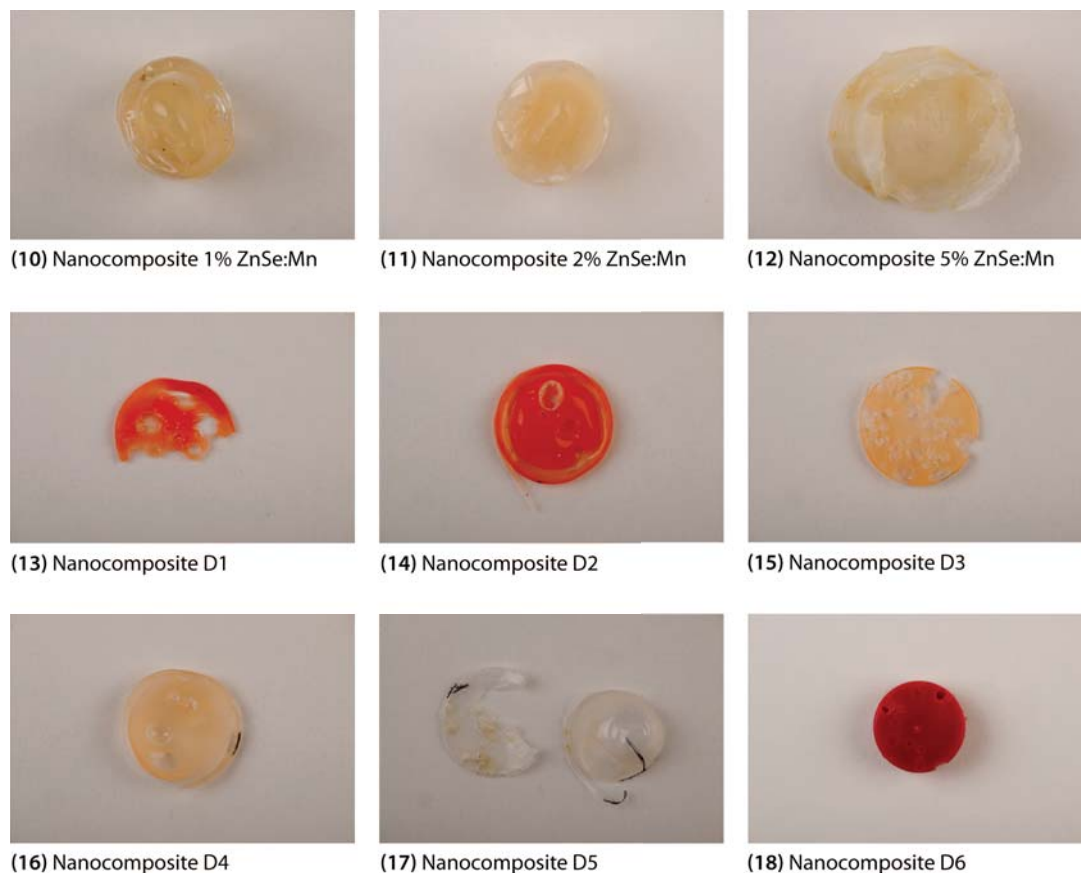
Figure 1b. Nanocomposite detectors (10–18) used in this project; see Table 1 for details

Experimental Design and Setup

The design for the detector mount required that numerous detectors be seated against a ~2.0 cm (¾ in.) photomultiplier tube (PMT). The mount was carefully constructed so that any one of the 18 nano-composite detectors might be inserted into the mount in a light-tight environment, and seated and interfaced to the PMT. The detectors were approximately 1 cm in diameter and 1 cm in length. They were not well polished. This small-sized geometry was fit onto the PMT with a light coupling, and inside a light-tight enclosure, in order to obtain good data. The mount was designed for easy exchange of detectors, and the PMT cap and assembly were seated so that data could be acquired with the detector in a light-tight environment. Figure 2 shows a picture of the detector mount, the protective cap, and the PMT assembly. Gamma-ray spectra from ^{241}Am, ^{137}Cs, and ^{60}Co were measured using each RMD nanoparticle detector. Gamma-ray spectra from a BC400 scintillation detector were also measured as a reference. The resulting spectra are presented in Figures 3 through 6.

Table 1. Nanoparticle detector material compositions and measurement results

Detector	Composition		Properties			Count Rate with Source (counts/second)				
	Nanoparticle	Type	Volume	Concentration	Comment	^{241}Am	^{137}Cs	^{137}Cs	^{60}Co	Background
					Source Intensity (μCi)	9.09	31.9	31.9	3.78	
					Source Distance (cm)	4	4	8	4	
1	CdSe/ZnS	Core/shell	1 cc	1.40%	Core/shell	2.4	20.72	10.54	18.09	1.29
2	CdSe/ZnS	Core/shell	1 cc	2.80%	Core/shell	0.2	12.69	9.29	23.74	1.63
3	CdSeS	QD	1 cc	0.20%	Epoxide-amine Polymer	0.07	16.47	11.57	16.64	3.01
4	CdTe/ZnS	Core/shell	1 cc	0.01%	Core/shell	—	—	—	—	—
5	CdTe/ZnS	Core/shell	1 cc	0.05%	Core/shell	—	—	—	—	—
6	CdTe/ZnS	Core/shell	1 cc	0.11%	Core/shell	—	—	—	—	—
7	CdTe/ZnS	Core/shell	1 cc	0.43%	Core/shell	—	—	—	—	—
8	CdTe/ZnS	Core/shell	1 cc	0.90%	Core/shell	0.09	52.95	16.69	33.74	7.34
9	CdTe/ZnS	Core/shell	1 cc	2%	Core/shell	—	—	—	—	54.13
10	ZnSe:Mn	QD	1 cc	1%	Polystyrene Matrix	0.07	64.82	20.7	49.4	2.59
11	ZnSe:Mn	QD	1 cc	2%	Polystyrene Matrix	3.97	61.46	25.76	50.68	2.64
12	ZnSe:Mn	QD	1 cc	5%	Polystyrene Matrix	0.05	683.39	471.66	20.88	9.25
13	Nano-composite D1	Core/shell	<1 cc	0.90%	Surfactant	—	—	—	—	—
14	Nano-composite D2	Core/shell	<1 cc	0.43%	Surfactant	—	—	—	—	—
15	Nano-composite D3	Core/shell	<1 cc	0.11%	Surfactant	—	—	—	—	—
16	Nano-composite D4	Core/shell	<1 cc	0.05%	Surfactant	—	—	—	—	—
17	Nano-composite D5	Core/shell	<1 cc	0.01%	Surfactant	—	—	—	—	—
18	Nano-composite D6	Core/shell	<1 cc	0.90%	Surfactant	—	—	—	—	—
19	BC400	—	1 cc	0%	—	—	170.22	—	—	1.27

Figure 2. A light-tight mount was made up of the (left) aluminum detector mount, (middle) outer protective cap, and (right) PMT

Discussion

Figure 3 shows typical background-subtracted γ-ray spectra acquired from the three γ-ray sources [241]Am, ^{137}Cs, and [60]Co. The figure shows the spectra from the 0.2% CdSeS QD detector as well as the background spectrum. Figures 4 and 5 show the spectra for the 2.8% and 1.4% CdSe/ZnS and the 0.9% CdTe/ZnS core/shell detectors, and the 1%, 2%, and 5% ZnSe:Mn QD detectors, respectively. The plots compare background-subtracted [241]Am, ^{137}Cs, and ^{60}Co spectra obtained with the 2.8% and 1.4% CdSe/ZnS, the 0.9% CdTe/ZnS core/shell, and the 5%, 2%, and 1% ZnSe:Mn QD detectors, respectively. In all figures, these spectra are successively overlaid. We have seen that higher photopeak γ-ray energies correspond to overall higher mean in the measured spectra. In addition, the lower livetime normalized count rate for [241]Am may be attributed to low energy discrimination, efficiency phenomena, and photopeak energy, as well as source strength (Table 2).

The measurement results show a direct correlation between the γ-ray energy and the centroid of the spectrum, as is evident by observing the spectra collected with the CdSe/ZnS core/shell detectors. The spectra in Figure 4 show a slight advance in the centroid of the main peak of counts as the photopeak energies increase, with the centroids for the ^{60}Co spectra much higher than for the other spectra. For example, a comparison of the ^{60}Co and ^{137}Cs spectra for either the 1.4% or the 2.8% CdSe/ZnS core/shell detectors (Figure 4) shows that the ^{60}Co spectrum has a higher centroid than the ^{137}Cs spectrum. This trend of a higher energy count distribution centroid for isotopes with photopeaks of higher energy, i.e., a higher energy centroid for ^{60}Co with its 1173 and 1332 keV photopeaks versus a lower energy centroid for ^{137}Cs with its 662 keV photopeak, are identical for the 1.4% and 2.8%

CdSe/ZnS detectors. A careful comparison will reveal that there is a small increase in differentiation between the ^{60}Co and ^{241}Am sources for the lower-percent nanoparticle detector. This is consistent with the small increase in spectral structural features in the 1.4% background when compared to the 2.8%. The lower concentration appears to provide a better contrast at discriminating energies when compared to higher nanoparticle concentrations.
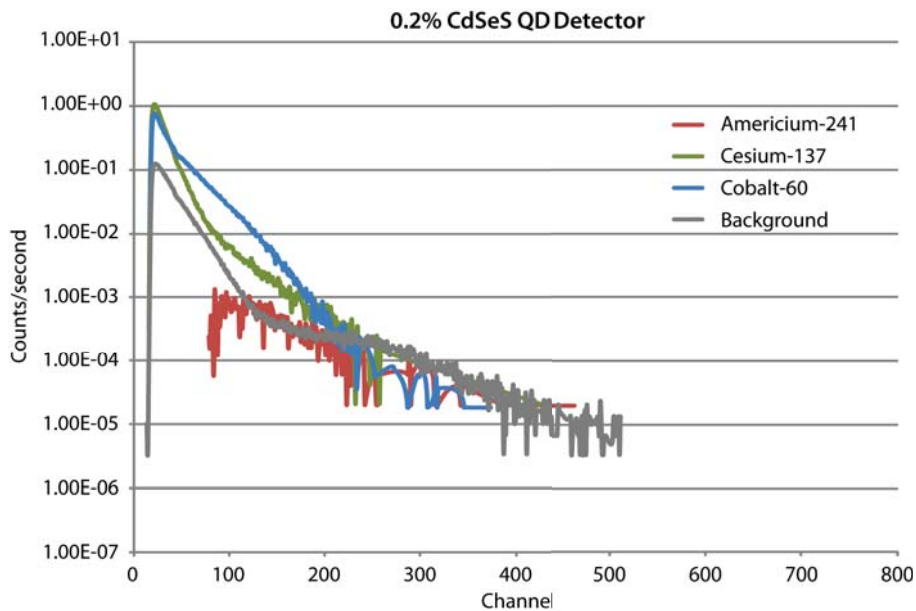
Figure 3. Typical background-subtracted spectra acquired with the 0.2% CdSeS QD nanoparticle detector (detector 3) compared to the background spectrum shows that the QD nanoparticle detector is responsive to manmade sources of radiation, by way of enhanced count rates in the lower energy region of interest. Further, a correlation between the isotopic γ photopeak energy and the centroid of the energy spectra is evident. Even the ^{241}Am spectrum, which does not exhibit this correlation strongly, can be understood in terms of the very low energy of its 60 keV γ-ray and the lack of optimization of the electronics, detector geometry, depth of interaction for 60 keV gammas, and the optical opacity of the nanoparticle detector.

The spectra presented in Figures 4 and 5, plotted on the left as counts per second, are reproduced on the right as normalized spectra per incident γ-ray for the entire detector set. The normalized probability distributions not only provide more characterization of the detectors by energy, but also seem to have a limited value as a diagnostic tool for data set comparison.

Figure 4. Data acquired for the 2.8% and 1.4% CdSe/ZnS and the 0.9% CdTe/ZnS core shell QD detectors; (left) raw counts per second and (right) normalized spectra per incident γ

Figure 5. Data acquired for the 5%, 2%, and 1% ZnSe:Mn QD detectors; (left) raw counts per second and (right) normalized spectra per incident γ

Results

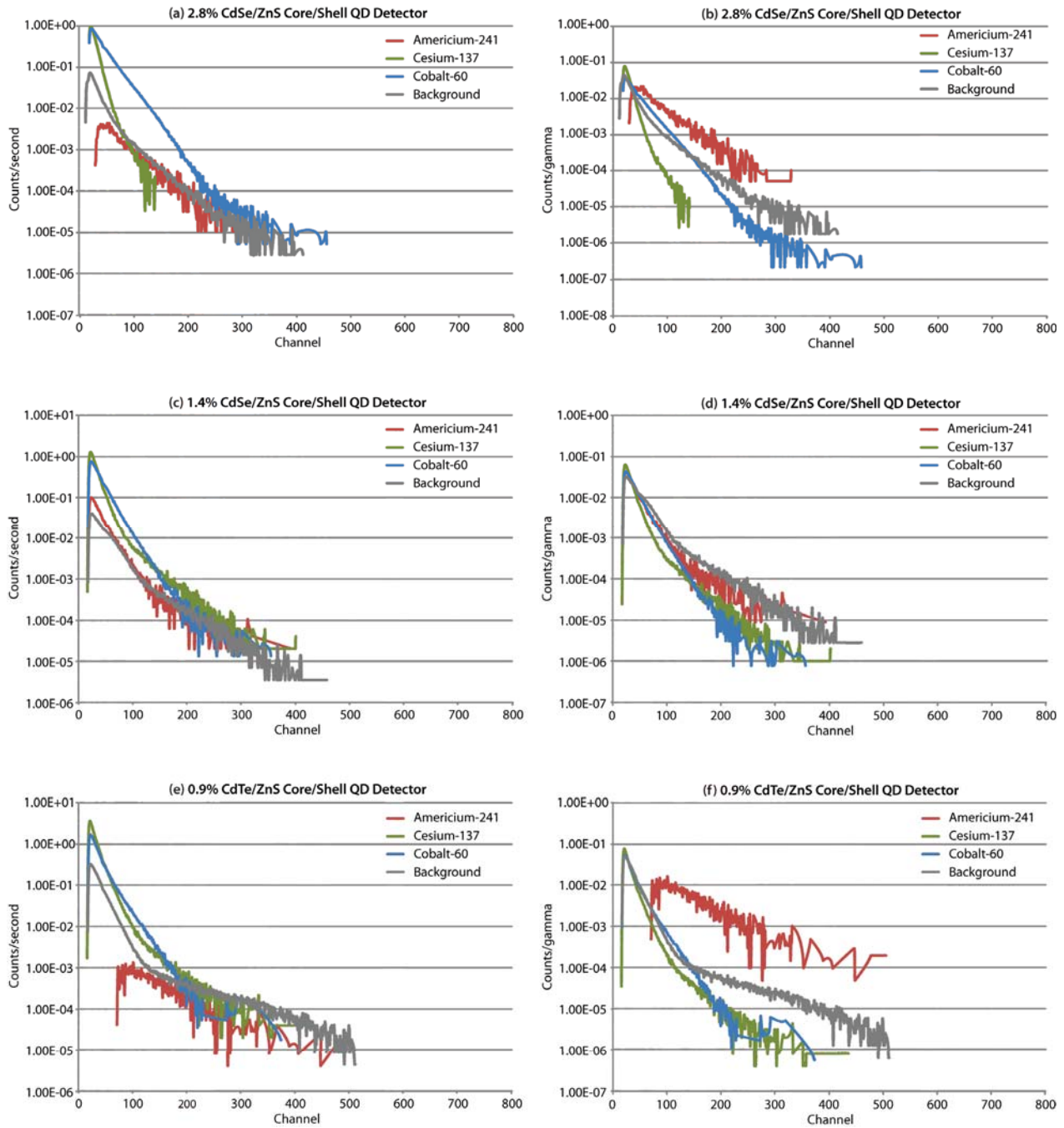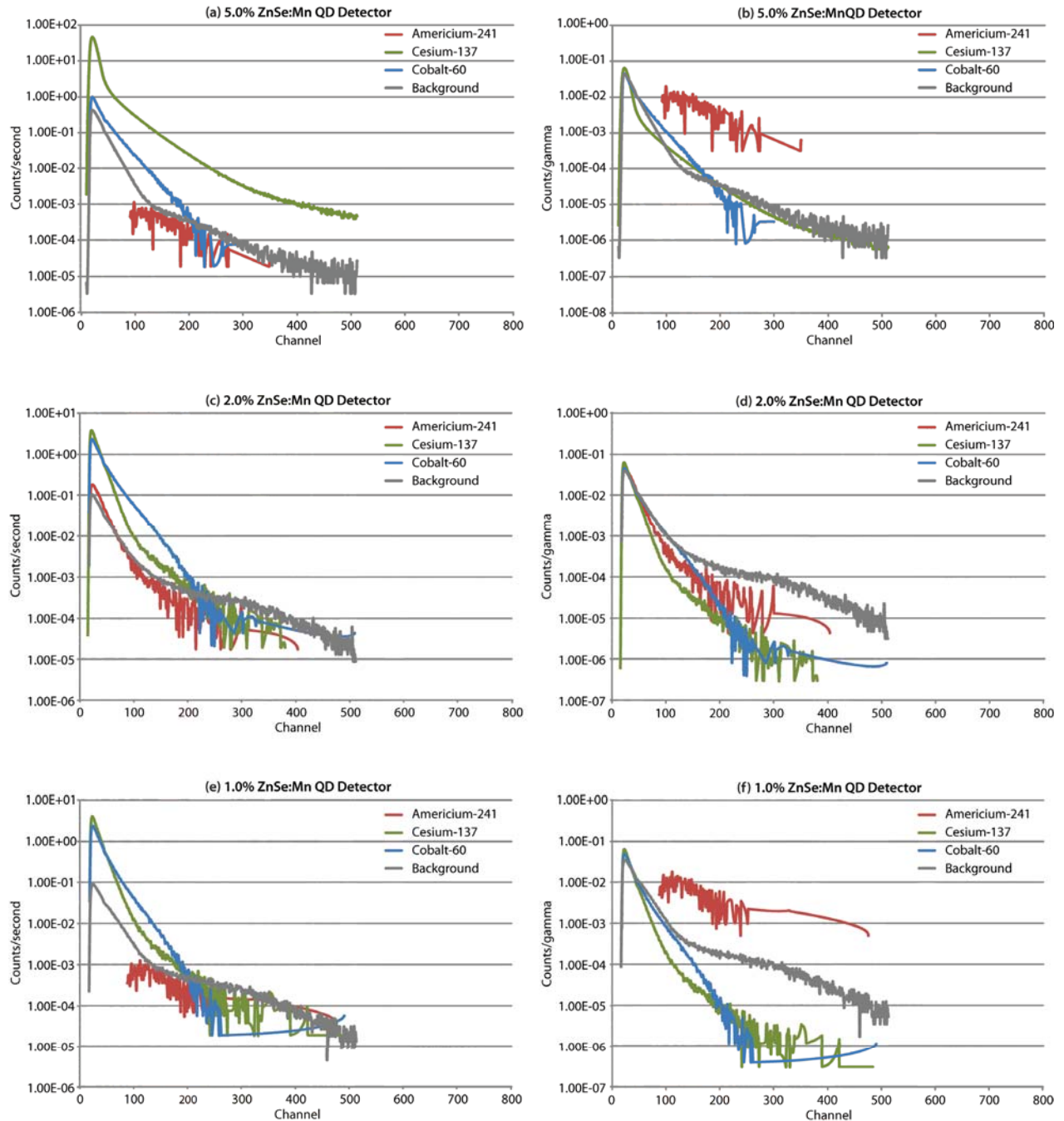Table 1 shows the measured count rates for all three sources, while Table 2 presents results. The [241]Am data appear less consistent than the other data. This is probably because the nanoparticle detector set was less sensitive to lower γ-ray energy and has a much lower signal-to-noise ratio. Additional characterization was performed with the detector set to determine the responses as compared to the plastic scintillation detector (BC400), and Figure 6 shows the results. The nanoparticle detector set produced a much weaker energy response than the BC400 detector.

Table 2. BC400 and nanodetector performance comparison

Source				Count Rate versus Source (counts/second)		
				2.8% CdSe/ZnS	1.4% CdSe/ZnS	BC400
Size	Intensity (μCi)	Source Distance (cm)	Energy (MeV)	16 mm D × 4 mm L	16 mm D × 4 mm L	12.5 mm D × 19 mm L
Background				1.63	1.29	1.27
[60]Co	3.78	4	1.33, 1.17	23.74	18.09	—
[137]Cs	31.9	4	0.662	12.69	20.72	170.22
[137]Cs	31.9	8	0.662	9.29	10.54	—
[241]Am	9.09	4	0.0595	0.2	2.4	—

Conclusion

For this project, we designed and fabricated prototype core/shell and QD detectors. Nanocomposite detectors are cheap, easy to fabricate, and respond to nuclear radiation (Medalia 2010). Nanocomposite detectors have the potential to meet many of the homeland security, non-proliferation, and border and cargo screening needs of the nation, and have the potential to replace all plastic detectors by virtue of a superior nuclear identification capability to plastic at roughly the same cost as plastic. Nanocomposites clearly have the potential of being a γ-ray detection material that would be sensitive yet inexpensive and easy to produce on a large scale. At this early stage, we have established the ability to distinguish different isotopes from the γ-ray spectra acquired with nanocomposite detectors. In particular, some have even observed photopeaks (Létant 2006, McKigney 2007), though the detector material we studied here did not. However, in this work we have learned that spectral fidelity increases with decreasing nanoparticle density, while efficiency increases with nanoparticle density. Correlations between spectra and γ-ray energy have been clearly observed. In addition, the nanocomposites are rich in hydrogen, which makes them ideal candidates for engineering concepts for neutron detection, a critical need due to the dwindling [3]He supply, the material most used now for neutron detectors. A significant improvement compared to BC400 was not clearly established, but more work is required to determine how best to obtain isotopic correlations and to optimize light yield.
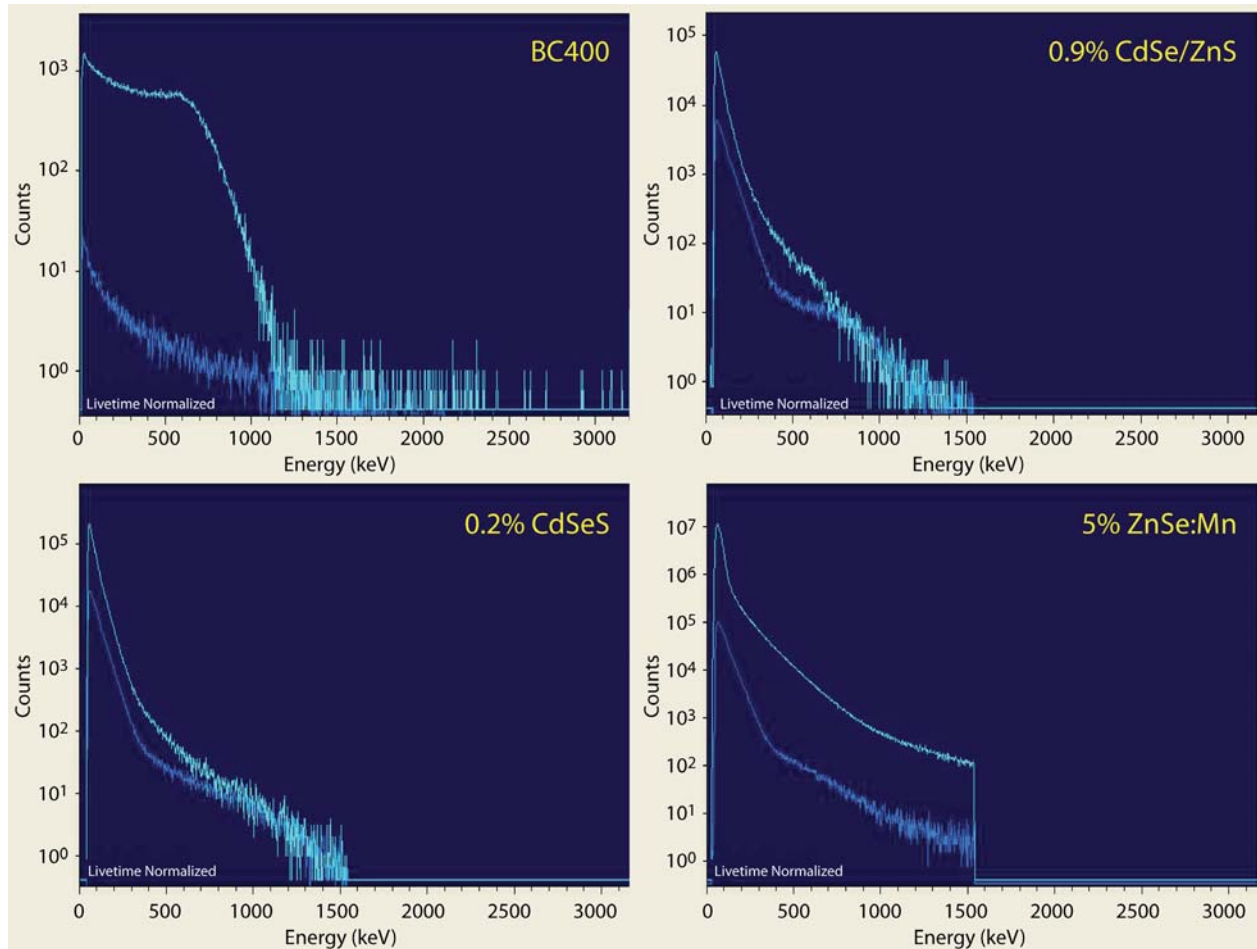
Figure 6. Measured spectra with (light blue) and without (blue) a 31.9 μCi ^{137}Cs source. One must compare the BC400 to the nanoparticle detectors. When comparing the ^{137}Cs spectrum using the BC400 detector to the ^{137}Cs spectra using the nanoparticle detectors, it is observed that the BC400 spectrum does a superior job of presenting the Compton shelf for ^{137}Cs.

Future work to advance the nanocomposite detector technology would include refining the MCNPX model to improve the match to experimental data, then adjusting MCNPX parameters to improve detector performance and assessing modeling results for future detector developments. In conjunction with the modeling, material studies involving different nanoparticle types and densities and different techniques for improving uniformity of the nanocomposite mixture are required. Finally, light luminescence and transmission measurements for the new concept materials are needed. This work will appear in a forthcoming publication, and preliminary results have been presented (Guss April 2010, June 2010, November 2010).

Acknowledgments

References

Alivisatos, A. P., "Semiconductor clusters, nanocrystals, and quantum dots," *Science* **271** (1996) 933–937.

Dabbousi, B. O., J. Rodriguez-Viejo, F. V. Mikulec, J. R. Heine, H. Mattoussi, R. Ober, K. F. Jensen, M. G. Bawendi, "(CdSe)ZnS core-shell quantum dots: Synthesis and characterization of a size series of highly luminescent nanocrystallites," *J. Phys. Chem. B* **101** (1997) 9463–9475.

Dai, S., S. Saengkerdsub, H. J. Im, A. C. Stephan, S. M. Mahurin, "Nanocrystal-based scintillators for radiation detection," *AIP Proc.* **632** (2002) 220–224.

Del Sesto, R. E., E. A. McKigney, D. W. Cooke, R. E. Muenchausen, K. C. Ott, R. D. Gilbertson, T. M. McCleskey, M. Bacrania, L. G. Jacobsohn, A. K. Burell, B. L. Bennett, S. C. Sitarz, J. F. Smith, "Development of nanocomposite scintillators," Spring 2007, http://www.lanl.gov/orgs/mpa/files/mrhighlights/LALP-07-030.pdf, accessed September 15, 2011.

Guss, P., D. Yuan, S. Mukhopadhyay. "Investigation into nanostructured lanthanum halides and CeBr$_3$ for nuclear radiation detection," *Proc. SPIE* **8144** (2011) 814405-1–814405-8.

Guss, P. P., R. Guise, S. Mitchell, S. Mukhopadhyay, D. Lowe, R. O'Brien, D. Yuan, "Nanostructured lanthanum halides and CeBr$_3$ for nuclear radiation detection," *Nevada National Security Site–Directed Research and Development*, FY 2010, National Security Technologies, LLC, Las Vegas, Nevada, 2011, 55–64.

Guss, P., S. Mukhopadhyay, D. Yuan, "Nanostructured lanthanum halides and CeBr$_3$ for nuclear radiation detection," 2010 RPSD, IRD & BMD Joint Topical Meeting; ANS Nevada Chapter 2010 Joint Topical Meeting, Las Vegas, Nevada, April 13–18, 2010.

Guss P., S. Mukhopadhyay, R. Guise, D. Yuan, "Nanostructured lanthanum halides and CeBr$_3$ for nuclear radiation detection," poster, LDRD Symposium, Washington, D.C., June 9, 2010.

Guss P., R. Guise, M. Reed, S. Mukhopadhyay, D. Yuan, "Nanostructured LaF$_3$:Ce quantum dot nuclear radiation detector," 2010 ANS Winter Meeting and Nuclear Technology Expo, Las Vegas, Nevada, November 7–11, 2010.

Henglein, A., "Small particle research: Physicochemical properties of extremely small colloidal metal and semiconductor particles," *Chem. Rev.* **89** (1989) 1861–1873.

Hines, M. A., P. J. Guyot-Sionnest, "Synthesis and characterization of strongly luminescing ZnS-capped CdSe nanocrystals," *J. Phys. Chem. B* **100** (1996) 468–471.

Létant, S. E., T. F. Wang. "Semiconductor quantum dot scintillator under gamma-ray irradiation," *Nano. Lett.* **6** (2006) 2877–2880.

McKigney, E. A., R. E. Del Sesto, L. G. Jacobsohn, P. A. Santi, R. E. Muenchausen, K. C. Ott, T. M. McCleskey, B. L. Bennett, J. F. Smith, D. W. Cooke, "Nanocomposite scintillators for radiation detection and nuclear spectroscopy," *Nucl. Instrum. Methods Phys. Res. A* **579** (2007) 15–18.

Medalia, J. "Detection of Nuclear Weapons and Materials: Science, Technologies, Observations. R401454. CRS Report for Congress," June 4, 2010, http://www.fas.org/sgp/crs/nuke/R40154.pdf, accessed on November 5, 2010.

Murray, C. B., D. J. Norris, M. G. Bawendi, "Synthesis and characterization of nearly monodisperse CdE (E = sulfur, selenium, tellurium) semiconductor nanocrystallites," *J. Am. Chem. Soc.* **115** (1993) 8706–8715.

Nirmal, M., L. E. Brus, "Luminescence photophysics in semiconductor nanocrystals," *Acc. Chem. Res.* **32** (1999) 407–414.

Osinski, M., "Emerging nanomaterials for nuclear radiation detectors," *Mater. Res. Soc. Symp. Proc.* **1051** (2008) 1051-CC01-06.

Peng, X., M. C. Schlamp, A. V. Kadavanich, A. P. Alivisatos, "Epitaxial growth of highly luminescent CdSe/CdS core/shell nanocrystals with photostability and electronic accessibility," *J. Am. Chem. Soc.* **119** (1997) 7019–7029.

Peng, Z. A., X. Peng, "Formation of high-quality CdTe, CdSe, and CdS nanocrystals using CdO as precursor," *J. Am. Chem. Soc.* **123** (2001) 183–184.

Qu, L., Z. A. Peng, X. Peng, "Alternative routes toward high quality CdSe nanocrystals," *Nano. Lett.* **1** (2001) 333–337.

Schmid, G., "Large clusters and colloids. Metals in the embryonic state," *Chem. Rev.* **92** (1992) 1709–1727.

Vasil'chenko, V. G., A. S. Solov'ev, "Properties of composite scintillators in static and dynamic states," *Instrum. Exp. Tech.* **46** (2003) 758–764.

this page intentionally left blank

Advanced High-Speed 16-Bit Digitizer System

Michael Jones,[1,a] Andrew Smith,[b] Wendi Dreesen,[a] Bradley Delamarter,[a] and Dennis Martin[b]

This project began development of a single-channel, PCB-level prototype digitizer system capable of digitizing frequencies greater than 1 GHz with a throughput of ~1 GS/s. This in-house solution has the potential to pave the way to creating low cost, expendable data acquisition systems. It can be used for collecting data in a variety of traditional (stockpile stewardship) and nontraditional mission applications. Three PCBs were designed this year for the analog front end, clock distribution, and clock phase shifting. A Nios II processor will be programmed into the field-programmable gate array located on the clock distribution board for development and evaluation of an Ethernet link for system control and data retrieval. Testing of these PCBs will begin in FY 2012.

Background

Historically the NNSS and government laboratories rely on large numbers of high-speed oscilloscopes or digitizers to perform analog-to-digital conversion and data storage. These oscilloscopes only offer 8-bit resolution, can cost over $100,000 each, and are large and bulky, resulting in wasted space. Companies such as Tektronix Component Solutions, formerly Maxtec, offer stand-alone digitizer modules, but these 8-bit resolution units require additional circuitry and packaging, and cost over $75,000. Migrating to 16-bit technology theoretically improves sensitivity by a factor of 256; however, commercially available 16-bit analog-to-digital converter (ADC) chips only operate at ~200 MS/s. In order to achieve a reasonable sample rate, multiple ADC chips would have to be interleaved. This method requires an analog fan-out circuit to impedance match the input signal to each ADC chip, a complex clock circuit to phase shift the ADC sample points, digital processing to realign the digital data into a single time domain, and a storage mechanism to store the digital data.

Project

The initial concept (Figure 1) was to use operational amplifiers and impedance matching networks to perform the analog fan-out; state-of-the-art, track-and-hold amplifiers to capture high-bandwidth signals; eight or fewer ADC chips for data conversion to reduce complexity; and a phase-locked loop (PLL) inside a field-programmable gate array (FPGA) to provide the necessary phase-shifted clocks for the clocking network. The FPGA would also realign the digital data from the ADC chips into a single time domain, provide a memory controller for data storage, and serve a web page for system control and data recovery.

---

[1] jonesmj@nv.doe.gov, 505-663-2126
[a] Los Alamos Operations; [b] Great Basin Technology, Inc.
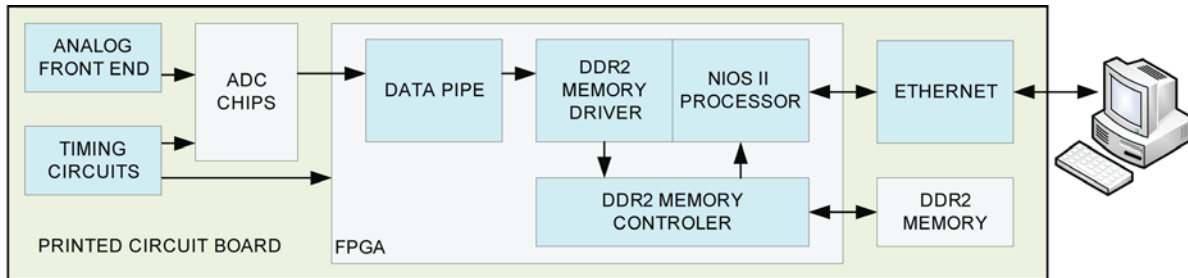
Figure 1. Conceptual system block diagram for the advanced high-speed 16-bit digitizer system. The analog front end takes a single input signal and fans it out to multiple ADC chips. The timing circuit creates multiple phase-shifted, low-jitter clocks to offset the ADC chips' sampling point, thereby allowing multiple time-shifted samples to be digitized within a single clock period. The data pipe realigns the interleaved data back into a single time domain to be stored into memory. The Nios II processor provides the web-based server for system control and data retrieval.

The ADC16DV160 ("ADC16DV160" 2011) by National Semiconductor was selected as a suitable ADC chip for the project for the following reasons:

- On-chip automatic calibration minimizes part-to-part variations.

- Built-in sample-and-hold circuit with a full-power bandwidth of 1.4 GHz removed the requirement for track-and-hold amplifiers.

- Dual ADC converters in a single package with sampling edge flipping will reduce the complexity of the clocking circuits.

- Programmable output data patterns can be used to guarantee proper data sequencing within a multi-chip system.

- Low-voltage differential signaling (LVDS) will help minimize noise and overall bus width.

- This 16-bit ADC chip can operate at 160 MS/s.

More in-depth research of the ADC16DV160 chip revealed that if the sampling edge flipping feature were used, the operating clock frequency could not be doubled to 320 MHz. This means that the ADC chips would only operate at 80 MS/s in this configuration. Utilizing eight chips operating at 80 MS/s would only offer a system capable of 640 MS/s, and a system operating at only 640 MS/s was too far away from the desired ~1 GS/s. We looked at the available ADC chips again, and still concluded that this chip had the best features available. Given that each ADC chip has two separate ADCs inside a single package operating on a common clock, we decided to investigate if there was any advantage to using the second redundant ADC for data averaging during the testing phase.

Extensive research was then started on the PLLs inside the FPGA. According to the datasheet on a Cyclone IV FPGA, using a dedicated clock output, and operating greater than 100 MHz, the PLL output jitter can be up to 300 ps. We felt that 300 ps of jitter would be too great for this system. Given this new revelation, research into a viable clocking solution began.

After researching what was readily available, we targeted high-performance clock distribution chips (Figure 2), settling on the LMK series from National Semiconductor. The LMK series offers femtoseconds of additive jitter, a selectable clock input from one of two ports, and up to eight clock outputs with independently programmable dividers and delay adjustments. It was initially thought that this chip could be used to generate eight independent clock outputs shifted 45° apart. Ultimately the part does not offer enough adjustment resolution to perform this task and suffers a performance hit in channel-to-channel skew and jitter when delay chains are used. Given the low jitter specifications, and a channel-to-channel skew of ±30 ps, this would still provide a clean clock fan-out solution. We utilized one clock input from our clean low-jitter clock source and the other from the FPGA PLL. This will allow us to study what impact the input clock jitter will have on the design. The D75A ("5x7" 2008) from Connor Winfield is a high-precision, temperature-compensated crystal oscillator (TCXO) that has a frequency stability of ±0.28 ppm and low jitter <1 ps. This feeds the LMX2531 high-performance frequency synthesizer system ("High" 2010) with an integrated voltage-controlled oscillator from National Semiconductor. After solving the clock fan-out issues, we began to investigate a reliable method to phase-shift the eight clocks, each 45° apart.
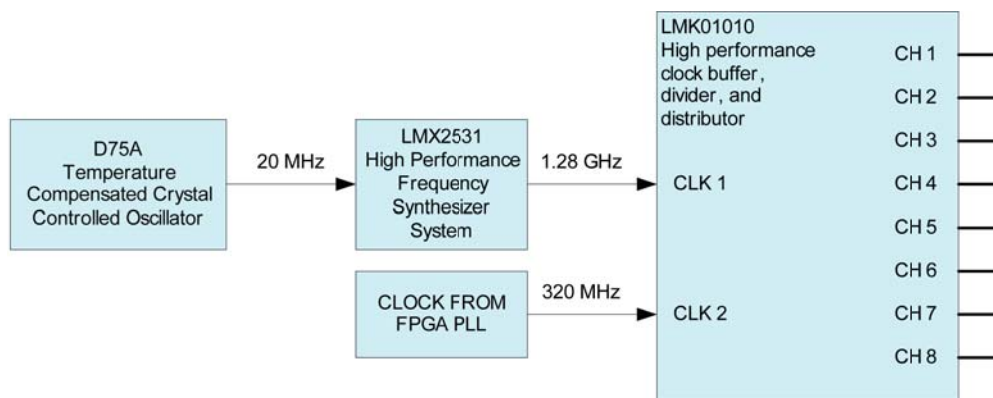
Figure 2. The components of a high-precision clock network. A 20 MHz TCXO drives the input to a frequency synthesizer system that generates a clock output of 1.28 GHz. The LMK01010 divides this clock down to 160 MHz and drives eight individual outputs. Alternatively, a 320 MHz clock from the FPGA PLL can be used to derive the required 160 MHz outputs; however, this clock will have significant jitter.

A cable cut to a specific length can be used to create a specific time delay. The delay of a cable is determined by its dielectric constant. The velocity factor, or cable delay, is the speed at which an RF signal travels through a material compared to the speed the same signal travels through a vacuum

("Cable Delay" 2011). Given that the output of the clocking circuits uses LVDS, eight pairs of cables would be required to perform this task. Using actual cables is undesirable, but the concept is sound. We decided to investigate what it would take to manufacture this inside a PCB (Figure 3).
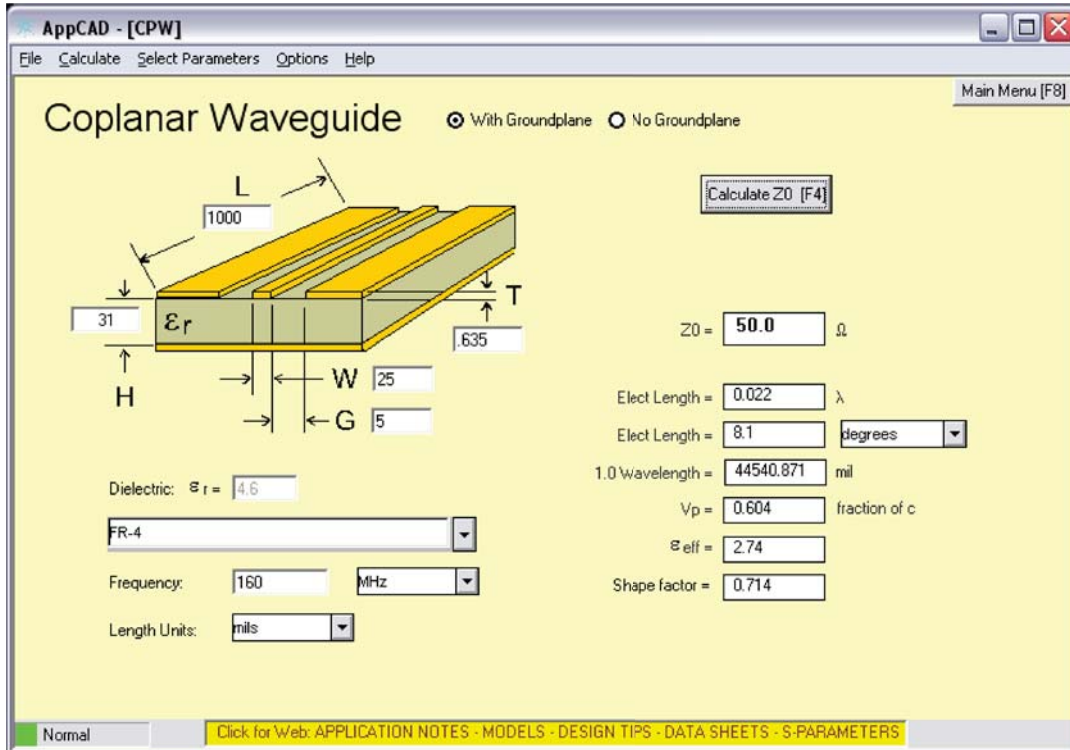
Figure 3. This particular board stack shows that the required 50-ohm trace length for one wavelength at 160 MHz is 44.5 inches long with a trace width of 25 mils. Changing the PCB material from FR4 to RO3010 will reduce the required trace length to 32.7 inches or 26.5% shorter. In addition, the trace width decreases to 15 mils, making the PCB routing easier. This information was obtained using AppCAD, a free RF and microwave design program developed by Agilent Technologies ("AppCAD" 2011).

This concept can create a clock delay PCB approximately 1 × 4 inches in size to generate the eight different phase shifts from the clock fan-out circuit by using accurate trace lengths. Designing this as a simple, dedicated board with no components other than two connectors allows for a cheap and easy way to remove chip-to-chip variations in semiconductors and to correct any phase-shift errors. One connector would have short equal-length traces to characterize the entire clocking design. In this configuration, all eight clocks should have the same phase. The second connector would have eight known trace lengths to create the desired phase shifts. The first version of this delay PCB would be used to characterize a new system. Using one clock as a reference, the phase shift for the other seven

channels can be measured with an oscilloscope. If a phase discrepancy is found, a second version of the delay PCB can be quickly manufactured and assembled in a few days to custom-tune a new system.

The impedance matching and fan-out for the input circuit has been difficult to design due to multiple factors. Initially we decided on a single amplifier stage with a 1-to-8 splitter to feed the ADC chips. We were concerned that a single amplifier might not have enough current to drive the eight ADC chips. We then chose a design with a single 50-ohm input to eight amplifiers. Two different impedance matching networks were required: one to match the 50-ohm input to the amplifier, and one to match the output of the amplifier to the ADC chip. This idea made its way to a final schematic. However, after much deliberation we decided against manufacturing. There was great concern over part-to-part variations in the amplifier circuits that could completely cripple the entire design. This type of design would need a methodology to calibrate amplitude, offset, gain, and phase variations, which was lacking. Thus, going back to the initial idea would resolve these problems. In order to create a 1-to-8 wideband filter approaching ~0 to 2.0 GHz, some assumptions had to be made (refer to Figure 4):

- The input impedance given on the ADC datasheet ("ADC16DV160" 2011) is correct for the currently manufactured devices.

- S11 was measured correctly with the reference plane at the ADC input pin and all other input/output pins properly terminated per S-parameters' definition.

- The reference impedance of the S-parameter measured was 50 ohms, which is standard. The datasheet does not say if the Smith chart is normalized.

- A valid systematic error-correction technique was used to calibrate the S11 measurement of the datasheet data.
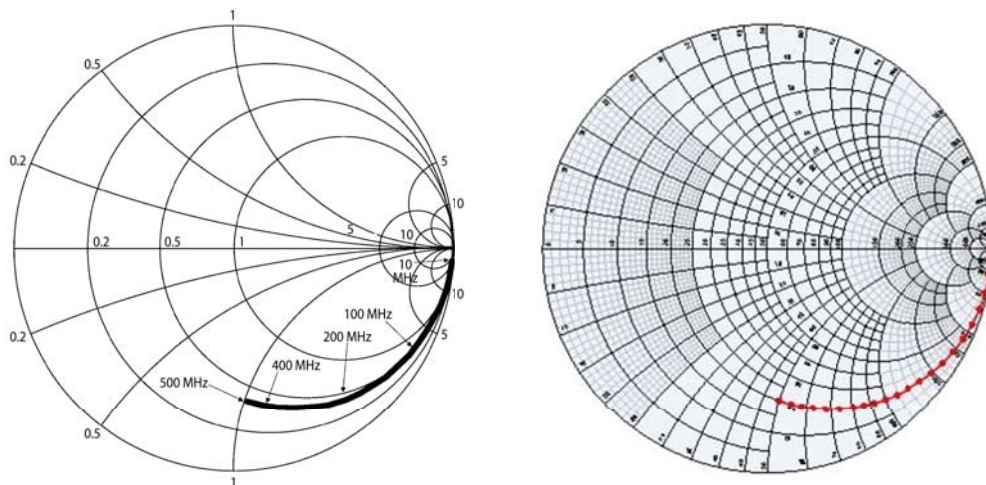
Figure 4. (left) An image from the ADC datasheet ("ADC16DV160" 2011) that shows Z_{IN} at 500 MHz = 20 – j 50 Ω, and (right) a model with a real Z_{IN} = 20 Ω and C_{IN} = 6.366 pF

Various design topologies were investigated within the range of 2 to 16 poles. This investigation yielded the following results:

- Series-connected microstrip lines utilizing Butterworth, Chebyshev, and L-networks all yielded hugely long layouts, unacceptable ripple, and unacceptable bandwidth/band pass. The Chebyshev method yielded unrealizable component values above the 8th order.

- Microstrip line stub matching, Pi networks, Tee networks, and L-networks all had bandwidths that were too narrow.

- Discrete high-Q inductors and capacitors yielded the best bandwidth/band pass.

Figure 5 shows the band-pass characteristics of different design approaches, Figure 6 the calculated values for the 12th order Besser method (Besser 1993) L-network, and Figure 7 the 12th order Besser L-network with real component values.
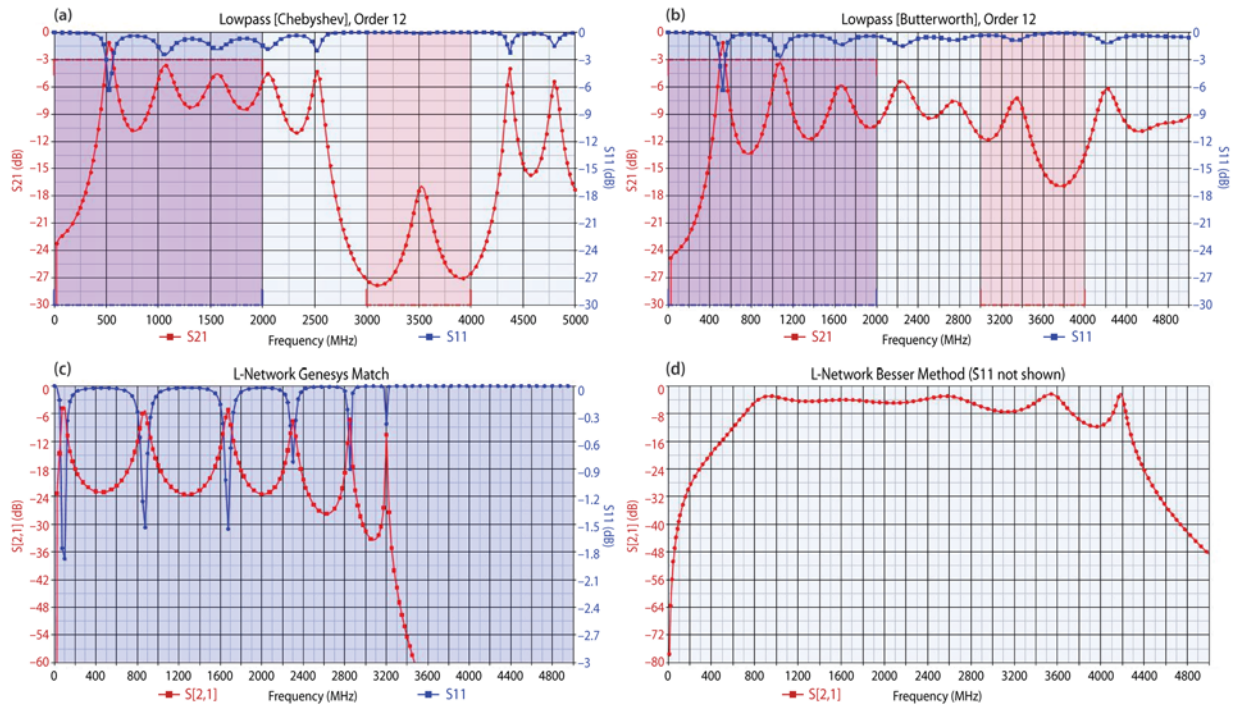
Figure 5. Characteristic comparisons of different types of band-pass filters: (a) Chebyshev, (b) Butterworth, (c) L-network Genesys ("Genesys" 2011) match, and (d) L-network Besser method (Besser 1993) (S11 response not shown)
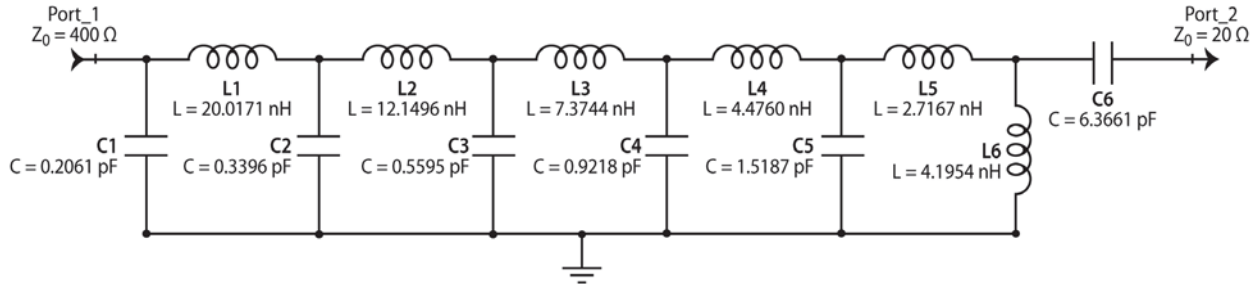
Figure 6. This schematic shows one channel for the input band-pass filter required for impedance matching the input signal to the ADC chip. Eight channels are required, configured in parallel, and share the same 50-ohm input connector. This filter is a 12th order Besser L-network with the calculated component values.
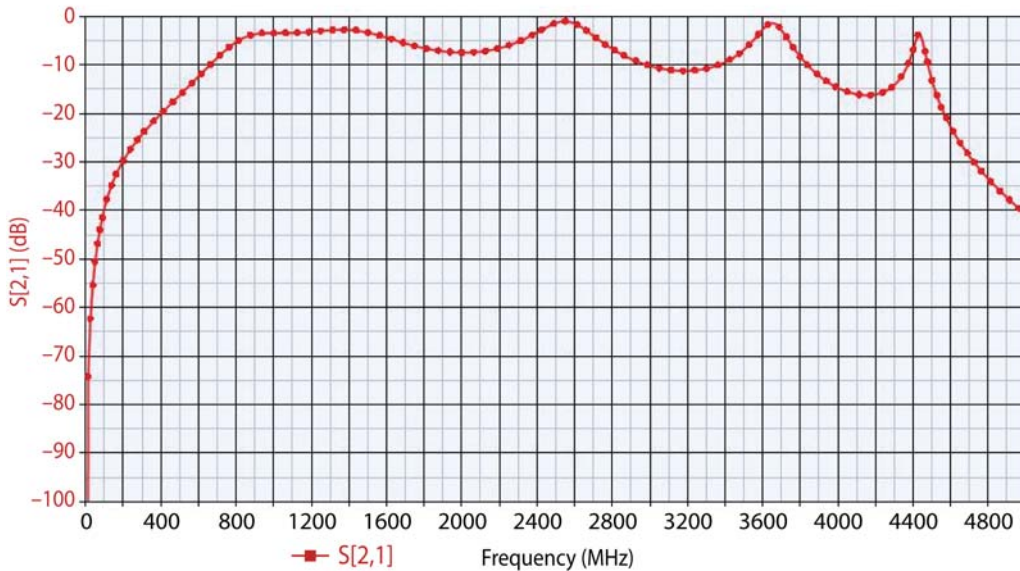
Figure 7. The simulated frequency response of the 12th order Besser L-network using real component values

Monte Carlo analysis, provided within Genesys ("Genesys" 2011), was used to determine what impact component tolerance would have on the circuit design; the simulation showed it will have very little impact. When we tried to manufacture this design, we found that the PCB impedances required could not be obtained due to the requirement to have 400-ohm traces. A 400-ohm trace on a PCB made with RT/duroid 5880LZ, 62.5 mils thick would require a trace width of 0.008 mils. State-of-the-art PCB manufacturing processes can only achieve 2-mil-wide traces. We shifted the fan-out

design impedance from 400 to 200 ohms. This impedance shift increased the trace width to ~6 mils, which will have a significant impact on the desired input impendence, shifting it from 50 ohms to 25 ohms. This can be corrected in the amplifier stage by creating a 50-ohm to 25-ohm impedance match. Figure 8 shows the new component values based on a 200-ohm source to the ADC input, and Figure 9 shows the frequency response for the circuit in Figure 8.
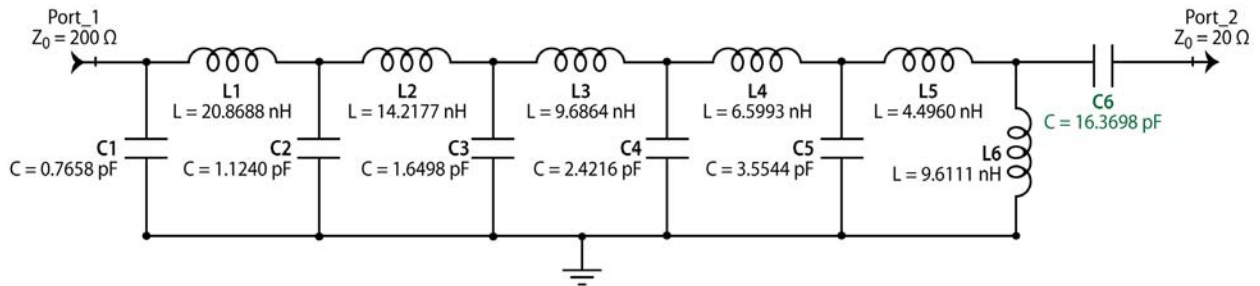
Figure 8. This schematic shows one channel for the input band-pass filter required for impedance matching the input signal to the ADC chip. Eight channels are required and configured in parallel. This schematic differs from Figure 6 by shifting the single string input impedance from 400 ohms to 200 ohms. This was necessary for manufacturing reasons. This filter is a 12th order Besser L-network with the calculated component values.
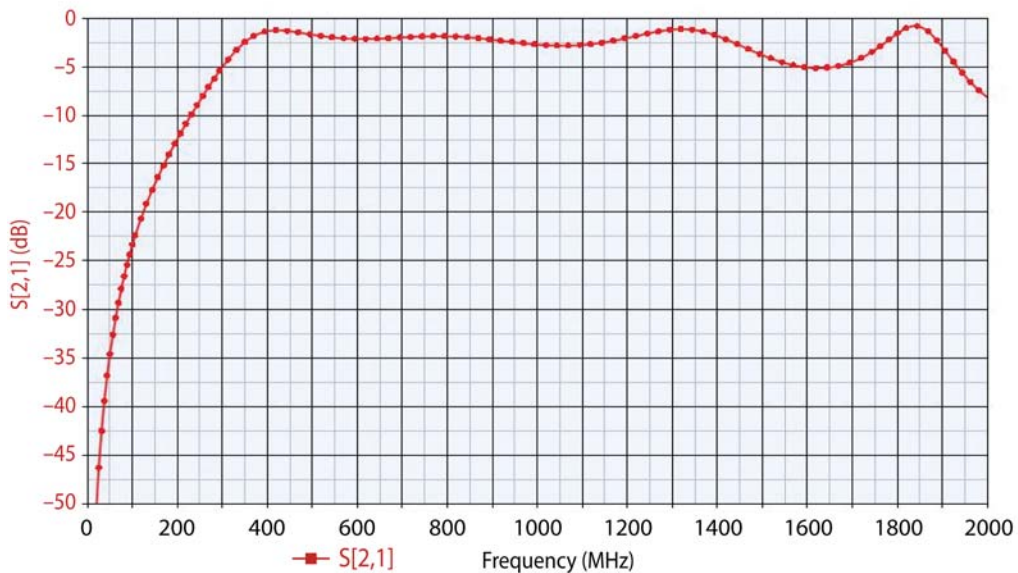
Figure 9. The simulated frequency response for the circuit shown in Figure 8

The 16-bit digital output of the ADC chip is on a double data rate (DDR) LVDS 8-bit wide bus, where the odd data bits are captured on the falling edge of the clock, and the even data bits are captured on the rising edge of the clock. Eight ADC chips require a minimum of 256 dedicated LVDS pins on the FPGA for the data transfer. With this in mind, an Altera Cyclone IV FPGA ("Altera" 2010) was initially selected for this design. After extensive research and simulation efforts, we had to abandon the Cyclone IV because timing requirements could not be met. Additional simulation was performed on the Stratix III EP3SL150F1152C2N FPGA. Simulation proved that the Stratix III FPGA could meet the timing requirements to capture the data from 16 different ADC converters operating in eight different time domains and successfully move the data into a single time domain. The Stratix III also supports DDR2 PC2-6400 memory. This was proven through simulation. In reality, PC2-5300 memory has adequate bandwidth to store the data for all 16 ADCs. If data averaging is performed within the FPGA, this requirement can be reduced to PC2-3200 memory. The Cyclone IV and the Stratix III FPGAs support the Nios II processor. The Nios II processor is capable of implementing triple-speed Ethernet within the FPGA. This removes the dependency of adding a processor or module to the design to serve a web page for system control. We have successfully performed two-way communication between a web browser and a Cyclone IV development kit. The connection between the web browser and the Cyclone IV will be mitigated to the Stratix III FPGA.

Conclusion

Three critical areas to the advanced high-speed 16-bit digitizer system were investigated and developed. The heart of the successful analog front end will be proper fan-out and impedance matching to the ADC chips while sharing a usable common input such as a 50-ohm connector. We have simulated this circuit and have an unpopulated PCB in hand. The clock distribution board contains our best attempt at creating a clean low-jitter clock distribution system. This PCB is assembled and ready for testing. This board also contains all of the necessary circuits for testing and developing an FPGA-based Ethernet control system and web page server. The clock delay board is based on the concept of cable delay. This design was completed but not manufactured in FY 2011; no hardware testing occurred.

In FY 2012, as the project continues, we expect to write a memory driver to bridge the gap between the data source and memory controller. A file transfer system needs to be developed to move raw data from memory through the FPGA Nios II processor to a host computer. A system-level PCB needs to be created, and additional work is required to prove simulation results in hardware. An intensive PCB design effort will be required to migrate the building blocks developed in FY 2011 into a prototype system. The Altera Stratix III FPGA that we are targeting has 1152 pins. This is the same scale as a modern computer CPU. This circuit board design will exceed any previous PCB design effort in both complexity and scale.

References

"ADC16DV160: 16-Bit, 160 MSPS Analog-to-Digital Converter with DDR LVDS Outputs from the PowerWise® Family," http://www.national.com/pf/AD/ADC16DV160.html#Overview, accessed June 2, 2011.

"Altera product catalog," Version 8.0, Altera Corporation, San Jose, California, August 2010.

"AppCAD," Agilent Technologies, www.hp.woodshot.com, accessed June 2, 2011.

Besser, L. "Reactive transformation of resistances," *Applied Microwave* Winter 1993, 104–110.

"Cable Delay FAQ," http://www.gpssource.com/files/Cable-Delay-FAQ.pdf, accessed June 2, 2011.

"5x7mm surface mount high precision TCXO," http://www.conwin.com/datasheets/tx/tx236.pdf, Connor Winfield, Aurora, Illinois, 2008, accessed June 2, 2011.

"Genesys RF and microwave design software," http://www.home.agilent.com/agilent/product.jspx?nid=-34275.0.00&cc=US&lc=eng, accessed June 2, 2011.

"High performance frequency synthesizer system with integrated VCO" http://www.national.com/ds/LM/LMX2531.pdf, National Semiconductor, 2010, accessed June 2, 2011.

Delayed Radiation Measurements Using the Dense Plasma Focus

Raymond Keegan,[1,a] Chris Hagen,[b] Francis Tsang,[a] Daniel Lowe,[c] and Robert O'Brien[c]

The primary objective of this work was to determine whether dense plasma focus (DPF) devices have any potential to find hidden fissionable materials inside shipping containers. We also sought to identify the components needed to build a full-scale interrogation system. This work focused on the measurement of delayed radiations induced in depleted uranium (DU) using a 2.45 MeV neutron-generating DPF. Tungsten, lead, and silver surrogates were compared with DU. Through demonstration, we conclude that it is feasible to use a DPF to interrogate standard aircraft shipping containers and identify fissionable materials.

Background

The primary objective of this work was to determine whether dense plasma focus (DPF) devices have any potential to find hidden fissionable materials inside shipping containers. The secondary objective was to identify the components needed to build a full-scale interrogation system. We planned to perform MCNPX simulations, to mock-up a full-scale interrogation system, and to conduct experiments using the deuterium-deuterium (D-D) DPF located at the A-1 Building at NSTec North Las Vegas (NLV) based on these simulations. The D-D DPF is capable of producing about 5×10^{11} neutrons that have an energy of 2.45 MeV within a single 100 ns pulse, and it can be pulsed once about every 10 seconds. This pulse is used to induce fission in any fissionable material placed in the interrogation flux. A worthwhile description of the operation of a DPF is provided by Zucker (1977).

There are two major benefits of using a D-D DPF for this type of work: (1) induced activity is less likely to be a problem than that of other approaches that use higher-energy neutrons or x-rays, and (2) the potential dose received by any person inadvertently close to the DPF when it pulses (~12 mrem whole-body at 1 m) is unlikely to exceed the limit for the public imposed by ICRP-103 (ICRP 2008), which is 100 mrem whole-body in a year above background. The fission process produces both prompt and delayed gamma rays and neutrons. SDRD work in FY 2009 by Keegan (2010) indicated that detection of prompt radiations from fission was complicated by event "clutter" due to radiations that are produced by shield and mask materials. It was difficult to separate the gamma-ray and neutron radiations that arise due to fission from those that are generated by other materials found inside shipping containers. Therefore, the approach taken in this project was to measure delayed radiations from fission. The concept was to pulse the DPF once, pause for several hundred milliseconds to allow

the electronics to stabilize, and then count gamma-ray and neutron detection events as a function of time up to about 60 seconds after the pulse. This allows most of the induced radioactivity to decay away and for the decay signature from fission to emerge in a relatively low and stable background.

There are six groups of delayed neutrons and associated gamma rays that have distinct yields and half-lives. It was anticipated that fissionable materials could be detected and identified using the unique slopes of the gross count curves compared to that of typical shielding materials. The six groups of delayed radiations for ^{235}U shown in Table 1 are reproduced from Keepin (1957). Note that Group Number 4, which has a 2.23-second half-life, has the largest relative abundance and is most likely to be observed in measurements of delayed radiations. Keepin (1957) also noted that other fissionable nuclides such as ^{238}U, ^{233}U, ^{239}Pu, ^{240}Pu, and ^{232}Th also have these six delayed groups and that the half-lives and relative abundances are very comparable to those shown in Table 1.

Table 1. The six delayed groups for ^{235}U and ^{238}U

Group Number	Delayed Radiations (^{235}U)		Delayed Radiations, DU (^{238}U)	
	Half-Life (seconds)	Relative Abundance	Half-Life (seconds)	Relative Abundance
1	54.51 ±0.94	0.038 ±0.003	52.38 ±1.29	0.013 ±0.001
2	21.84 ±0.54	0.213 ±0.005	21.58 ±0.39	0.137 ±0.002
3	6.00 ±0.17	0.188 ±0.016	5.00 ±0.19	0.162 ±0.020
4	2.23 ±0.06	0.407 ±0.007	1.93 ±0.07	0.388 ±0.012
5	0.496 ±0.029	0.128 ±0.008	0.490 ±0.023	0.225 ±0.013
6	0.179 ±0.017	0.026 ±0.003	0.172 ±0.009	0.075 ±0.005

Gross-counted delayed gamma rays have a yield that is a factor of ten greater than that of delayed neutrons. These gamma rays tend to be high energy (>1 MeV) and are therefore more robust in their ability to penetrate shielding as described by Gosnell (2004). An example of earlier work by Slaughter (2003) using a 14 MeV neutron source indicates that measuring delayed gamma radiation is the approach most likely to succeed; however, such an energetic neutron source also induces activity problems that would be reduced by using a lower neutron energy.

Project

Portal system polyvinyltoluene (PVT) detectors were used to perform gross counting of radiations after the DPF pulse. Eight detectors were salvaged from retired portal systems that were undergoing disposition at the NNSS. The detectors had dimensions of 109 × 68.6 × 5.1 cm (43" × 27" × 2") (Figure 1) and the plastic type was BC-200. Each detector had two photomultiplier tubes that enabled two digital gamma spectrometers (ORTEC digiBASE-E) procured for this project to collect data. Data were extracted from the detectors in list mode and then post-processed to produce the die-away

curves shown later in this report. Initial inspection indicated that some of the detectors had light leakage issues; however, the team found two detectors suitable for this work. Detector checkout occurred at the University of Nevada, Las Vegas (UNLV) and at the NLV D-D DPF laboratory, while all of the experimental work occurred at the DPF laboratory.

Figure 1. A view of one of the PVT detectors used on this project with two ORTEC digiBASE-E digital gamma spectrometers used for data acquisition

DPF runs were executed during March and June 2011. Because the June data collection included reruns of some of the March runs, the more optimized June data are included in this report.

A standard aircraft shipping container was relocated to the DPF laboratory from NSTec's Remote Sensing Laboratory–Nellis for the June data collection. The dimensions of this container were 1.5 × 2.0 × 1.6 m. The distance between the DPF target and the PVT panel was set to be 2.1 m with the 1.5 m dimension of the container placed between the target and the detector. The goal was to demonstrate that fissionable materials could be identified if located inside a typical commercial shipping container. This type of container was also chosen over a typical steel one used for shipment of items by sea because it can be readily moved around the laboratory by hand. A single PVT detector, housed inside a Faraday cage to protect it from the electromagnetic pulse produced when the DPF fires, was used in the DPF runs. The combination of the DPF, shipping container, and the Faraday cage are shown in Figure 2. Depleted uranium (DU) was placed unshielded inside the container on a pole stand at its center.

Figure 2. An aircraft shipping container being interrogated using the DPF. The shipping container is in the center, the detector enclosed inside a Faraday cage is on the left, and the DPF assembly is on the right.

The yield of the DPF during the June runs was consistently about 3×10^{11} neutrons per pulse. Gross count data were counted as a function of time between 100 ms and 60 seconds to determine how the count rate varies as a function of time for various target materials. The chosen target materials were DU, tungsten, lead, and silver. The tungsten block had a mass of 5.7 kg ($10.2 \times 10.2 \times 2.9$ cm in dimension), the lead was 11.9 kg ($5.1 \times 10.2 \times 20.3$ cm), and the silver was 2.8 kg (100 oz) of silver coins. Background was measured by passive counting using the laboratory setup without the DU in place and not pulsing the DPF, then with the DU in place and not pulsing the DPF, and then pulsing the DPF without the DU in place. This allowed the laboratory background, the natural radioactivity of the DU, and then the induced radioactivity to be subtracted out as separate components.

A comparison of DU, tungsten, and silver count rate profiles is shown in Figure 3. Note that the DU die-away curve is very different than that of tungsten or silver. DU displays the integrated six-fission product group decay, but both tungsten and silver appear flat in this time range. The leading component of the DU curve has a 1.93-second half-life, which is observed in these data. The comparison between DU and lead is shown in Figure 4. Activation in lead is such that decay is observed in the 100 ms to 60-second time window; however, the half-life of this single decay is 810 ms. Therefore, it is possible to distinguish between DU and the other surrogates used in this experimental work. The

experimentally observed delayed count rates were an order of magnitude larger than those calculated prior to the experimental work using MCNPX (version 2.7d, Los Alamos National Laboratory). This is probably because MCNPX tracks some of the fission fragments but not all of them. The model had a one-to-one correspondence with the physical setup in the laboratory, and the discrepancy is likely due to a deficiency internal to MCNPX.
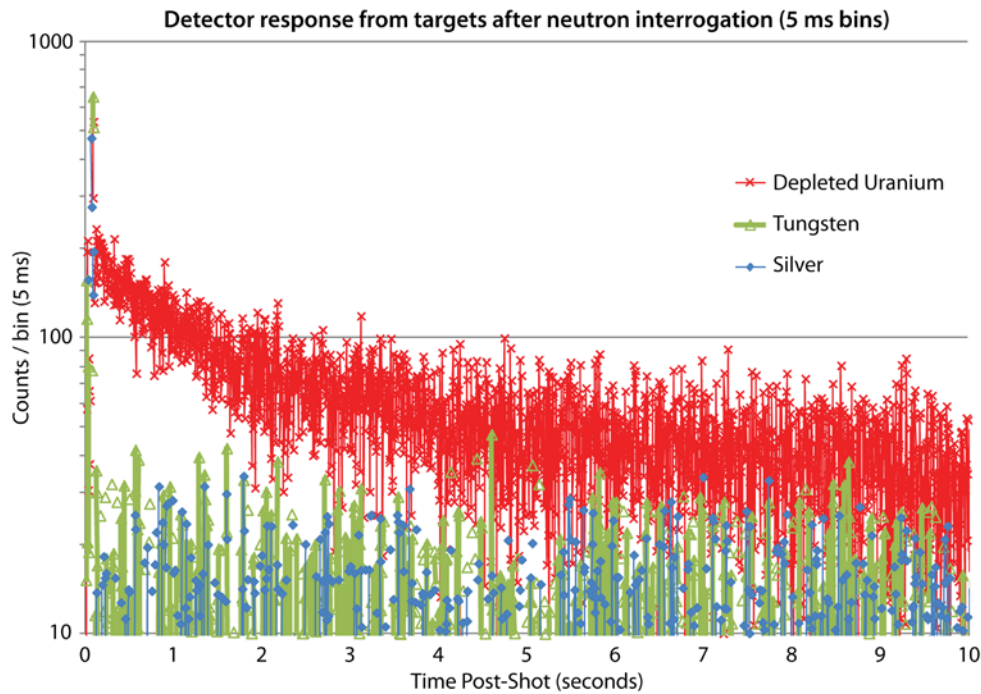
Figure 3. A comparison between count rate profiles after DPF shots with DU, tungsten, and silver targets. Note the clearly defined decay from DU, while the profiles for tungsten and silver are very flat. The time bin width was 5 ms.

The interrogation neutrons interact with the target nuclides shown in Table 2 to generate gamma-ray fluxes that die-away with the half-lives shown. Note that the half-lives are very long in comparison to the 1.93-second ^{238}U die-away. This means that we can reasonably expect a flat background from most interrogated objects inside a time window measured in tens of seconds.

Table 2. Summary of (n, γ) reactions that interfere with fission detection from Slaughter (2003)

Target Nuclide	^{27}Al	^{63}Cu	^{65}Cu	^{55}Mn	^{50}Cr	^{54}Cr
Half-Life (seconds)	1.4×10^2	4.6×10^4	3.1×10^2	9.4×10^3	2.4×10^6	2.1×10^2
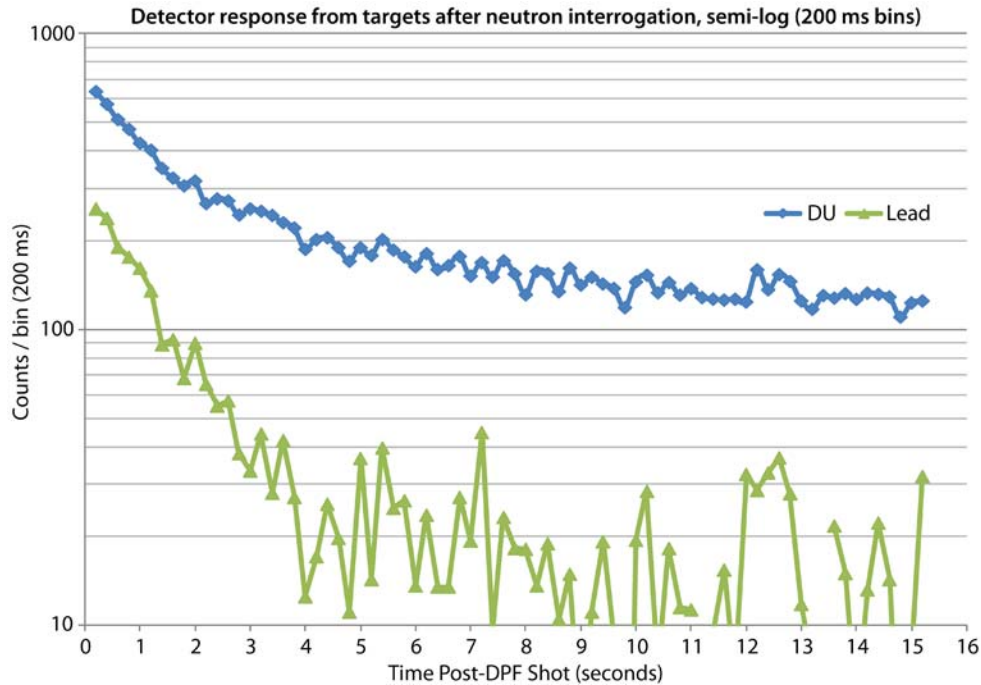
Figure 4. A comparison between DU and lead after DPF shots. Note that the decay from DU has a different half-life than that of lead, which enables differentiation between DU and lead. The time bin width in this graph was 200 ms.

If fission is observed, then it is desirable to distinguish DU from fissile material. A concept we considered during this project was to place an optimized polyethylene shutter between the DPF and the cargo container to thermalize the neutron field. The shipping container would be irradiated first using a fast 2.5 MeV neutron pulse. If fission were observed, then the shutter would be closed down between the DPF and the shipping container, and then the DPF pulsed again. The shutter thermalizes the neutron field so that the fission cross section approaches about 1000 barns from about 1 barn. If fissile material is present, then the fission signature should be observed again and will likely be enhanced. Yet another concept is to form a cavity lined with polyethylene to house the shipping container and to pulse the DPF once so that the shipping container is immersed in a sea of thermal neutrons. If fission is observed, then fissile material is present. The use of polyethylene for thermalization was not investigated further in this work.

A comparison was made between the response of one of the PVT panels and that of a single 6-inch cube PVT detector that was available at the DPF laboratory. It was found that the smaller but thicker PVT detector was capable of at least matching the larger detectors in count rate. This indicates that the thickness of the detector is an important consideration in the design of a real-world system. The thicker detector is more effective at stopping gamma-ray and neutron radiation.

Conclusion

We demonstrated that it is possible to distinguish between DU and surrogate targets of tungsten, lead, and silver. Identification of fission must be based on the measurement of the half-life of the decay curve after the DPF pulse. If the half-life is found to be 2.1 ±0.2 seconds, then fissionable material is present in the system. It is preferable to count in a time window that starts at about 100 ms after the DPF pulse and ends after 10 seconds. The difference between fissionable material and other materials will likely be most obvious in this period. In order to minimize background, the detectors need to be mounted vertically to minimize the cross section presented to cosmic radiation. The thickness of a detector is an important consideration in the design of a real-world system. The thicker detector is more effective at stopping delayed radiations. These detectors could be stacked together to form a wall on the far side of the shipping container to the DPF. For an aircraft shipping container like the one used here, an entire shipping container could be scanned using a single DPF pulse. Induced activity produces a constant background, except for lead, within the 10-second time window after the DPF pulse, which enables the DU die-away to be more easily observed; the 810 ms half-life of lead allows it to be identified. This activation can be minimized by thermalizing the DPF pulse, which cuts down background and at the same time likely enhances the fission signature.

References

Gosnell, T. B., "Detection of nuclear threats in large cargo containers," UCRL-TR-203678, Lawrence Livermore National Laboratory, Livermore, California, 2004.

ICRP, *ICRP Publication 103: 2007 Recommendations of the International Commission on Radiological Protection*, Elsevier, New York, 2008.

Keegan, R. P., P. Hurley, J. Tinsley, R. Trainham, "Portable tagged neutron triple-coincidence counter system," *Nevada Test Site–Directed Research and Development*, FY 2009, National Security Technologies, LLC, Las Vegas, Nevada, 2010, 137–143.

Keepin, G. R., T. F. Wimett, R. K. Ziegler, "Delayed neutrons from fissionable isotopes of uranium, plutonium and thorium," *Phys. Rev.* **107**, 4 (1957) 1044–1049.

Slaughter, D., M. Accatino, A. Bernstein, J. Candy, A. Dougan, J. Hall, A. Loshak, D. Manatt, A. Meyer, B. Pohl, S. Prussin, R. Walling, D. Weirup, "Detection of special nuclear material in cargo containers using neutron interrogation," UCRL-ID-155315, Lawrence Livermore National Laboratory, Livermore, California, 2003.

Zucker O., W. Bostick, J. Long, J. Luce, H. Sahlin, "The plasma focus as a large fluence neutron source," *Nucl. Instrum. Methods* **145**, 1 (1977) 185–190.

this page intentionally left blank

Monte Carlo Modeling of Porous Silicon Neutron Detectors

Craig Kruschwitz[1,a]

A modeling study of the potential performance of a proposed porous silicon neutron detector was performed. The detector consists of a porous silicon matrix loaded with a neutron reactive converter material. This study concentrated on ^{235}U. The potential detector performance was studied for a broad parameter space, looking at different pore sizes and pore depths. It was shown that ^{235}U offers a credible alternative to other detector materials, offering similar detection efficiencies with superior noise suppression.

Background

The development of new, highly efficient neutron detectors is of importance for applications ranging from homeland security to astronomy. In the past, semiconductor neutron detectors based on a planar diode configuration with a thin-film coating of a converter material (such as enriched boron [^{10}B], lithium [^{6}Li], or gadolinium [Gd]) were used. More recently silicon (Si) diode devices etched with perforated microstructures that are filled with converter material have been studied and found to be more efficient than the simple planar diode configurations (Conway 2009, McGregor 2009, Bellinger 2010, Nikolić 2010). In this study, the concept of a similar type of detector based on a porous Si matrix loaded with a fissile material, ^{235}U, was explored.

^{235}U offers an intriguing alternative to the more commonly used thermal neutron detector materials such as ^{10}B, ^{6}Li, or Gd. Some of the possible advantages of a ^{235}U-based converter are:

- While the cross section for thermal neutron fission of ^{235}U is smaller (580 b) than the thermal neutron capture cross sections for ^{6}Li and ^{10}B (940 b and 3840 b, respectively), the energy released in the fission reaction is much larger (fission products have >165 MeV energy, vs 4.8 MeV and 2.3 MeV for ^{6}Li and ^{10}B, respectively). This could potentially lead to orders of magnitude greater electron-hole pair production.

- Uranium also has a relatively high fast neutron fission cross section, so it could be used to detect faster neutrons as well. This study, however, only investigated thermal neutrons.

For these reasons, uranium and uranium compounds are being increasingly considered as replacement materials for ^{3}He, as ^{3}He supplies continue to dwindle. In a recent review paper (Caruso 2010), the possibility of using uranium as a dopant in an indirect-conversion etched Si device and of using oxides of uranium (many of which are themselves semiconductors) in a direct-conversion device was

---

[1] kruschca@nv.doe.gov, 505-663-2023

[a] Los Alamos Operations

enthusiastically encouraged. The same paper pointed out that a study of the optimum geometric parameters for the former type of device was needed. This study was an attempt to partially fulfill that need.

Project

The primary tool used in this project was the MCNPX code developed at Los Alamos National Laboratory. MCNPX is a general-purpose Monte Carlo radiation transport code for modeling the interaction of radiation with everything. MCNPX is fully three-dimensional and time dependent. It utilizes the latest nuclear cross section libraries and uses physics models for particle types and energies where tabular data are not available. The MCNPX versions used for these calculations were 2.7e and 2.7.0.

Because the major goal of this project was to compare ^{235}U to ^{6}Li, ^{10}B, and Gd as converter materials for solid-state neutron detectors, obtaining simulation results for ^{235}U that were directly comparable to simulation results for ^{6}Li and ^{10}B was of utmost importance. Therefore, the methodology of the study mirrored that of Shultis (2009), who investigated various detector geometries for ^{6}Li and ^{10}B in order to find the optimal detector configurations for detectors using each material. Time did not permit an investigation of the parameter space for ^{235}U as complete as that done by Shultis (2009) for ^{6}Li and ^{10}B, so the present study was restricted to the detector geometry shown in Figure 1. This geometry consists of uranium-filled holes etched into a Si matrix. The ^{235}U is taken to be full density (19 g/cc). Figure 1 shows a unit cell of the detector configuration. To simulate an infinite array of such cells, reflecting boundaries are set as shown in Figure 1. Following Shultis (2009) different cell sizes, defined as the length of the sides of the reflecting boundary shown in Figure 1 (left panel), were investigated. The cell sizes for this study were 5, 10, and 20 μm. A range of different pore diameter to cell width ratios (D/W) was also investigated, with D/W varying from 0.1 to 0.9. Finally, pore depths of 50, 100, 300, and 1000 μm were studied. The thermal neutron source (energy = 0.0253 eV) was taken to be normal to the surface and filled the area of the cell for all simulations (source neutrons are represented by green dots in Figure 1). Thus, the maximum possible detection efficiency for the detector is the porosity of the uranium, which ranges from 0.7% to 64%, because Si is extremely insensitive to thermal neutrons.

Thermal Neutron Conversion Efficiency

The first step in investigating the efficiency of a given neutron detector design is to determine the efficiency with which the source neutrons cause reactions in the converter fissions in the ^{235}U. This is shown in Figure 2a for the different pore depths. The maximum fission efficiency is about 52% and is obtained for a pore depth of 1000 μm. Because a given interaction between a thermal neutron and a ^{235}U nucleus is likely to produce fission about 82% of the time, this is near the theoretical maximum that can be expected for thermal neutron fission efficiency for this detector and source geometry. Thus, it appears that approximately 1000 μm of ^{235}U are required to achieve the maximum possible thermal neutron absorption.
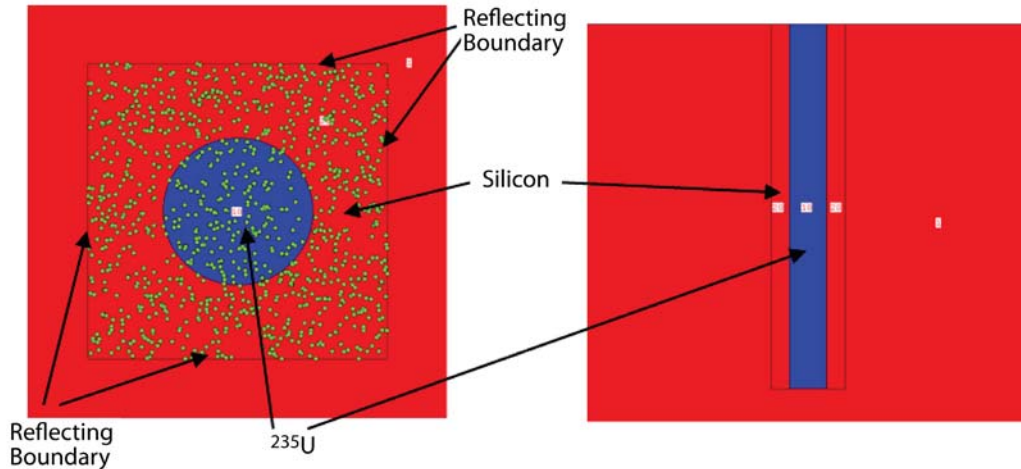
Figure 1. Geometry used for the MCNPX simulations. A variety of different pore sizes (blue cylinder) and cell sizes were investigated. Reflecting boundary conditions were used at the cell boundaries to simulate an infinite array of cells. Green dots are source neutrons.

Because fission creates neutrons, which can then lead to further fissions, it was important to study the effect of such "secondary fissions." Because we were investigating the feasibility of using ^{235}U for neutron detection, secondary fissions must not be a dominant effect. This was a simple matter to study with MCNPX. Figure 2b shows both source neutron fissions and total fissions, which includes the secondary fissions. It is clear that secondary fissions, at least for the pore parameters studied, are a small (~1%) effect.
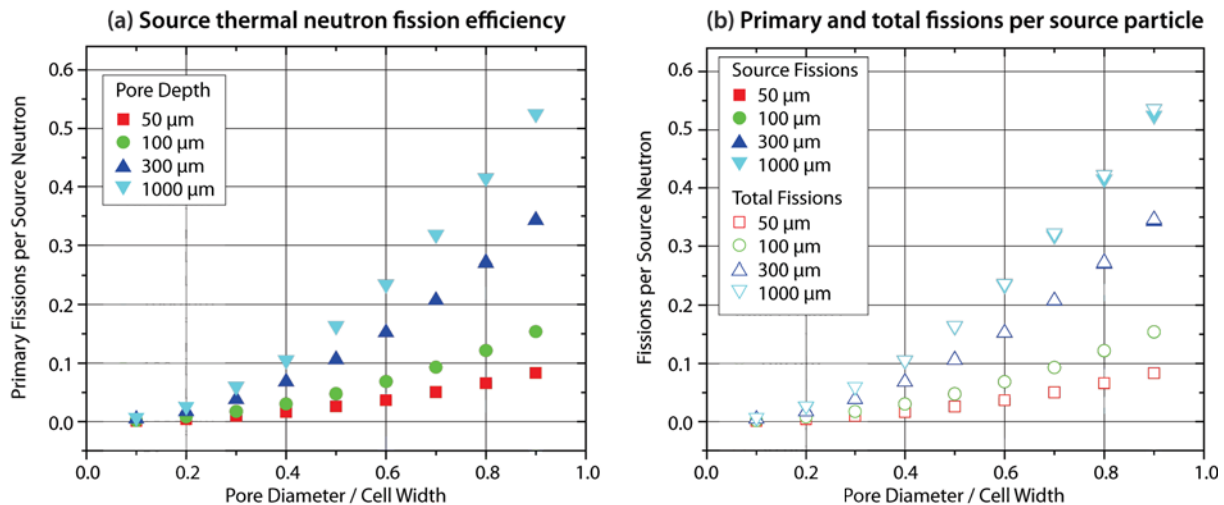
Figure 2. Neutron-fission efficiency. Graph (a) shows primary fissions per source neutron for different pore depths as a function of pore diameter to cell width ratio. Peak neutron conversion efficiency is ~52% for a 1000 μm pore. Graph (b) shows total fissions per source neutron. Secondary fissions are clearly a small (~1%) effect.

Fission Fragment Tracking

The second issue that must be investigated when modeling detector efficiency is the efficiency with which the reaction products, in this case fission fragments, deposit energy in the Si matrix. The fission of a ^{235}U nucleus releases an enormous amount of energy, creating two massive fission fragments with a >165 MeV kinetic energy. This energy is much greater than the 2.3 MeV and 4.8 MeV produced in the ^{10}B and ^{6}Li reactions, respectively. These massive and energetic fragments deposit energy in the ^{235}U (self absorption) and in the Si, where they create copious electron-hole pairs and hence a detectable signal.

An unfortunate limitation of MCNPX is that it does not allow for the tracking of fission fragments from thermal neutron–induced fissions. The fragments are created and their creation can be tallied, but MCNPX does not assign energy or direction to them. Figure 3 shows the distribution of fragments from a typical simulation. ^{235}U produces a light fragment with an atomic mass near 95 amu and a heavy fragment with atomic mass near 140 amu (Müller 1984), with the lighter fragment having greater energy and greater range. Figure 3 indicates that there is a wide variety of possible fission products that can result.
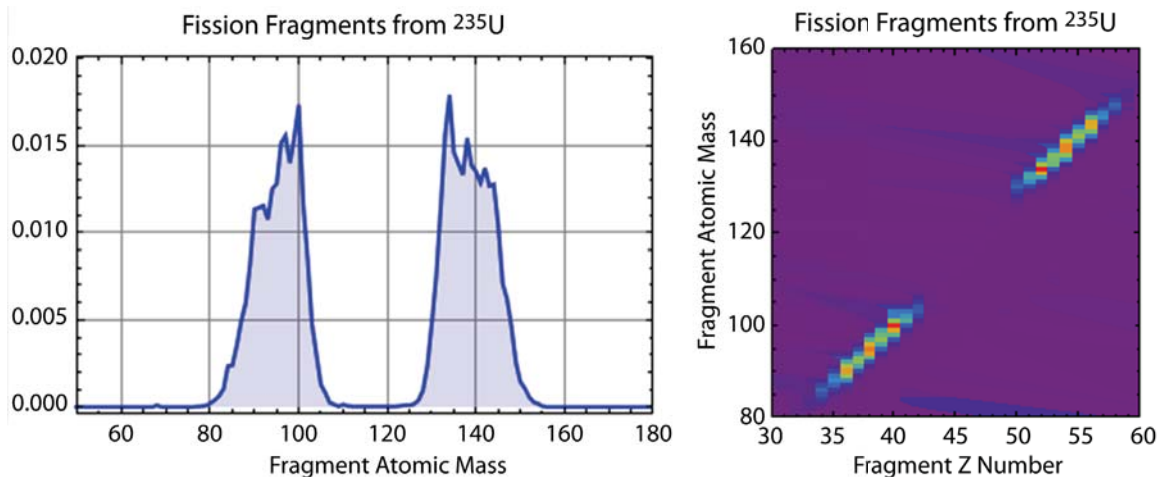
Figure 3. Fission fragment distribution resulting from thermal neutron fission of ^{235}U. MCNPX creates the fragments but is not able to track them in the current implementation of the code.

Because of the inability of MCNPX to track fission fragments as they are created, an alternative method was needed to study the effects of the fragments. The solution was to use the heavy ion transport capability of MCNPX. MCNPX allows one to define a heavy ion source, which is essentially any nucleus heavier than an alpha particle, and to transport the heavy ions through media. As a method to approximate the transport of fission products, a heavy ion source is defined at random locations

within the ^{235}U of the unit cell and with random directions. The energies of the heavy ions are taken from measured distributions of the energies of the light and heavy fragments (Wahl 1954). The energy deposited by the fragments is then tallied to determine the fragment detection efficiency.

Using the heavy ion transport capability of MCNPX offers a way to approximate the fission fragment transport in the hypothetical detector, but it does have two major shortcomings. First, the two fragments are not properly correlated, so momentum is not conserved. Second, the heavy ions are assumed to be fully stripped of electrons. Fission fragments, however, while highly ionized (typically 20e–26e), retain some of their electrons (Watson 1967). Combined with the fact that there is no model for charge pickup where an ion takes charge from the outer shells of surrounding atoms, this means that the range of the fragments is likely underestimated. However, because excluding these effects should lead to an underestimate of the amount of energy deposited in the Si, we proceeded with confidence that detector performance is likely to be somewhat better than predicted here.

Figure 4 shows the fission fragment detection efficiency for the different cell sizes investigated. The 5 µm cell offered 90% to 100% detection efficiency at all D/W ratios, while the 10 µm and the 20 µm cells showed significant self-absorption in the ^{235}U when the pore diameter was larger than ~6 to 7 µm. This is consistent with a fission fragment range in ^{235}U of ~6 to 10 µm. The conclusion here is that pore diameters smaller than ~4 to 5 µm are preferred, at least if full-density ^{235}U is used as the dopant. Figure 4 only shows results obtained for the 1000 µm pore depth. Little dependence on the pore depth was observed in the simulations.
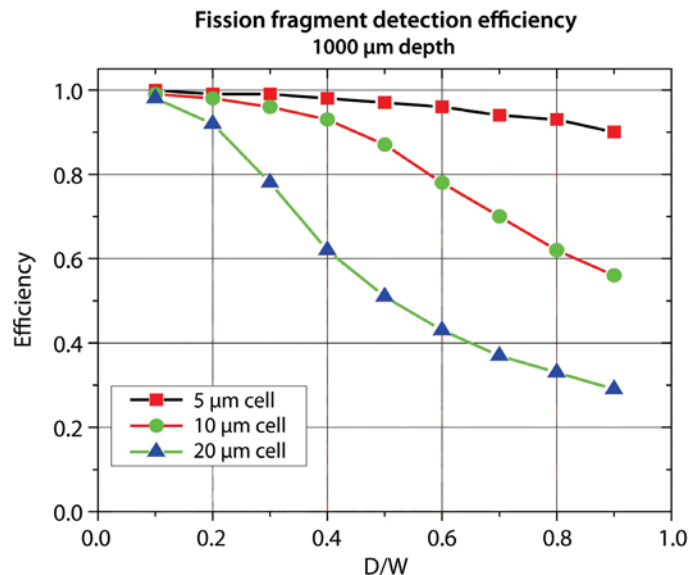

Figure 4. Fission product detection efficiency for the lighter fragment. For the 5 µm cell, 90% to 100% of the light fragments deposit energy in the Si. Larger cell sizes start to see substantial self-absorption in the uranium.

Overall Neutron Detection Efficiency

The overall neutron detection efficiency is approximated by multiplying the efficiency with which incident source neutrons induce fissions by the efficiency with which the fission products deposit (measurable) energy in the Si. Figure 5 shows the results obtained by combining the two efficiency parameters. The peak overall thermal neutron detection efficiency is ~48% for a 5 μm cell and a D/W ratio of 0.9 (4.5 μm pore diameter) and a pore depth of 1000 μm. It seems the smaller the structures can be made, the better the detection efficiency.
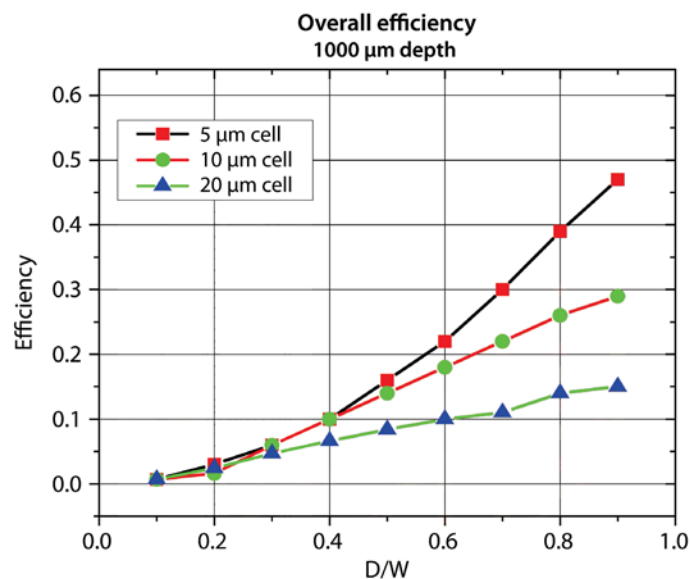
Figure 5. Overall thermal neutron detection efficiency. The peak efficiency is around 48% for a 5 μm cell, with a D/W ratio of 0.9, and a pore depth of 1000 μm.

Because noise discrimination is an issue for real detectors, some authors simulate detection efficiency as a function of lower-level discriminator (LLD) setting. As the LLD setting is raised in order to eliminate detector noise from gamma rays, cosmic rays, or leakage current, for example, neutron-induced events depositing small amounts of energy can then be lost, thereby reducing the overall detector efficiency. Thus, a detector whose efficiency is relatively insensitive to the LLD setting is highly desired.

The efficiency as a function of the LLD setting for the 5 μm cell with a 1000 μm pore depth is shown in Figure 6, where it is seen that for LLD settings below about 4 MeV, the efficiency is essentially independent of the LLD setting. For higher settings some variation is seen for the larger D/W ratios. Generally, most detectors use an LLD setting around a few hundred keV to suppress noise. However, it is reasonable to expect that a higher setting might be necessary for a [235]U-based detector because

of fission-induced background and the background resulting from the decay of [235]U (half-life of 700 million years), which leads to the emission of a 4.7 MeV alpha-particle. Therefore, it is reassuring to see the insensitivity of the detection efficiency to such high LLD settings. This also highlights the great advantage of using [235]U for neutron detection. The massive amount of energy imparted to the fission fragments and then deposited in the Si dwarfs typical noise sources.
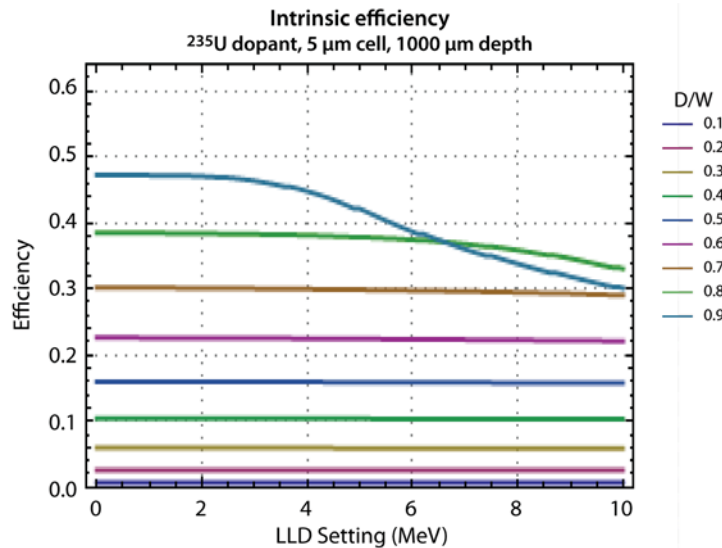
Figure 6. Overall detection efficiency as a function of LLD setting. There is little variation for the LLD setting below about 4 MeV, indicating uranium-loaded detectors are extremely noise insensitive.

Though the efficiencies shown in Figure 6 look extremely promising (as high as 48%), there is an important caveat that must be mentioned. The results in Figure 6 are for a 5 μm cell and a pore depth of 1000 μm, which corresponds to an etched feature aspect ratio of ~200:1, well beyond the ~25–50:1 ratio that is typically found in the literature. Thus, to get an idea of what is achievable given current Si etching technology, we present the results for a 5 μm cell with a 300 μm pore depth, corresponding to an aspect ratio of ~60:1 in Figure 7; the plot indicates a maximum detection efficiency of ~31% for a D/W ratio of 0.9, corresponding to a pore size of 4.5 μm. Once again it is clear that the [235]U-based detector is extremely insensitive to LLD settings below about 4 MeV.

Comparison to Other Detectors

Because this study examined the possibility of using [235]U as an alternative to [6]Li and [10]B as [3]He replacements, it was important to compare these results with those of [6]Li- and [10]B-based detectors. We chose two groups to compare our work to. The first group was Kansas State University (KSU),
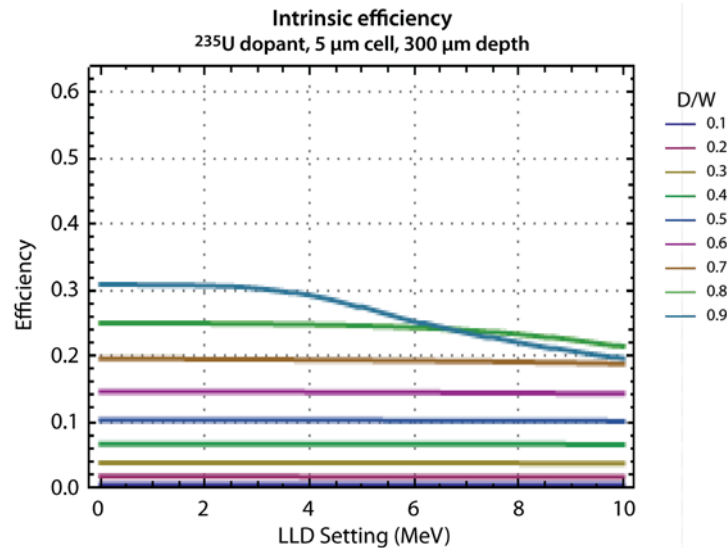
Figure 7. Overall detection efficiency for a 5 μm cell and 300 μm pore depth. This is a more realistic set of parameters given the current state of the art in Si etching. Peak efficiency is ~31%.

who fabricated etched Si detectors consisting of trenches filled with ^{6}LiF powder. The KSU group predicted efficiencies for their detector of ~30% for a 250 μm deep, 30 μm wide trench with ~15 μm of Si (Shultis 2009). They predicted yet higher efficiencies (up to ~50%) for different trench depths/widths. The published peak performance of their detector is ~40% for two coupled, stacked devices, or about 20% for a single detector.

The other group whose work was used as a basis for comparison is located at Lawrence Livermore National Laboratory (LLNL). The LLNL group developed a detector consisting of Si pillars surrounded by ^{10}B. Their device consisted of pillars 26 μm high, 2 μm wide, with a 2 μm separation. They predicted efficiencies from 15% to 25% for such a device, heavily dependent on the LLD setting. They predicted much higher efficiencies (~70%) for taller pillars, but again these would be very dependent on the LLD setting. Also, their predictions are not directly comparable to others since they assume a 4π neutron source rather than a surface normal source. The published performance of the LLNL detector is ~20%, within the range of their predictions (Nikolić 2010).

The predicted performance of our ^{235}U-based detector is comparable to the predictions reported by the KSU and LLNL groups, with the possibility of much better noise discrimination.

Conclusion

This project studied ^{235}U-doped, etched Si neutron detectors. MCNPX was used to calculate thermal neutron detection efficiency. We investigated 5, 10, and 20 μm cells with pore diameters/cell width

ratios of 0.1 to 0.9 (porosity of 0.7% to 64%) and pore depths of 50 to 1000 μm. Because of the inability of current versions of MCNPX to track fission fragments, the study was done in two steps. First the thermal neutron-fission conversion efficiency was found, and then the heavy ion tracking capability was used to approximate the energy deposition of the fission fragments. Because MCNPX assumes heavy ions to be fully ionized, and has no mechanism for charge pickup, we believe the results presented here underestimate the possible detector efficiency. For the parameters studied, peak detection efficiencies are ~48%. However, taking into account more realistic, currently achievable geometric parameters, detection efficiencies in the range of 15% to 30% seem more likely. Therefore, thermal neutron detection efficiencies are expected to be similar to similar detectors using ^{6}Li and ^{10}B. The great advantage of ^{235}U as a converter is in noise discrimination due to the very high energy of the fission reaction products.

Acknowledgments

References

Bellinger, S. L., R. G. Fronk, W. J. McNeil, J. K. Shultis, T. J. Sobering, D. S. McGregor, "Characteristics of the stacked microstructured solid state neutron detector," *Proc. SPIE* **7805** (2010) 78050N.

Caruso, A. N., "The physics of solid-state neutron detector materials and geometries," *J. Phys. Cond. Matter* **22** (2010) 443201.

Conway, A. M., T. F. Wang, N. Deo, C. L. Cheung, R. J. Nikolić, "Numerical simulations of pillar structured solid state thermal neutron detector: Efficiency and gamma discrimination," *IEEE Trans. Nucl. Sci.* **56**, 5 (2009) 2802–2807.

McGregor, D. S., W. J. McNeil, S. J. Bellinger, T. C. Unruh, J. K. Shultis, "Microstructured semiconductor neutron detectors," *Nucl. Instrum. Methods A* **608**, 1 (2009) 125–131.

Müller, R., A. A. Naqvi, F. Käppeler, F. Dickmann, "Fragment velocities, energies, and masses from fast neutron induced fission of ^{235}U," *Phys. Rev. C* **29**, 3 (1984) 885–905.

Nikolić, R. J., A. M. Conway, R. Radev, Q. Shao, L. Voss, T. F. Wang, J. R. Brewer, C. L. Cheung, L. Fabris, C. L. Britton, M. N. Ericson, "Nine element Si-based pillar structured thermal neutron detector," *Proc. SPIE* **7805** (2010) 78050O.

Shultis, J. K., D. S. McGregor, "Design and performance considerations for perforated semiconductor thermal-neutron detectors," *Nucl. Instrum. Methods A* **606**, 3 (2009) 608–636.

Wahl, J. S., "Energy distributions of fragments from fission of U^{235}, U^{238}, and Pu^{239} by fast neutrons," *Phys. Rev.* **95**, 1 (1954) 126–132.

Watson, R. L., J. O. Rasmussen, "Electron binding energies for highly ionized fission-fragment atoms," *J. Chem. Phys.* **47**, 2 (1967) 778–783.

Miniaturizing Time-of-Flight Mass Spectrometers[†]

Manuel J. Manard[1,a]

The design and performance of a proof-of-concept, prototype, reduced-size time-of-flight (TOF) mass spectrometer is described. The system consists of an ion acceleration/focusing/steering region, an 8 cm field-free region, a 4 cm dual-stage reflectron and a miniature microchannel plate detector. The resulting flight length of the system is 12 cm, approximately one order of magnitude less than typical TOF systems. In FY 2010, the design details as well as the simulated theoretical performance for the system were reported (Manard 2011). In FY 2011, modifications to the TOF were made to improve upon the original design, and a hybrid ion funnel/ion trap was added to the system. This addition improved the performance of the instrument and provided a secondary method for pulsing the TOF. Mass spectra, produced by the TOF system, were obtained for argon and krypton. The ratio of the measured flight times of the two noble gases were in excellent agreement with theoretical values and, thus, provided evidence toward proving the concept that the miniature TOF system can provide mass spectra data for the analysis of chemical species.

Background

Time-of-flight (TOF) mass spectrometry is well known for its ability to combine high-resolution mass analysis with high sensitivity and selectivity. TOF is unique among mass analysis techniques due to both its relatively simple implementation and its inherently unlimited mass range. Compared to other mass spectral methods that require the use of taxing experimental parameters, such as a homogeneous magnetic field or high-amplitude RF electric fields to facilitate mass analysis, TOF requires only DC potentials and simple timing circuitry to generate a mass spectrum. TOF functions by accelerating a packet of ions in an electric field of a known strength. To a first-order approximation, this results in all ions in the packet having the same kinetic energy (E_k),

$$E_k = \tfrac{1}{2}\, mv^2, \tag{1}$$

where *m* is the mass of the ion and *v* is the velocity of the ion. However, the velocity of an individual ion will depend upon its mass-to-charge (m/z) ratio, with more massive ions moving more slowly than less massive ions. Because the length of the ion's flight path (*l*) is fixed, one can directly relate the flight time of an ion (*t*) to its mass by combining Equations 1 and 2 to yield Equation 3.

$$v = \frac{l}{t} \tag{2}$$

[1] manardmj@nv.doe.gov, 805-681-2121
[a] Special Technologies Laboratory
[†] Project continued from FY 2010

$$t = \frac{\sqrt{m}}{\sqrt{2\,E_k}}\,l \qquad\qquad (3)$$

Therefore, if the ion packet is pulsed into the system at a time $t = 0$, then the measured flight time of each ion is directly proportional to the square root of its mass, with lighter ions arriving at the detector with shorter flight times than heavier ions.

Despite its relatively straightforward nature, TOF has remained largely a laboratory technique. This can primarily be attributed to the large size of the instrumentation. Most commercially available TOF systems use flight tubes that measure 100 cm in length. Although reducing the size of the flight tube will reduce the vacuum requirements of the system, doing so will also have a negative impact on the mass resolution of the system. However, due to the extremely high resolution of most TOF instruments that use a 100 cm long flight tube, the reduced mass resolution that comes with miniaturizing the system will likely still produce mass spectra with resolvable peak separations.

Project

Ion Funnel/Ion Trap (IF/IT)

The design of the IF/IT is based on the IF designed as part of an FY 2009 SDRD project (Manard "Differential Mobility Spectrometry/Mass Spectrometer" 2010, "Differential Mobility Spectrometry/Mass Spectrometry" 2010). An IF is a device used to guide an ion beam under conditions where the mean-free-path is less than the distance being traversed. In order to efficiently guide the ion beam under these conditions, an RF field is superimposed over a DC bias potential. The RF field on each electrode of the funnel is applied 180° out of phase with neighboring electrodes. The DC ramp guides the beam toward the entrance orifice to the high-vacuum TOF chamber, while the RF-modulated electric field confines the beam to the center of the ion funnel.

In FY 2011, an ion trapping region was incorporated into the design of the IF (Figure 1). The resulting IF/IT is based on a design published by Clowers (2008). The trapping region is made up of three electrodes that define the trap: a DC-only entrance electrode and two DC-only exit electrodes. A 90% transmission nickel mesh is mounted to the DC-only electrodes using a conductive epoxy. The DC potentials are applied to these electrodes independently of the DC gradient applied to the other regions of the IF/IT. This allows for the entrance and exit electrodes to be individually pulsed to fill and evacuate the ion trap. All of the trapping electrodes have an inner diameter measuring 10 mm. The increase in the volume of the trapping region serves to reduce Coulomb repulsion and increases the ion storage capacity of the trap.
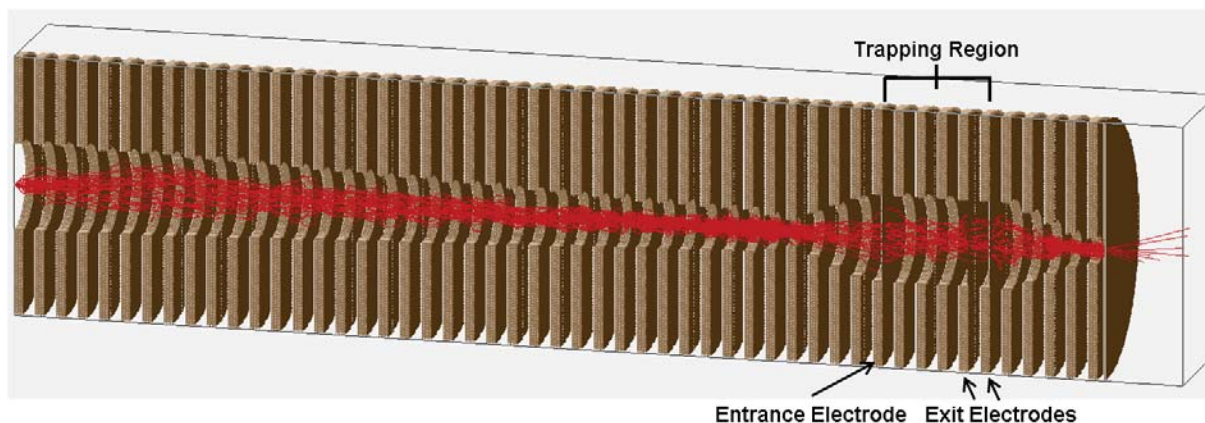
Figure 1. A three-dimensional cross section of an ion trajectory simulation, generated by Simion 8, of the IF/IT shown in ion transmission mode. Ion trajectories are shown in red.

The IF/IT can operate in one of four modes: (1) transmission mode, where the device functions as a normal ion funnel; (2) filling mode, where the trap is filled for a period of time; (3) trapping mode, where the ions are held in the trap; and (4) ejection mode, where the trapped ions are released. The timing of the IF/IT is controlled by using a Stanford Research Systems DG535 delay generator. The fourth mode can be used to define $t = 0$ for the TOF measurement.

TOF

The design details of the TOF portion of the system have been described previously (Manard 2011); therefore, only a brief description will be provided here. Simion 8 was used to generate ion trajectory simulations for the 12 cm TOF system. The resulting arrangement of components required to assemble the instrument is shown in Figure 2. It consists of (a) an accelerating, focusing, and steering assembly (AFSA), which accelerates, collimates, and deflects the ion beam into the TOF; (b) an 8 cm field-free region, where the majority of the ion flight occurs; (c) a dual-stage (Wang 1994) reflectron (Mamyrin 1973), which corrects for deviations in the kinetic energy of the ion packet when pulsed into the TOF; and (d) a commercially available microchannel plate (MCP) ion detector.

In FY 2011, the design of the TOF was updated to include the ion shield, shown in Figure 3, which is mounted directly to the entrance electrode of the reflectron. This component serves to shield the ion packets from the external vacuum chamber that is held at ground (0 V). Thus, the flight of the ion packet in the field-free region of the TOF occurs at the acceleration potential (–1750 V) and is not influenced by the ground potential of the vacuum chamber.
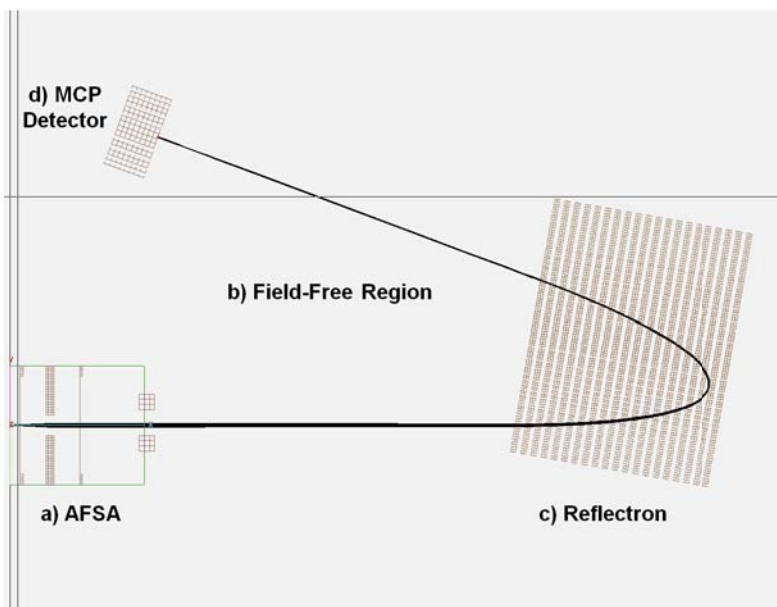
Figure 2. Ion trajectory simulation generated by Simion 8, which illustrates the components that make up the TOF system. Ion trajectories are shown in black.

Figure 3. Mini-TOF reflectron assembly with the ion shield mounted to the entrance electrode of the device. The resistor bridge is shown along the outside of the lens stack. Holes were cut into the ion shield so that background gases could be efficiently evacuated during pump down. A nickel mesh (not shown) was placed over the holes using a conduct epoxy.

Results/Discussion

IF/IT

The IF/IT was initially tested in transmission mode to compare its performance to the FY 2009 design. An increase in ion signal of approximately a factor of 2 was measured for the revised IF/IT design when compared to the original IF under similar operating conditions. This is attributed to the redesigned in-vacuum circuit board that delivers the electric fields to the IF/IT. With the updated design, higher amplitude RF fields can be applied to the funnel. This increases the ability of the IF/IT to radially confine the ion beam and results in increased ion transmission.

Following the confirmation of adequate ion transmission efficiency, the IF/IT was tested in ion trapping mode. Figure 4a shows a screen capture of the oscilloscope measurement for argon ions confined in the IF/IT. The purple trace is the pulse that is applied to the exit electrodes of the IF/IT, and the green trace is the measured ion signal, detected using the TOF. It is clear that the IF/IT is capable of trapping and releasing a packet of ions. Furthermore, Figure 4a also illustrates that it is feasible to use the IF/IT to establish $t = 0$ for the TOF measurement. Figure 4b shows a zoomed out view of the oscilloscope readout so that the entire timing sequence can be observed. Here, the purple and green traces are as described above, and the blue trace shows the amount of time that the trap is filled with ions. In the timing sequence shown in Figure 4b, the trap is filled for 20 ms, the ions are held in the trap for 10 ms, and the ions are released with an ejection pulse-length of 0.5 ms.

In order to determine the optimal filling and ejection times for the trap, the aforementioned parameters were varied, and the resulting ion signals were measured. Figure 5 shows the data collected for trap filling times that were varied from 1 to 80 ms while the ejection pulse duration was kept constant at 0.5 ms. From the data in Figure 5, it is apparent that the measured ion signals are approximately the same for all filling times used except for the shortest duration (1 ms). This suggests that the capacity of the ion trap is reached at a fill time of approximately 5 ms and that longer fill times do not add to the measured ion signal due to Coulomb repulsion.

Once the optimal trap filling time was determined, the ejection pulse duration was then varied to establish how quickly the ions confined in the trap could be injected into the TOF chamber. The ejection pulse must be shorter in duration than the flight time of the ions being pulsed into the TOF in order to maintain the mass resolution of the system. Figure 6 shows the measured ion signals for ejection pulses ranging in duration from 0.2 to 2 ms. It is clear that as the pulse is shortened, the measured ion signal is reduced, because fewer ions are released from the trap with faster ejection pulses. These data suggest that the ejection pulses required to produce TOF spectra will result in low ion signal intensity.
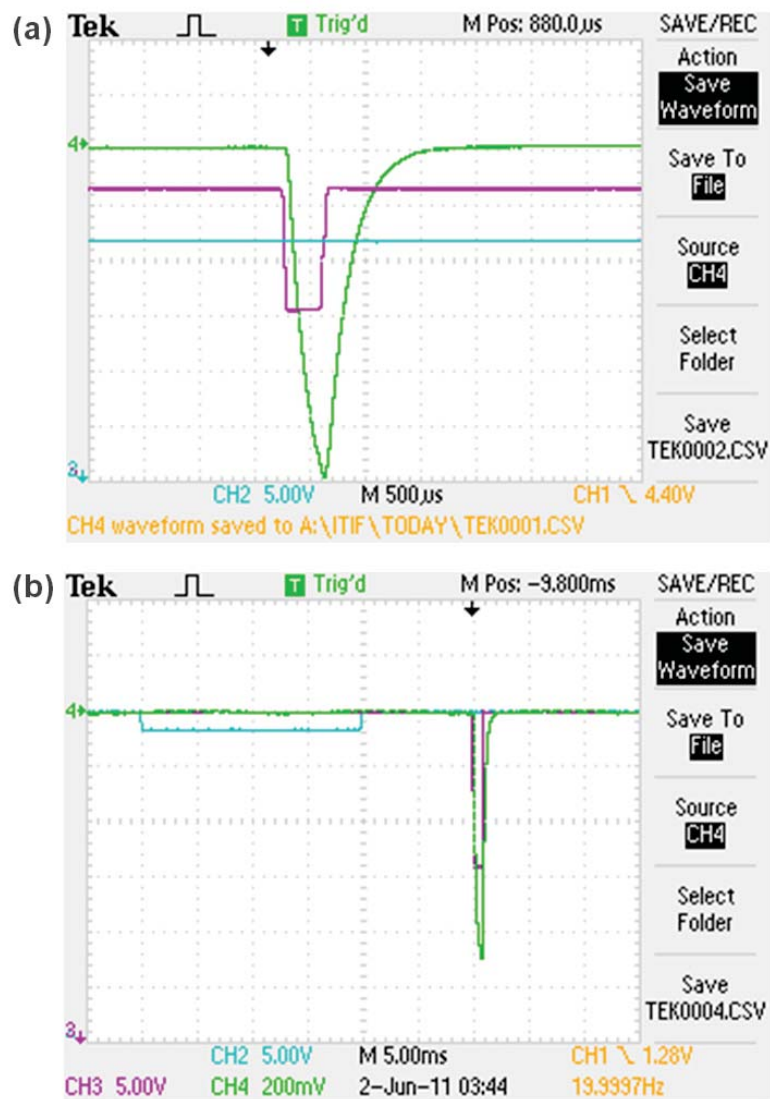
Figure 4. An oscilloscope screen capture showing (a) the ejection pulse applied to the IF/IT (purple trace) and the resulting ion signal (green trace) measured by the TOF system, and (b) the complete timing sequence for filling, trapping, and ejecting ions from the IF/IT. The blue trace is the fill time for the trap.
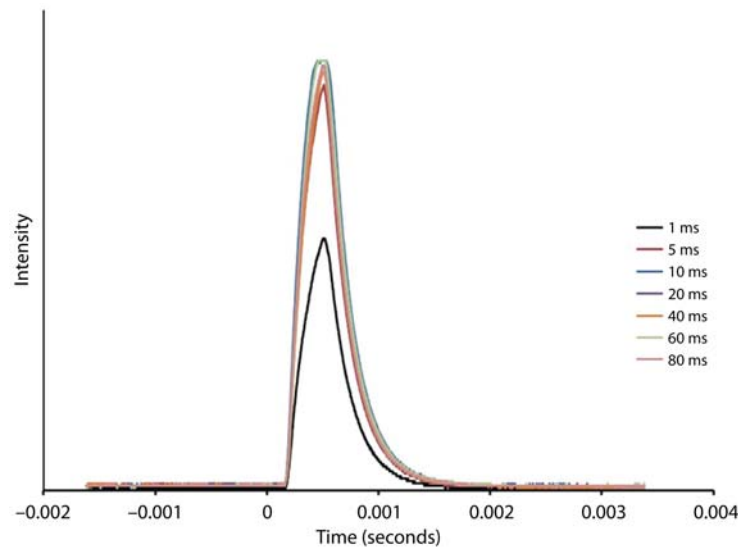
Figure 5. A plot of the measured ion signal intensity as a function of the fill time of the IF/IT. The filling times for each curve are shown in the inset. Time $t = 0$ is defined as the instant the ejection pulse, applied to the exit electrodes of the IF/IT, is triggered. The duration of the ejection pulse is 0.5 ms for all curves shown.

Figure 6. A plot of the measured ion signal intensity as a function of the ejection pulse duration of the IF/IT. Ejection times for each curve are shown on the right of the plot. Time $t = 0$ is defined as the instant the ejection pulse, applied to the exit electrodes of the IF/IT, is triggered. The fill time of the ion trap is 20 ms for all curves shown.

TOF

Using the IF/IT ejection pulse to establish t = 0, argon ions (m/z = 40) were injected into the TOF to test the capability of the system to produce mass spectra. In order to precisely control the width of the ejection pulse, an Agile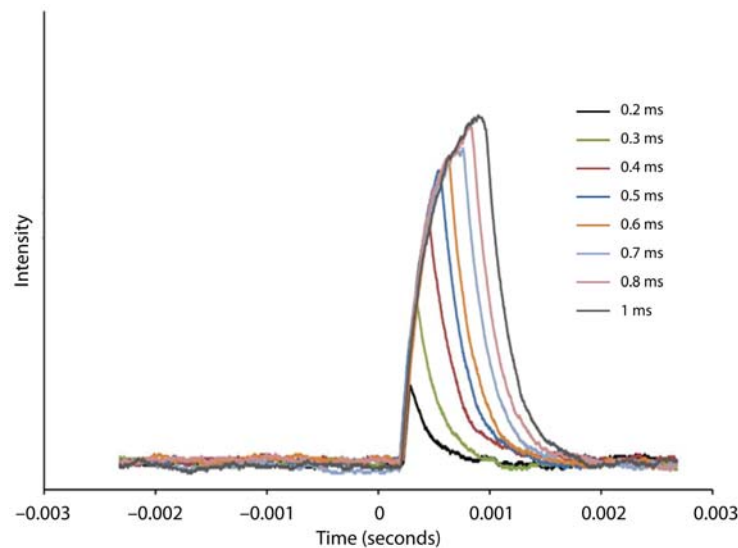nt function generator (Model 33250A) was used. The pulse supplied by the function generator was applied to the exit electrodes of the IF/IT trapping region. Using this method, the "on-time" (referring to when ions are being injected into the TOF) for the ejection pulse can be precisely varied to balance the trade-off between mass resolution (shorter on-time) and a detectable ion signal (longer on-time). Although precise timing for the duration of the pulse width was obtained using this method, an undesirable noise level was also found to be associated with the measurement due to the lack of a well-established reference to ground. Given this result, additional pulse averaging was required to improve signal fidelity. An example of typical data produced by the system using this pulsing method is given in Figure 7. Here, a 50 µs ejection pulse was used to generate the data shown. Additionally, the data were processed by an oscilloscope set to average 128 ion pulses to reduce the noise level.

The data in Figure 7 show that the ion signal is on the cusp of being irresolvable from the noise. As such, an alternative data collection scheme, which sums multiple averaged scans, similar to the one shown in Figure 7, was used. Figure 8a shows a TOF mass spectrum, which was acquired by summing 100 averaged scans, using a 10 µs ejection pulse from the trapping region of the IF/IT. Again, argon was studied as the test species for this investigation. A flight time of approximately 19.2 µs was measured.
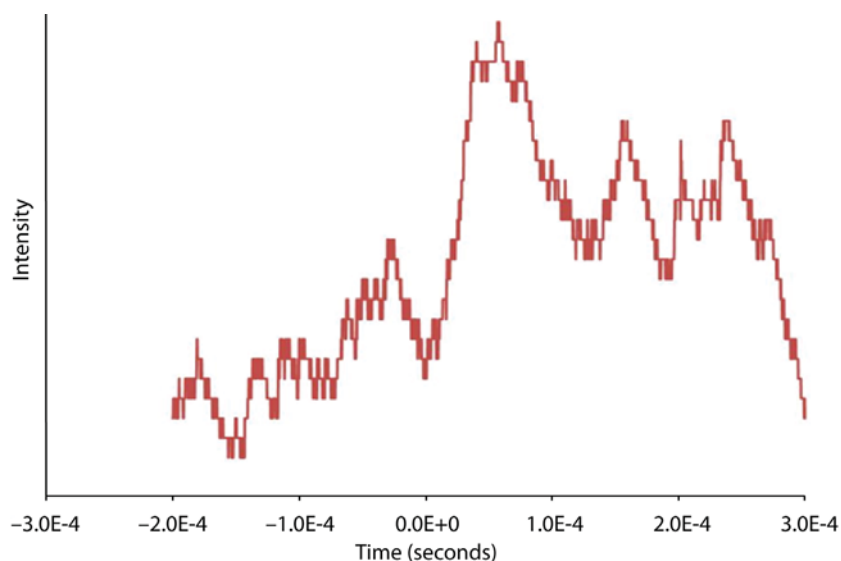

Figure 7. A plot of the measured ion signal intensity as a function of the flight time of argon. Time t = 0 is defined as the instant the ejection pulse is applied to the exit electrodes of the IF/IT. The duration of the applied ejection pulse is 50 µs.

The peak in Figure 8a can clearly be observed in the data shown. However, it is also apparent that the ion signal is tapering off over a relatively long time following the crest of the ion signal intensity. This phenomenon appears to be directly related to the relatively high pressure of the IF/IT region of the system (3×10^{-3} torr for the data shown in Figure 8a). At this pressure, the ions exiting the trap experience multiple collisions with the background gas. This causes the ion packet to spread out in space as it approaches the entrance of the TOF. The effects of the pressure can be clearly seen by increasing the pressure in the IT/IF and measuring the resulting TOF spectrum. For comparison, Figure 8b shows the TOF spectrum for argon where the pressure in the IF/IT has been increased to 7×10^{-3} torr. The measured peak has become wider than that of Figure 8a. The data illustrate that as the pressure is increased, the time required for the ions to exit the trap also increased. Thus, in order to acquire high-resolution TOF data using the ejection pulse of the IF/IT to define $t = 0$, the pressure in this region should be held at a relatively low value.
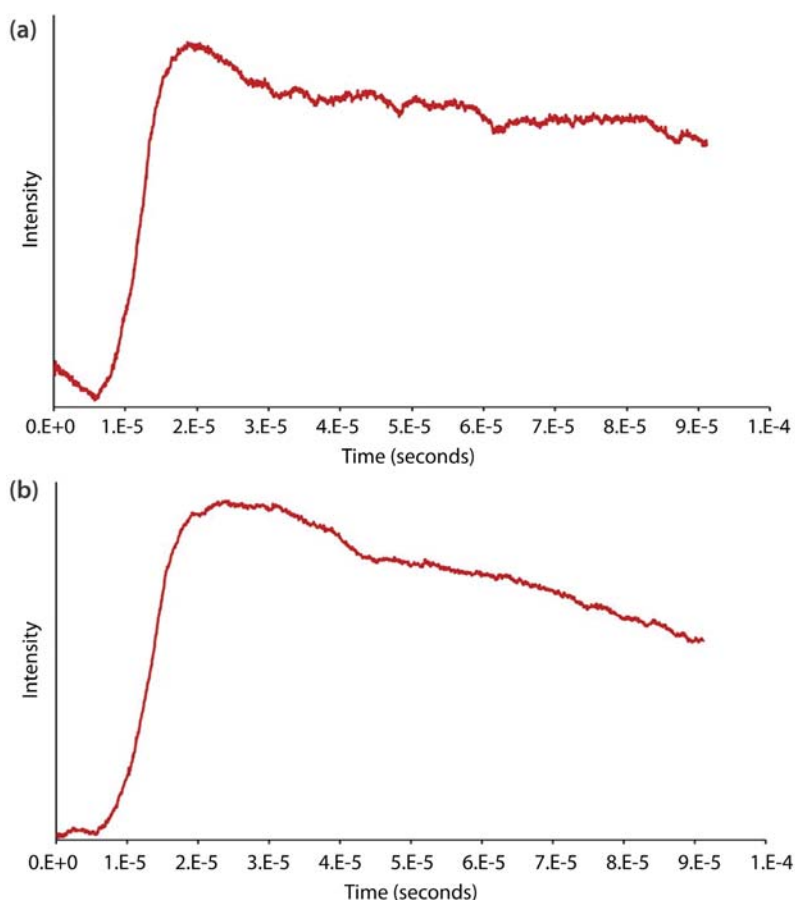

Figure 8. A plot of the measured flight time of argon acquired at an IF/IT background pressure of (a) 3×10^{-3} torr and (b) 7×10^{-3} torr. Time $t = 0$ is defined as the instant the ejection pulse is applied to the exit electrodes of the IF/IT. The duration of the ejection pulse is 10 µs.

To establish that the data produced by the system were actual flight times of the ions being studied, the sample gas was changed to krypton ($m/z_{average}$ = 83.8) and the flight time was acquired. Because the average mass of krypton is approximately twice the mass of argon, a longer flight time should be observed (as indicated by Equation 3). Figure 9 shows the measured flight time of krypton plotted along with the measured flight time for argon. The spectra were acquired using identical experimental conditions. It is clear that the measured flight time for krypton (27.5 μs) is longer than that obtained for argon using our system. Note that the krypton peak in Figure 9 is wider than the peak acquired for argon under similar experimental conditions. This is attributed to the fact that multiple, naturally occurring isotopes of krypton are contributing to the distribution of the peak. The distribution for naturally occurring isotopes of krypton is: ^{78}Kr (0.35%), ^{80}Kr (2.25%), ^{82}Kr (11.6%), ^{83}Kr (11.5%), ^{84}Kr (57.0%), and ^{86}Kr (17.3%). Only one isotope of argon, ^{40}Ar, is found in nature.

The data in Figure 9 can also provide a key piece of evidence as to the performance of the TOF system. Because both the argon and krypton TOF spectra were acquired under identical experimental conditions, using Equation 3, one should be able to calculate the flight time of one of these chemical species using the flight time of the other. Given that, to a first-order approximation, all ions in the system are accelerated to the same kinetic energy (E_k) and all ions traverse the same distance (l), a ratio of flight time (t) to square root of the mass (m) can be used to calibrate the system and convert a

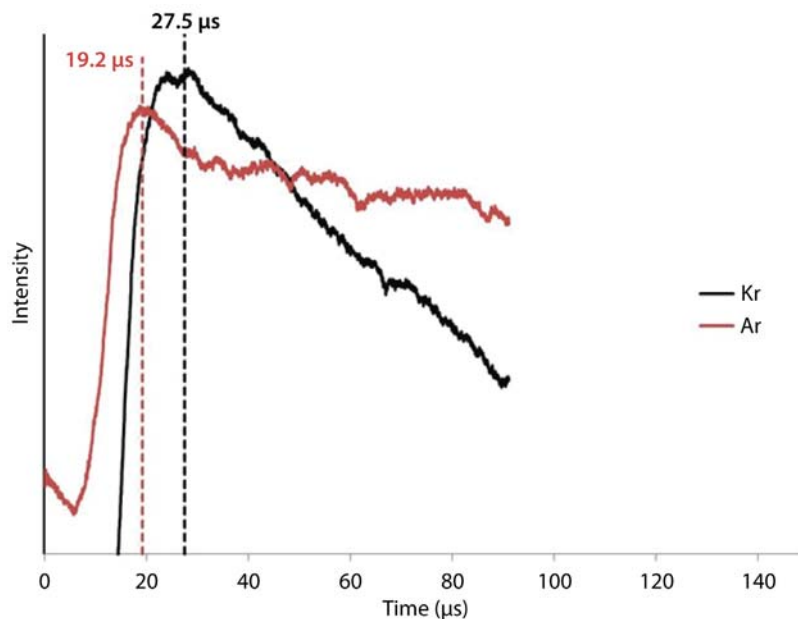**Figure 9. A plot of the measured flight time of argon (red) and krypton (black) acquired at an IF/IT background pressure of 3 × 10⁻³ torr. The measured flight times of the two chemical species are shown. Time t = 0 is defined as the instant the ejection pulse is applied to the exit electrodes of the IF/IT. The duration of the ejection pulse is 10 μs.**

measured flight time into a value of m/z. Accordingly, if the measured flight time for argon (19.2 µs) is divided by the square root of its mass (40 amu) and multiplied by the square root of the average mass of krypton (83.8 amu), then the calculated flight time of krypton should be 27.8 µs. This value is in excellent agreement with what is found experimentally (27.5 µs), differing by only 1.1%. Thus, the relationship between the ratio of the two measured flight times provides irrefutable evidence that the instrument does provide TOF mass spectra data.

Finally, a pulsing scheme that utilizes the steering electrode of the AFSA (Figure 2), located in the high-vacuum TOF chamber and a new method for processing the TOF data that uses a multichannel scaler (Ortec Corp.), was incorporated into the system to improve the resolution of the data. Preliminary TOF data, acquired for krypton using a 250 ns pulse width and the multichannel scaler, is shown in Figure 10. These data illustrate the improvement in resolution and reduction in the background noise level using the new pulsing scheme and data acquisition method.
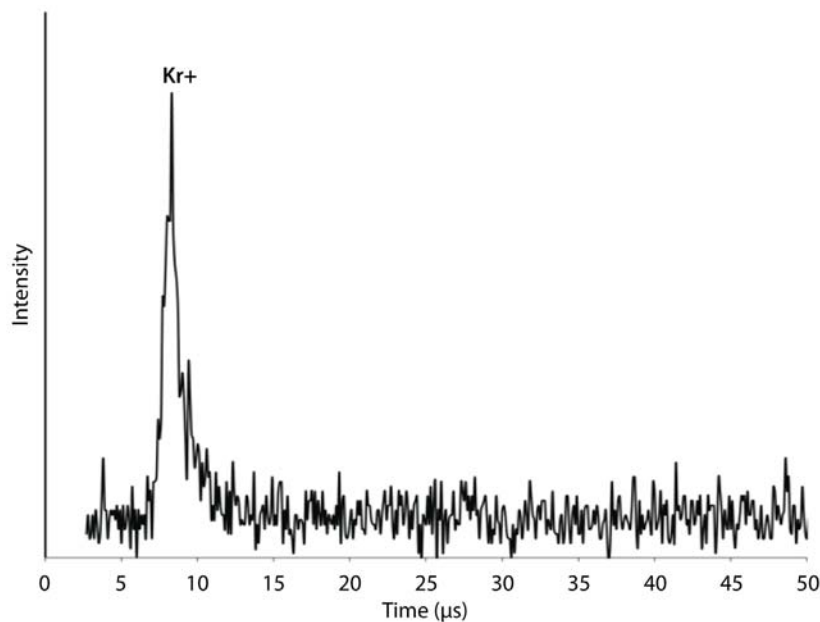
Figure 10. A plot of the measured flight time of krypton acquired using a multichannel scaler. Time *t* = 0 is defined by pulsing the steering electrodes of the AFSA. The duration of the ejection pulse is 250 ns.

Conclusion

The design and performance of a 12 cm, proof-of-concept, prototype TOF mass spectrometer has been described. The TOF portion of the system is primarily made up of an ion acceleration/focusing/ steering region, an 8 cm field-free region, a 4 cm dual-stage reflectron, and a specialized miniature

MCP detector. Modifications to the original FY 2010 design of the system were discussed. Additionally, the design and performance of a hybrid IF/IT, added to the system in FY 2011, were also described. The IF/IT was subsequently used to pulse the TOF, defining $t = 0$ for the measurement of the flight times of the ionic species studied. Mass spectra for argon and krypton were obtained using the miniature TOF system. The ratio of the measured flight times of the two noble gases were in excellent agreement with theoretical calculations and, thus, provide critical evidence to support the claim that the miniature TOF can provide mass spectra data for the analysis of chemical species. The mass resolution of the system is found to be negatively affected by using the IF/IT to pulse the TOF because the relatively high pressure of this region leads to peak broadening due to collisions with the background gas. Accordingly, a pulsing scheme was developed that utilizes the steering electrode of the AFSA. This scheme resulted in significant improvement over the IF/IT pulse loading method.

Acknowledgments

References

Clowers, B. H., Y. M. Ibrahim, D. C. Prior, W. F. Danielson, M. E. Belov, R. D. Smith, "Enhanced ion utilization efficiency using an electrodynamic ion funnel trap as an injection mechanism for ion mobility spectrometry," *Anal. Chem.* **80**, 3 (2008) 612–623.

Mamyrin, B. A., V. I. Karataev, D. V. Shmikk, V. A. Zagulin, "The mass-reflectron, a new nonmagnetic time-of-flight mass spectrometer with high resolution," *Sov. Phys. JETP* **37** (1973) 45–48.

Manard, M. J., R. Trainham, "Differential mobility spectrometry/mass spectrometer," *Nevada Test Site–Directed Research and Development*, FY 2009, National Security Technologies, LLC, Las Vegas, Nevada, 2010, 67–75.

Manard, M. J., R. Trainham, S. Weeks, S. Coy, E. V. Krylov, E. G. Nazarov, "Differential mobility spectrometry/mass spectrometry: The design of a new mass spectrometer for real-time chemical analysis in the field," *Int. J. Mass Spectrom.* **295**, 3 (2010) 138–144.

Manard, M. J., "Miniaturizing time-of-flight mass spectrometers," *Nevada National Security Site–Directed Research and Development*, FY 2010, National Security Technologies, LLC, Las Vegas, Nevada, 2011, 65–75.

Wang, T. I., C. W. Chu, H. M. Hung, G. S. Kuo, C. C. Han, "Design parameters of dual-stage ion reflectrons," *Rev. Sci. Instrum.* **65**, 5 (1994) 1585–1589.

Custom Photonic Band Gap Crystals

Mark Morey[1,a]

This project explored the potential customization of a new material for optical sensing and counterfeit identification applications using photonic band gap crystals. These crystals, structured solids consisting of periodic arrays of high and low dielectric domains, can generate unique optical signatures by their unique interaction with light and can be tuned to operate in the UV or near-infrared while remaining colorless in the visible spectrum. Materials were developed and procured according to specifications. Resultant films and powders were applied to slides, and their optical properties were assessed.

Background

Photonic band gap materials (PBMs) are structured solids consisting of periodic arrays of high and low dielectric domains such that the propagation of some wavelengths of light is restricted. This behavior is analogous to a band gap in semiconductors, which feature energy levels that prohibit occupation by electrons. A familiar naturally occurring PBM is a crystal of opal (Figure 1), which is composed of a close-packing of silica spheres and subsequent void spaces. The periodic arrays of spherical particles make similar arrays of interstitial voids, which act as a natural diffraction grating for light waves in photonic crystals, especially when the interstitial spacing is of the same order of magnitude as the incident light wavelength.
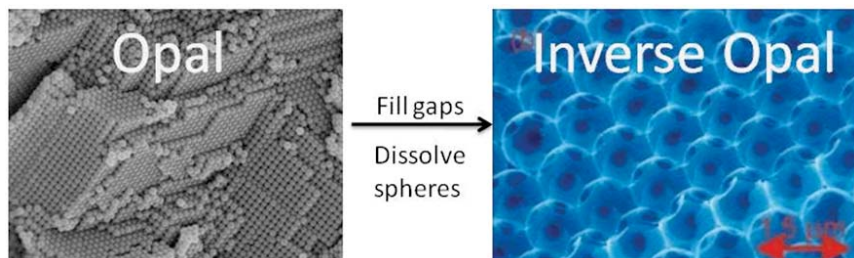
Figure 1. (left) Scanning electron microscope image of natural opal; (right) gaps between spheres are filled with polymer followed by removal of spheres to create the inverse opal

In the last few years, PBMs have advanced from the theoretical, to the novel, and then to the commercial. We have identified a company that has developed a way to create "inverse opals" in which the void space between the silica spheres is intercalated with a polymer, which creates an

[1] moreyms@nv.doe.gov, 805-681-2206
[a] Special Technologies Laboratory

ordered porous structure upon removal of the silica. This "inverse opal" can be tailored to reflect light over a wide range of wavelengths. While there are other techniques for building these unique materials, the inverse opal method is the most feasible at the moment, enabling the manufacture of larger quantities.

Project

Opalux, Inc., located in Canada, was formed to commercialize a technical breakthrough in producing inverse opals from the research lab of Dr. Geoffrey Ozin at the University of Toronto (Blanco 2000). Their lab developed a way to add the flexible polymer to the voids in a synthetic opal to make thin flakes that would change reflected color upon application of an electric potential. Our strategy was to ask them to modify their process and shift their wavelengths of interest out into the near-infrared (NIR). All work was to be on a "best effort" basis. Initial and final specifications for the custom material were as shown in Table 1.

Table 1. Material specifications

	Initial Specification	Final Specification
Maximum reflectance	850 nm (negotiable)	850 nm ±100 nm
Narrow-band reflectivity	<~75 nm FWHM (negotiable)	Preferably <75 nm FWHM; no more than 150 nm FWHM
Minimal reflectivity in the visible	<5%–10% and/or colorless	<10% and/or colorless
Lack of reflectivity in visible region (400–740 nm)	Maintained when viewed 0°–45° off-normal	Maintained when viewed 0°–25° off-normal
Suspension properties	Can be suspended in a binder to be used as an ink for counterfeit detection	Can be suspended in a binder to be used as an ink for counterfeit detection
Flake size	<90 μm or reasonably small enough to obtain the optical effect with no sacrifice in reflectivity	Material could be a thin film, and/or a divided powder or flake

Upon receipt of the material, the Special Technologies Laboratory (STL) noted that the thin film was very white and disappointingly opaque (Figure 2).

The monolithic thin film had also been scraped off the clear plastic support film and pulverized into a coarse powder resembling about 5 g of laundry detergent (Figure 3).

This high opacity raised some concern since an initial sample obtained a year ago from the same company was more transparent as a thin film and had better optical qualities. The need for the film to be not only colorless but transparent is important for counterfeit identification. When placed on a surface of any color, a clear flake does not need to color-match the underlying surface; it can simply transmit the surface color while reflecting the wavelength of interest.

Figure 2. Opalux thin film on clear plastic substrate placed over colored text on black background. Note high opacity.

Figure 3. Opalux pigment was a coarse powder

The thin film reference material consisted of a monolithic film of inverse opal (Figure 2). As with other designer materials, the thin film is important because it provides the theoretical maximum of reflectance at the desired wavelength. The package was accompanied by a reflectance spectrum measured at Opalux (Figure 4). We repeated measurements of the reflectance spectrum of this film on a Cary 5000 UV-VIS-NIR spectrophotometer at STL (Figure 5). This testing was completed using the integrating sphere and a collection of total (specular + diffuse) reflectance. The film was placed over the integrating sphere's sample aperture with no backing and a dark cover.

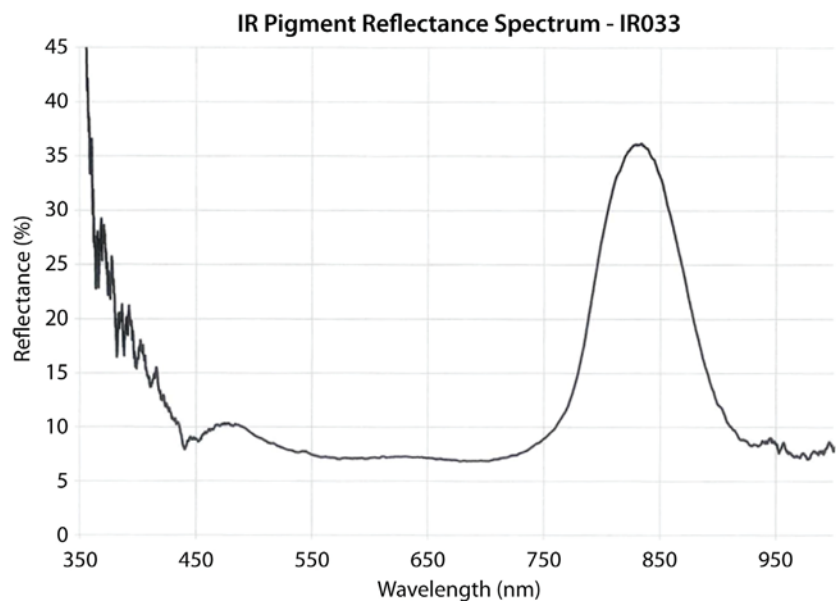**Figure 4. Reflectance of Opalux thin film on clear plastic substrate measured by vendor. A reflectance peak centered at 830 nm is noted.**
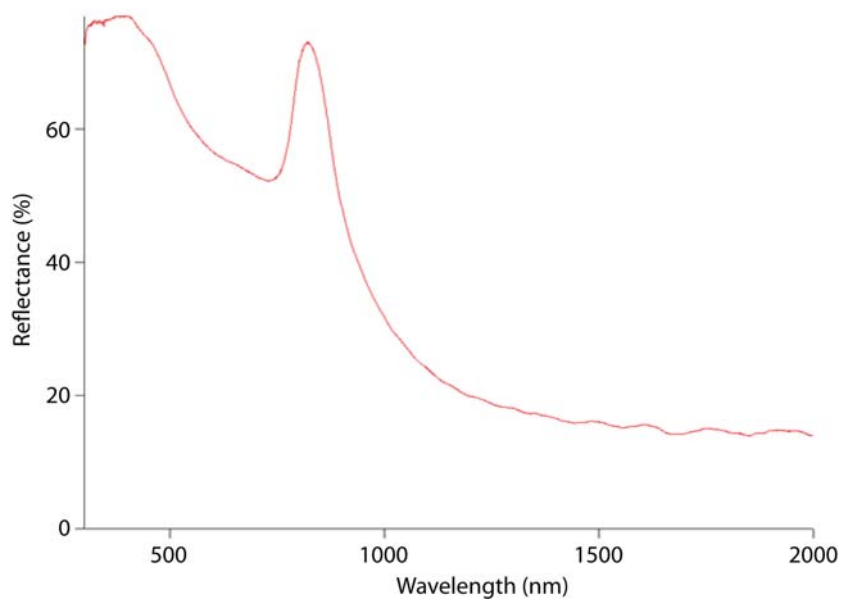

Figure 5. Reflectance spectrum of the same Opalux thin film collected at STL on a Cary 5000 showing the reflectance peak at 830 nm on top of a broad reflectivity from the UV to nearly 1500 nm. Strong overall reflectivity from the UV to 1000 nm results in a white reflective material.

The powdered material was then tested in the lab to find the best formulation to create an ink or paint. The powder itself was found to be highly hydrophobic. A small amount in a test tube of water formed a floating mass on the surface. A drop of Silwet L-7602 organosilicone surface-tension reducing agent was added to wet the material and form a suspension. A second portion was placed in a test tube with a few milliliters of ethanol. The powder went from lily-white to nearly transparent, which was encouraging. A third concoction was made with a clear binder (Clear-Advantage) with a proven track record for suspending engineered flake materials. It is a water/alcohol-based binder that dries clear and glossy when used by itself. As a liquid it is very milky, so a suspension of flakes was difficult to assess. Each mixture was painted on cleaned glass microscope slides and dried for 20 minutes under a bright light (Figure 6).
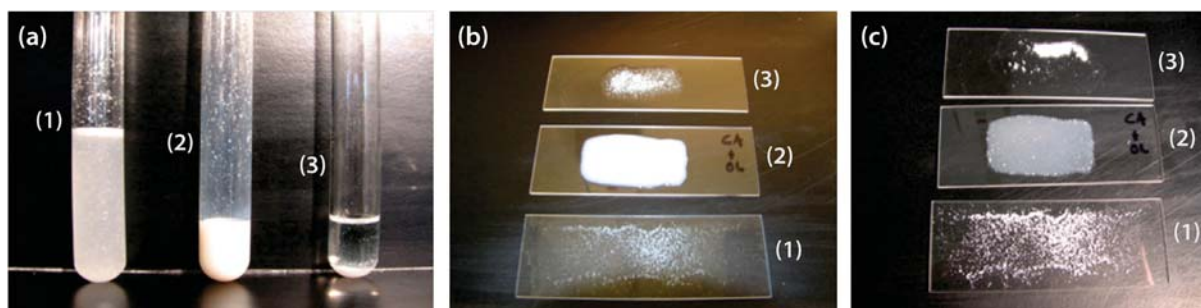

Figure 6. (a) Mixtures of photonic band gap material flakes in test tubes, (b) applied to slides, (c) and dried. Samples are numbered 1–3 as follows: Opalux flakes in (1) ethanol, (2) Clear-Advantage, and (3) water/surfactant.

When dry, the water suspension looked poor, with large flake agglomerations. The ethanol suspension started out nicely, but when the ethanol evaporated, the flakes resumed their bright white appearance. The Clear-Advantage suspension looked the best, forming a slightly lumpy but clear film with a slight tint. A reflectance spectrum was collected on the Clear-Advantage slide using the Cary 5000 (Figure 7). The other suspensions were discarded.

Discussion

Preliminary enthusiasm for the possibility of inverse opal PBMs to be used in our applications was premature and quickly dampened when we received the samples and measured the spectra. The monolithic thin film was suspect due to its high reflectance and white, semi-opacity. Placing the film on a dark surface with text in Figure 2 showed a marked obscuration of the model substrate. The manufacturer's reflectivity spectrum looked promising with a maximum reflectance at 830 nm, but when duplicated in house, the spectrum collected on the Cary 5000 was more realistic, confirming our observations. It should be noted that at wavelengths longer than ~1200 nm, the overall reflectivity drops dramatically and might indicate a more appropriate place to locate the reflectance peak. Size features within the structure are on the size scale of visible light and are likely subject to Brillouin scattering, which occurs in any periodic medium where light interacts with optical density variations.
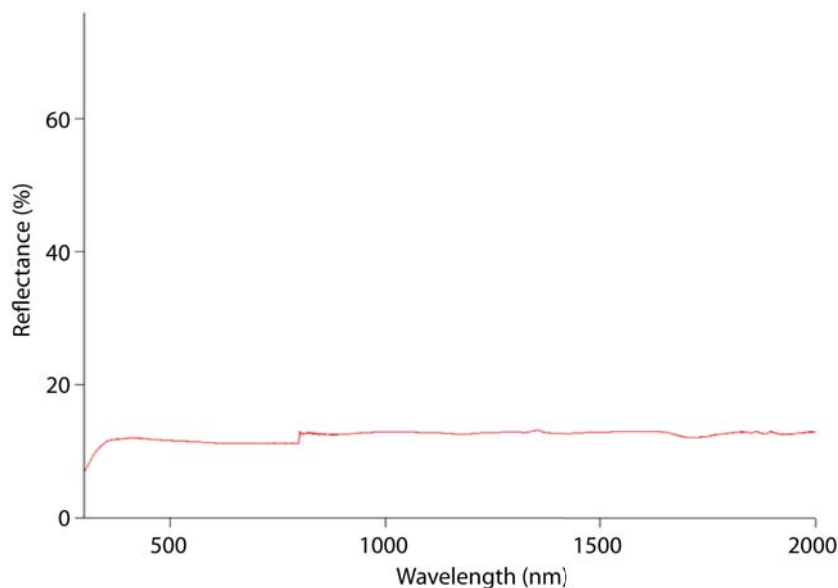
Figure 7. The reflectance spectrum of Opalux flakes suspended in Clear-Advantage water-based binder dried on glass was measured at STL on the Cary 5000. Data indicate that all reflectance, even at the desired region of 830 nm, has been extinguished by wetting and filling of the pores.

Broader distribution of template sphere diameters could be another reason for the high reflectance in the visible. If the spheres have different diameters, the resulting light reflected will have a broader distribution and a shorter maximum peak reflectivity. A thorough scanning electron microscopy study would reveal this information.

The Opalux film is made up of a hexagonal close-packing of spheres, which leads to an angular dependence of the reflectivity. The reflectivity peak is optimized when the PBM crystal is created as a monolithic thin film. When this film is pulverized, the resulting chunks and flakes are randomly orientated, broadening out the narrow reflectance peak they worked so hard to achieve. Expectedly, the powdered flakes fared even worse when made into a rudimentary paint. In suspension in ethanol, the flakes were wetted, and they "index matched" the solvent to some degree. The inverse opals are essentially a well-ordered, polymer sponge that easily soaks up the solvent to form a translucent suspension. But when the solvent evaporates, the flakes return to being broad-band reflectors. The suspension in Clear-Advantage looked promising as a liquid, but upon drying it remained clear and nonreflective. This was expected but not to this degree. It appears that the pores were filled with the binder, cancelling the periodic array of high/low dielectric.

Conclusion

A new, commercially available material was obtained in the hope that it could be a low-cost alternative to other designer materials used for counterfeit identification. While this material is admittedly designed for another application, we felt that it could be made according to our specifications. Unfortunately, the results were not promising. For this material to be of use, the inverse opal would have to be sealed somehow to prevent the pores from filling with binder or solvent. The original application of the material calls for its structure to swell and shrink with electric current. Because this color shift is irrelevant at the moment, we should consider a more rigid framework made of an inorganic metal oxide with a much higher index of refraction, such as traditional titanium dioxide. Moving to longer wavelengths might also help decrease any light scattering in the visible.

References

Blanco, A., E. Chomski, S. Grabtchak, M. Ibisate, S. John, S. W. Leonard, C. Lopez, F. Meseguer, H. Miguez, J. P. Mondia, G. A. Ozin, O. Toader, H. M. van Driel, "Large-scale synthesis of a silicon photonic crystal with a complete three-dimensional bandgap near 1.5 micrometres," *Nature* **405**, 6785 (May 2000) 437–440.

this page intentionally left blank

Straw Detector—Dual Fission Meter for Gamma and Neutron Multiplicity Measurements

Sanjoy Mukhopadhyay,[1,a] Ronald S. Wolff,[a] Ryan B. Detweiler,[a] Ethan Smith,[b] Stephen Mitchell,[c] Paul P. Guss,[d] and Richard Maurer[a]

This report describes the work performed in FY 2011 for a 2-year SDRD project that incorporated straw detectors for gamma-ray and neutron multiplicity counting. The two-panel detector system is called the neutron multiplicity counter (NMC). We used solid ^{10}B (in the form of boron carbide) for neutron detection instead of ^{3}He, which is in short supply globally. The project intended to find a near-term replacement for ^{3}He and to provide a high-efficiency, lightweight NMC for maritime applications. In the first year, the project procured a panel of "straw neutron detectors," investigated its characteristics, and developed a data acquisition system to collect neutron multiplicity information from spontaneous fission sources using a single panel consisting of 60 straws equally distributed over three rows (Mukhopadhyay 2011). In FY 2011 we developed the field-programmable gate array and associated data acquisition software. This SDRD effort successfully produced a prototype NMC with approximately 33% detection efficiency as compared to a commercial fission meter.

Background

A straw neutron detector is a narrow copper tube (4 mm in diameter and 2 mil thick) coated inside with a very thin (1 μm) layer of ^{10}B that works as a proportional counter when biased with a high voltage. A collection of closely packed straws embedded in a high-density polyethylene moderator form a panel detector that provides high detection efficiency, large solid angle, and enough spatial resolution for it to be useful as a neutron imaging system. Proportional Technologies, Inc., manufactured the panels used in this research.

The scientific value of this effort is that the prototype neutron multiplicity counter (NMC) seeks to provide an effective way to meet two contradictory physics requirements in detecting neutrons via the exothermic neutron absorption on ^{10}B. The mean free path of thermal neutrons in ^{10}B is about 18 μm. It takes about a 60 μm layer of ^{10}B to completely stop thermal neutrons. The α-particles generated in the reaction have ranges of about 2–3 μm, hence the thin layer of boron coating on the copper tube. The thinness of this layer reduces the intrinsic neutron counting efficiency. One solution is to make the coating in the shape of narrow tubes (straws) to increase the total ^{10}B surface area.

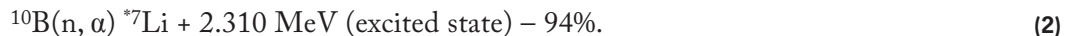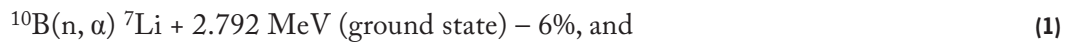[1] mukhops@nv.doe.gov, 301-817-3319
[a] Remote Sensing Laboratory–Andrews; [b] Great Basin Technologies, Inc.; [c] North Las Vegas; [d] Remote Sensing Laboratory–Nellis

The project leveraged two core technology bases: (1) the ability to provide uniform thin (approximately a few microns) large surfaces of ^{10}B to interact with neutrons to produce α-particles in a proportional counter configuration, and (2) a high-speed field-programmable gate array (FPGA) to exploit the time correlations between neutrons from different sources. For example, cosmic or background neutrons in a maritime environment are only mildly correlated, primarily because of the high rates of spallation neutrons created by cosmic interactions. Neutrons from (α, n) channels are completely uncorrelated, and neutrons from fission, particularly when multiplications are taking place following spontaneous or induced fission, are very highly correlated. By following the detected neutron counting distributions with very narrow time gates ranging from 1 to 512 μs, one can partition between fission and cosmic neutrons within a very short time, on the order of 10 minutes. This approach provides a unique solution to discriminate against cosmic neutrons in a maritime search environment (in real time) and enables effective measurement of a neutron source on the ground from a large standoff distance. Neutron detection, counting, and partitioning in a maritime environment is complex due to the presence of spallation neutrons (commonly known as the "ship effect") and to the complicated nature of the neutron scattering in that environment. By careful study of the higher-order moments of the multiplicity distribution, one can estimate the source strength and generate intelligent inferences on the surrounding materials around the neutron source.

In the form of boron carbide (B_4C), ^{10}B is uniformly and very thinly sputtered (approximately 1 μm thick) on large, thin (2 mil thick) copper sheets. With the boron enriched to 96%, the effective percentile weight proportion of ^{10}B in the boron carbide is ~76.9% (Lacy 2008). Low-energy neutrons incident on a ^{10}B-coated surface will go through the following nuclear reactions:

$$^{10}\text{B(n, α)} \, ^7\text{Li} + 2.792 \text{ MeV (ground state)} – 6\%, \text{ and} \tag{1}$$

$$^{10}\text{B(n, α)} \, ^{*7}\text{Li} + 2.310 \text{ MeV (excited state)} – 94\%. \tag{2}$$

The respective kinetic energies of the positive ions generated from Equation 2 are $E_{*\text{Li}}$ = 0.84 MeV and E_α = 1.47 MeV; this restricts the α-particles to have a mean free path of approximately 2 μm in bulk ^{10}B. This limitation on the kinetic energy available to the α-particles requires that the ^{10}B layer be thin so that the α-particles can be drawn from the ^{10}B surface out to the high-voltage anode wire of the proportional chambers. The thermal neutron cross section for the ^{10}B(n, α) ^{7}Li reaction is 3840 barns. This cross section drops rapidly with increasing neutron energy and is proportional to 1/v (the reciprocal of the neutron velocity). The corresponding value for ^{3}He is 5330 barns, significantly higher than that for the boron reaction, and ^{3}He is insensitive to gamma rays as well. Typically, these characteristics make ^{3}He a better intrinsic thermal neutron detector than ^{10}B. The gamma-ray responses can be separated completely by simple pulse height separation. A lower-level discriminator at 100 keV separates out the gamma-ray responses from the neutrons. Only neutron pulse height is used by the current electronics for n/γ discrimination. Gamma responses were registered but were not processed for multiplicity determination. No results on gamma multiplicity are given in this report.

Project

In FY 2011, the project procured a detector panel with 100 straws, providing a two-panel straw neutron detector with 160 straws. Each NMC straw has an inner radius of 2.2×10^{-1} cm and an average active length of 50 cm. With a layer of 1 mm thick ^{10}B coating, 160 straws contain 1.3×10^{23} atoms of ^{10}B. At thermal neutron energy, the absorption cross section being 3.84×10^3 barns (1 barn = 10^{-24} cm^2), the total thermal neutron absorption cross section in cm^2 for ^{10}B would be 4.98×10^2 cm^2. A commercial fission meter contains 46 liters of ^{3}He under one atmospheric pressure, and with the thermal neutron absorption cross section of 5.33×10^3 barns for ^{3}He, the total thermal neutron absorption cross section would be 6.6×10^3. These above physical constants provide some important useful ratios; for example, the ratios of absorption probabilities (^{10}B:^{3}He) = 7.56%, the number of atoms (^{10}B:^{3}He) = 10.50%, and the thermal neutron absorption cross section (^{10}B:^{3}He) = 72.00%.

Component Descriptions

In FY 2011 a data acquisition system was developed using a new, single-board FPGA (SBRIO-9602 manufactured by Nuclear Instruments) and the LabVIEW software platform. Using the data acquisition system and the NMC, benchmark measurements of the response functions in terms of the neutron counting efficiency for spontaneous fission neutrons from a modest ^{252}Cf neutron source (2 µCi, 8.6K neutrons per second) were compared to an existing fission meter. Fundamentally the data acquisition system consisted of six components:

1. System Initialization (SI)

2. Microsecond Counter (MC)

3. Real-Time Data Acquisition (RDA)

4. Characterization Data Acquisition (CDA)

5. Accidental Neutron Counting (ANC)

6. Neutron Search Alarm Algorithm (NA)

Functionally, the SI component has to ensure that the system and memory are reset prior to turning on concurrently the rest of the system modules: the MC, RDA, and CDA.

The MC is a very fast master clock with a 25 ns pulse rate clocking at 40 MHz. This provides a self-consistent internal clock (master clock) that tracks neutron counts per microsecond. It also provides the shortest length of time characteristic for the data acquisition. The MC examines the state of a pin for indication of a new pulse. If a new pulse is found, then the previous count data are incremented by one; otherwise, the count data remain the same. After the pulse detection algorithm, the MC examines a counter to determine if 1 µs has elapsed. Once the MC has elapsed 1 µs, the MC examines the operating states of the RDA and CDA. If they are active, the MC will pass the collected count data

to their respective first-in first-out (FIFO) buffers, before resetting the count data to zero. Neutron arrival-time statistics are correlated in a histogram of the numbers of neutrons arriving within a time gate for a range of gate widths (1 μs through ~65 ms in steps of 1 μs).

The RDA keeps track of multiplets statistics (singles, doubles, triples, etc.), calculates instantaneous value of the excess of variance above the true random Poisson distribution (called the Feynman variance [Y2F]), and determines trends of Y2F to perform partitioning of neutrons according to their origin: cosmic or man-made. The RDA operates within a loop, which has two phases, Get Parameters and Acquire Data. In the first phase, the RDA continually gathers parameters. After the Acquire switch is pressed, the RDA passes the last gathered parameters and begins the second phase to acquire data. The RDA gathers microsecond count data from its FIFO, from which it builds the real-time log file. The RDA sums data from the FIFO (bin width/1 μs) times. It then increments the summed position in the Multiplet Array and resets the summed value to zero. After repeating the previous process, Bin Count times, the Multiplet Array is passed to the host computer via a second FIFO, and then the Multiplet Array is reset to zero. The host is responsible for generating the log file. The RDA's second phase can be stopped and reconfigured at any point during operation. However, the second phase will only halt after the completion of a host FIFO transfer. The RDA will then reenter the first phase.

The CDA builds statistics of the higher moments Y2F, Y3F, Y4F and generates asymptotic values of R2F, R3F, and R4F, respectively, at the end of all cycles. Fitting of R1F, R2F, R3F, and R4F yields the neutron fission source term S, the neutron die away time (λ^{-1}), multiplication (M), efficiency (ε), and the Rossi alpha (α) ratio, which can be defined as the functions of the (α, n) channel strength to the spontaneous fission channel strength. Similar to the RDA, the CDA operates in two phases of Get Parameters and Acquire Data. The CDA continually gathers parameters until the Acquire switch is pressed. After the switch is pressed, the CDA passes the last gathered parameters and gathers the microsecond count data from its FIFO, from which it constructs the 2A log file. The CDA sums data from the FIFO (bin width/1 μs) times. It then increments the Multiplet Matrix (MM) based on the summed count and the active gate. After incrementing the MM, the CDA returns to the previous step and collects data for the next gate. The summed count data is reset to zero after the data for the last gate/bin were incremented in the MM (also known as the completion of a cycle). A cycle's duration can be calculated as Bin Width × Bin Count. The above steps are repeated the number of times specified by the cycle parameter. The MM is transferred to the host when all cycles are completed. When data acquisition is complete, the CDA reenters the Get Parameters phase. The host is responsible for generating the log file.

The CDA has the ability to append data to previously acquired data by not clearing the memory for the MM. The previous data file will not be overwritten. The CDA Acquire Data routine can be stopped at any time; however, the routine will only halt after a full cycle is completed, at which point it will transfer the MM to the host computer and reenter the first phase.

System Description

The physical characteristics of the two-panel straw NMC are listed in Table 1. The two panels have a different number of straws, but they have the same effective lengths (50 cm), widths (40 cm), and thicknesses (6.25 cm).

Table 1. Dimensions and physical characteristics of NMC panels

Physical dimensions	Panel 1 (60 straws)	Panel 2 (100 straws)
Panel length	70 cm	70 cm
Straw length	50 cm	50 cm
Effective straw length	48.3 cm	48.3 cm
Straw inner diameter	4.43 mm	4.43 mm
Panel weight	14.5 kg	14.9 kg
Separation between tubes	6.5 mm	4.0 mm
Solid angle at 1 meter	0.015 str	0.015 str
Power input	+12 VDC at 0.83 A	+12 VDC at 0.25 A (lower power, newer battery supply; battery life is 16 hours)

Figure 1. Two-panel NMC. The left panel has 100 straws and the right one has 60 straws. Each panel's external dimension is 70 × 39 × 6.25 cm and the combined weight is 29.4 kg (64.8 lb).

With a 12 VDC power input, each of the NMC panels individually generates one each of an analog pulse and one transistor-to-transistor logic (TTL) pulse. The TTL output is about 500 ns wide and 3.3 VDC in amplitude. The two TTL outputs could be summed up electronically so that the NMC works as a single unit for neutron counting purposes. The TTL pulses were fed to the FPGA input, which is a single board reconfigurable input/output system personal computer board. The data acquisition software to control the FPGA sorts and time stamps counts neutrons in list mode. The NMC is shown in Figure 1.

Experimental Results with Straw NMC and Fission Meter Systems

Sensitivity Analysis

A 2 μCi ^{252}Cf source was used to compare the neutron counting efficiency of the two-panel straw NMC against a fission meter. Fifteen-minute average counts from the source were measured with the two systems, for the source placements at different distances from the detector surface centers. The moderated side of the fission meter was facing the source to maximize the count rates. Measurements with distance up to 2 m between the source and the system were also performed. The neutron count rates per second as a function of the distance between the bare source and the detector are plotted in

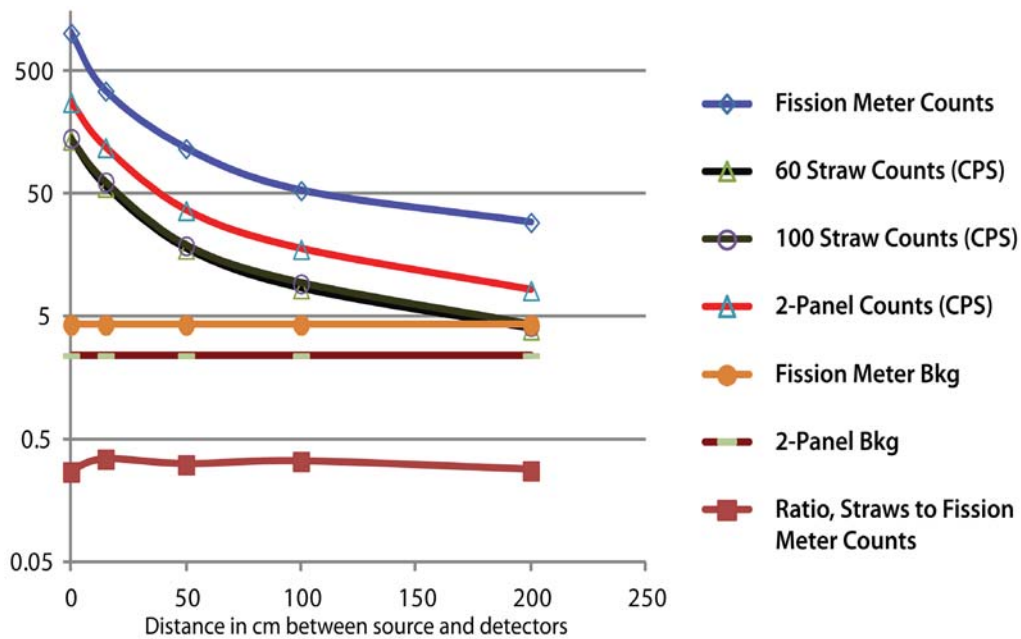Figure 2. Separate counts from two panels were tracked from a bare 2 μCi ^{252}Cf source. The ratio of the NMC neutron counts per second to the fission meter neutron counts is shown at the bottom part of the plot; the ratio is flat across the distance between the source and the detectors. Bkg stands for the average background neutron counts for each of the detectors; CPS is counts per second.

Figure 2. As seen from the figure, the NMC is ~33% efficient with ^{252}Cf as compared to the fission meter for counting neutrons. Similar measurements were carried out with the same ^{252}Cf source but with ~2.5 cm (1 inch) of polyethylene moderator surrounding the neutron source. The detected neutron count rates are shown in Figure 3.
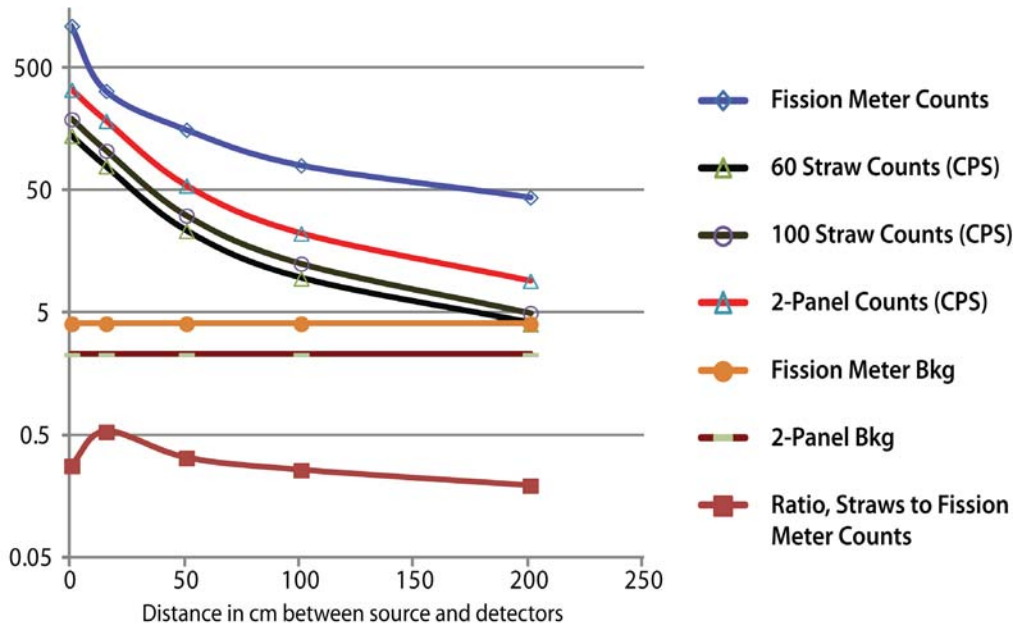

Figure 3. Separate counts from two panels were tracked from a moderated 2 µCi ^{252}Cf source surrounded by a polyethylene moderator. The ratio of the NMC neutron counts per second to the fission meter neutron counts is shown at the bottom part of the plot. Bkg stands for the average background neutron counts for each of the detectors; CPS is counts per second.

Neutron Partitioning

The RDA creates a data log file that tallies the number of zeros, singles, doubles, triples, and up to septuplets (seven sets of neutrons that arrive at the same time within a preset time bin). The Y2F can be determined from these data tables to obtain the multiplicity distribution. Depending on the initial value of the Y2F in the background, one can calculate the relative percentile contributions of the (cosmic) background and the correlated neutrons. Table 2 shows the results of neutron partitioning obtained with the total average neutron counts in the counter. The averages vary from 1.7 to 3.0 times the average background counts. In this regime of low neutron counts, the partitioning is not exact, but the introduction of a time-correlated neutron source always shifts the cosmic contribution substantially (100% to start with for the background).

Table 2. Real-time data (partitioning of neutrons by origin)

Total Source Strength (Length of Run)	Mean Count Rate Total Cps ±Error	Y2F ±Error	Calculated Cosmic Percentile	Calculated Non-Cosmic Percentile	Actual Cosmic/ Non-Cosmic Percentile
1.7 × Background (60 minutes)	6.9 ±0.6	0.00153 ±0.00034	74 ±7	26 ±3	58.8/41.2
1.8 × Background (71.4 minutes)	7.5 ±0.8	0.0015 ±0.0003	74 ±8	26 ±3	55.6/44.4
2.0 × Background (63.8 minutes)	8.0 ±0.9	0.00145 ±0.00030	70 ±8	30 ±4	50/50
2.2 × Background (24 minutes)	8.8 ±0.4	0.000888 ±0.000500	46 ±14	54 ±15	45.5/54.5
3.0 × Background (30 minutes)	11.4 ±0.8	0.00095 ±0.00040	46 ±5	54 ±5	33.3/66.7

Table 3. Measured spontaneous fission parameters for the prompt neutrons

Fission Properties	Bare Source	Moderated Source	Comments and Explanation
Spontaneous fission source strength in gm	4.06E–09	3.71E–09	Actual mass of 2 μCi ^{252}Cf (with specific activity of 540 Ci/gm) is 3.7 E–09 gm.
Neutron die away time λ^{-1} (in μs)	52.62	97.28	The bare source die away value is true neutron die away value; the excess of about 45 μs die away time for moderated source accounts for neutrons traveling through the polyethylene moderator.
Total multiplication	1	1	There is no other medium to undergo induced fission; therefore, there is no multiplication for ^{252}Cf.
Absolute percentile efficiency (neutrons detected/ neutrons emitted)	1.49	2.2	Moderation lowers the neutron energy and makes the sensor more efficient.
α-parameters (ratio of (α, n)) channel to spontaneous fission channel	0.01	0.01	The prompt neutrons emitted from the ^{252}Cf source are mostly due to spontaneous fission.

Characterization of Data

Characterization data contain the counts of a progressive 40 × 512 elements matrix (up to 40 multiplets are kept for each time gate width, ranging from 1 to 512 μs) from which the statistics for Y2F, Y3F, and Y4F are built. Their corresponding asymptotic values, namely R2F, R3F, and R4F, respectively, are determined at the end of the 512 μs gate. The algebraic operations involved in calculating the Feynman variances are lengthy and cumbersome (Walston 2009). The fission parameters calculated from the characterization data (obtained from the two-panel NMC using a 2 μCi ^{252}Cf source in close proximity) are tabulated in Table 3.

Conclusion

This 2-year SDRD project has demonstrated and produced a prototype neutron multiplicity detector using ^{10}B-lined straw neutron detectors with approximately 33% detection efficiency when compared to a commercial fission meter. Successful experiments were carried out to characterize a 2 μCi ^{252}Cf source in close proximity for 15 minutes. The NMC successfully discriminated between cosmic neutrons and time-correlated neutrons within 5 minutes at a distance of 2 m. The NMC determined the average neutron die away time (λ^{-1}) to the order of ~50 μs. Using the same source (once bare and once moderated), the NMC was able to determine the thickness of the polyethylene in terms of additional neutron delay time (~18 μs/cm or 45 μs/inch). Unless bundled together to produce more ^{10}B surface, or without having a complex deposition pattern, the NMC will not have the neutron detection efficiency of a commercial fission meter. Neutron detection efficiency of 160 straws is about one-third of that of a fission meter up to a distance of 2 m from both a bare and a moderated ^{252}Cf source. The NMC data acquisition system has the unique advantage over the fission meter because it can simultaneously parse data in real time and perform characterization analysis. In addition, the current FPGA can sort neutron data like a shift register.

Acknowledgments

References

Lacy, J. L., A. Athanasiades, C. S. Martin, L. Sun, T. D. Lyons, "Fabrication and materials for a long range neutron-gamma monitor using straw detectors," *Nuclear Science Symposium Conference Record IEEE* (2008) 686–691.

Mukhopadhyay, S., R. S. Wolff, S. Mitchell, P. P. Guss, R. Maurer, "Straw detector—dual fission meter for gamma and neutron multiplicity measurements," *Nevada National Security Site–Directed Research and Development*, FY 2010, National Security Technologies, LLC, Las Vegas, Nevada, 2011, 77–85.

Walston, S., "The idiot's guide to the statistical theory of fission chains," LLNL-TR-414245, Lawrence Livermore National Laboratory, Livermore, California, 2009.

Nanoparticle-Based Analytical Biosensor[†]

Shayla Sawyer Armand,[1,a,b] Irina Barash,[b] Sydney Halperin,[b] Kevin Kyle,[a] Kethia Mathieu,[b] Liqiao Qin,[b] Chris Shing,[b] and Stephan Weeks[a]

The goal of this FY 2011 SDRD project was to explore bioaffinity methods of detection using aptamers. This biological layer will be deposited on nanoparticle-based detectors. Previous SDRD work (Sawyer 2011) focused on ZnO nanoparticle detectors for UV wavelengths. A new metal oxide material, indium oxide, was investigated to facilitate longer wavelength fluorescence detection for use with the biological layer. Preliminarily, aptamers were deposited on various substrates with corresponding chemical protocols and then characterized. Progress was made toward a rugged, lower power, compact, multipurpose device array.

Background

The FY 2010 investigation of colloidal nanoparticle-enhanced, UV photodetectors presented the potential for a hybrid material sensor. The objective was to directly couple scintillator light into a visible blind, UV nanoparticle detector by multilayer deposition of materials with different functions (Sawyer 2011). In FY 2011, a new functional layer is introduced, namely aptamers, a biorecognition element used to achieve selective biosensing. The intended biosensor will use intrinsic blue fluorescence for signal transduction and a new material, indium oxide (In_2O_3), in order to extend the wavelengths of detection from the UV to the blue. Specific wavelengths within this region correspond to intrinsic aptamer fluorescence peaks that can be used for biodetection.

Biorecognition elements with high specificity such as antibodies or enzymes have dominated applications in biomedical research and medical point-of-care systems. However, the invention of aptamers by Ellington and Szostak (1990) in addition to the enabling technology by Tuerk and Gold (Irvine 1991) opened new avenues for environmental sensing. DNA and RNA aptamers are engineered to bind to various molecular targets by repeated rounds of in vitro selection, otherwise known as the SELEX [systematic evolution of ligands by exponential enrichment] process. They provide important advantages over antibodies (Que-Gewirth 2007, Dollins 2008, Song 2008, Han 2010), including:

- A markedly broadened range of potential targets, demonstrating high affinity to both small and macromolecules, beyond capabilities of antibodies (see Table 1).

- Bulk synthesis by chemical processes, which significantly reduces the cost of fabrication.

- The ability to be created in the exact environment of its operational conditions.

[1] sawyersm@nv.doe.gov, 805-681-2262; sawyes@rpi.edu, 518-276-2164
[a] Special Technologies Laboratory; [b] Rensselaer Polytechnic Institute
[†] Project continued from FY 2010

- Ease of chemical modifications, creating unique biosensing opportunities for probes, quenchers, fluorophores, etc.

- Greater stability at elevated temperatures.

- The ability to be regenerated and reused by chemical or thermal denaturation, improving longevity and reducing cost.

- The ability to interact with other DNA or RNA molecules, leading to hybridization of structures with differing functionality.

Currently, there is no ideal method for aptamer development. While aptamers are available commercially and easy to obtain using specific sequence information gathered from the literature, there is significant potential for non-specific binding. A method to verify the binding would create a more reliable and accurate biosensor. Ultimately, a microbial biosensor can be created using an aptamer specifically created for a target such as Escherichia coli (*E. coli*) and then verified by its tryptophan, nicotinamide adenine dinucleotide (NADH), or flavin intrinsic fluorescence response.

Table 1. Examples of aptamer targets

Target	Types	References
Microbial pathogens (whole cells, lysates, spores)	*Pseudomonas aeruginosa*, anthrax spores, *L. acidophilus* cells, *E. coli*	Bruno 1999, Hamula 2008, So 2008, Wang 2010
Viral pathogens	Hepatitis, influenza, HIV	Kumar 1997, Misono 2005, Tombelli 2005
Cancer cells	Leukemia, prostate	Herr 2006, Bagalkot 2007, Smith 2007
Drugs and explosives	Cocaine, TNT	Liu 2005, Li 2007, Ehrentreich-Forster 2008
Vitamins and metal ions	B12, potassium	Lorsch 1994, Zhao 2008
Toxins	Cholera, abrin, microcystin-LR	Bruno 2002, Gu 2004, Tang 2007

Low-dimensional, metal-oxide semiconductor nanomaterials have stimulated great interest and extensive research due to their novel electronic and optical properties in addition to their biocompatibility. They are compelling as a platform for interfacing biorecognition elements with transducers for signal amplification. Specifically, colloidal nanoparticles are attractive as they take advantage of three-dimensional quantum confinement effects, are easy to fabricate, have a high surface area for light coupling, and are relatively low cost. Furthermore, our recent research to create metal-semiconductor-metal (MSM) devices demonstrated that the current carrying mechanism creates a high internal photoconductive gain due to the presence of oxygen-related hole-trap states

at the nanoparticle's surface and the high resolution of interdigitated electrodes (Qin "Comparison" 2010, "Metal-semiconductor-metal" 2010, "Low-pass" 2011, Sawyer 2011). The material results presented here are for In_2O_3, chosen for its band gap properties that correspond with the detection of NADH intrinsic fluorescence from potential biohazards. It is a wide-band semiconductor material with a documented band gap value of 2.9 eV. ZnO was the focus of previous work and is best suited for tryptophan intrinsic fluorescence detection in the UV range. ZnO is a direct wide band gap semiconductor material (documented values range from 3.2 to 3.4 eV). These materials fill a significant niche where inexpensive and traditionally used photomultiplier tubes (PMTs) and silicon (Si)-based photodetectors show a marked reduction in responsivity.

Project

In this project, the biorecognition layer process includes the following steps: (1) identify an aptamer sequence for a specific proof-of-concept target; (2) investigate surface immobilization (aptamer binding) approaches; and (3) characterize aptamer binding. We pursued this process in tandem with In_2O_3 nanoparticle device development in which commercial thin film and laboratory-fabricated nanoparticle materials were compared, device structures including wavelength selective detectors were created, and device characterization was performed. In FY 2012 the biorecognition layer will be immobilized on In_2O_3 nanoparticle devices, and the composite device will be tested.

Biorecognition Layer Selection and Immobilization

As a proof-of-concept, the chemical tryptophan was chosen as the target. Tryptophan was chosen for its high fluorescence signal, compatibility with previously developed detectors, and the availability of an aptamer sequence in recent literature. Figure 1 shows the emission spectrum of the bacteria, *Enterobacter Aerogenes*. The largest peak at 340 nm from 280 nm excitation is due to the intrinsic fluorophore tryptophan. This peak is near the maximum responsivity of the ZnO-based detector created from SDRD work pursued in FY 2010.

The original aptamer sequence to bind the chemical L-tryptophan is 5'BiotinTTTTTTTTTT-GCACGTTGGTTAGGTCAGGTTTGGGTTTCGTGC (Yang 2011). This aptamer sequence was ordered from Integrated DNA Technologies, Inc., with three additional terminating molecular variations to accommodate different binding methods (Table 2). The two binding methods are streptavidin-coated substrates with biotin-terminated aptamers, and silica surface modification with thiol-terminated aptamers. Both the biotin and thiol-terminated aptamers were also purchased with a fluorescent aptamer molecule (FAM), 6-FAM (6-carboxyfluorescein), to be used as a preliminary binding and characterization step. The expected emission from 6-FAM is at 520 nm under 495 nm excitation.
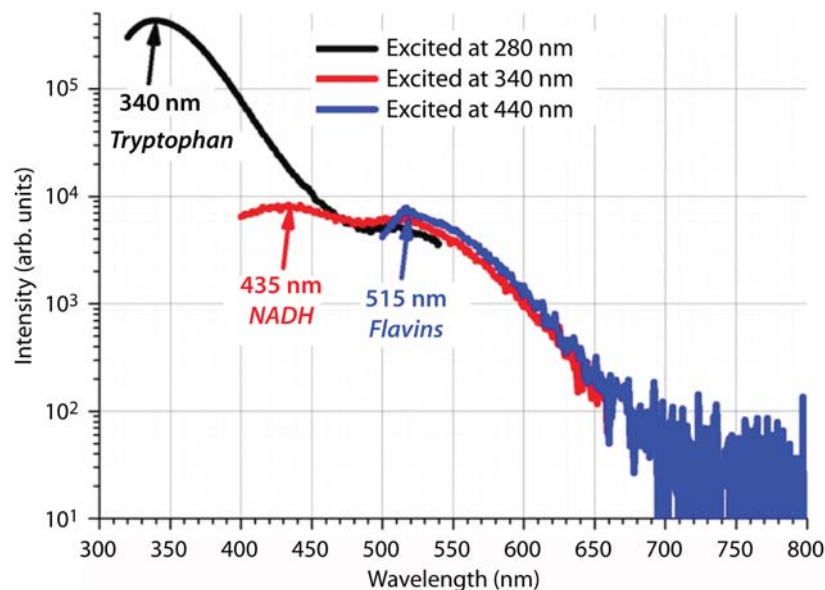
Figure 1. Intrinsic fluorescence emission spectrum of *Enterobacter Aerogenes* when excited at specific wavelengths

Table 2. Aptamer variations

Aptamer Name	Description
5'Biotin-Trp3a-1	Original aptamer sequence for streptavidin/biotin binding protocol to L-tryptophan
5'Thiol-Trp3a-1	Original aptamer sequence for thiol/fused silica binding protocol to L-tryptophan
5'Biotin3'FAM-Trp3a-1	Fluorescent aptamer molecule (FAM) labeled and biotin-terminated aptamer sequence (used without tryptophan as a preliminary step)
5'Thiol3'FAM-Trp3a-1	FAM labeled and thiol-terminated aptamer sequence (used without tryptophan as a preliminary step)

The streptavidin/biotin binding process is as follows: aptamers (Integrated DNA Technologies) were dissolved with different buffers, including PBS (KCl 2.68 mM, KH_2PO_4 1.47 mM, NaCl 136.89 mM, Na_2HPO_2 8.10 mM), PBS+ (PBS with 20 mM of $MgCl_2$), and a binding buffer (NaCl 137 mM, $MgCl_2$ 0.5 mM, KCl 2.7 mM, KH_2PO_4 2 mM, Na_2HPO_4 10 mM). The concentrations of aptamers tested were 2, 5, 10, and 100 nmol/mL. They were denatured in a 90°C or 95°C water bath for 5 minutes and chilled immediately on ice. The cooling process was altered to reduce the temperature gradually, using 5-minute steps in a 40°C water bath, sitting at room temperature, and then on ice.

We activated the fused silica slides for the thiol/silica binding process by immersing them in HPLC methanol, deionized water, 1 M of KOH and a 10% 3-aminopropyltriethoxysilane solution inside a petri dish. The petri dish was sealed with tape and put into the oven at 100°C for 4 hours. It was checked every hour to refill with liquid if necessary. The slides were then incubated with 10 µL of modified DNA and 15 µL of binding buffer solution at 37°C for 5 hours in a small centrifuge tube. Next, they were immersed in 10 mM HCl in a separate dish, sealed, and incubated at 100°C for 1 hour. Soon after, they were immersed in distilled water. Circles were drawn on the back of the slides to mark where the DNA would be spotted. The S-SMCC solution provided by Uptima was spotted with a diameter of 1 mm. It was sealed and incubated for 1 hour at 37°C, then washed with binding buffer.
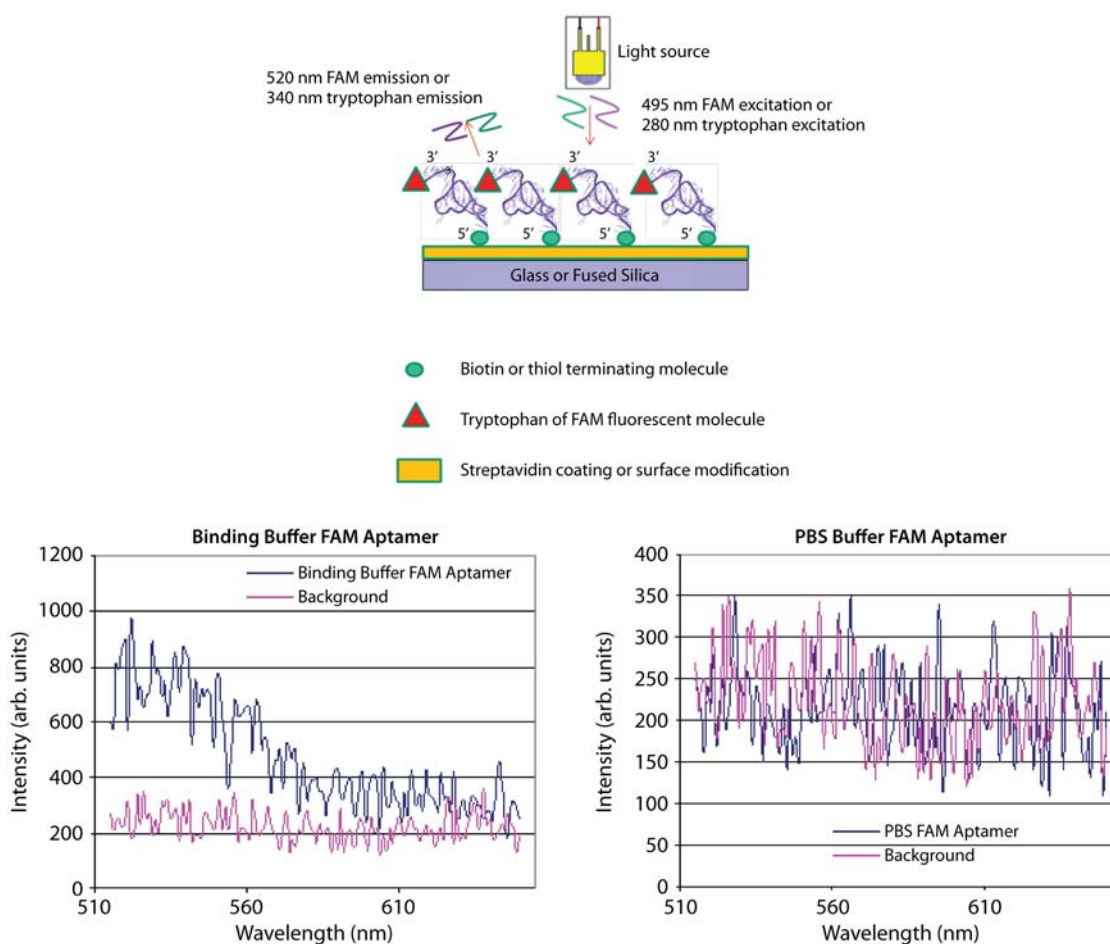

Figure 2. Composition of binding solutions shown with fluorescence comparison of solutions for 5'Biotin3'FAM-Trp3a-1 on a quartz substrate. The expected peak of FAM is 520 nm, as shown. The binding buffer listed in literature performed better than the PBS buffer often used for streptavidin/biotin interactions.

The substrates were covered with denatured aptamer solutions, sealed, and incubated for different periods of time (1 hour, 3 hours, overnight), at room temperature for streptavidin-coated slides, or at 37°C for activated fused silica slides. After incubation, the slides were washed and dried. The best result for both substrates was achieved using binding buffer, aptamer concentration of 10 nmol/mL, denaturation at 90°C with gradual chilling, a fused silica substrate, and a 1-hour incubation time (Figure 2).

Tryptophan binding was measured using a spectrofluorimeter Spex Fluorolog Tau-3 (HORIBA Jobin Yvon, Inc.) or an LED-based setup in which the sample was excited by a 280 nm LED and detected by a filtered (340 nm) photon-counting PMT. Only a small peak from the expected fluorescence appeared in each experiment (Figure 3), indicating that the concentration of aptamers bound to the surface through this method is very small. Furthermore, as demonstrated in Figure 2, we have confirmed that binding is best when the conditions under which the aptamer was created are matched in the binding protocol. The binding buffer solution listed in the literature performed better than the PBS buffer often used for streptavidin/biotin protocol.

The marginal success of binding aptamers to a substrate indicates a need for further investigation. Steps for improvement include increasing the surface area for binding sites by using coated microspheres and nanoparticles, followed by deposition on a substrate via drop or spin casting. Fluorescence testing in solution prior to and following immobilization should be performed. All samples should then be tested using MALDI [matrix-assisted laser desorption/ionization] characterization.
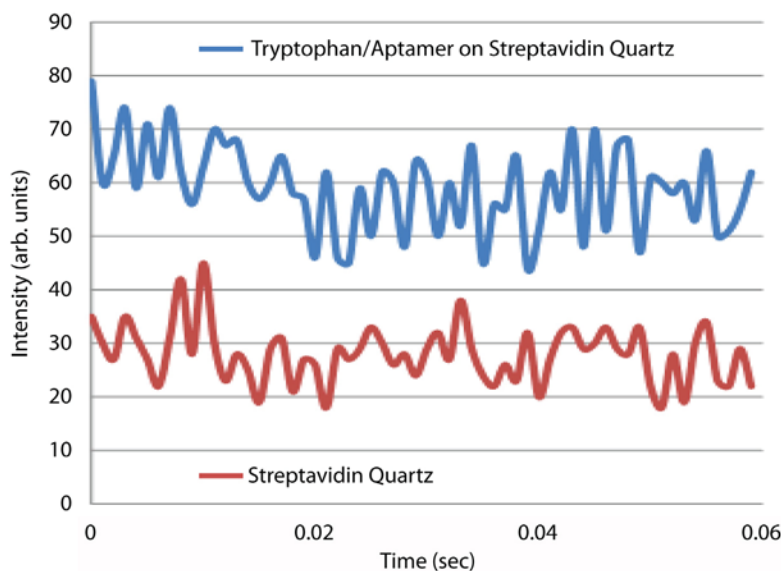

Figure 3. Fluorescence of 5'Biotin-Trp3a-1 on LED/photon-counting PMT setup with 280 nm excitation and a 340 nm emission filter. The signal is slightly above background.

In$_2$O$_3$ Nanoparticle–Based Detectors

In$_2$O$_3$ is a wide-band semiconductor material with documented band gap values of 2.9 eV. In order to ultimately create a microbial biosensor, the intrinsic fluorophore NADH and its corresponding emission (from 420 to 460 nm) must be detected. Our investigation of In$_2$O$_3$ follows a plan similar to that for ZnO material. Like ZnO, one prominent issue for In$_2$O$_3$ nanomaterials is the parasitic blue-green emission, which is due to oxygen vacancies. The material and device development process outlined below investigates: (1) surface states and how they affect photoresponse performance in two different In$_2$O$_3$ nanomaterials; (2) surface modification methods using polyvinyl-alcohol (PVA) on commercial In$_2$O$_3$ nanoparticles; (3) photoconductor device development on a quartz substrate; and (4) band-pass, wavelength-selective photodetector device development on a GaN substrate.

In$_2$O$_3$ nanorods were grown on silica substrates by using the self-catalytic vapor-liquid-solid growth process. Isolated nanorods were difficult to deposit onto any substrate; therefore, they were ground using mortar and pestle. After the grinding process, the nanorods were annealed in air at 1200°C for 2 to 6 hours to relieve the surface and bulk defects created by mechanical grinding. The photoresponse of the nanorods were compared to thin film, tin-doped indium oxide (ITO). The difference between thin films and nanostructures is exemplified in this study. A photoresponse is observed for the nano-structures but not for the thin film. The imperfection of In$_2$O$_3$ nanorods helps to form the Schottky contacts and creates an MSM photodetector with significant photoresponse. Schottky barrier heights are higher in nanostructures due to the surface defects inherent in nanostructures. When the barrier heights are lowered, as in the thin-film ITO, the dark current becomes large and dominates the total current even when they are under illumination by LEDs. The small photogenerated current is not noticeable compared to the large dark current. This work is fully described in detail in a study by Qin ("Photoresponse" 2011).

The enhancement effect of surface passivation on In$_2$O$_3$ using PVA was also demonstrated. Commercial In$_2$O$_3$ nanoparticles (US Research Nanomaterials, Inc.) with a purity of 99.995% and sizes ranging from 20 to 70 nm were used. They were divided into two batches. The first batch was dispersed in ethanol to form a 40 mg/mL suspension. The second batch was treated with PVA solutions (1% in weight in water), providing surface passivation. Then the PVA-coated In$_2$O$_3$ nanoparticles were centrifuged and dispersed in ethanol. The concentration of the suspension was also 40 mg/mL. These solutions were then spin-coated onto quartz plates and annealed in air at 120°C for 5 minutes. The PVA-coated and uncoated materials were characterized using photoluminescence (PL), absorption, and point-contact current and voltage measurements. The PL spectra (Figure 4b) demonstrate the enhancement of the UV-blue emission and suppression of the parasitic green emission. Furthermore, the absorption of PVA-coated nanoparticles is enhanced in the UV-blue region and the dark current is significantly reduced (figures not shown). These results are promising in developing a photodetector with high responsivity. The details of this study can be found in an article by Shao ("Optical" 2011).
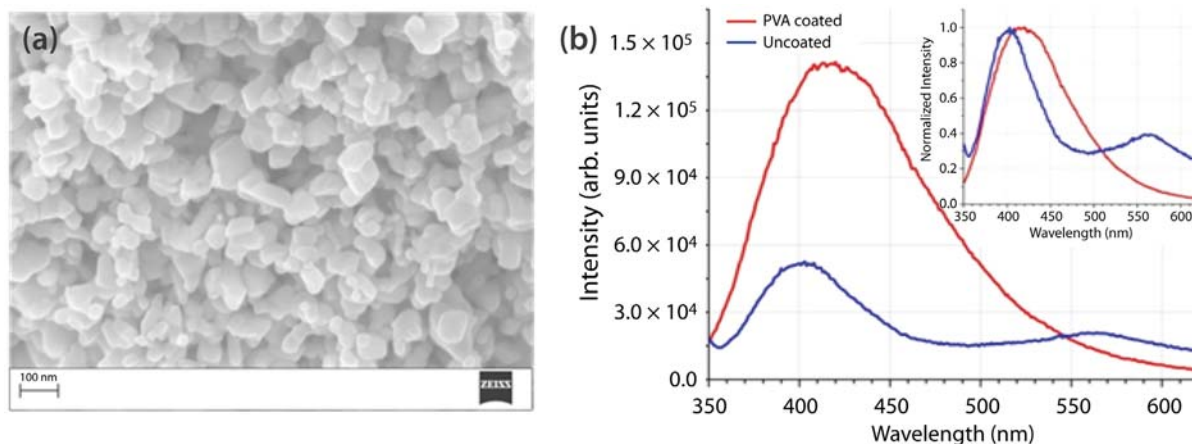
Figure 4. (a) High-resolution scanning electron microscope image of PVA-coated In$_2$O$_3$ nanoparticles. (b) PL spectra of In$_2$O$_3$ excited at 335 nm show enhanced UV-blue emission and suppressed green emission by PVA coating (the inset is the normalized spectra, from Shao "Optical" 2011).

An MSM photodetector and band-pass wavelength-selective photodetector (Figure 5) were created by depositing PVA-coated In$_2$O$_3$ nanoparticles on quartz and GaN substrates respectively (Shao "Bandpass" 2011, "Ultraviolet-blue" 2011). The responsivity of the device, defined as photocurrent per unit incident optical power, has been determined to be approximately 11 A/W at 340 nm and 9 A/W at 400 nm for the MSM photodetector. For the band-pass, GaN-based photodetector, the responsivity is 149 A/W at 340 nm and 97 A/W at 400 nm. In comparison, the responsivity for most commercial UV photodetectors is in the range of 0.1 to 0.2 A/W (Monroy 2003). However, there is a significant trade-off between responsivity and time response. The time response for each device is slow; commercial UV photodetectors have an ideal response on the order of ns, though ms are typical. The rise time (measured from 10% to 90%) and fall time (from 90% to 10%) for the PVA-coated In$_2$O$_3$ nanoparticle MSM photodetector are 500 and 1600 seconds, respectively. This is nearly half the time response of the same device with uncoated In$_2$O$_3$ nanoparticles (1100-second rise time and 3200-second fall time). The band-pass detector demonstrates rise and fall times of 700 and 1350 seconds, respectively.

Conclusion

The feasibility of using aptamers as biorecognition layers on a solid-state device was investigated. Surface immobilization on a substrate is a significant challenge, but marginal success was demonstrated after iterations of chemical protocol changes to temperature, buffer solutions, time, and concentration were made. The best result was achieved using a binding buffer, an aptamer concentration of 10 nmol/mL, denaturation at 90°C with gradual chilling, a fused silica substrate, and a 1-hour incubation time. A small fluorescence signal was detected by both a fluorimeter and LED-based setup. This research
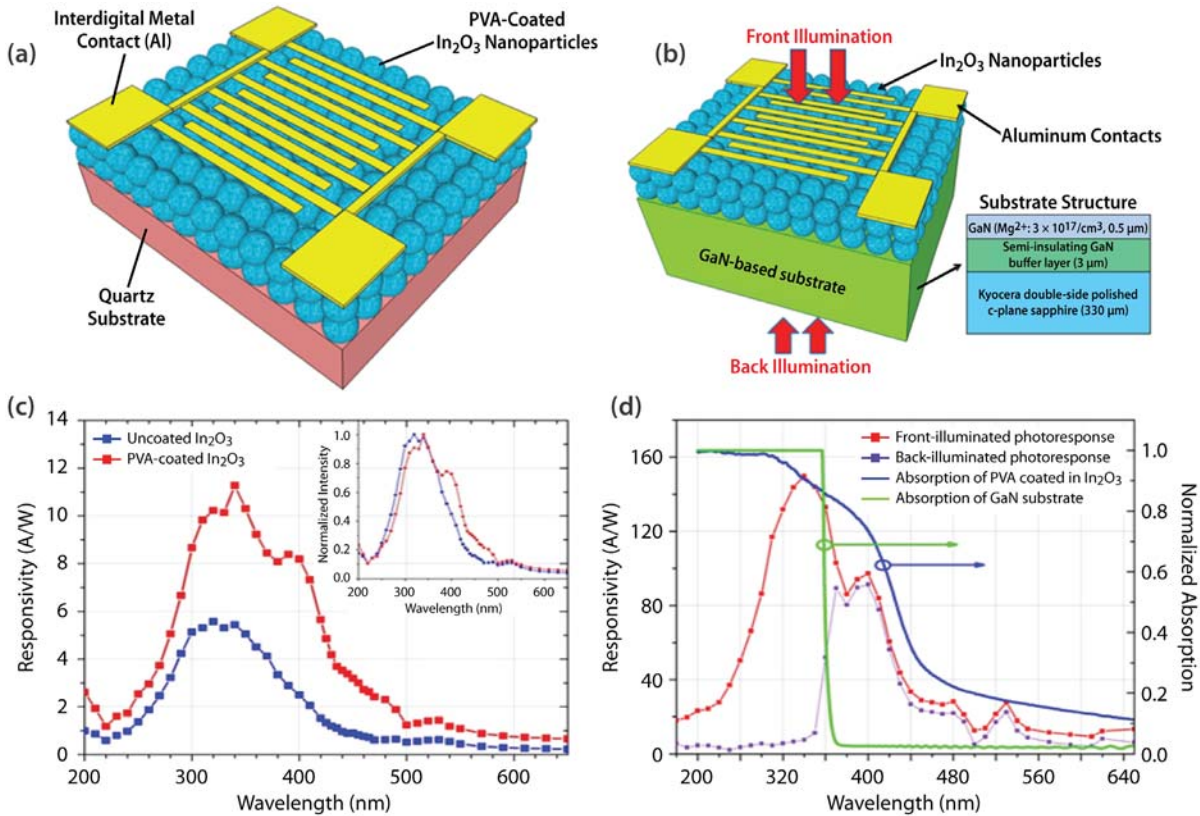
Figure 5. (a) Schematic of MSM photodetector fabricated from PVA-coated In$_2$O$_3$ nanoparticles on a quartz substrate; (b) schematic of band-pass UV-blue photodetector fabricated from PVA-coated In$_2$O$_3$ nanoparticles on top of GaN-based substrate; (c) photoresponse of MSM photodetector on a quartz substrate; and (d) band-pass photoresponse of PVA-coated In$_2$O$_3$ nanoparticles on a GaN-based substrate (Shao "Bandpass" 2011)

will continue in an FY 2012 SDRD project. Future work includes using streptavidin–coated glass beads to increase the fluorescence signal by increasing the surface area to which the aptamers can bind and adjusting the binding protocol binding of aptamers to In$_2$O$_3$ nanoparticles.

In$_2$O$_3$ nanomaterials were obtained, processed, and compared. PVA provided surface passivation that enhanced the UV-blue photoresponse, while suppressing the parasitic green response. While the responsivity of these devices is significantly higher than that of commercial devices, the time response is slow. Improvement in the time response through device structure modification is also a part of future work.

Acknowledgments

References

Bagalkot, V., L. Zhang, E. Levy-Nissenbaum, S. Jon, P. Kantoff, R. Langer, O. Farokhzad, "Quantum dot-aptamer conjugates for synchronous cancer imaging, therapy, and sensing of drug delivery based on bi-fluorescence resonance energy transfer," *Nano Lett.* **7**, 10 (September 2007) 3065–3070.

Bruno, J. G., J. L. Kiel, "In vitro selection of DNA aptamers to anthrax spores with electrochemiluminescence detection," *Biosensors and Bioelectronics* **14**, 5 (May 1999) 457–464.

Bruno, J. G., J. L. Kiel, "Use of magnetic beads in selection and detection of biotoxin aptamers by electrochemiluminescence and enzymatic methods," *Biotechniques* **32**, 1 (January 2002) 178–180.

Dollins, C. M., S. Nair, B. Sullenger, "Aptamers in immunotherapy," *Human Gene Therapy* **19**, 5 (May 2008) 443–450.

Ehrentreich-Forster, E., D. Orgel, A. Krause-Griep, B. Cech, V. Erdmann, F. Bier, F. Scheller, M. Rimmele, "Biosensor-based on-site explosives detection using aptamers as recognition elements," *Analytical and Bioanalytical Chemistry* **391**, 5 (May 2008) 1793–1800.

Ellington, A., J. Szostak, "In vitro selection of RNA molecules that bind specific ligands," *Nature* **346**, 6287 (August 1990) 818–822.

Gu, K., M. Famulok, "In vitro selection of aptamers against microcystin-LR," *Chinese Journal of Preventive Medicine* **38**, 6 (November 2004) 369–373.

Hamula, C., H. Zhang, L. Guan, X.-F. Li, X. Le, "Selection of aptamers against live bacterial cells," *Anal. Chem.* **80**, 20 (September 2008) 7812–7819.

Han, K., Z. Liang, N. Zhou, "Design strategies for aptamer-based biosensors," *Sensors* **10**, 5 (May 2010) 4541–4557.

Herr, J. K., J. E. Smith, C. D. Medley, D. Shangguan, W. Tan, "Aptamer-conjugated nanoparticles for selective collection and detection of cancer cells," *Anal. Chem.* **78**, 9 (March 2006) 2918–2924.

Irvine, D., C. Tuerk, L. Gold, "SELEXION: Systematic evolution of ligands by exponential enrichment with integrated optimization by non-linear analysis," *J. Mol. Biol.* **222**, 3 (December 1991) 739–761.

Kumar, P., K. Machida, P. Urvil, N. Kakiuchi, D. Vishnuvaradhan, K. Shimotohno, K. Taira, S. Nishikawa, "Isolation of RNA aptamer specific to the NS3 protein of hepatitis C virus from a pool of completely random RNA," *Virology* **237**, 2 (October 1997) 270–282.

Li, Y., H. Qi, Y. Peng, J. Yang, C. Zhang, "Electrogenerated chemiluminescence aptamer-based biosensor for the determination of cocaine," *Electrochemisty Communications* **9**, 10 (October 2007) 2571–2575.

Liu, J., Y. Lu, "Fast colorimetric sensing of adenosine and cocaine based on a general sensor design involving aptamers and nanoparticles," *Angewandte Chemie International Edition* **45**, 1 (November 2005) 90–94.

Lorsch, J., J. Szostak, "In vitro selection of RNA aptamers specific for cyanocobalamin," *Biochemistry* **33**, 4 (February 1994) 973–982.

Misono, T., P. K. Kumar, "Selection of RNA aptamers against human influenza virus hemagglutinin using surface plasmon resonance," *Anal. Biochem.* **342**, 2 (May 2005) 312–317.

Monroy, E., F. Omnés, F. Calle, "Wide-bandgap semiconductor ultraviolet photodetectors," *Semiconductor Science and Technology* **18**, 4 (March 2003) R33–R51.

Qin, L., C. Shing, S. Sawyer, "Comparison of UV optical properties of ZnO nanoparticles dispersed in traditional organic and novel bio-molecular solvents," *Phys. Status Solidi C* **7**, 10 (June 2010) 2463–2466.

Qin, L., C. Shing, S. Sawyer, "Metal-semiconductor-metal ultraviolet photodetectors based on zinc-oxide colloidal nanoparticles," *IEEE Electron Device Letters* **32**, 1 (December 2010) 51–53.

Qin, L., C. Shing, S. Sawyer, "Low-pass and band-pass alternative ultraviolet photoconductor based on zinc oxide nanoparticles on intrinsic gallium nitride-based substrate," *IEEE Photonic Device Letters* **23**, 7 (January 2011) 414–416.

Qin, L., S. Sawyer, P. Dutta, "Photoresponse of indium oxide particulate-based thin films fabricated using milled nanorods grown by the self-catalytic vapor-liquid-solid process," *Semiconductor Science and Technology* **27** (2011) 045005.

Que-Gewirth, N., B. Sullenger, "Gene therapy progress and prospects: RNA aptamers," *Gene Therapy* **14** (February 2007) 283–291.

Sawyer, S., L. Qin, C. Shing, "Zinc oxide nanoparticles for ultraviolet photodetection," *International Journal of High Speed Electronics and Systems* **20**, 1 (2011) 183–194.

Shao, D., L. Qin, S. Sawyer, "Optical properties of polyvinyl alcohol (PVA) coated In_2O_3 nanoparticles," *Optical Materials*, submitted (December 2011).

Shao, D., L. Qin, S. Sawyer, "Bandpass UV-violet photodetector based on PVA coated In_2O_3 nanoparticles on GaN based substrate," *IEEE Photonic Devices*, submitted (December 2011).

Shao, D., L. Qin, S. Sawyer, "Ultraviolet-blue photodetector fabricated from PVA coated In_2O_3 nanoparticles," *IEEE Electron Devices*, submitted (October 2011).

Smith, J. E., C. D. Medley, Z. Tang, D. Shangguan, C. Lofton, W. Tan, "Aptamer-conjugated nanoparticles for the collection and detection of multiple cancer cells," *Anal. Chem.* **79**, 8 (March 2007) 3075–3082.

So, H., D. Park, E. Jeon, Y. Kim, B. Kim, C. Lee, S. Choi, S. Kim, H. Chang, J. Lee, "Detection and titer estimation of *Escherichia Coli* using aptamer-functionalized single-walled carbon-nanotube field-effect transistors," *Small* **4**, 2 (February 2008) 197–201.

Song, S., L. Wang, J. Li, J. Zhao, C. Fan, "Aptamer-based biosensors," *Trends in Analytical Chemistry* **27**, 2 (February 2008) 108–117.

Tang, J., T. Yu, L. Guo, J. Xie, N. Shao, Z. He, "In vitro selection of DNA aptamer against abrin toxin and aptamer-based abrin direct detection," *Biosens. Bioelectron.* **22**, 11 (May 2007) 2456–2463.

Tombelli, S., M. Mununni, E. Luzi, M. Mascini, "Aptamer-based biosensors for the detection of HIV-1 Tat protein," *Bioelectrochemistry* **67**, 2 (October 2005) 135–141.

Wang, K.-Y., Y.-L. Zeng, X.-Y. Yang, W.-B. Li, X.-P. Lan, "Utility of aptamer-fluorescence in situ hybridization for rapid detection of *Pseudomonas aeruginosa*," *Eur. J. Clin. Microbiol. Infect. Dis.* **20**, 2 (October 2010) 273–278.

Yang, X., T. Bing, H. Mei, C. Fang, Z. Cao, D. Shangguan, "Characterization and application of DNA aptamer binding L-tryptophan," *Analyst* **136** (2011) 577–585.

Zhao, W., W. Chiuman, J. Lam, S. McManus, W. Chen, Y. Cui, R. Pelton, M. Brook, Y. Li, "DNA aptamer folding on gold nanoparticles: From colloid chemistry to biosensors," *J. Am. Chem. Soc.* **130**, 11 (February 2008) 3610–3618.

COMPACT ACCELERATOR WITH INTEGRAL, COAXIALLY COUPLED RF POWER

David D. Schwellenbach,[1,a] Al Meidinger,[a] Wendi Dreesen,[a] and James M. Potter[b]

Initial design studies have been performed on a new, advanced concept for an electron linear accelerator (linac) that integrates an electron gun, klystron, and linac into one resonant structure. This integrated device, or "klynac," will be capable of variable energy, pulse widths, and pulse repetition rates and can be coupled to various targets to produce high-energy photons or neutrons as required. The novel component of the klynac is a coupling cavity to simultaneously couple RF power and transport the electron beam. Coupling cavity designs were studied, and a cold model of a coupling cavity was constructed for RF studies. This investigation was driven by the continuing need for field-deployable, compact interrogation sources for detection of special nuclear material. The klynac concept is the first of its kind to have a complete electron gun, klystron, and accelerator in a single device.

Background

This novel concept for a compact linac system integrates the accelerator cavities, RF power source, klystron, and electron gun as a single device called a "klynac". By reducing the size, weight, and power consumption, this coupled design paves the way for an innovative *portable* accelerator system. Traditional linacs are based on using the accelerators in laboratory/industrial settings; typically these systems are designed to accommodate commercial RF power sources. A consequence of using commercial, off-the-shelf components is that parameters such as size, weight, and wall plug efficiency are defined primarily by the vendor rather than by the end user's requirements. Although advanced RF cavity designs have resulted in very compact accelerator cavities, supporting systems such as RF power, waveguides, and drive electronics can be at least an order of magnitude larger in size than the accelerator itself.

The klynac accelerator design is driven by its application and not by the availability of off-the-shelf components. Currently, linac development is limited to existing RF bands, thereby restricting the versatility of accelerator radiation production as shown in Figure 1. Using the klynac design approach, the RF frequency will be one of the independent parameters considered by the accelerator designer. Accelerator parameters such as energy, pulse width, and duty cycle can be easily changed and will be determined by the application.

As discussed in the "Special Nuclear Materials Movement Detection Program Radiation Sensor and Sources Roadmap" ("Special" 2009), photon and neutron sources are needed for interrogation of objects to scan for special nuclear material (SNM). The roadmap specifically calls for development of

[1] schweldd@nv.doe.gov, 505-663-2017
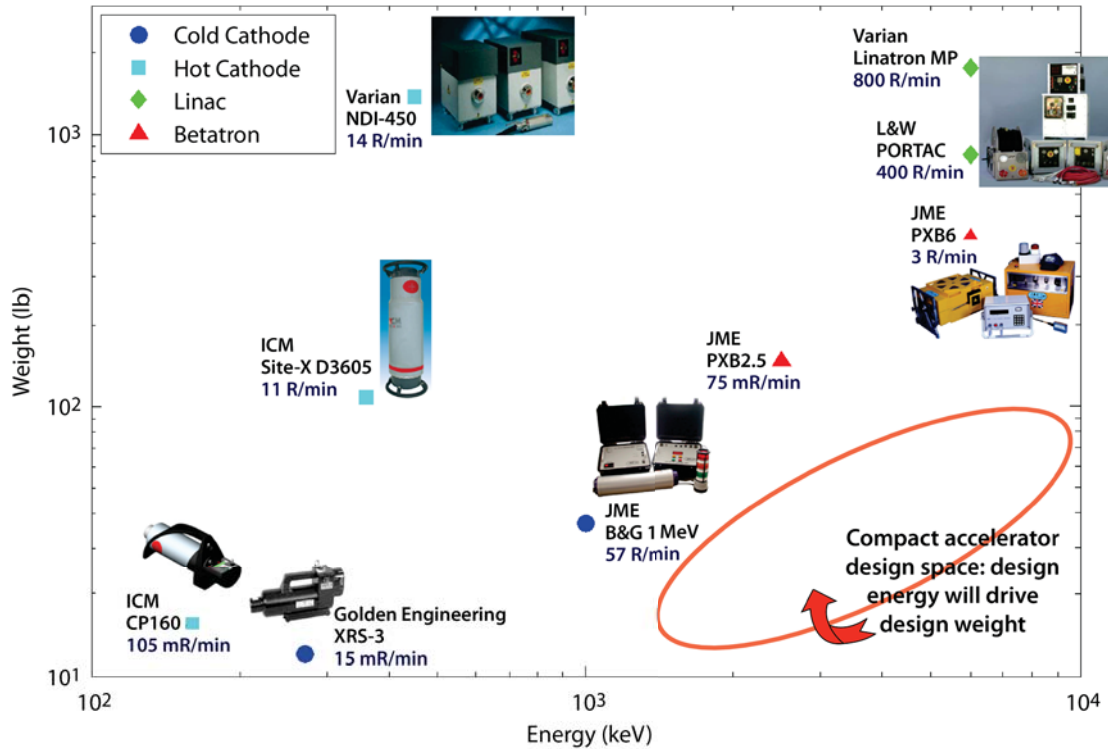[a] Los Alamos Operations; [b] J. P. Accelerator Works, Inc.

Figure 1. A weight vs energy comparison of currently available active interrogation sources with range of applicability of proposed klynac shown in the area circled

next-generation accelerator concepts and development of compact, mobile photon sources, both topics listed as high-priority and high-impact. In a more general sense, both portable and fixed systems are needed; both types of systems fit within our design envelope. The proposed integrated accelerator systems will be capable of variable energy and a wide range of pulse widths and pulse repetition rates. The roadmap also specifically calls for high-repetition-rate linacs (1–10 kHz) to increase photon flux compared to traditional linacs, allowing detection of both prompt and delayed signatures. The proposed design for compact electron accelerators will meet these needs and can be used as a source of photons independently of neutrons; alternatively, the same accelerator system can be a simultaneous source of neutrons and photons.

In the long term, developments in technology for compact accelerator systems will also have applications in areas outside of SNM detection. Pulsed, accelerator-based neutron sources can be used for time-of-flight spectroscopy and to reduce background noise by synchronizing detectors with the source. In addition, there is growing interest in replacing sealed radiological sources in industrial and medical fields, but stringent size and power constraints for these types of applications require advances in present accelerator technology. The technologies developed in this accelerator design study

can be adapted to replace sealed radiological sources in such applications, thereby reducing source inventories and consequently reducing the risk of sealed source theft and diversion for terrorist activities. The advanced capabilities of pulsed and variable energy radiation on a compact accelerator will also permit improvements in areas such as well logging and industrial radiography.

Project

The design concept for the coaxially coupled klynac, shown in Figure 2, directly couples the klystron RF source to the RF linac using a resonant coupling cavity. The cavity transports both RF power and the electron beam from the klystron to the linac. The beam is initially bunched in the first cavity of the klystron with additional bunching in the second cavity. RF power is extracted from the klystron output (third) cavity and delivered to the linac through the RF coupling cavity. The klystron is illustrated as a three-cavity device, but the final klystron design will depend on the end application.
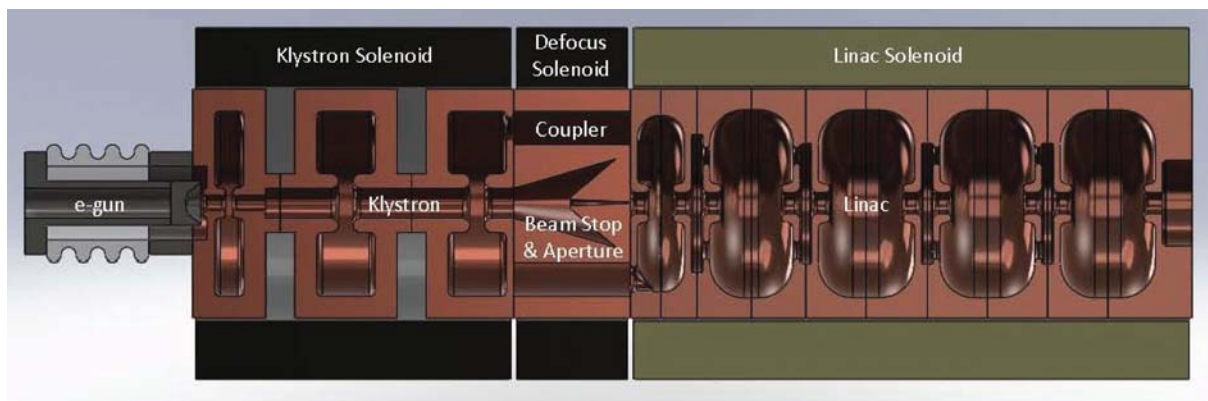

Figure 2. Klynac combined RF source and accelerator design concept

RF power is resonantly coupled from the klystron output cavity through a transverse electromagnetic (TEM)–mode coupler. A small fraction of the klystron beam is transported through the resonant coupler for injection into the accelerator section, thus eliminating the need for a separate cathode for the linac. If required, a positive feedback signal can be coupled from the accelerator back to the klystron input cavity to make the system self-oscillating. Because the klystron output cavity is resonantly coupled to the accelerator, the klystron could be configured as a discrete monotron oscillator (Carlsten 1996), eliminating the need for a separate RF feedback path.

The advantages of resonant coupling of accelerator structures are well established (Knapp 1968), but this technique has not been applied to an entire RF source/linac system. With resonant coupling the klystron output cavity will be designed as part of the accelerator resonant system. Because the entire system is designed as a coupled cavity resonator, the frequency will automatically be corrected with no tuning required to keep the linac at resonance with the klystron. Surrounding the coupler will be

a defocusing solenoid to disperse most of the klystron beam over the beam stop surface. The beam aperture and focusing system determine the fraction of the klystron beam entering the accelerator; the fraction of klystron beam passing through the coupler can be tuned using the solenoid. The geometry of the klystron output cavity and the accelerator input cavity are designed so that beam bunches decelerate in the klystron output cavity and then arrive at the first accelerator gap in time to be accelerated.

Resonant Coupler Design

The primary focus of this project was to verify the physics of a resonant coupling cavity that could simultaneously couple RF and the electron beam between a klystron and an accelerator section. Complete designs and performance data were available for an s-band linac through the design and commissioning of the NSTec Los Alamos Operations (LAO) linac (Bender 2008). Therefore, all designs in this study were performed in s-band in order to eliminate the need to independently redesign linac cavities. It is a straightforward process to scale basic linac and coupler designs in the future to include any RF frequency required for an application.

The coupler assembly design, shown in Figure 3, includes the first cavity of the LAO RF linac (half-cavity shown on the right) and an identical cavity emulating the output cavity of a klystron (half-cavity shown to the left). Ultimately a klystron design optimized for these applications needs to be devised, but showing that RF power can be resonantly coupled between spaced-apart accelerator/decelerator cavities is a sufficient demonstration for this project. Complete klystron designs are beyond the scope
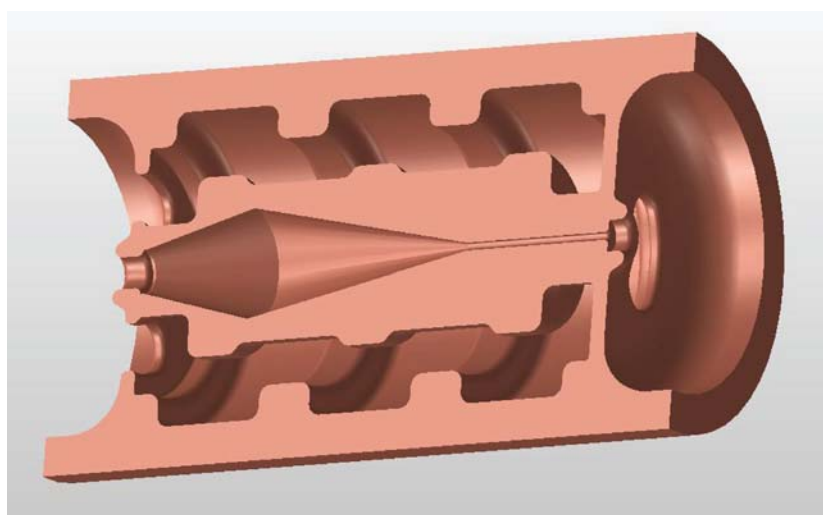

Figure 3. Preliminary design model of the klynac coupling cavity. Electron beam would enter from the klystron on left side of the model. It simultaneously couples RF power in phase with the electron beam to the first accelerator cavity on the right.

of this project. The RF power is coupled to the accelerator through a TEM-mode half-wave coupler. For the coupler to function as a true resonant coupler with zero power flow phase shift and with the amplitude and phase-locking characteristic of a resonant coupler, the coupler will have features designed to compensate for the self-inductance of the coupling slots.

This design provides resonant coupling between the klystron and the accelerator by maintaining the same resonant frequency for the coupler as the main mode of the accelerator. The coupler, shown in Figure 3, acts as a transmission line that is a resonator with a standing-wave pattern at the main mode frequency. Resonant coupling of the klystron and accelerator reduces sensitivity of the field distribution to tuning errors introduced by environmental factors such as temperature.

The coaxial TEM-mode coupler has two modes as shown by HFSS (3-D E&M software by Ansoft/ANSYS) simulations in Figure 4. The transmission mode corresponds to open-circuit boundary conditions while the coupling mode corresponds to short-circuit boundary conditions. The open-circuit transmission mode carries the RF power from the klystron to the accelerator. It must resonate at the accelerator frequency and have a length such that the decelerated electron bunch from the klystron arrives at the right time to be accelerated in the first accelerator cavity. Because there is no current flow at the open circuit ends, the inductive reactance of the slot has no effect on the frequency. The transmission mode was tuned by the addition of disks to the outer wall to add capacitive reactance at the voltage antinodes of an open-circuit resonance.

The coupling mode frequency, however, is affected in that the inductive reactance of the slots lowers the frequency because current is flowing at both ends. The design requires that the coupling frequency is initially above the transmission frequency. The transmission frequency is then lowered by adding disks to the inner wall, adding capacitive reactance at the voltage antinodes of the short-circuit mode. The tuning for both modes are interleaved since the elements for one mode's electric field are in the magnetic field region of the other mode. So lowering the frequency of one mode will slightly raise the frequency of the other. However, the electric field effect is dominant, and the tuning process quickly converges.

Cold Model Fabrication and Testing

Once the cavity coupler design had matured, it became clear that a full simulation of RF power and beam dynamics would require a comprehensive klystron modeling effort, which was beyond the scope of this project. To further the understanding of the coupling cavity, a cold model of the cavity was fabricated and tested. Complete RF characteristics of the system can be established using a cold model driven by low RF power. The cold model, shown in Figure 5, was used to verify and tune the RF properties of a resonant structure. Aluminum was used for construction (typically copper is used for high-power accelerator structures). All tests were performed at atmospheric pressure, instead of vacuum, the environment for an accelerator, and no electron beam was introduced.
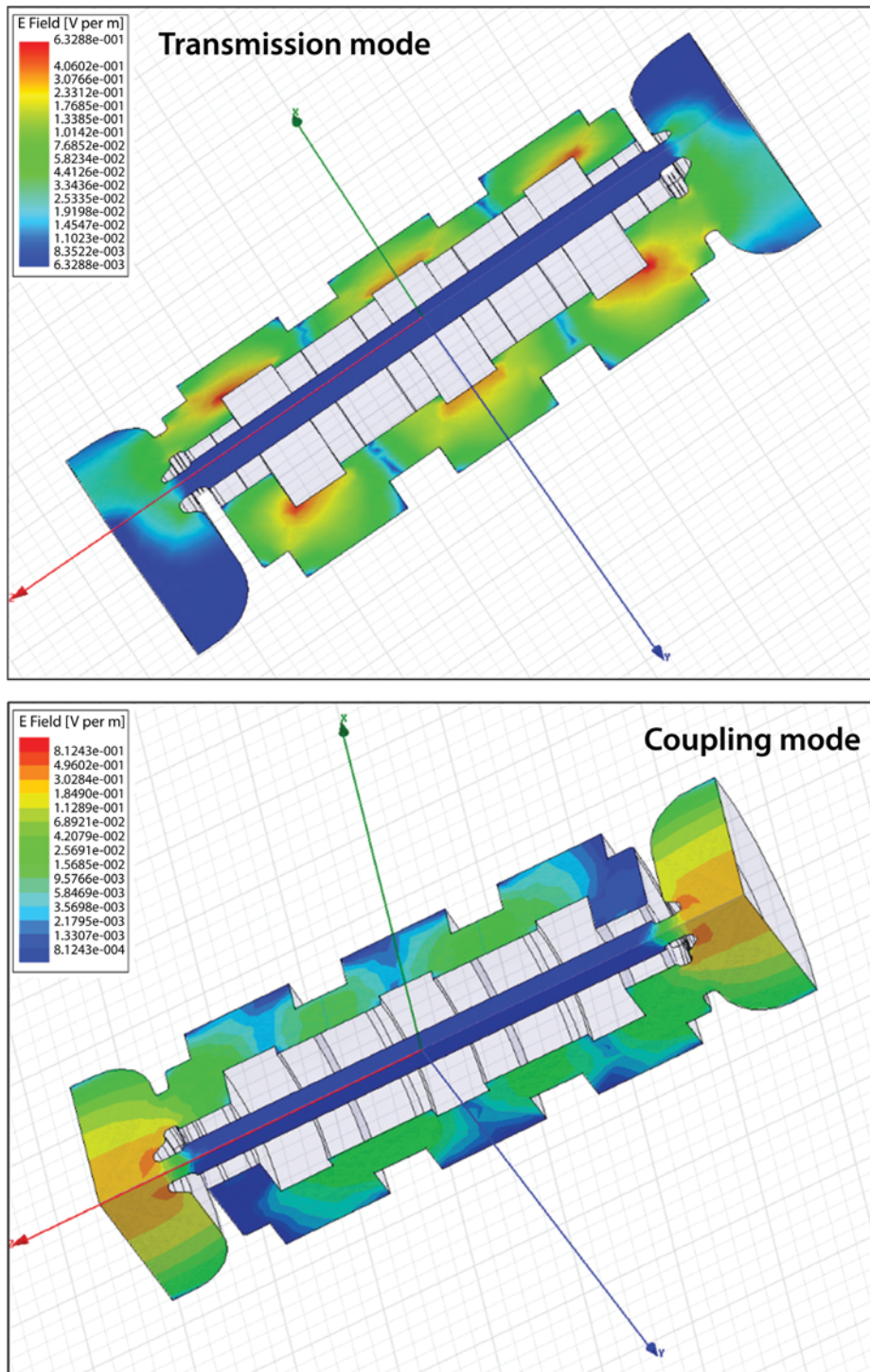
Figure 4. HFSS simulations showing (top) operating and (bottom) coupling modes of the resonant coupling cavity
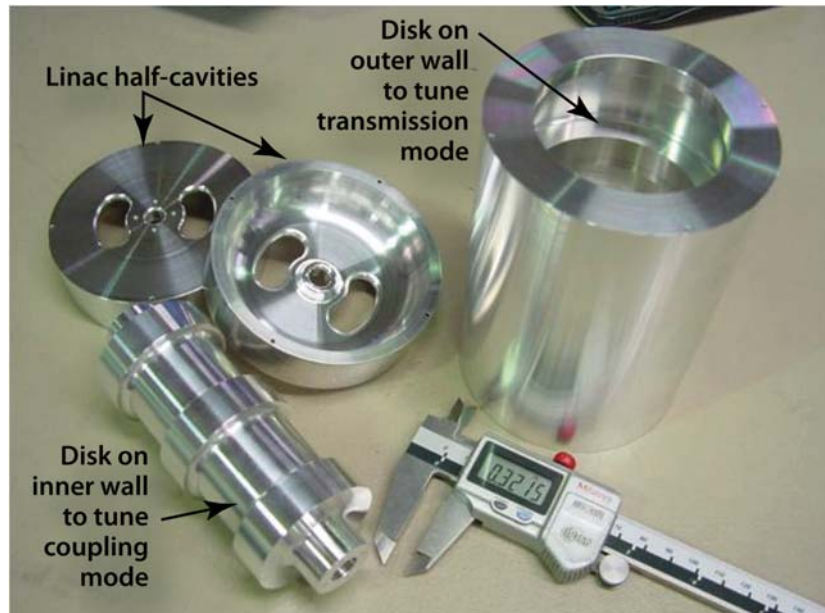
Figure 5. View of components of the cold model used for s-band RF testing. The components were clamped together in a coaxial geometry for testing.
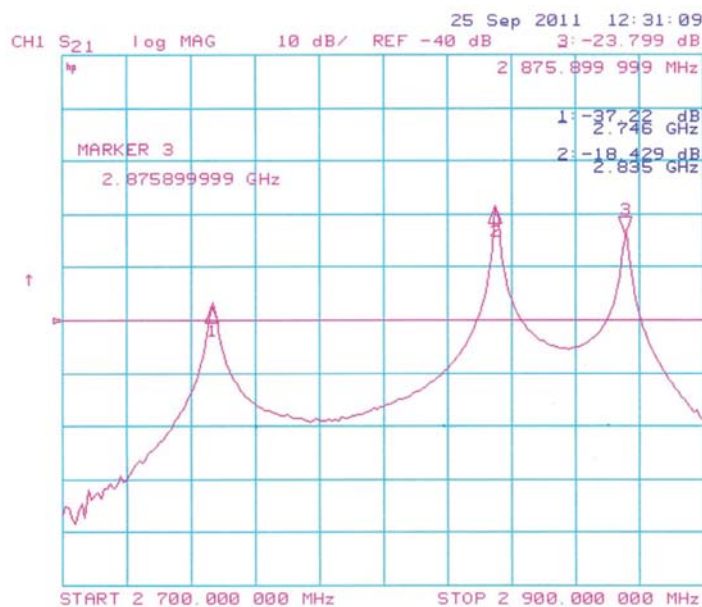

Figure 6. Preliminary test data from the cold model show that the coupling cell is initially tuned low in frequency as designed

In the demonstration case where there are two cavities that interact with the beam, i.e., the klystron output cavity and the accelerator input cavity, the mode spectrum will have three modes. The central mode is the operating mode. When the coupler is properly tuned, the operating frequency will be unchanged by the coupler, and the mode spectrum will be symmetrical.

Another indication that the coupler is tuned properly is that the open circuit mode of the model will have the same frequency as the operating mode. While this could be simulated in the HFSS calculations, there was no way to achieve a perfect open circuit boundary with a physical structure.

Figure 6 shows the initial mode, where both modes are deliberately tuned low in frequency. As the coupling mode frequency is raised, the lower mode will move up. The upper mode will also move up, but at a slower rate. When the mode spectrum is symmetrical, the structure is approximately tuned.

The correct tuning can be verified by the tilt sensitivity technique. When properly tuned, the amplitude ratio of the two end cells is independent of their relative tuning.

Conclusion

The goal of the project was to develop designs for resonant couplers relevant for application to a klynac accelerator and to simulate the performance. A resonant coupler was designed that meets all of the requirements for an s-band accelerator. Scaling this design to any other frequency is straightforward. Beyond design and simulation, a cold model of the resonant coupler was fabricated and tested. The resonant coupler is the innovation necessary to ultimately design and build a klynac, which consists of an electron gun, klystron, and linac built as one resonant structure. This study gives high confidence that an integrated system can be built. However, significant engineering remains to be done: a klystron must be designed that is matched to the resonant coupler, and beam dynamics on the klystron/coupler must be performed in order to predict linac performance and refine the final design. Ultimately, a modulator and other electronics must be designed in order to minimize the overall size and weight of the system. Follow-on proposals have been submitted to interested parties to complete the full-scale engineering and development.

Acknowledgments

References

Bender, H., D. D. Schwellenbach, R. Sturges, J. M. Potter, C. P. Trainham, "Variable energy 2-MeV S-band linac for x-ray and other applications," 11th European Particle Accelerator Conference, Genoa, Italy (2008) 1845–1847.

Carlsten, B. E., W. B. Haynes, "Discrete monotron oscillator," *IEEE Trans. Plasma Science* **24** (1996) 1249–1258.

Knapp, E. A., B. C. Knapp, J. M. Potter, "Standing wave high energy linear accelerator structures," *Rev. Sci. Instrum.* **39** (1968) 979–991.

"Special Nuclear Materials Movement Detection Program Radiation Sensors and Sources Roadmap," Office of Nonproliferation and Verification Research and Development (NA-22), NA22-OPD-01-2010, October 2009.

this page intentionally left blank

Passive Imaging of Warhead-Like Configurations with Cosmic-Ray Muon Tracking Scanners

David D. Schwellenbach,[1,a] Derek Aberle,[b] Jeffrey Bacon,[c] Konstantin N. Borozdin,[c] Wendi Dreesen,[a] J. Andrew Green,[a] Steven Greene,[c] George Glen McDuff,[b] Edward C. Milner,[c] Christopher Morris,[c] John Perry,[c] and Michael Sossong[d]

Experiments to develop an imaging system for warheads or warhead-like configurations based on cosmic-ray muon counting and tracking along with gamma and neutron measurement capability were conducted. The proposed technology offers an innovative, efficient, portable, robust, and inexpensive solution as a passive imaging system. The technology has been proven for the detection of dense materials in cargo container configurations. The project reconfigured an existing system and developed algorithms specifically to scan for special nuclear material in deployed configurations for applications such as treaty verification.

Background

A new, passive imaging technology has been developed by Los Alamos National Laboratory (LANL) and commercially by Decision Sciences International Corporation (Decision Sciences) that utilizes cosmic-ray muons to detect special nuclear material (SNM) in shielded configurations such as cargo containers. This project has adapted passive imaging to develop warhead monitoring and treaty verification applications. High-energy protons bombarding our atmosphere shower down in the atmosphere, decaying into many different particles, including muons (Figure 1). At sea level the muon flux is approximately 10,000/min/m^2. Their mean energy is about 3 GeV, which means they have an effective lifetime of $\gamma\tau = (28) \times (2.2~\mu s) = 61.6~\mu s$. At this energy muons can penetrate approximately 19 meters of iron, 15 meters of water, or 12.5 kilometers of air. The distribution of these particles is roughly $\cos^2(\theta)$, θ from zenith, with 55% of the muons positively charged (μ^+) and 45% negatively charged (μ^-). A muon's properties make it a great candidate for passive imaging for several reasons. Muons are similar to electrons but 200 times the mass (m_μ = 105 MeV). Unlike protons and neutrons, muons are subject only to weak and electromagnetic forces. The decay of a muon is described as $\mu^+ \rightarrow e^+ + \upsilon_e + \upsilon_\mu$ with a lifetime of τ = 2.2 μs at rest. At higher energies, the muon is highly penetrating through matter because of its high mass. When muons replace electrons in an atom, muonic atoms are generated, resulting in high-energy x-rays. Muon-induced fission is an event that occurs when a negatively charged (μ^-) muon is captured by the nucleus of an atom; these negatively charged muons were of great interest in this project.
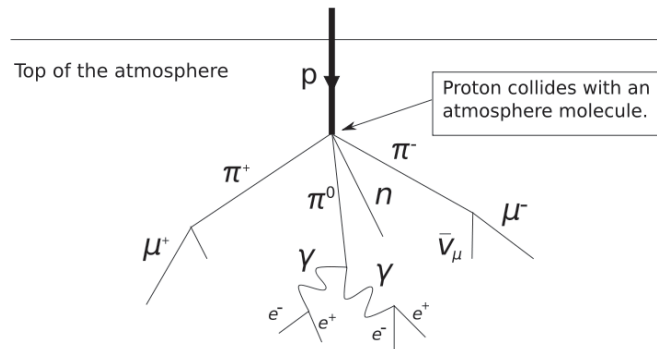
Figure 1. Decay tree for an inbound cosmic ray entering the atmosphere

In general, two modes of operation can be used for cosmic-ray muon tracking and imaging: tomographic and telescopic. Tomographic mode relies on multiple coulomb scattering, and has been shown to detect and image high-Z material in shielded configurations. Tomographic mode requires detectors above and below the object of interest, since it relies on tracking of incoming and outgoing scattered muons. Recent proof-of-concept experiments indicate (Borozdin 2010) that high-Z materials can be located using single-sided imaging (telescopic mode) by combining muon and secondary particle detectors. By developing the telescopic mode of muon imaging, advanced sensors can be developed for warhead monitoring and standoff detection applications. Telescopic mode tracks the incoming muons that are seen in coincidence with gamma rays or neutrons, which are a signature of the muon-induced fission. Because of this ability, the telescopic mode can be very sensitive to SNM, and requires only single-sided detectors.

The New START treaty limits the Russian and U.S. nuclear arsenals to a maximum of 1550 nuclear warheads, down from the current ceiling of 2200. As allowable warhead levels decrease, the approach for the confirmation of warhead numbers becomes more important, dictating the development of new methods of warhead counting. The existing process for inspection is intrusive and requires considerable handling and protection of sensitive/classified material, while providing only limited inspector transparency; some handling is done out of sight of the inspectors. Future treaties will need an enhanced ability to monitor or count warheads; these requirements include minimal intrusiveness on operations; shareable technology; information barriers (intrinsic or built-in) that provide confidence to all parties that warheads are, in fact, being counted without revealing sensitive or classified information; and transparency and simplicity of data collection and processing methods so that no hidden weapons capabilities are possible. Systems that can count warheads in situ are particularly needed, whether deployed on launchers or bombers, or in storage containers at storage sites. X-ray radiography (Mozley 1990) and counting fast neutrons (Ewing 1990, Byrd 1992) have been proposed to address this need, as well as neutron (Zalyubovskii 1993) or gamma-ray interrogation. So far these methods have not been adopted as part of standard treaty verification protocol because they are too

invasive or unreliable in the presence of variable background signals. Muon tracking technology satisfies the requirements, as it is based on nonintrusive imaging of the warheads, enabling their reliable identification without any need for classified material exposure.

A prime candidate for the deployed use of telescopic mode is warhead counting on submarines as depicted in Figure 2. The penetrating properties of the muon particle enable the detector to acquire data from outside the vessel. A submarine can be inspected in dry dock or at sea; therefore, no intrusion into the vessel is required. Additional applications include vehicle-mounted detectors that could look for buried SNM or SNM hidden inside buildings, stored fuel rods that could be monitored outside of containment vessels or even externally to the storage facility, and transportation systems (ships, trains, and trucks) that could be monitored, without exposure or knowledge by the occupants, to detect movement of SNM. Only one-sided access to the object is required to identify fissile material, but two-sided access enables faster detection and higher-resolution imaging.
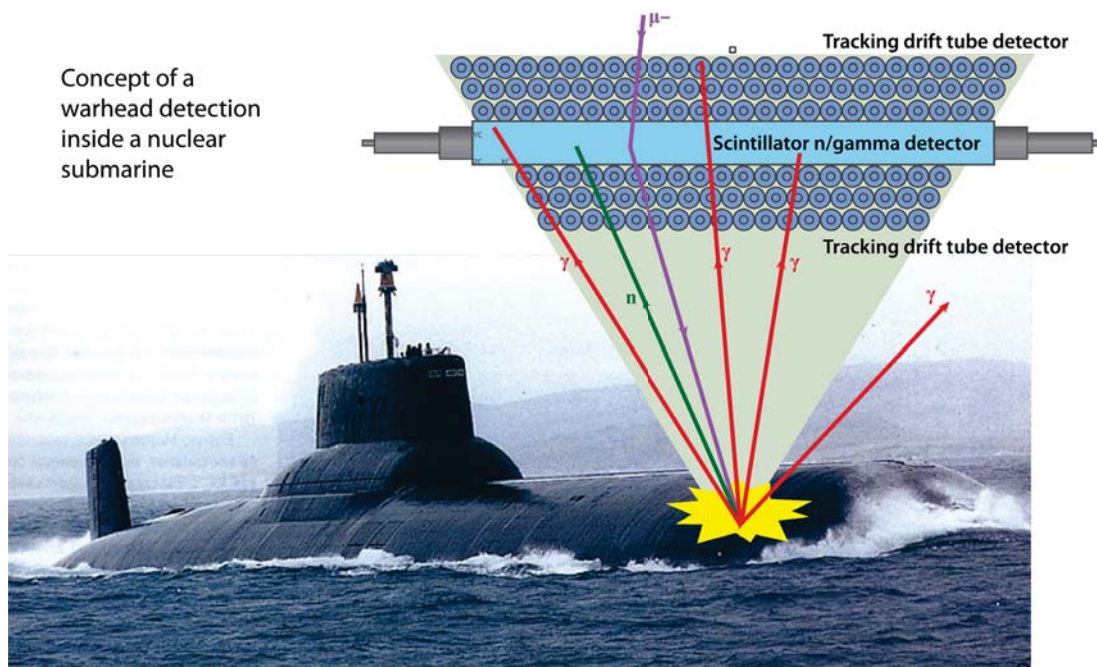

Figure 2. Conceptual design of telescopic mode application for warhead detection inside a nuclear submarine (based on Borozdin 2010)

Project

This project's goal was to prove concepts toward the development of advanced imaging systems using cosmic-ray muons designed for applications such as warhead monitoring and standoff detection. Muon tomography has been developed at Los Alamos National Laboratory (LANL) to address the

problem of nuclear smuggling (Borozdin 2003, Morris 2008). LANL has constructed several muon tracking detectors; the most recent one is the Mini Muon Tracker (MMT) shown in Figure 3, which was used in this project. The MMT's 24 planes of 4-foot long drift tubes track muons in x and y directions.
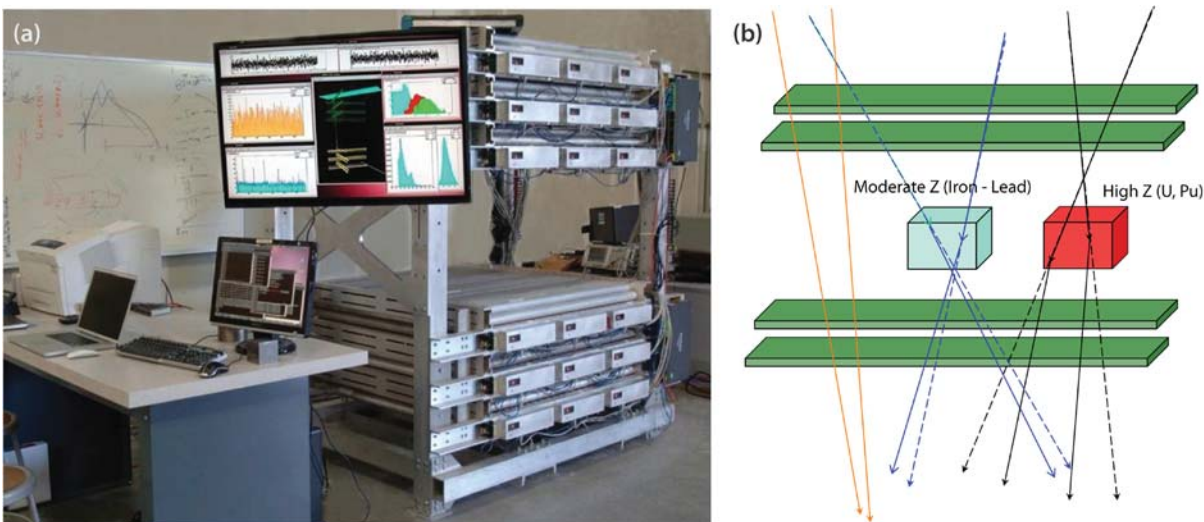

Figure 3. (a) The MMT as configured for these experiments, and (b) the muon track deflections are greater through higher Z materials. The MMT design calculates the deflections and infers the type of material under inspection.

Advancements in Tomographic Mode

In terms of material detection, the emphasis has been on categorizing materials to be low, medium, or high Z, where the latter is consistent with SNM or shielded SNM. Simple categorization of material shortens the scan time, which is important for applications such as monitoring a border crossing. Longer scan times give the additional data needed for warhead monitoring, allowing shape recognition through 3-D reconstructions based on the muon scattering angles through materials. For this project, we developed algorithms for rapid 3-D imaging of materials of interest. A representative test determined the sensitivity of muon imaging for quick detection. An empty lead spherical shell (8-inch outer diameter with 1.3-inch walls) was imaged for 1 minute; 2 kg of depleted uranium (DU) was then placed inside the lead shell and imaged. Figure 4a shows an image from 1 minute of tracked muon data for the empty sphere, and Figure 4b shows data for the same exposure time with DU inside the lead sphere. The colors indicate the degree of deflection (or "scattering density") of the muons, and allow quick detection of DU hidden by lead due to the higher Z of DU.
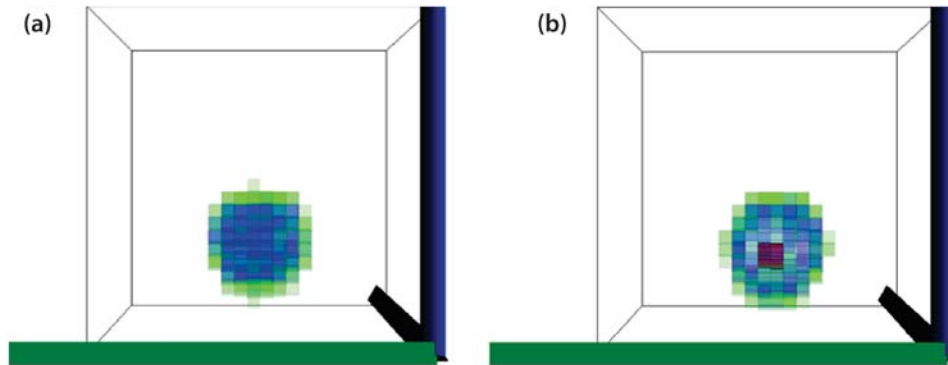
Figure 4. (a) One minute of tracked data for the empty lead sphere and (b) one minute of tracked data with DU inside lead sphere showing detected DU as dark red

It has been established (Morris 2011) that highly enriched uranium (HEU) can be hidden from most border portal monitors using the so called "DTRA [Defense Threat Reduction Agency] Box." The DTRA Box uses approximately 1 inch of lead around the suspect material with approximately 6 inches of polyethylene. A DTRA Box was constructed (Figure 5) to test the ability of muon technology to image through shielding and to define resolution limits. In as little as 1 minute of scanning, the presence of high-Z uranium was detected, and images with sufficient information to estimate size were available with tens of minutes of imaging. Representative images with an integration time of 75 minutes are shown in Figure 6.
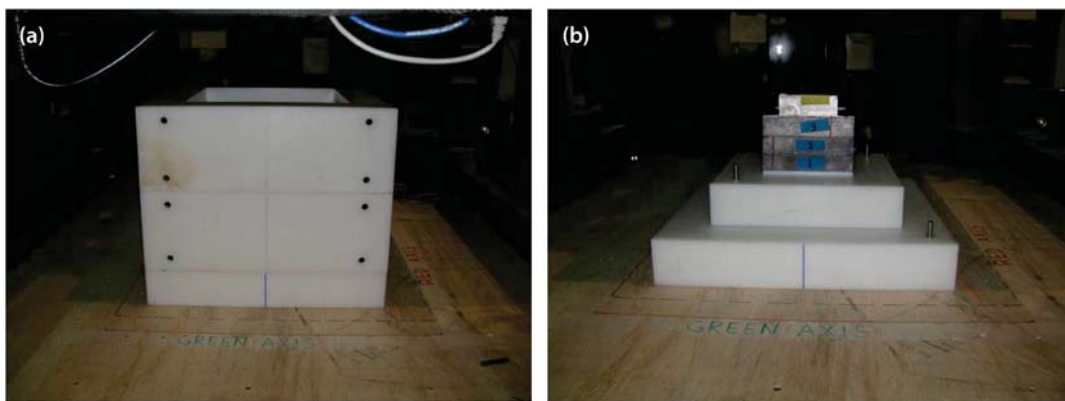

Figure 5. (a) An enclosed DTRA Box designed to hide and shield HEU from commercially available port detectors, and (b) contents of DTRA Box are a cube of DU, shown exposed here
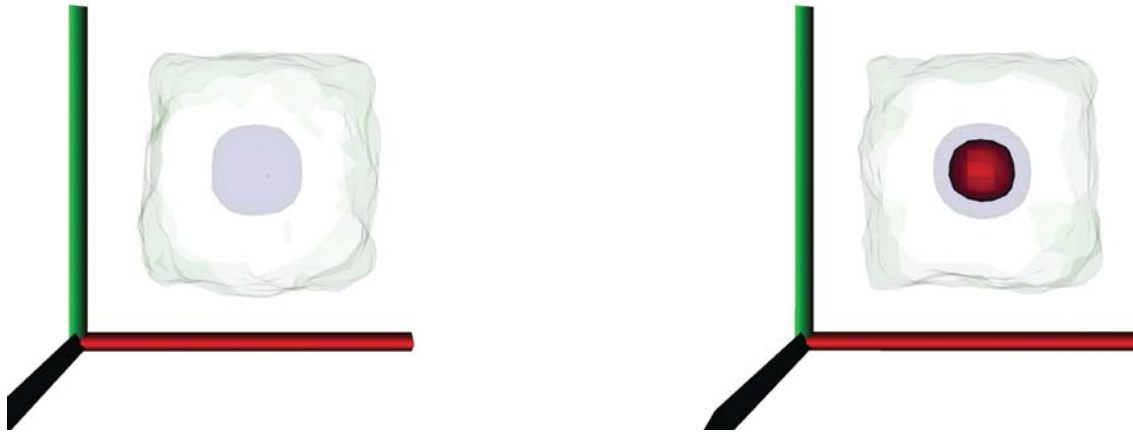
Figure 6. Images with 75 minutes of integration time for (left) an empty DTRA Box and (right) a DTRA Box concealing a 20 kg cube of DU

Telescopic Mode

In tomographic mode, the tracking system detects the muon path before and after it passes through the object. This mode is only possible when the scanned object can be placed between muon tracking detectors. This geometry provides the most expedient 3-D information available, but using this method is not always possible. Telescopic mode, however, tracks muons prior to interacting with the object while correlating with muon-induced fission neutrons or gammas in time coincidence. After several muon tracks produce coincident fission neutrons/gammas, sufficient information exists to locate a candidate parcel of SNM. Longer integration times will improve statistics and allow imaging of the SNM.

The concept of one-sided detection and warhead imaging for treaty verification was studied in this project. Earlier demonstration experiments (Borozdin 2010) showed time coincidence between cosmic-ray muons in the material and neutron/gamma detection (Figure 7), but no imaging was performed.

These early telescopic-mode experiments established that there was a signal to explore and that present muon tracking technology could be modified for this work. Experiments were limited in that they did not include object imaging or enrichment measurements, two components that are essential for successful demonstration of this technique for treaty verification. One of the basic requirements of the application is the ability to count warheads, which is only achievable with some form of imaging. Another requirement is the ability to distinguish between inert material, such as DU, and a weapon-grade material.
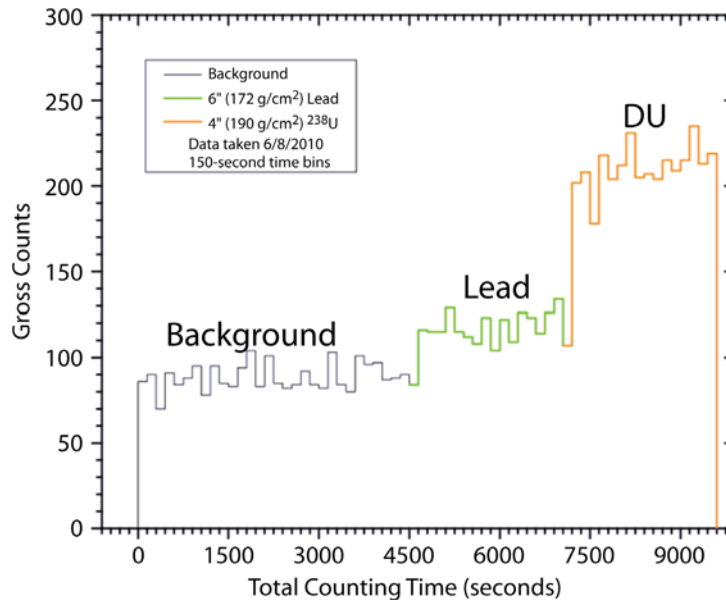
Figure 7. Telescopic mode demonstration experiments (Borozdin 2010) show coincidence signal between incoming cosmic rays and neutron/gamma signal. Presence of lead can be detected, and lead is clearly distinguished from uranium. Imaging was not attempted.

The MMT was modified to simultaneously track cosmic-ray muons into objects and detect muon-induced fission neutrons. Data were saved in event mode, which preserves geometric information along with a time stamp for all events. The data were post-processed using various time windows to generate telescopic mode images. These images were produced by correlating stopped tracks with neutrons. Stopped tracks are muons that are tracked into the scene from the top and are not detected in the bottom detectors. These muons were stopped in the vicinity of the object of interest and are candidates for inducing fission. Time correlations between stopped tracks and detected neutrons are shown in Figure 8. In the field, data from the bottom detectors would not be available; therefore, neutron statistics need to be improved to generate satisfactory images without relying on stopped track determinations. Using a time coincidence window determined by the results shown in Figure 8, images of a 10 × 10 × 10 cm cube of low-enriched uranium were taken using telescopic mode, as shown in Figure 9.

A low-efficiency neutron detector was used for these preliminary studies, but it clearly demonstrated that for detecting and imaging SNM, telescopic mode has promise.
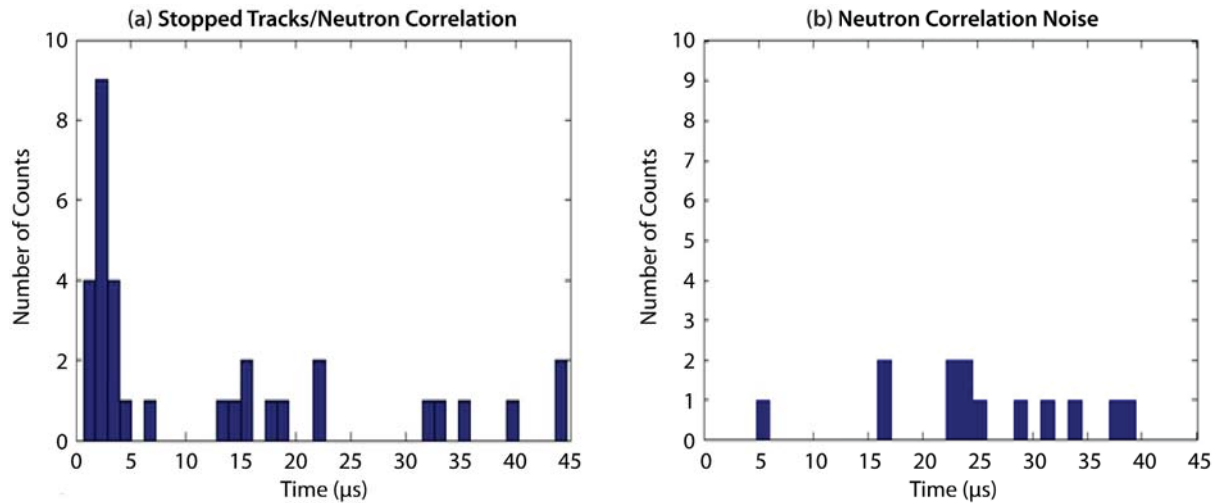
Figure 8. (a) Time correlation between stopped muons and detected neutrons and (b) background data obtained by shifting the time window by 1 second
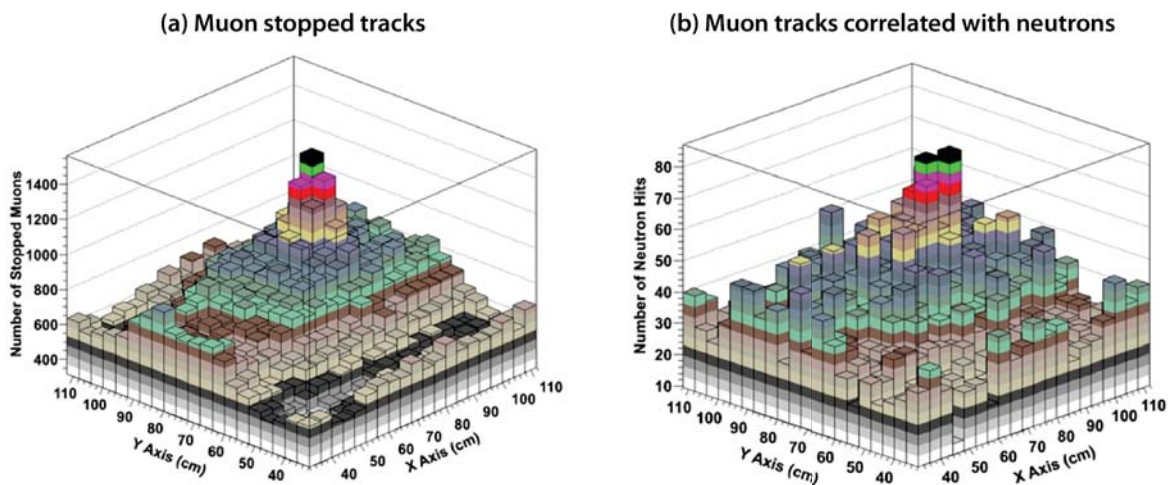

Figure 9. (a) A modification of tomographic mode was used to show stopped muon tracks, muons that were detected by the top bank of tubes but were missing in the bottom detector. Stopped muons have the potential to induce fission and be detected using telescopic mode. By correlating stopped tracks with detected neutrons the (b) object is clearly detected while details of its geometry are limited due to count rate.

Finally, this SDRD project explored the possibility of using an MMT-type device to image the melted core of the Fukushima reactor in Japan. The MMT was disassembled into two separate modules and placed in the upper right and lower left positions of the concrete masses shown in Figure 10a,

a mock-up of the reactor. Special calibrations were performed for the new configuration with separated modules, and data were collected in several multi-week runs. Long data collection times were required due to the low muon tracking rate in this geometry. Figure 10b shows the preliminary data indicating that areal density variations can be detected and imaged through significant shielding.
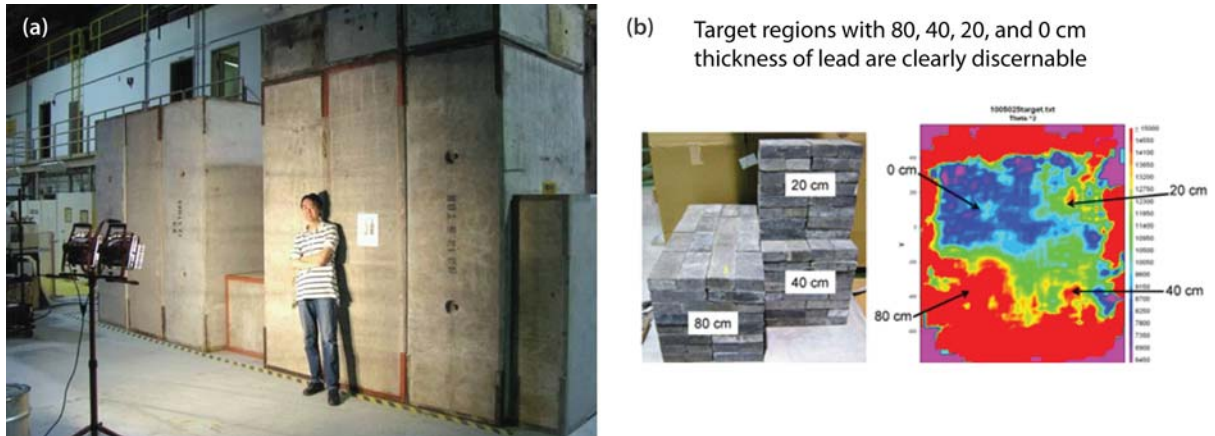

Figure 10. (a) An 18 ft concrete mock-up of the Fukushima reactor, and the (b) preliminary data from the experiment are shown color coded according to mean scattering angle through a region. Different depths of lead were used to emulate the expected areal density variation between shielding and fuel in a reactor configuration. The color coding shows that regions of differing areal density can be distinguished even through significant shielding.

Conclusion

There were three major accomplishments for the muon tracker project this year. The MMT was upgraded to allow for real-time imaging. The project established the first experiments with promising results demonstrating the validity of the telescopic mode. With higher efficiency detectors and future improvements to the software we believe more promise holds for this mode of operation. In addition, the project demonstrated the ability to detect and image threat objects in a highly shielded configuration with the so-called DTRA Box. Proposals to DTRA and NNSA have been submitted to expand this work toward construction of a fieldable warhead monitoring system.

Acknowledgments

We would like to thank Nick Wilcox for his efforts in reconfiguring the large-area neutron detector for use with the MMT.

References

Borozdin, K. N., G. E. Hogan, C. Morris, W. C. Priedhorsky, A. Saunders, L. J. Schultz, M. E. Teasdale, "Surveillance: Radiographic imaging with cosmic-ray muons," *Nature* **422** (2003) 277.

Borozdin, K. N., C. Morris, A. V. Klimenko, R. Spaulding, J. Bacon, "Passive imaging of SNM with cosmic-ray generated neutrons and gamma-rays," *2010 IEEE Nuclear Science Symposium Conference Record* **R05-70** (2010) 3864–3867.

Byrd, R. C., G. F. Auchampaugh, C. E. Moss, W. C. Feldman, "Warhead counting using neutron scintillators: Detector development, testing, and demonstration," *IEEE Trans. Nucl. Sci.* **39**, 4 (1992) 1051–1055.

Ewing, R. I., K. W. Marlow, "A fast-neutron detector used in verification of the INF Treaty," *Nucl. Instrum. Methods A* **299** (1990) 559–561.

Morris, C. L., C. C. Alexander, J. D. Bacon, K. N. Borozdin, D. J. Clark, R. Chartrand, C. J. Espinoza, A. M. Fraser, M. C. Galassi, J. A. Green, J. S. Gonzales, J. J. Gomez, N. W. Hengartner, G. E. Hogan, A. V. Klimenko, M. F. Makela, P. McGaughey, J. J. Medina, F. E. Pazuchanics, W. C. Priedhorsky, J. C. Ramsey, A. Saunders, R. C. Schirato, L. J. Schultz, M. J. Sossong, G. S. Blanpied, "Tomographic imaging with cosmic ray muons," *Science & Global Security* **16** (2008) 37–53.

Morris, C., "New Technology for Detecting Enriched Uranium in Cargo," Public Interest Report, Spring 2011, http://www.fas.org/pubs/pir/2011spring/Detect-Radiation.pdf, accessed June 15, 2011.

Mozley, R., "Verifying the number of warheads on multiple-warhead missiles through on-site inspections," *Science & Global Security* **1** (1990) 303–321.

Zalyubovskii, I. I., A. A. Lomako, O. N. Morgun, V. V. Chernyi, "Method for active remote detection of nuclear warheads," *Atomic Energy* **74**, 6 (1993) 464–467.

RADIATION-HARDENED SEMICONDUCTOR DETECTORS AND DETECTOR ARRAYS[†]

Ke-Xun (Kevin) Sun,[1,a] Anita Behnke,[a] and Rob Buckles[a]

A continued need exists for radiation-hardened (RadHard) detectors for many applications, including space missions and high radiation environments in nuclear experimentation. In this project, we built upon our previous work by examining RadHard AlGaN semiconductor devices and their performance. First, we developed two new types of RadHard AlGaN devices: photodiode arrays and a photodiode with a built-in calibration LED. Second, we successfully acquired, installed, and commissioned TOPAS (Traveling-Wave Optical Parametric Amplifier Light Source), a femtosecond, widely tunable optical parametric amplifier, emitting light from 190 to 20,000 nm. The TOPAS provides a powerful tool for temporal and spectral characterization of AlGaN optoelectronics devices. We also accomplished architectural studies for larger AlGaN detector arrays and CCDs, which has laid the groundwork for future work in high-energy density diagnostics.

Background

The need for radiation-hardened (RadHard) detectors, detector arrays, and imagers has become increasingly more important for many applications. In particular, the National Ignition Facility (NIF) can reach a neutron yield of up to 10^{15} per shot or even higher. There is evidence that neutron damage to diagnostic instrumentation occurs unambiguously, lowering image quality and causing diagnostic malfunctions at the 10^{14} neutron yield level. Sophisticated diagnostics are frequently moved out of the target chamber area to avoid damage, but this creates data blanks for high-yield experiments. To mitigate radiation effects, NIF is now planning to build "dog house" shields for diagnostics, with 5 tons of shielding materials for each banker. Complex x-ray optics are needed to route the signal beam to the diagnostics input. In addition, the neutron flux at 10^{15} per experiment can be seriously threatening to worker safety.

Since FY 2010, we have been conducting experimental demonstrations of the radiation hardness of the AlGaN photodetector up to a fluence of 3×10^{12} protons/cm^2. Our previous work on proton radiation hardness studies of AlGaN optoelectronics devices, UV LED and UV photodiodes (Sun 2006, UV LED 2009, "Space" 2009, "Radiation hardness" 2010, "GaN radiation" 2010, "Extreme" 2010, "Robust" 2010) led us to examine more specialized devices geared toward diagnostics to be fielded at NIF and other high flux environments. Because proton damage is typically more severe than neutron damage, this result may indicate higher neutron hardness of 10^{13}–10^{14} neutrons/cm^2,

which is equivalent to 1,000 ~ 10,000 high-yield experiments if the AlGaN detector is placed 1 meter away from the target chamber center. This could solve the radiation damage problems for NIF high-yield experiments, and even for future Laser Inertial Fusion Energy (LIFE) facility experiments, which will yield neutrons 2 to 3 orders of magnitude higher than NIF.

Project

Our FY 2011 SDRD project had several large components:

1. Development of RadHard AlGaN photodiode arrays

2. Development of RadHard AlGaN UV photodiode with built-in UV LED calibration source

3. RadHard AlGaN imager architectural studies

4. Acquisition, installation, and commission of TOPAS, a widely tunable femtosecond optical parametric amplifier (OPA), and associated safety compliances

5. Neutron test preparation

Development of RadHard AlGaN Photodiode Arrays

For the first demonstration device, we worked with the vendor to design and fabricate a 2 × 2 quadrant AlGaN photodiode array. The device design is based on our previous single AlGaN photodiode with similar quantum well structure (Sun 2011). The photodiode array is fabricated by scanning a large wafer and selecting a region containing four good photodiodes with the most uniform performance. The wire jump leads to external read-out electronics circuitry.

Figure 1 shows the device in two styles of packaging: TO3 and TO39, both containing a 2 × 2 AlGaN photodiode array. Ten-pin external connections are used for both packages. The chipset inside both the TO3 and TO39 packages is also shown in Figure 1. Each photodiode contains an active area of approximately 350 × 350 μm, excepting minimal device connection areas and wire bond shadows. The four photodiodes shown in Figure 1 have a common cathode connection, and four independent anode connections. In another batch, one had both a common anode connection and a common cathode connection for responsivity testing. Yet another batch had totally independent anode and cathode connections.

We initially thought the TO3 package with the larger window would be the preferred package for optical mounting, because of the larger base. However, the TO39-packaged 2 × 2 AlGaN photodiode array actually had more stable electrical performance thanks to the shorter wire jump distance to the leads and tighter shielding.
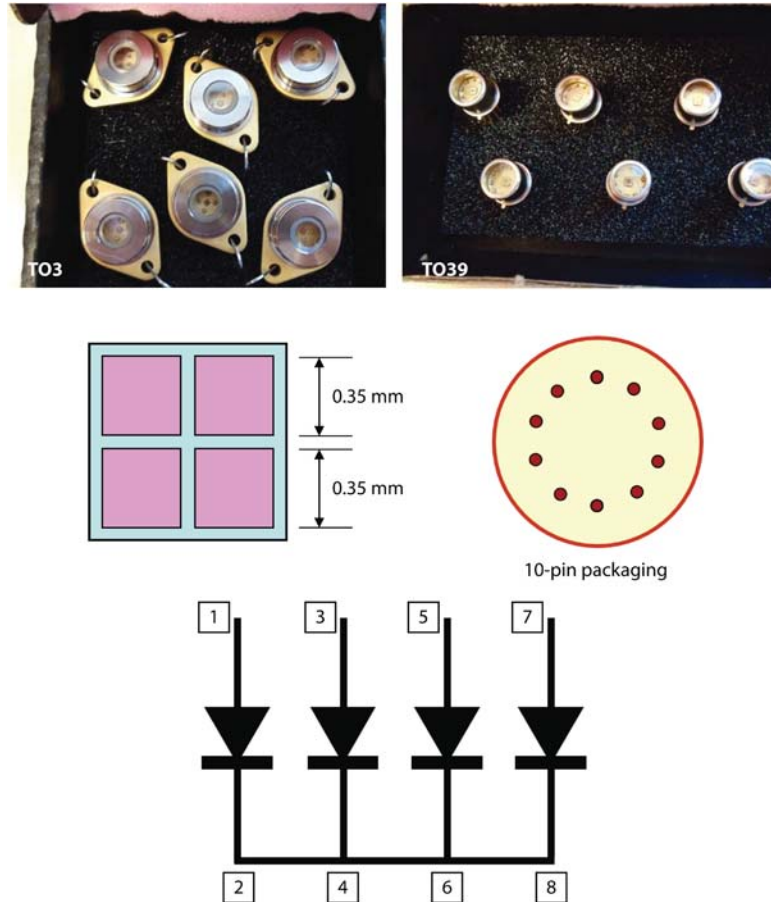
Figure 1. AlGaN 2 × 2 quad photodiode arrays. The top row shows the TO3 and TO39 packaging; the middle row, the photodiode array chipset layout and 10-pin package and connection; and the lower row, the pin connection diagram.

The central response wavelength of these photodiodes is at 255 nm, with ~15 nm bandwidth. The responsivity wavelength center and bandwidth are adjustable via proper design and fabrication techniques.

Development of RadHard AlGaN UV Photodiode with Built-In UV LED Calibration Source

Self-diagnostics and calibration are important to long-term operation of RadHard detectors. To accomplish this goal, we designed and fabricated a special package that contains an AlGaN photodiode, an AlGaN UV LED, and proper optics parts for light collection. The UV LED functions as a UV light source for the diagnostics and calibration of the UV photodiode.

Both the UV photodiode spectral responsivity and UV LED emission spectrum are centered at 255 nm, with a bandwidth of ~12 nm. Three new packing styles were developed for the integrated photodiode and UV LED: TO39 with a tall flat window, TO39 with a hemisphere lens (Figure 2), and flat ceramic packaging with surface mounting.
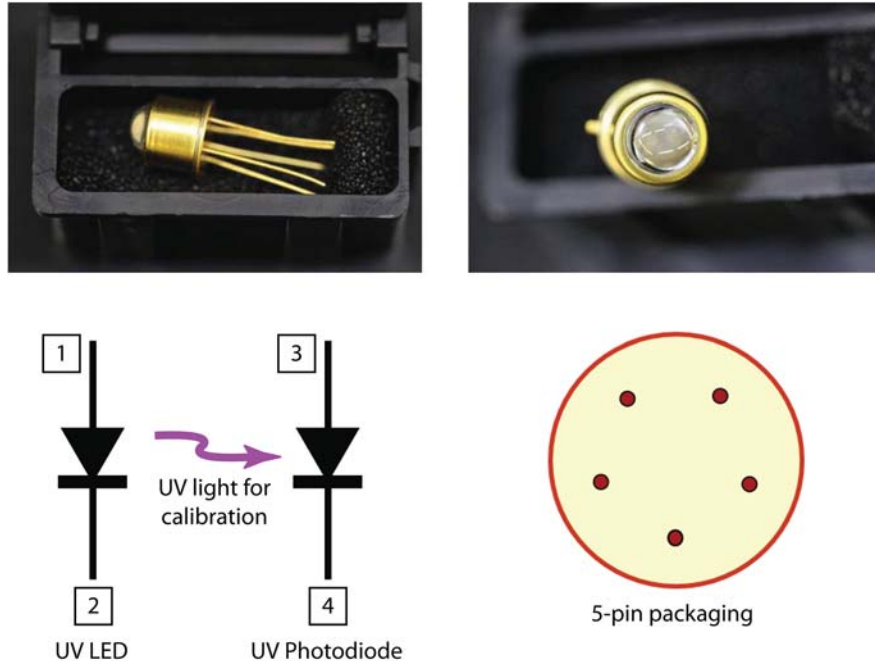

Figure 2. Special packaging containing both an AlGaN photodiode and an AlGaN UV LED. The top row shows a side and top view of the TO39 packaging, and the bottom row its functional schematic and pin connection.

Additional experiments have shown that these devices have exceptional mechanical and thermal stability; they survived rigorous environmental testing, including mechanical vibration and shock, and multiple extreme thermal cycles. These devices have passed NASA space qualification tests, and will be flown in a NASA-sponsored mission. The technology of integrating a single photodiode and a UV LED can be applied to AlGaN photodiode arrays to facilitate self-diagnostics and calibration functions.

RadHard AlGaN Imager Architecture Studies

An important goal is to eventually design and fabricate RadHard AlGaN and AlInGaN imagers. We studied the architectures for RadHard AlGaN imagers. Based on current technology availability, and future needs, we will design and fabricate three versions of RadHard imagers (Figure 3). The common task is to develop an AlGaN imaging layer composed of an AlGaN photodiode or charge collection well. Meanwhile, we will develop three versions of readout circuits following the plan below.

1. Develop AlGaN imager grown on sapphire structure or other bases with similar lattice constant. The interface circuits are routed outside at the rim. This is currently the most available technology.

2. Develop AlGaN imager grown on conventional silicon interface electronics. This configuration will have a fast interface bit rate. However, it is more complex, and the silicon interface circuit is a weak link in terms of radiation hardness.

3. Develop AlGaN imager grown on new AlGaN interface electronics. The advantage is much better radiation hardness thanks to the thorough AlGaN structure. However, AlGaN electronics interface electronics needs to be newly developed.

We are actively pursuing these areas and have made good progress in the FY 2012 SDRD project.
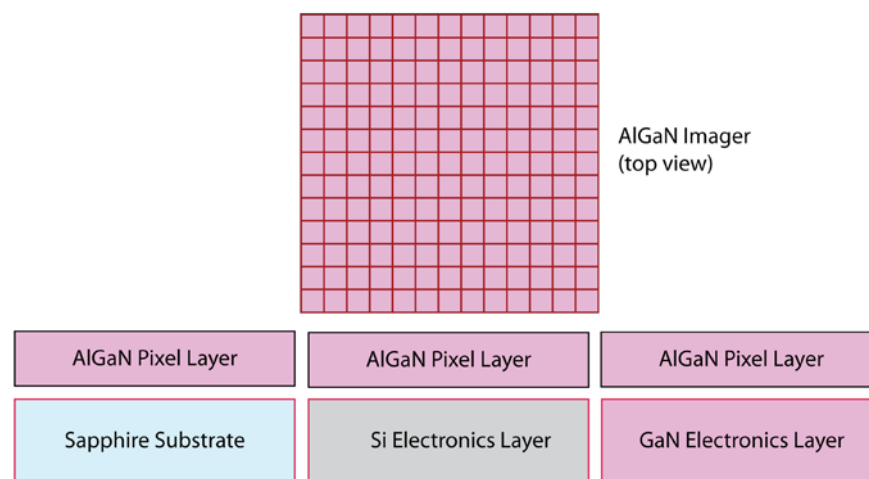

Figure 3. Three architectures for AlGaN imager and backplane. (left) AlGaN imager grown on sapphire; (center) AlGaN imager grown on Si electronics; (right) AlGaN imager grown on GaN electronics.

TOPAS—*Ultrafast Traveling-Wave Optical Parametric Amplifier of White-Light Continuum*

The SDRD program has heavily invested in TOPAS, a widely tunable OPA of white-light super continuum (Light Conversion "TOPAS," "Frequency," "Deep," 2009). An external femtosecond pump laser at ~800 nm is required. The most significant feature of TOPAS is its wide wavelength tunability. As shown in Figure 4, the TOPAS wavelength ranges from 190 to 20,000 nm, including many regions that are difficult to access by known lasers. The UV-C (100–280 nm) region and mid-IR (3–8 μm) region are important to security-related spectroscopy detection.
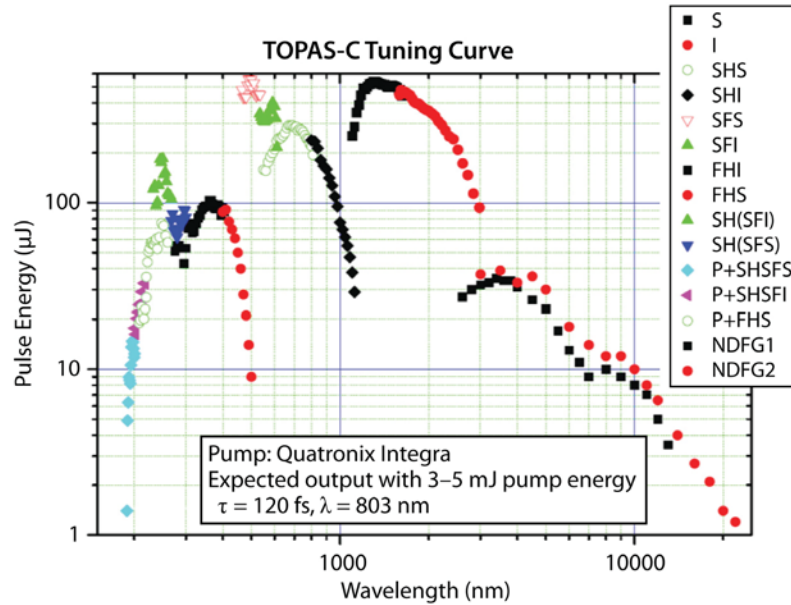
Figure 4. TOPAS output spectral range from 190 to 20,000 nm

The TOPAS wavelength tuning is computer controlled, either via GUI or programming scripts. Because TOPAS is a nonlinear optics device, its pulse width does not broaden relative to the pump pulse.

Figure 5 shows two examples of TOPAS wavelength tuning, recorded by an Ocean Optics CCD spectrometer. Figure 5 shows the TOPAS wavelength centered at (left) 255 nm and (right) 405 nm. The wavelength spread around the center is ~20 nm, consistent with the typical value of a mode-locked laser. TOPAS now can deliver these wavelengths easily.
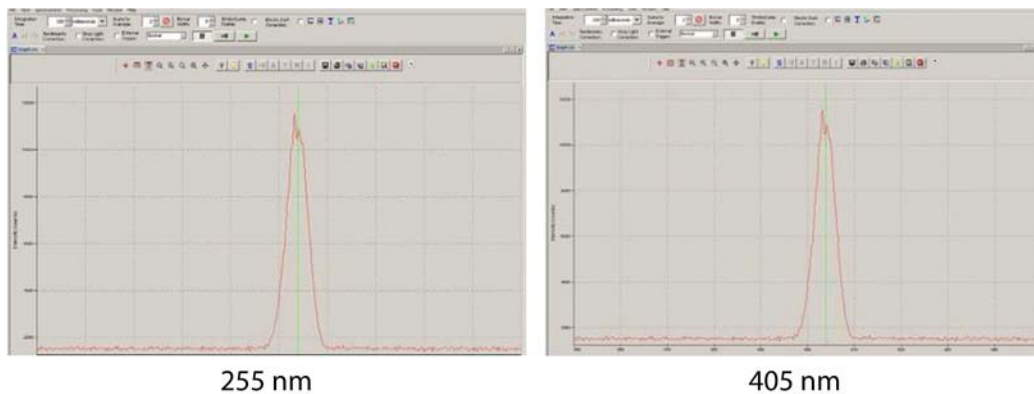

Figure 5. Spectrometer wavelength readout for TOPAS with output set to (left) 255 nm and (right) 405 nm. Spectrometer scale is 10 nm/div, and calibration is ±2 nm.

Figure 6 shows the TOPAS-C optics layout. TOPAS-C is the module directly pumped by the external femtosecond laser light. The pump beam first generates the white-light continuum in a piece of glass material. The white-light pulse is stretched by a dispersion element. By adjusting the matching time delay, a selected section of stretched pulse at a certain wavelength will be amplified by the OPA, thus generating the signal and idler beams. Output nonlinear optics mixers are used to mix the signal beam, the idler beam, and the transmitted pump beam to further generate wide ranging wavelength.
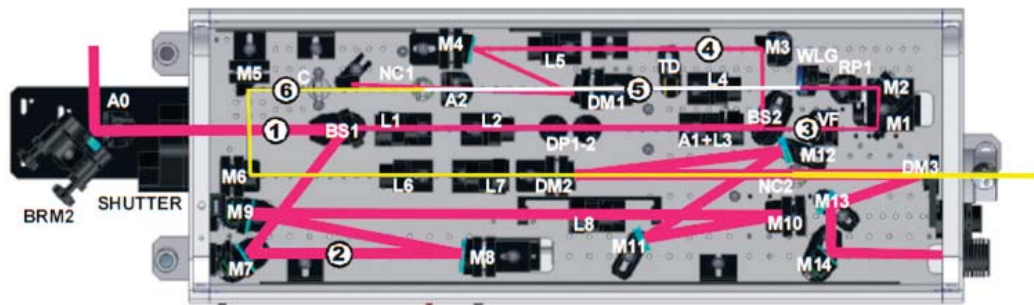

Figure 6. TOPAS-C optics layout. TOPAS-C is the module directly pumped by the external femtosecond laser light entering from A0, which first generates a white-light continuum. Tunable OPAs are used to achieve higher power. The output signal beam is shown by the yellow trace. All optomechanical mounts responsible for spectral tunability are computer controlled.

Figure 7 shows the TOPAS system as installed at NSTec Livermore Operations. Our TOPAS system is a full version of the commercially available TOPAS product family, with a full tuning range from 190 to 20,000 nm. Currently, we are using TOPAS for responsivity and temporal testing for fast-GaN photodiodes and photodiode arrays. The pump laser can deliver ~1 mJ per pulse of coherent energy, which is sufficient to commission TOPAS.

In addition, the TOPAS wavelength tuning is now achieved through mechanical position adjustment of the bulk mirror mounts. Use of electro-optical methods or micro-electro-mechanical systems devices can significantly accelerate the wavelength tuning rate, thus facilitating spectroscopy data-taking.

Neutron Test Preparation

We have made arrangements with the NSTec Dense Plasma Focus group and the Los Alamos Neutron Science Center for testing of neutron radiation hardness. The characterization tests before and after neutron irradiation will comprise electrical tests using a Keithley semiconductor parameter analyzer, transient electrical characteristics, optical spectral response, optical temporal response, and uniformity testing.

Figure 7. The TOPAS-C system as installed at Livermore Operations. Shown are the TOPAS-C, the mixer stage, the deep ultraviolet module, the delay line, and a corner of the pump laser.

Conclusion

In FY 2011, we accomplished several important tasks. First, we developed two types of new RadHard AlGaN devices: photodiode arrays and a RadHard photodiode with a built-in calibration LED. Second, we laid out the development path for RadHard AlGaN imagers. Third, we successfully acquired, installed, and commissioned TOPAS, which provides for temporal and spectral characterization of AlGaN optoelectronics devices. We also accomplished architectural studies for larger AlGaN detector arrays and CCDs. We have presented our research at several conferences, inspiring a surge of interest in AlGaN radiation hardness studies. This has laid the foundation for future growth in this area of research.

References

Light Conversion, *TOPAS-C Traveling-Wave Optical Parametric Amplifier of White–Light Continuum: User's Manual*, 2009.

Light Conversion, *Frequency Mixer Stages User's Manual*, 2009.

Light Conversion, *Deep UV Pulse Generator User's Manual*, 2009.

Sun K.-X., B. Allard, S. Buchman, S. Williams, R. L. Byer. "LED deep UV source for charge management for gravitational reference sensors," *Class. Quantum Grav.* **23** (2006) S141–S150.

Sun, K.-X., N. Leindecker, S. Higuchi, J. Goebel, S. Buchman, R. L. Byer, "UV LED operation lifetime and radiation hardness qualification for space flights," *J. Phys. Conf. Ser.* **154** (2009) 012028.

Sun, K.-X., N. Leindecker, J. Goebel, S. Buchman, R. Byer, "Space qualification for radiation hard UV LED," 3rd NASA EJSM Workshop, Applied Physics Lab, John Hopkins University, July 7–9, 2009.

Sun, K.-X., L. MacNeil, "Radiation hardness of AlGaN photodiodes," 4th NASA/ESA EJSM Workshop, Jet Propulsion Laboratory, July 26–29, 2010.

Sun, K.-X., L. MacNeil, "GaN radiation hard properties and detectors," SPIE Hard X-ray, Gamma Ray, and Neutron Detection, San Diego, August 1–5, 2010.

Sun, K.-X., L. MacNeil, K. Balakrishnan, E. Hultgren, J. Goebel, Y. Bilenko, J. Yang, W. Sun, M. Shatalov, X. Hu, R. Gaska, "Extreme radiation hardness and space qualification of AlGaN optoelectronic devices," International Workshop on Nitride Semiconductors 2010, Tampa, Florida, September 2010.

Sun, K.-X., "Robust, radiation hard AlGaN optoelectronic devices and their applications in physics research under extreme conditions," Physics and Astronomy Seminar at University of Nevada, Las Vegas, November 15, 2010.

Sun, K.-X., L. MacNeil, "Radiation-hardened wide-gap semiconductor detectors," *Nevada National Security Site–Directed Research and Development*, FY 2010, National Security Technologies, LLC, Las Vegas, Nevada, 2011, 97–104.

this page intentionally left blank

Laser Polar Nephelometer for Aerosol Studies[†]

Michael P. Taylor[1,a]

The ability to measure the concentration and size of suspended aerosol particles is crucial for reducing the threat of harmful particulate inhalation. This project addressed the challenges of making such measurements in real time with the use of a laser polar nephelometer. Presented here are the results of measurements taken with the laser polar nephelometer system. This instrument is capable of collecting high-resolution data on the order of several seconds. It has successfully quantified the light-scattering behavior of polystyrene latex (PSL) spheres as predicted by Mie theory. As such, the full Mueller matrix was accurately determined for 903 nm PSL spheres, laying the foundation for optical characterization of more complex systems.

Background

The monitoring of hazardous air pollutants is an area of increasing interest in a number of fields. Advances in techniques for in situ, real-time detection of aerosols have been driven by the concern over the health effects of airborne particulates, which vary with size, concentration, and chemical composition. Radioactive aerosols and industrial aerosols can cause disease and respiratory problems in the workplace and the environment (Willeke 1993, Pope 2006). Some airborne bacteria and viruses transmit infectious diseases and have been used as biowarfare agents. Fine particulates are of great concern; they can be inhaled deeply into the lungs and remain there indefinitely. The DOE is particularly interested in airborne beryllium (Be) particulates. Beryllium plays a major role in the production of nuclear weapons and has been extensively used by DOE since the 1940s. The major hazard associated with Be processing is the inhalation of Be aerosol particulates. Those exposed risk contracting chronic Be disease, an incurable, often debilitating, and sometimes fatal, lung condition. There is a need for improved methods for rapid detection and characterization of aerosols in both indoor and atmospheric environments (McMurry 2000).

This work continues the FY 2010 SDRD project of the same name (Taylor 2011). In FY 2011 we report measurements of all 16 elements of the Mueller matrix. The Mueller matrix completely describes the scattering properties of aerosol particulates as a function of scattering angle. This was accomplished with a laser polar nephelometer, which we developed, that measures the angular distribution of the intensity and polarization changes of light from a laser beam scattered by airborne particles. This instrument was designed to be an unattended unit, providing real-time, high-resolution data in a fraction of the time associated with most current systems (McMurry 2000).

---

[1] taylormp@nv.doe.gov, 301-817-3308
[a] Remote Sensing Laboratory–Andrews
[†] Project continued from FY 2010

Scattering Matrix

Light scattering is conveniently described by Mueller matrix algebra. The state of polarization of a beam of light along with its intensity can be described by the Stokes vector, $\mathbf{F} = \{I, Q, U, V\}$, where I = total intensity of light, $\langle E_l E_l^* + E_r E_r^* \rangle$; $Q = \pm 90°$ polarization, $\langle E_l E_l^* - E_r E_r^* \rangle$; $U = \pm 45°$ polarization, $\langle E_l E_r^* + E_r E_l^* \rangle$; V = circular polarization, $\langle i(E_l E_r^* - E_r E_l^*) \rangle$; and E_l and E_r are complex electric field vectors parallel and perpendicular to the scattering plane, respectively. When a beam of light is incident upon some obstruction, it scatters radiation in all directions, altering the intensity and, in most cases, the polarization state of the incident light. The efficiency of this scattering process depends on the physical and optical properties of the scatterer and therefore carries the signature of the scatterer. The effect of this scattering process can be represented by a 16-element Mueller matrix $\mathbf{M}$ that transforms the Stokes vector for incoming light to the vector representing scattered light (van de Hulst 1957) such that $\mathbf{F}_s = \mathbf{M}\mathbf{F}_i$:

$$\begin{pmatrix} I_s \\ Q_s \\ U_s \\ V_s \end{pmatrix} = \frac{1}{k^2 r^2} \begin{pmatrix} S_{11} & S_{12} & S_{13} & S_{14} \\ S_{21} & S_{22} & S_{23} & S_{24} \\ S_{31} & S_{32} & S_{33} & S_{34} \\ S_{41} & S_{42} & S_{43} & S_{44} \end{pmatrix} \begin{pmatrix} I_i \\ Q_i \\ U_i \\ V_i \end{pmatrix}.$$

(1)

The subscripts i and s refer to incident and scattered light; k is the wave vector, and r is the distance from the scatterer to the detector. The elements of $\mathbf{M}$ are functions of scattering angle and contain all the elastic light-scattering information available at a given wavelength. The Mueller matrix is determined by size, structure, symmetry, orientation, and the complex index of refraction of the scatterers.

In nearly all cases, symmetry reduces the number of independent elements in the scattering matrix. For a suspension of randomly oriented, arbitrarily sized particles with a plane of symmetry, the scattering matrix simplifies to

$$\mathbf{M} = \begin{matrix} S_{11} & S_{12} & 0 & 0 \\ S_{12} & S_{22} & 0 & 0 \\ 0 & 0 & S_{33} & S_{34} \\ 0 & 0 & -S_{34} & S_{44} \end{matrix}.$$

(2)

Furthermore, if the particles are spherically symmetric, $S_{11} = S_{22}$ and $S_{33} = S_{44}$. Other scattering media to which this applies include isotropic cylinders and ellipsoids of substances such as glass and cubic crystals. However, randomly oriented isotropic spheroids is an exactly soluble system for which Equation 2 applies (Asano 1980). In this case, scattering can be predicted by Mie theory. Each Mueller matrix element, for any scatterer, may be expressed as a θ-dependent intensity curve by the appropriate adjustment of various optical element combinations fore and aft of the scattering medium.

Measuring the normalized matrix elements is a more sensitive approach to characterizing scattering media. In this process, each matrix element, except S_{11}, is divided by S_{11} (Quinby-Hunt 1989) and displayed in bold: $\mathbf{S}_{ij} = S_{ij}/S_{11}$.

In this work, we experimentally determined the two elements, S_{11} and $\mathbf{S}_{12}$ (the normalized S_{12} element), of the Mueller matrix. S_{11} is simply the total intensity as a function of scattering angle for unpolarized incident light. This matrix element, also referred to as the scattering phase function, provides information on particle size and is obtained from

$$I = I_\perp + I_\parallel,$$
(3)

where $I_\perp$ and $I_\parallel$ are scattered light intensities perpendicular and parallel to the scattering plane, respectively. $\mathbf{S}_{12}$, the ratio of the S_{12} and S_{11} elements, provides information on the degree of polarization and is given by

$$P = \mathbf{S}_{12} = -S_{12}/S_{11} = \frac{I_\perp - I_\parallel}{I_\perp + I_\parallel}.$$
(4)

Polarization is an important quantity to exploit. With it, we can determine the particle's degree of sphericity and whether the particle is an oblate or prolate spheroid or cube, or some other irregular shape.

Project

Optical Design and Experimental Arrangement

Figure 1 shows a schematic of the optimized nephelometer system. The scattering volume is located at the first focus of an ellipsoidal reflector (Opti-forms, Inc., Temecula, CA); the optical system treats this volume as an aperture stop in order to collect data by angle. Light is scattered from the beam within the scattering volume into a range of polar angles. Scattered light is reflected off the sides of the reflector towards the ellipse's second focus. Polarizing and analyzing components are placed fore and aft the scattering medium, respectively, for the purpose of producing the appropriate Mueller matrix elements. Additional lenses are necessary to (1) remove the extreme field curvature created by the reflector; (2) collimate the light in an area with small angular extent, for the introduction of a polarization analyzer; and (3) bring the light to a focus on a camera imaging array. The optics image the scattered light such that various positions on the imaging array correspond to light scattered at a given angle in 3-D space.

Polystyrene latex (PSL) spheres in distilled water were aerosolized with a constant output aerosol generator (TSI, Inc., Model 3079), and the resulting flow was passed through a silica gel diffusion dryer (TSI, Inc., Model 3062) that dried the aerosol and removed water vapor from the flow before it was passed through conductive tubing and directed through an aperture at the vertex of the reflector.
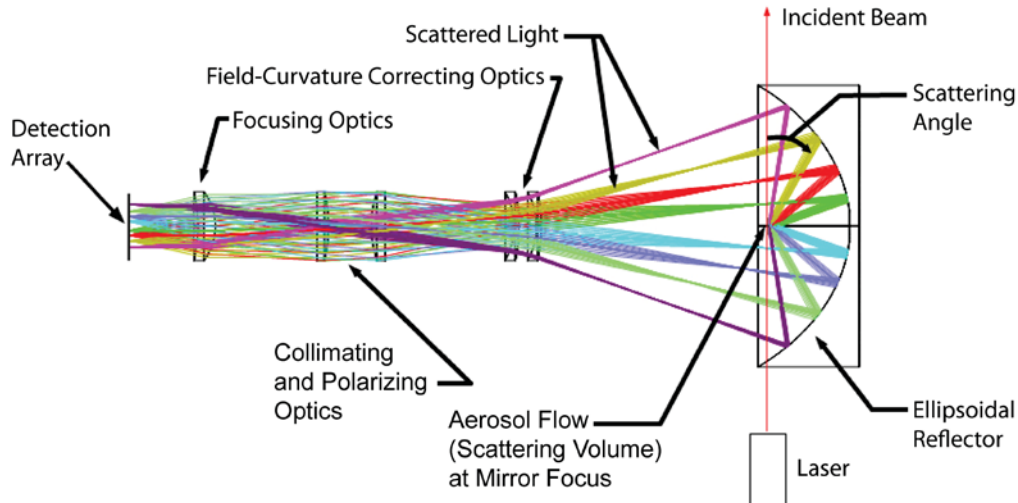
Figure 1. Schematic diagram of the scattering region and optics in the nephelometer system

The reflector (Figure 2) has a semi-major axis of 5.96 inches, a semi-minor axis of 4.23 inches, and an eccentricity of 0.705. The diameter of the reflector is 7.25 inches, and its depth is 2.126 inches. A set of two holes, 0.197 inches in diameter, were cut through the reflector by means of electrical discharge machining (EDM). The aerosol particulates intersect a laser beam that passes through the EDM holes of the reflector, 1.761 inches from its vertex and perpendicular to its optical axis.
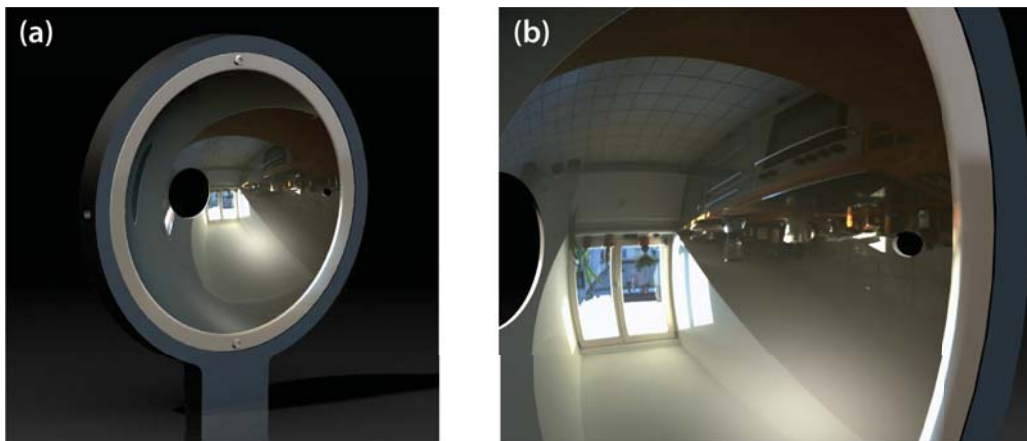
Figure 2. (a) 3-D rendering of the ellipsoidal reflector showing the reflector and custom mount, and (b) a close-up view that reveals one of the cut holes through which the beam enters and exits

The CCD imaging system, comprising the detection array (Princeton Instruments, Model PIXIS 2048), was positioned at the imaging plane of the focusing optics. The light detected by each element of the CCD array could be traced back to a specific scattering angle (Figure 3). The scattering angle

is defined relative to the direction of the incident beam. Forward scattering occurs at θ = 0° and back-scattering at θ = 180°. The useful angular range of this device is ~10° < θ < 178°. The CCD camera is situated such that the scattered hemisphere maps to a circle with a radius equal to the linear dimension of the array. The system has an angular resolution of better than 1°, although not all scattering angles map linearly to positions on the array.
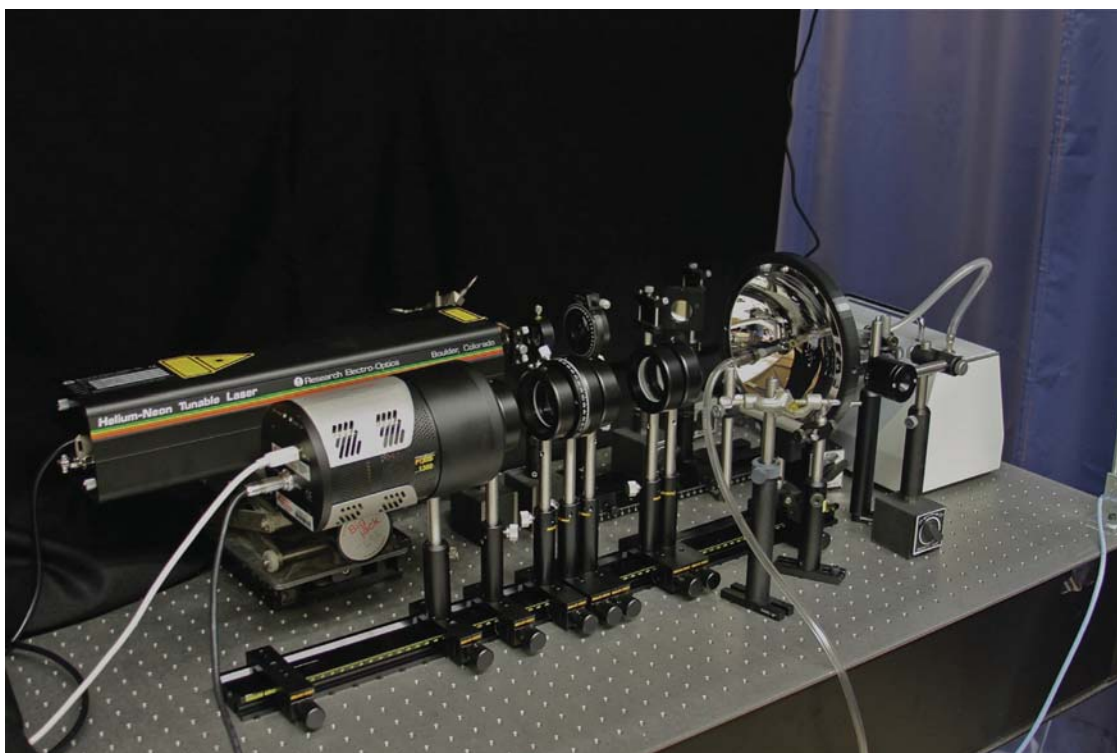

Figure 3. Experimental setup, including optical filters, polarizers, lenses, a tunable HeNe laser, an ellipsoidal reflector, CCD camera, aerosol generator (to the far right), and a sampling pump (not seen) for collecting measured aerosols

Results and Discussion

The CCD camera is typically set to image for time intervals between 1 and 10 seconds, depending on the specific measurement. A typical image from the CCD array, along with its associated scattered intensity plot, is shown in Figure 4. These measurements were taken for 903 nm PSL spheres (Thermo Fisher Scientific), a suspension of monodisperse spheres with a particle density of 1.05 g/cm^3 and a particle count of 10^9/mL. The index of refraction for these spheres is m = 1.59 at a wavelength of 589 nm. They were dispensed directly from the package via an eyedropper. The laser beam wavelength used in the experiment was 543 nm. Figure 4a shows the scattering pattern for these PSL spheres with the incident laser beam polarized parallel to the scattering plane. On the left side of

the image is the entrance aperture of the elliptical mirror, through which the laser beam enters the sampling volume. The exit aperture of the elliptical mirror is situated on the right side of the mirror. The concentric rings that span the entire image were initially thought to be caused by diffraction; however, their large scale and repeatability suggest they are more likely artifacts of the reflector's manufacture.

Each pixel number was associated with a scattering angle from 0° (forward scattering at right) to 90° (top of the image), to 180° (backscattering at the left). Forward scattering is dominant, indicating the presence of larger particles. The amount of structure throughout the image, seen as alternating light and dark regions, is also indicative of large particles. In the backscattered direction, structure is seen as a number of "rings" that appear to be concentric about the entrance hole of the reflector. Because the scattering plane is defined by the laser beam and any angle, θ, about the beam, this is expected. Figure 4b shows the results of mapping pixels from the CCD array to scattering angle. Also shown is the theoretical light intensity pattern determined from a Mie theory calculation for PSL spheres of the same size, distribution, and refractive index. The results agree well with the theory associated with 903 nm PSL spheres. There is a noticeable shift in the measured signal toward the forward scattered region. This is a result of errors due to slight optical misalignment or deviations from an ideal elliptical geometry for the mirror surface. Other departures in the peaks and valleys can be attributed to the moisture content present in aerosol flow. Although dry particles were generated, the drying capacity of the diffusion dryer leaves a relative 20% humidity at its exit.
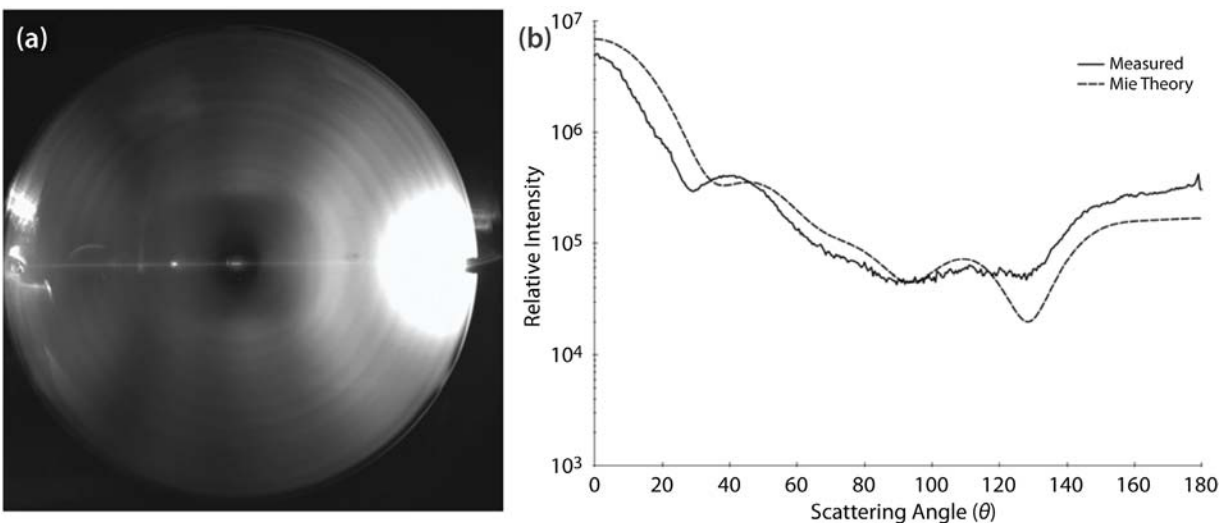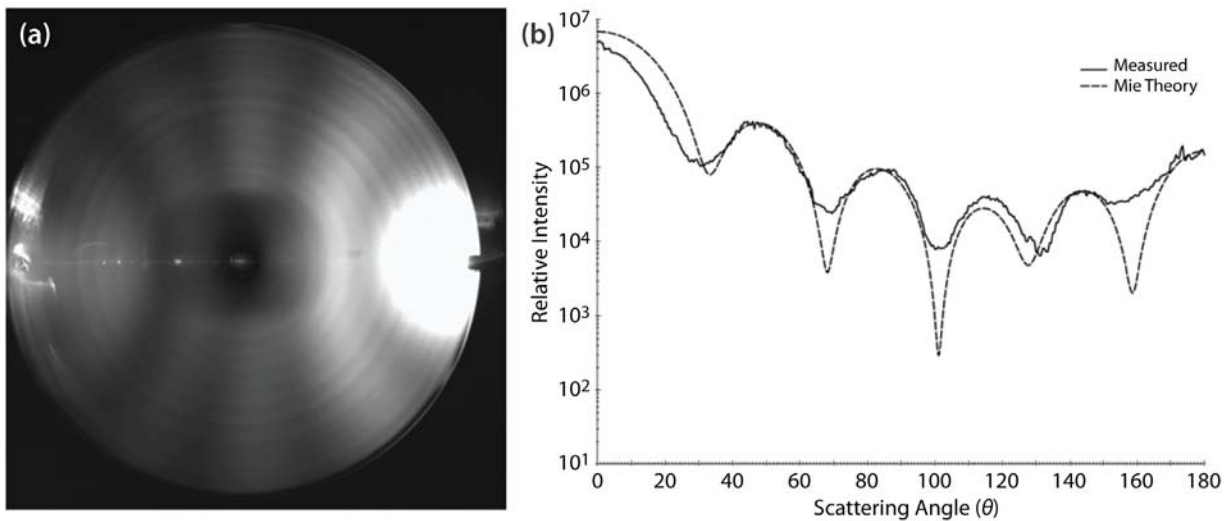

Figure 4. (a) CCD image of scattered light from 903 nm PSL spheres, with incident light polarized parallel to the scattering plane, and (b) the associated raw PSL scattering data (solid line) and theoretical Mie calculation (dashed line)

Figure 5a shows the scattering pattern for these PSL spheres with the incident laser beam polarized perpendicular to the scattering plane. Again, forward scattering is dominant, as expected. The scattering patterns differ slightly from those seen in Figure 4a, and the overall signal is stronger, with more defined structure and noticeable differences in the backscattered patterns. By contrast, structure is largely absent from water droplet curves, and the measured signal is typically due to a distributed range of smaller particles.

Figure 5. (a) CCD image of scattered light from 903 nm PSL spheres, with incident light polarized perpendicular to the scattering plane, and (b) the associated raw PSL scattering data and theoretical Mie calculation

Figure 6 displays the results of measuring the normalized, 16-element Mueller matrix for 903 nm PSL sphere suspensions. The S_{11} element is the total scattered light intensity as a function of angle. It is the linear combination of the parallel and perpendicular signals shown in Figures 4 and 5, respectively, and denotes the Mie phase function. Note the amount of structure present in S_{11} is indicative of that found in larger particles, as expected. For spherical particles, we know that $S_{11} = S_{22}$; however, because the normalized elements have been measured, $S_{22}/S_{11} = \mathbf{S}_{22} = 1$. $\mathbf{S}_{12}$ is the degree of linear polarization, P, as defined by Equation 4. Where P is positive, the scattered light is partially polarized perpendicular to the scattering plane; where P is negative, the scattered light is partially polarized parallel to the scattering plane; the degree of polarization is $|P|$. Note that $\mathbf{S}_{12} = \mathbf{S}_{21}$. Furthermore, $\mathbf{S}_{13} = \mathbf{S}_{14} = \mathbf{S}_{23} = \mathbf{S}_{24} = \mathbf{S}_{31} = \mathbf{S}_{32} = \mathbf{S}_{14} = \mathbf{S}_{42} = 0$, as well as $\mathbf{S}_{33} = \mathbf{S}_{44,}$ and $\mathbf{S}_{34} = -\mathbf{S}_{43}$, as predicted in Equation 2.
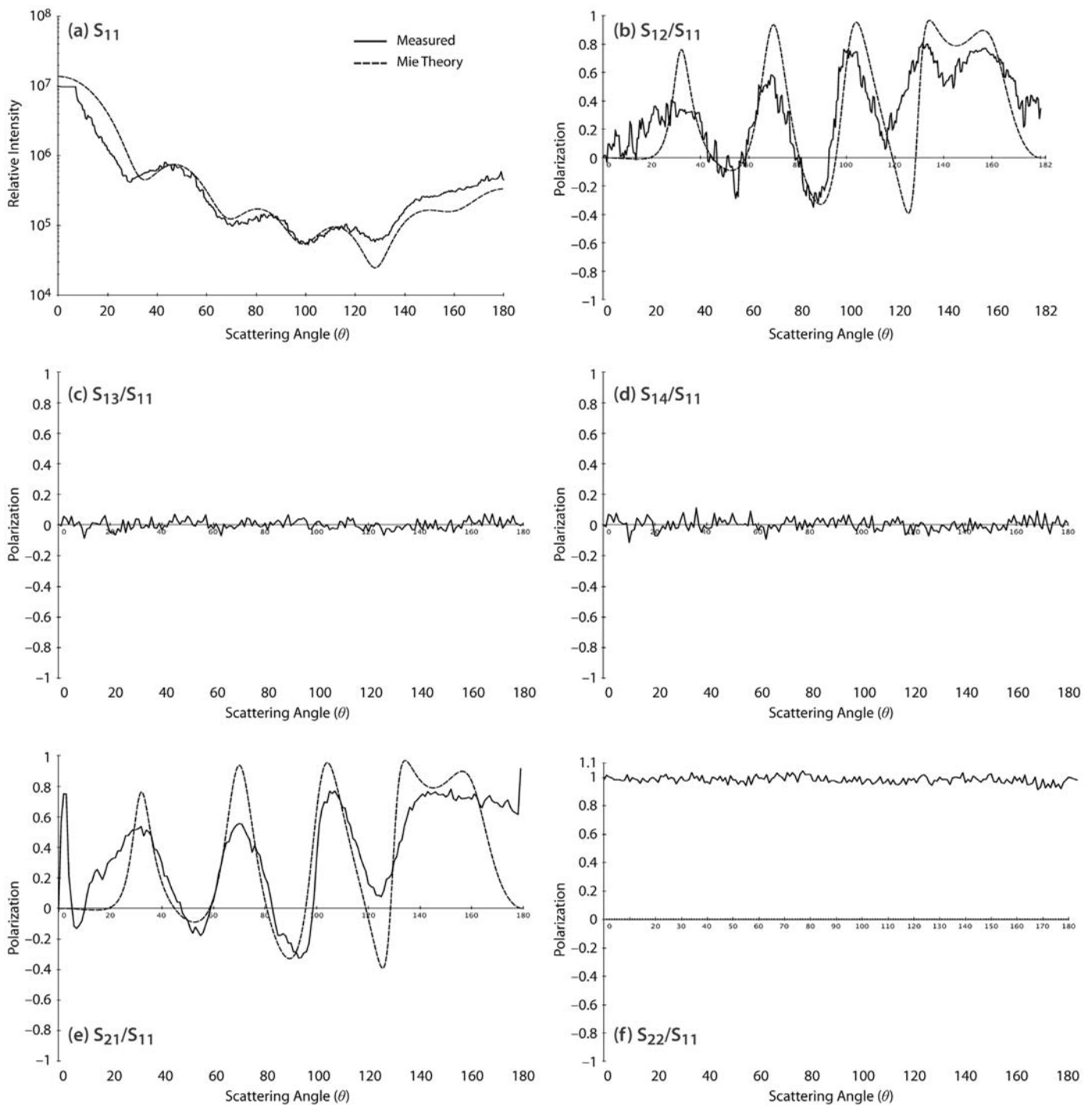
Figure 6. Measured Mueller matrix for 903 nm PSL spheres as a function of scattering angle (degrees). Shown are the nature of the data and comparisons with some models. As predicted by theory, symmetry reduces the number of non-zero elements to eight, for which $S_{12} = S_{21}$, $S_{33} = S_{44}$, and $S_{34} = -S_{43}$.
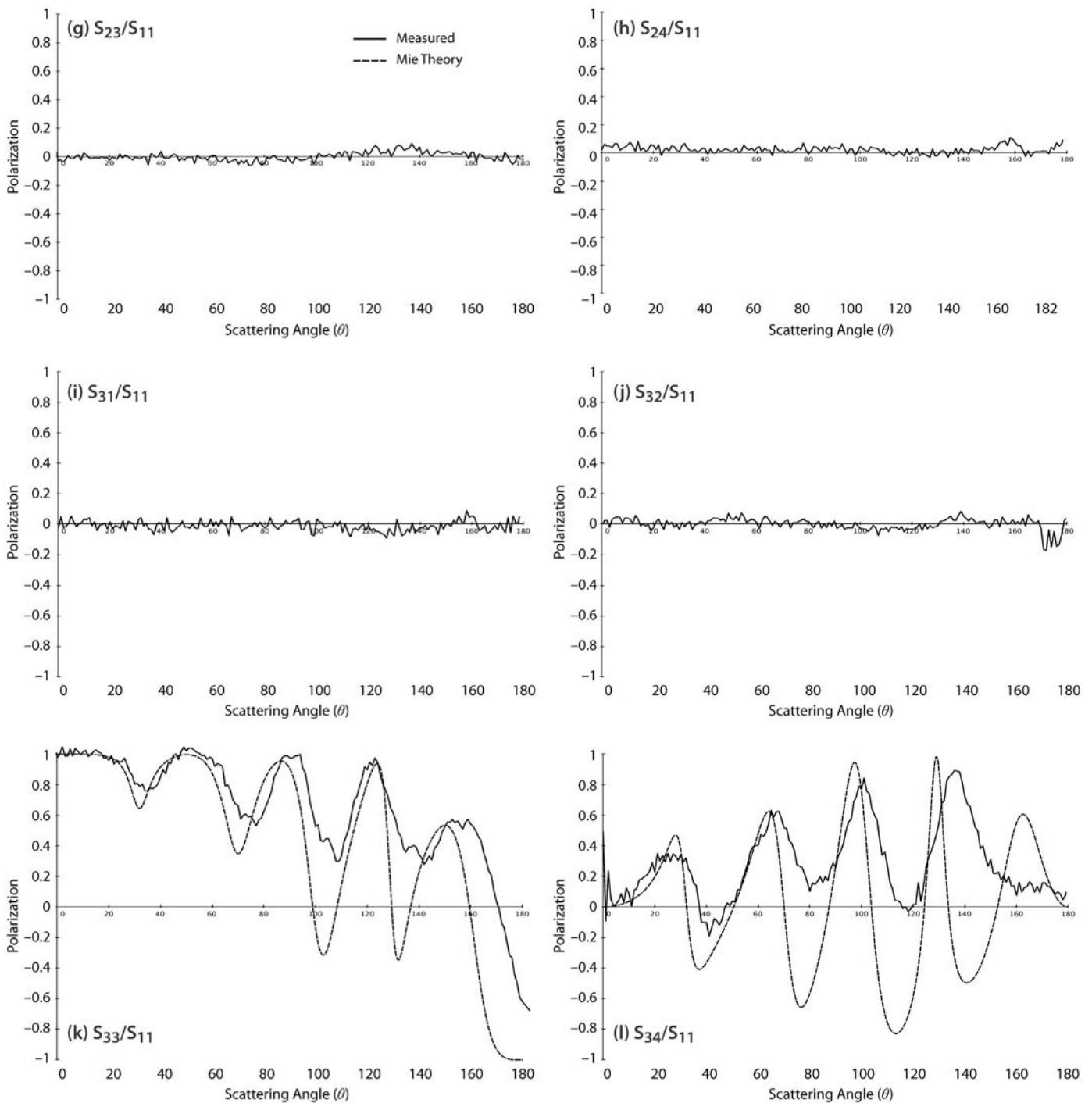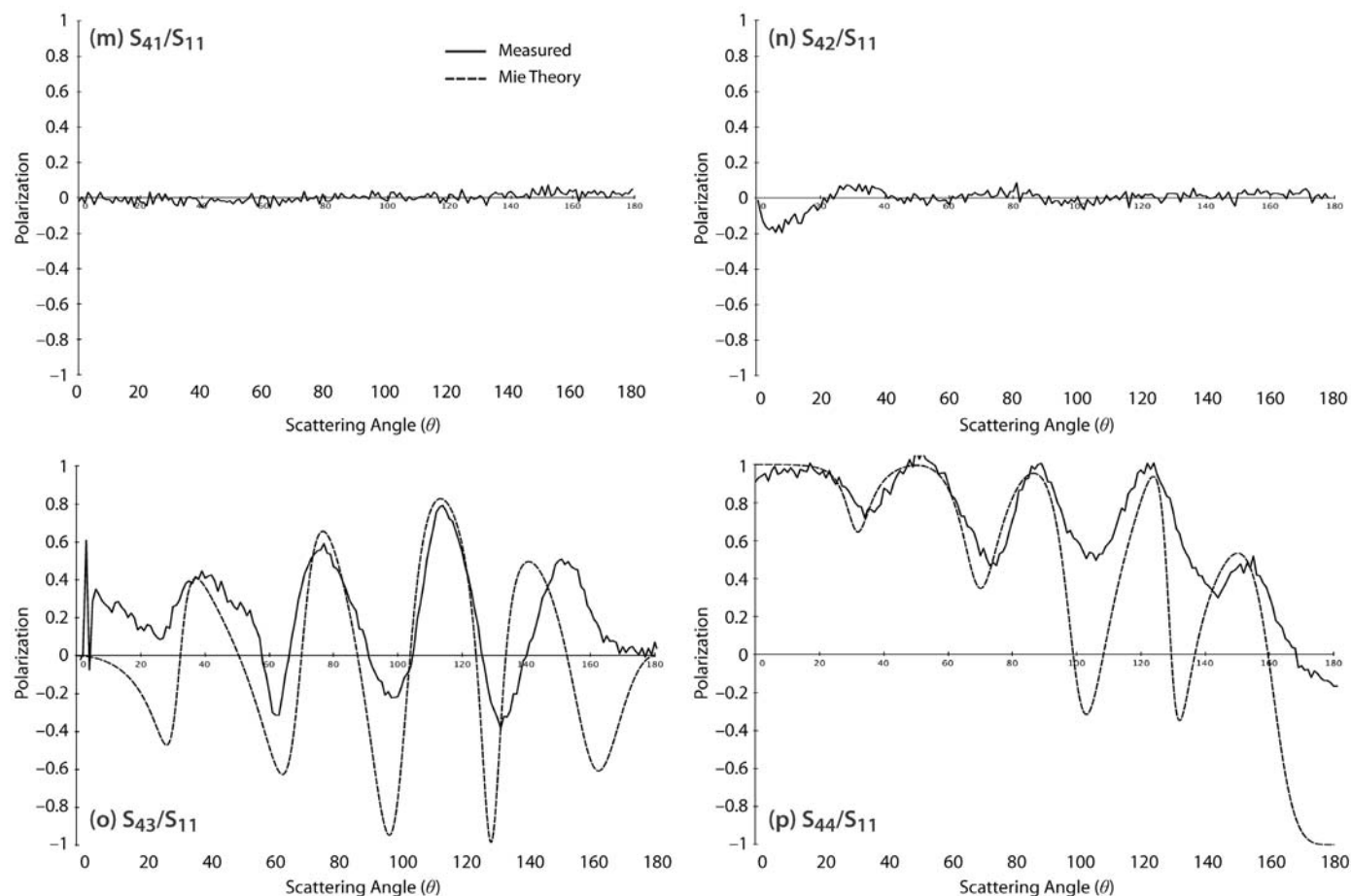
Figure 6 (continued). Measured Mueller matrix for 903 nm PSL spheres as a function of scattering angle (degrees). Shown are the nature of the data and comparisons with some models. As predicted by theory, symmetry reduces the number of non-zero elements to eight, for which $S_{12} = S_{21}$, $S_{33} = S_{44}$, and $S_{34} = -S_{43}$.

Figure 6 (continued). Measured Mueller matrix for 903 nm PSL spheres as a function of scattering angle (degrees). Shown are the nature of the data and comparisons with some models. As predicted by theory, symmetry reduces the number of non-zero elements to eight, for which $S_{12} = S_{21}$, $S_{33} = S_{44}$, and $S_{34} = -S_{43}$.

Comparing the measured scattering data to scattering calculations provides a means of accurately sizing particles and determining article concentration. A quantitative estimation could be obtained from a least-squares method, combining a fit and a gradient algorithm. The theoretical matrix corresponding to a given size distribution can be computed as a function of the scattering angle by means of Mie theory calculations. The size distribution is varied to fit the experimental curves over the whole range of scattering angles. In addition, only four elements are relevant for such results, S_{11}, S_{12}, S_{33}, and S_{34}.

Conclusion

A proof-of-concept device, a robust, laser polar nephelometer, was developed and tested; it offers a unique approach to vigorous, real-time aerosol characterization. Modeling efforts have set a foundation for system design, calibration, and the prediction of results. This instrument allows for comparison between measured optical properties and theoretical model calculations. The system has no moving parts, offering a more reliable and accurate measurement scheme than current nephelometer systems. The nephelometer collects high-resolution data in real time. The phase function Mueller matrix measurements we obtained agree with scattering theory. Small departures from theory can be attributed to errors due to slight optical misalignment, deviations from an ideal elliptical geometry for the mirror surface, or traces of moisture in the resultant aerosol flow. Further optimization and the implementation of an empirical calibration and response function for the imaging system will account for such errors.

A number of unique measurements for which this system is well suited may be performed in future research. It can be anticipated that this system will be used extensively for characterizing polydisperse, nonspherical particulates. Current measurements are being performed for ammonium sulfate and sodium chloride, for which important deviations from the ideal situation of spherical symmetry are expected. To understand light scattering phenomena from these irregular particles, the knowledge base that the present study offers will be used as a baseline. Imperfections and defects can then be added slowly and treated as perturbations, thereby creating irregular systems that exist in the real world.

Further studies of the matrix element $\mathbf{S}_{34}$ (S_{34}/S_{11}) may uncover its sensitivity to the characteristics of biological scatterers. Studies have shown that reproducible differences in $\mathbf{S}_{34}$ were found for particles that could not be readily distinguished by common means (Bohren 1983). Further studies in this area may reveal the potential of this instrument to identify chemical and biological agents as well as workplace contaminants.
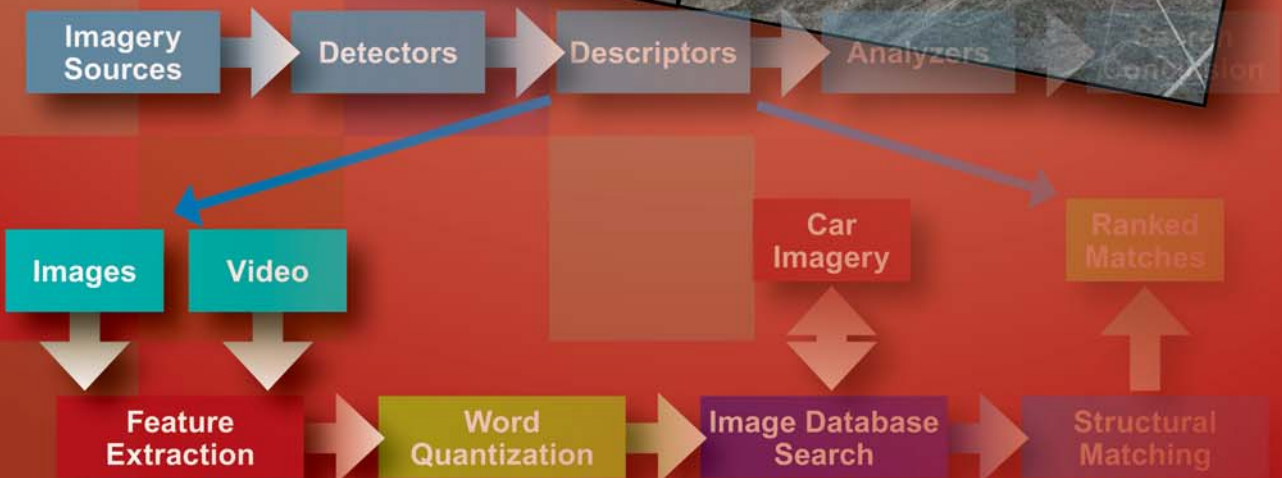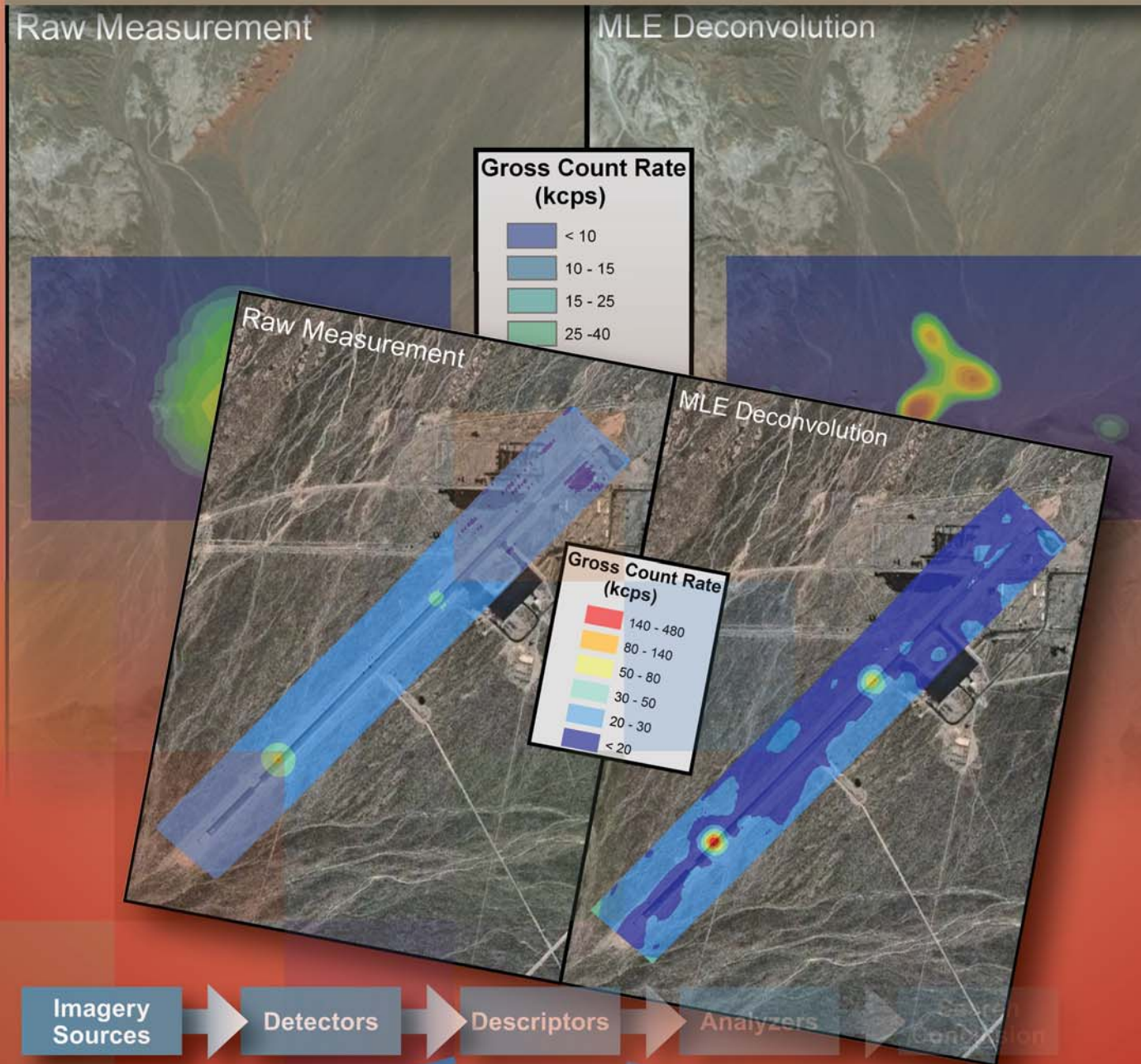
Acknowledgments

References

Asano, S., M. Sato, "Light scattering by randomly oriented spheroidal particles," *Appl. Opt.* **19** (1980) 962–974.

Bohren, C. F., D. R. Huffman, *Absorption and Scattering of Light by Small Particles*, John Wiley & Sons, Inc., New York, 1983.

McMurry, P. H., "A review of atmospheric aerosol measurements," *Atmos. Environ.* **34** (2000) 1959–1999.

Pope, C. A., D. W. Dockery, "Health effects of fine particulate air pollution: Lines that connect," *J. Air Waste Manage. Assoc.* **56** (2006) 709–742.

Quinby-Hunt, M. S., A. J. Hunt, K. Lofftus, D. Shapiro, "Polarized-light scattering studies of marine *Chlorella*," *Limnol. Oceanogr.* **34**, 8 (1989) 1587–1600.

Taylor, M. P., D. K. Frayer, "Laser polar nephelometer for aerosol studies," *Nevada National Security Site–Directed Research and Development*, FY 2010, National Security Technologies, LLC, Las Vegas, Nevada, 2011, 123–133.

van de Hulst, H. C., *Light Scattering by Small Particles*, John Wiley & Sons, New York, 1957.

Willeke, K., P. A. Baron, *Aerosol Measurement: Principles, Techniques, and Applications*, Van Nostrand Reinhold, New York, 1993.

Computational Sciences

Raw Measurement

MLE Deconvolution

Gross Count Rate (kcps)

	< 10
	10 - 15
	15 - 25
	25 - 40

Raw Measurement

MLE Deconvolution

Gross Count Rate (kcps)

	140 - 480
	80 - 140
	50 - 80
	30 - 50
	20 - 30
	< 20

Imagery Sources → Detectors → Descriptors → Analyzers → Conclusion

Images   Video

Car Imagery

Ranked Matches

Feature Extraction → Word Quantization → Image Database Search → Structural Matching

Enhanced Methods of Object Recognition and Classification within a Scene[†]

Mary D. O'Neill,[1,a] Marcus Jang,[b] and Pamela Robinson[a]

We have further improved methods to extract meaningful object recognition data from video and condense them into very small packets that can be sent over low-bandwidth telecommunication paths. As part of this study, we improved upon algorithms developed in the FY 2010 SDRD project of the same name (O'Neill 2011), developed a preprocessing algorithm for background removal, investigated handheld techniques, and field-tested these algorithm improvements. Algorithms were refined and demonstrated in August 2011. This field test confirmed the feasibility of creating these compact algorithms.

Background

Our national security organizations are collecting an increasing volume of full-motion video and still images. While the applications of object recognition technology can be wide-reaching, there are immediate needs within the National Nuclear Security Administration's mission to automate the detection of known threats within video surveillance operations as a means to streamline alarming and response operations. Although research in this area has been conducted by commercial entities (Bostrom 2003, Quantum Signal 2009), there is a continuing need for government agencies to aggressively develop compact, low-power algorithms that would benefit their applications. These algorithms are useful to a number of NSTec sponsors. Continuing from work begun in FY 2010 (O'Neill 2011), this project refined and demonstrated methods to extract meaningful data and condense it into very small packets that can be sent over low-bandwidth telecommunication paths.

Project

The goal of this project was to improve and evaluate enhanced object recognition algorithms to make them suitable for implementation in sponsor products. These algorithms extract meaningful data from imagery and reduce it to a small byte count such that it can be transmitted via a very low-bandwidth telecommunication path. The FY 2011 project included (1) making improvements to the FY 2010 prototype algorithms; (2) exploring optimization techniques for future implementation into graphics processing units (GPUs) using Compute Unified Device Architecture (CUDA) (NVIDIA 2011) technology and object detection on handheld devices, including Android and iPhone cell phones; and (3) investigating possible future enhancements associated with spectral (multiband) detection.

---

[1] oneillmd@nv.doe.gov, 805-681-2477

[a] Special Technologies Laboratory; [b] University of California, Santa Barbara

[†] Project continued from FY 2010

Algorithm Improvements

We reengineered our EagleEye software developed under the FY 2010 SDRD to provide even more modular functionality. The core of the EagleEye feature extraction algorithm is "speeded-up robust features" (SURF) (Bay 2008). Improvements and expansions made to EagleEye are intended to both enable the use of alternative imagery sources (such as webcams, surveillance cameras, network cameras, and prerecorded video images), and to supplant the original image database search with new descriptor data to increase the confidence of search results. The extra descriptor data may then be included in a very compact search result summary to either be stored locally, or sent via a low-bandwidth communication network to a remote machine. These improvements greatly expand the reach of EagleEye's object recognition beyond car recognition. However, the FY 2011 project continued its focus on vehicle recognition.

Figure 1 shows the organization of the improved EagleEye architecture. Data flow from left to right, with imagery source plug-ins passing raw images to the detector plug-in. Each detector plug-in is responsible for detecting a specific kind of information. Initial scene filtering is accomplished with motion detection, i.e., detecting when there is motion in imagery, and segmenting the moving object from the background. The detector then passes filtered images to the descriptor plug-ins. The descriptors are responsible for extracting useful metadata or other knowledge from the imagery.
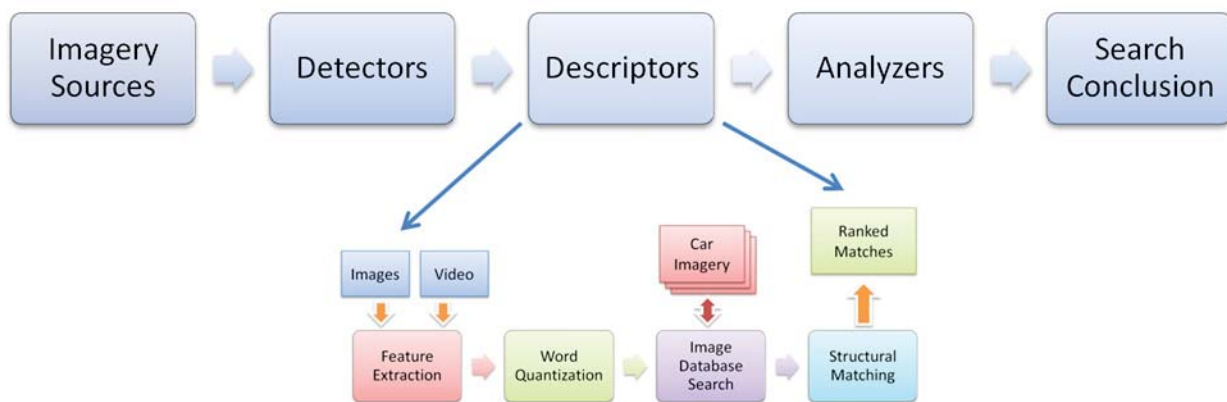

Figure 1. EagleEye updated architecture. New plug-ins improved the performance of these algorithms.

The original EagleEye image database search is now implemented as a descriptor plug-in, as indicated by the graphic. The information extracted by descriptors is passed to the analyzer plug-ins. Analyzers are responsible for taking data from multiple descriptors, across multiple video frames, and distilling this information into a compact search conclusion for local or remote storage. These conclusion data may then be reviewed by an operator at any time.

New plug-ins for any stage of the EagleEye architecture are extremely simple to implement and integrate. We have implemented the following plug-ins from four categories:

Imagery Source Plug-ins

- OpenCV – basic webcam and video camera connection (OpenCVWiki 2011)

- Motion JPEG – networked motion JPEG streams

- Smartvue – surveillance camera system with streaming network video

- Cobham ADVISR – proprietary network camera system

- Test Imagery – readable test images used for debugging without a camera

- Image Folder – reads and plays back still image sequences from disk

Detector Plug-ins

- Motion Detection – detects motion in video and segments moving objects from the background

- QR Codes – detects quick response (QR) codes (two-dimensional barcodes) in imagery (ZXing 2011)

- Target Match – detects a small number of objects (scale, rotational invariant) in video

- External Trigger – manually controls event detection via start/stop button event detection

- Capture – records all incoming imagery to disk

Descriptor Plug-ins

- Image Search – classic EagleEye image database search algorithm

- Dimension – calculates the width and height of motion-segmented objects in video

- Color – calculates a histogram of the pixel colors in an object, and finds the most likely colors in the object (as a human-readable color name, such as white, blue, red, etc.)

- Mass Ratio – given a motion-segmented object and its bounding box, calculates the ratio of the number of pixels in the object over all the pixels in the bounding box

- QR Code – decodes a detected QR code in an image to human-readable characters

- Edge Detector – converts ordinary images into their edge-detected form

- Status – reports on the time, date, GPS location, and EagleEye identifier of where and when an image was captured

Analyzer Plug-in

- Simple Analyzer – takes all data returned from the descriptor plug-ins across multiple detected video frames and condenses them into a single conclusion package. This conclusion is typically less than 1 KB and can easily be sent over even the most bandwidth-limited networks.

All plug-ins were developed by NSTec with the exception of the OpenCV imagery source plug-in listed above (OpenCVWiki 2011). In parallel with the EagleEye update, we developed additional image preprocessing algorithms that can be used as a future plug-in. This front-end plug-in will improve the robustness of the EagleEye algorithms for all times of day. The plug-in creates a number of image masks that allow the extraction of the wheels from the vehicle. The algorithm then determines the vehicle height, vehicle length, wheel height, and wheel base. Wheel height versus wheel width is used to determine the approximate aspect angle of the vehicle with respect to the sensor.

Motion detection and segmentation algorithms work well in full sun. Low light conditions such as at dawn and dusk create challenges for many of these algorithms because the image contrast is significantly reduced. The automatic threshold adjustment in the algorithms allows both the dark and light vehicles to be detected and the wheels to be extracted under various lighting conditions as shown in Figures 2 and 3, respectively.

In Figure 2 two sets of four images represent two times of day. The top set of images is from a red (dark) vehicle at 1:00 p.m. (full sun), and the bottom set of images is for the same vehicle at 7:00 p.m. (dusk). The four images for each time of day are (1) top left—original image with the wheel centroids in green; (2) top right—detected mask; (3) bottom left—wheel mask; and (4) bottom right—extracted vehicle without the background to be sent to the EagleEye algorithm. Figure 3 shows these same images for a white vehicle.

GPUs and Handheld Devices

GPUs speed up processing of parallelizable algorithms such as those in SURF. GPUs are programmed in CUDA. To verify the speeding up of these algorithms, we tested a CUDA versus Java implementation of a stable SURF algorithm. The CUDA version ran three to four times faster than the Java, allowing frame rates from 16 to 19 Hz.

In addition to the GPU research, we verified the feasibility of porting the EagleEye algorithms to an Android phone. Because the EagleEye algorithms use the OpenCV library, we found an open-source OpenCV Android software development kit (SDK). This SDK is not an EagleEye algorithm, but a similar OpenCV algorithm used to verify the portability of this type of application to the Android platform. The phone type and the output of this application are shown in Figure 4.
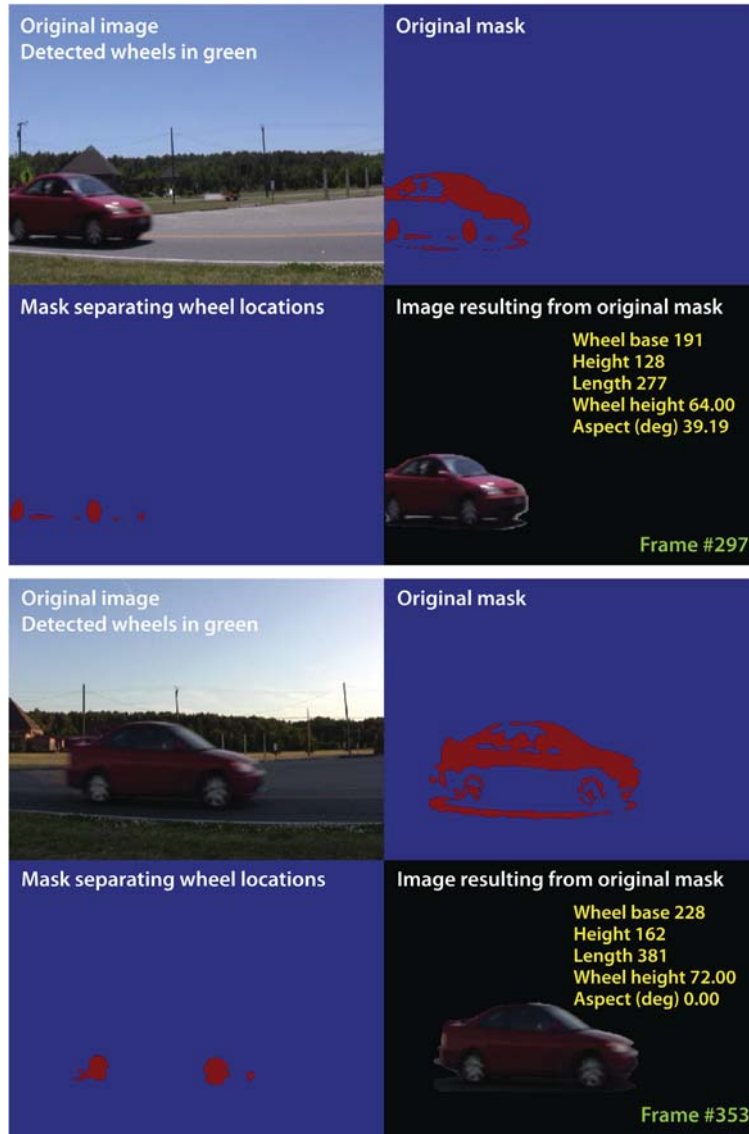
Figure 2. (top) Vehicle at 1:00 p.m. full sun; (bottom) images are for the same vehicle at 7:00 p.m. For each set of four images: (top left) original image with the wheel centroids in green; (top right) detected mask; (bottom left) wheel mask; (bottom right) extracted vehicle without the background. Dusk creates challenges for motion detection; atmospheric effects above tree lines and moving poles can cause false detects. The algorithms use a spatial filter to remove small areas of motion.
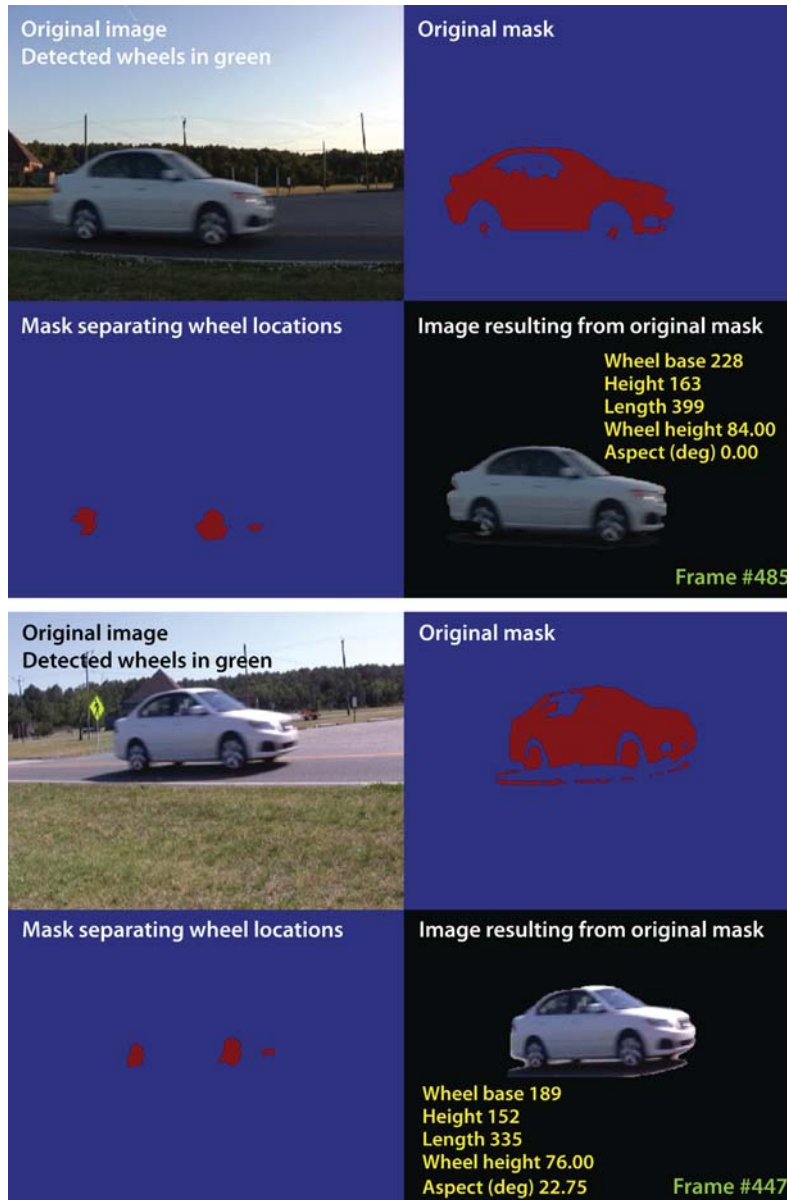
Figure 3. Images for a white vehicle in (top) full sun and (bottom) at dusk. The automatic threshold adjustment in the algorithms allows both the dark and light vehicles to be detected and the wheels extracted under various lighting conditions. This front-end plug-in allows the SURF algorithm to be effective at all times of day.

Figure 4. (left) Android phone and (right) output of application run on Android phone. The purple dots are overlaid on the image captured by the phone and represent the output of this OpenCV edge algorithm.

The iPhone implementation used OpenCV compiled specifically for Acorn RISC Machine (ARM) V7 architecture. It also used the LuceneKit, which is an objective C port version of Java's Lucene for the image database search. A protocol was implemented to send key points of the image to Raptor's EagleEye plug-in over a WiFi. Once sent, the Raptor plug-in returned the match or no-match response and information relating to the match. In addition, we implemented a video-quality reduction algorithm for faster processing and a geo-tagging of images and map display for match locations as shown in Figure 5.
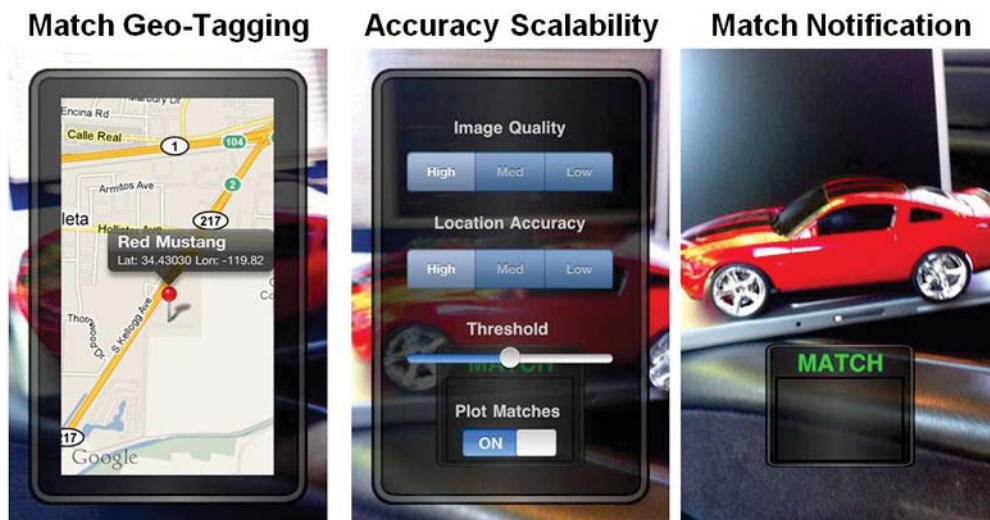
Figure 5. EagleEye implementation on an iPhone, showing (left) match geo-tagging display, (center) user interface, and (right) match notification

Multiband Research

Use of multiband data for accurate determination of vehicle color is quite complex. Most research in the area of car paint concentrates on the visible spectra. Spectral reflectance is affected by the view angle (Takagi 2005, 2007) especially for color-shift paints. This effort concentrated on examining the spectral content of a variety of paints extending into the short-wave infrared (SWIR) spectral region. Our premise was that additional information in the near infrared (NIR) and SWIR spectral bands could be exploited in identifying vehicles more accurately based on color.

We leveraged hyperspectral measurements taken for another NSTec program. These reflectance measurements were taken with the Analytical Spectral Devices, Inc., QualitySpec Pro Vis/NIR Spectrometer in full sun. We combined this reflectance data with the ASTM G173 spectra developed by the American Society for Testing and Materials (ASTM) Terrestrial Reference Spectra for Photovoltaic Performance Evaluation (ASTM International 2008). The ASTM G173 spectra represent terrestrial solar spectral irradiance on a surface at a 37° tilt angle toward the equator, facing the sun under the following atmospheric conditions:

- The 1976 U.S. Standard Atmosphere with temperature, pressure, aerosol density (rural aerosol loading), air density, molecular species density specified in 33 layers

- An absolute air mass of 1.5 (solar zenith angle 48.19° south)

- Angstrom turbidity (base e) at 500 nm of 0.084

- Total column water vapor equivalent of 1.42 cm
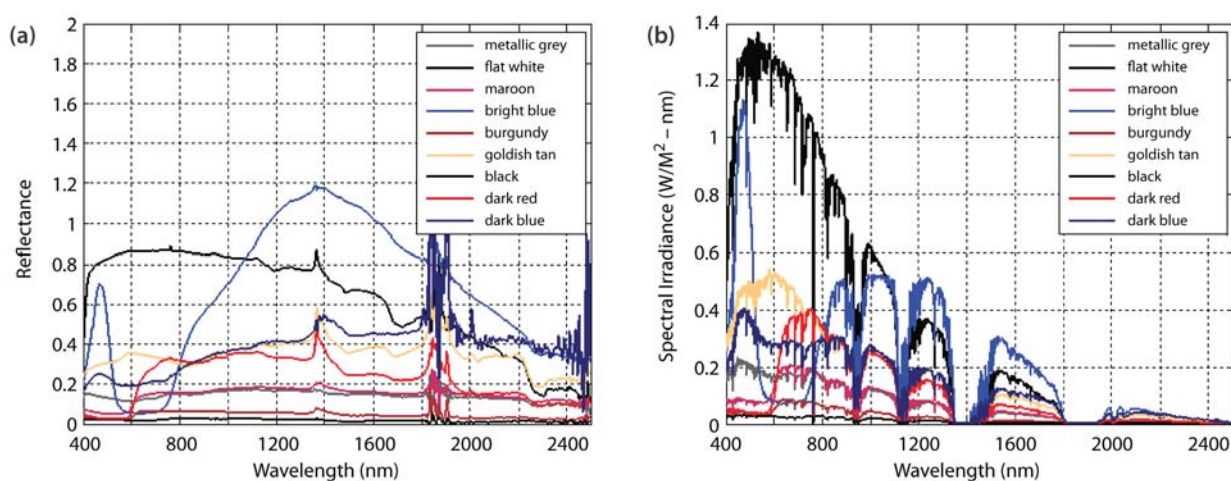
- Total column ozone equivalent of 0.34 cm

Figure 6. Plots showing (a) reflectance versus wavelength for nine vehicles of various colors and (b) the spectral irradiance from these vehicles when illuminated with full sun

The measured reflectance and the expected spectral irradiance for nine vehicles of different colors are shown in Figure 6.

The spikes in the reflectance data are the result of the low spectral irradiance of the sun in the water and CO_2 absorption bands (1.4, 1.9, and 2.7 µm), which are removed when recombined with the solar spectrum. These data indicate that there are no distinct spectral lines in the NIR or SWIR regions of the spectrum for these paints. However, there are distinct differences over the entire band area in the total reflectance, which may help in discrimination.

Algorithm Testing

Algorithm testing was conducted off site in August 2011 and was well received by two potential sponsors. In a true concept of operation, the algorithm would be used to create the initial database, and would then be used to determine if the same vehicle appeared again. The hardware for this test consisted of a laptop and a Logitech HD Pro Webcam C910. On August 8, 2011, at approximately 2:00 p.m., we collected database imagery for three vehicles (both sides, multiple angles) as they passed a checkpoint from a distance of approximately 5 meters. During this data collection, EagleEye automatically motion-segmented images of vehicles (detected the vehicle motion and extracted the vehicle image). These vehicle image frames became the database for the subsequent algorithm testing and evaluation and are summarized in Table 1.

Table 1. Database for algorithm testing and evaluation. Example image is a segmented image automatically created by the EagleEye algorithms.

Database Vehicle	Example Image	# Database Frames
Forester		197
Xterra		217
Humvee		184

On the following day, at approximately 2:00 p.m., we captured query imagery of these same vehicles. The query images were taken at roughly the same view angle as the database imagery, using the same motion segmentation as was done in the database collection phase. The image search algorithm has a threshold parameter that allows the user to vary the confidence of the match quality. Each image search result includes a match value. This value is a count of the number of structurally matched SURF descriptors between the query and resulting database image. Higher match values correspond to a higher confidence in a good database search result.

During our query data collection, several non-database cars drove through our makeshift checkpoint. We captured motion-segmented images from these extraneous cars. The resulting frames allowed us to determine EagleEye's ability to suppress unlikely or incorrect matches. These extraneous vehicles included a red sedan, a black sedan, and a white SUV (Figure 7).

Figure 7. Three vehicles that were captured by EagleEye. The image frames served as possible false positives.

The algorithm was evaluated at two different threshold parameters for a true positive and false positive detection rate. A high true-positive rate and a low false-discovery rate are indicative of mature, well-performing algorithms. Let N be the total number of frames in the query, and M be the total number of detections, including false detections. The common statistical definitions for the four fundamental numbers (Newberg 2011) are given in Table 2.

Table 2. True conditions and detected states

	Database Car	Non-Database Car	Total
Detected by Algorithm	True Positive, TP	False Positive, FP	M
Not Detected by Algorithm	False Negative, FN	True Negative, TN	FN + TN
Total	N	FP + TN	

The true-positive rate (sensitivity) is the probability the algorithm will detect a database car of interest,

$$P_D = TP/((TP + FN) = TP/N. \tag{1}$$

The false-discovery rate is the probability that a detected car is not the desired database car,

$$P_{FP} = FP/(TP + FN) = FP/M = 1 - P_{TP}. \tag{2}$$

Tables 3 and 4 show the algorithm performance for threshold levels of 8 and 25, respectively.

Table 3. EagleEye algorithm performance for a threshold level of 8

Vehicle	Total Frames	True Positive	False Discovery	True-Positive Rate (P_D)	False-Discovery Rate (P_{FP})
Forester	81	64	0	79.0%	0.0%
Xterra	69	59	0	85.5%	0.0%
Humvee	103	88	23	85.4%	20.7%
Total	253	211	23	83.4%	9.8%

Table 4. EagleEye algorithm performance for a threshold level of 25

Vehicle	Total Frames	True Positive	False Discovery	True-Positive Rate (P_D)	False-Discovery Rate (P_{FP})
Forester	81	49	0	60.5%	0.0%
Xterra	69	42	0	60.9%	0.0%
Humvee	103	76	0	73.8%	0.0%
Total	253	167	0	66.0%	0.0%

With a threshold of 8, the algorithm provided an indication of the correct vehicle 83.4% of the time, with 9.8% of the total detections being false indications. With a threshold of 25, the false indications were reduced to 0, but the indication of the correct vehicle also dropped to 66%. This is expected, as the higher threshold places a higher quality match value requirement on each database search. Thus, the number of correct matches was reduced while the confidence of each match was increased.

What is not shown in these tables is that no query frames (at either threshold) were ever miscategorized to an incorrect car type. The only false positives were those vehicles not in the database. This means that an operator viewing these results would instantly determine which car type is the best overall match, and as vehicles get added to the database, false positives will be reduced.

These statistics represent detection probability on a frame-by-frame basis. Because a sequence of frames will be processed as one event, the probability of an alert will be higher.

Conclusion

The goal in this second year of the project was to improve and evaluate the enhanced object recognition algorithms to make them suitable for implementation in sponsor products. These algorithms extract meaningful data from imagery and reduce it to a small byte count such that it can be transmitted

via a very low-bandwidth telecommunication path. In FY 2011, we improved the FY 2010 prototype algorithms by adding plug-ins that expand the capabilities of these algorithms. We developed new preprocessing algorithms for improved performance based on time of day and aspect angle. These same algorithms can extract the vehicle aspect angle with respect to the sensor, the relative height and length, and the wheel base of the vehicle. We explored optimization techniques for future implementation into GPUs using CUDA technology and object detection on handheld devices, including Android and iPhone cell phones. We successfully ran the EagleEye algorithms on an iPhone. We reduced hyperspectral data and began investigating how these data might be used.

At the end of this project, we demonstrated the EagleEye algorithms for two potential sponsors in a field test, which shows promise for obtaining future work. The test resulted in a true-positive rate of 83.4% with a false-discovery rate of 9.8% for a low threshold, and a true-positive rate of 66% with a 0% false-discovery rate for a high threshold.

References

ASTM International, ASTM G173 - 03(2008) Standard Tables for Reference Solar Spectral Irradiances: Direct Normal and Hemispherical on 37° Tilted Surface, 2008, http://www.astm.org/Standards/G173.htm, accessed July 25, 2011.

Bay, H., T. Tuytelaars, L. Van Gool, "Speeded-up robust features (SURF)," *Computer Vision and Image Understanding* **110**, 3 (2008) 346–359.

Bostrom, G., A. Liew, J. Frilund, "Method and device for registering the outer characteristics of a vehicle in a road toll unit," U.S. Patent 6,538,580, issued March 25, 2003, http://www.freepatentsonline.com/y2002/0105440.html, accessed September 30, 2010.

Newberg, L., Some Useful Statistics Definitions, 2005–2006, http://www.rpi.edu/~newbel/misc-publications/SomeStatDefs.html, accessed September 1, 2011.

NVIDIA Corp, CUDA 2011, http://www.nvidia.com/object/cuda_home_new.html, accessed April 5, 2011.

O'Neill, M., M. Jang, P. Robinson, "Enhanced methods of object recognition and classification within a scene," *Nevada National Security Site–Directed Research and Development*, FY 2010, National Security Technologies, LLC, Las Vegas, Nevada, 2011, 197–204.

OpenCVWiki, http://opencv.willowgarage.com/wiki/, accessed June 1, 2011.

Quantum Signal, LLC, Signal Processing Solutions, Vehicle Tracking/ID, http://www.quantumsignal.com/video_analytics/vehicle_tracking_id/, accessed December 1, 2009.

Takagi, A., A. Watanabe, G. Baba, "Prediction of spectral reflectance factor distribution of automotive paint finishes," *Color Research & Application* **30**, 4 (August 2005) 275–282.

Takagi, A., S. Sato, G. Baba, "Prediction of spectral reflectance factor distribution of color-shift paint finishes," *Color Research & Application* **32**, 5 (October 2007) 378–387.

ZXing Multi-Format 1D/2D Barcode Image Processing Library, http://code.google.com/p/zxing, accessed August 1, 2011.

this page intentionally left blank

Application of Inverse Transport to Contouring of Radiological Measurements

Michael Reed[1,a] and James Essex[a]

The goal of this project was to determine whether modern particle transport capabilities and processing power in conjunction with formalized inverse techniques can advance the state of the art with regard to Aerial Measuring System contour map data products. An algorithm capturing the dominant photon transport mechanisms was designed, and test problems were run to investigate applying deconvolution in the form of maximum likelihood estimation to the underlying data. The techniques provide a basis to convert measured spectra at altitude to quantitative data products at ground level. The methods perform well within the relevant parameter space, and the work appears to have many programmatic applications at the NSTec Remote Sensing Laboratory.

Background

The Aerial Measuring System (AMS) flies large sodium iodide (NaI:Tl)–based detection systems over regions of radiological contamination and provides insight into the characteristics of contamination. The predominant data products provided by the AMS include either the gross count-rate response or some scalar multiple of that value (Kiser 2010). Although careful experimental measurements may be used to inform the derivation of such multiplicative constants, these methods tend to be more qualitative in nature and do not yield quantitative results such as µCi, µCi/m², or µR/hr. Most importantly, such an experimental approach requires careful ground truth measurement and allows for very little extrapolation to other scenarios. The primary objective of this work was a proof-of-principle illustrating that theoretical methods, in conjunction with deconvolution techniques, can significantly advance the degree of quantification that is possible within AMS data products. Such techniques have shown significant promise in related fields such as astronomy and medical imaging, and we have more recently begun to see application in aerial radiation measurements (Lee 2003, Curry 2011).

[1] reedms@nv.doe.gov, 702-295-8695
[a] Remote Sensing Laboratory–Nellis

Project

Introduction

Deconvolution describes a mathematical algorithm that seeks to undo the effects of a process whereby a desired signal has been degraded by some physical process that may be represented as a convolution. Using standard terminology, this process can be represented by Equation 1,

$$f \circ g + \varepsilon = h, \tag{1}$$

where f represents the desired signal, g (in operator notation) represents the effects of the undesired process, h is the measured signal, and ε represents the addition of some amount of noise. In practice, the presence of the ε term accounts for counting statistics or the effects of other processes not specifically accounted for by the mathematical model of g. Given the presence of ε and imperfect knowledge of g, there exists no unique solution to this equation. Furthermore, attempts at direct inversion are typically very ill suited. Instead, the problem is normally tackled using an iterative technique whereby estimates of f are convolved with g to generate projections of h. These projections are then compared to the measured value, subsequently defining another guess; thus, it is an iterative process.

Many algorithms exist for obtaining successive iterates from this equation. The nature of each of the various techniques concerns the ability to preserve particular characteristics of the solution. For scenarios in which ε is governed by Poisson noise, maximum likelihood estimation (MLE) converges to the solution that is most probable (Myung 2003). Given this property and its significant historical success, MLE was chosen for the current work. The Richardson-Lucy formulation of MLE is most commonly used and is written in matrix notation for a discretized system as

$$x^{(k+1)} = x^{(k)} \left[G^T \frac{h}{Gx^{(k)}} \right], \tag{2}$$

where $x^{(k+1)}$ is the new iterate of the desired signal, $x^{(k)}$ represents the previous iterate, h is the measured signal, and G, known as the point spread function (PSF), represents the convolution action.

For illustrative purposes, we begin by considering a simple case whereby Gaussian energy broadening of spectral response is applied to energy deposition in a NaI:Tl crystal to produce a measured spectrum. In this scenario, the original signal represents the pulse height spectrum describing energy deposition in the crystal. The PSF represents the Gaussian energy broadening, whereby the true energy deposition in the crystal is broadened according to a Gaussian function centered about the energy deposition to produce the measured spectrum. More specifically, for spectra taken at 1024 channels of resolution, the matrix G is of size 1024 × 1024 with element $G_{i,j}$ representing the probability that an event depositing energy j within the NaI:Tl crystal, registers a pulse within channel i. By carefully measuring the resolution of the NaI:Tl crystal, it is possible to improve the energy resolution of measured spectra. Figure 1 illustrates such a process applied to a ^{152}Eu spectrum. Without introducing artifacts, the

MLE deconvolution is able to significantly increase energy resolution. Though the complexity of operator *G* can vary significantly, this example suggests a very large class of methods exploiting this concept.
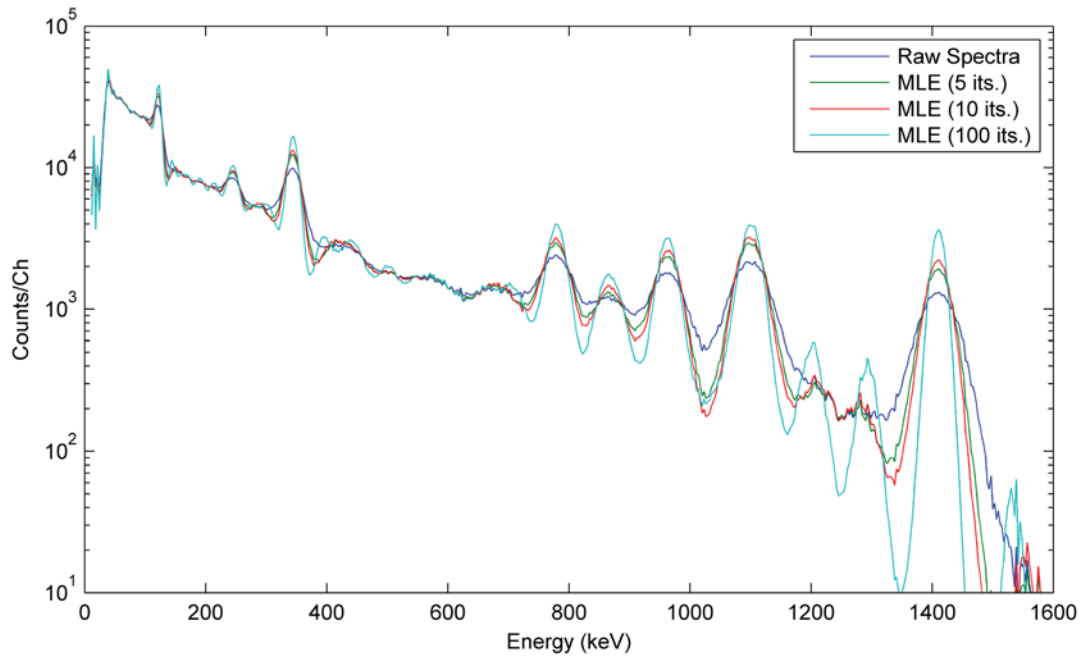

Figure 1. Demonstration of MLE deconvolution applied to a ^{152}Eu spectra (note the increased resolution with iteration number and separation of peaks)

Derivation of MLE for Aerial Detection

The derivation of an aerial MLE proceeds by first discretizing the system in matrix form. With no loss of generality, we shall develop equations for a gross count-rate treatment and then conclude with details of how it can be extended to be fully spectral. We begin by considering a collection of measurements taken from an aerial platform. These count rate measurements consist of vectors of length equal to the total number of measurements *Npts*:

$$\underline{h} = \left\{ h_1, h_2, \ldots, h_{Npts} \right\}. \tag{3}$$

Using a universal transverse mercator (UTM) projection, the associated GPS positions are converted to a suitable Cartesian coordinate system with equal aspect ratio

$$\underline{r}^{meas} = [x, y, z] = \left[\left\{ x_1, x_2, \ldots, x_{Npts} \right\}, \left\{ y_1, y_2, \ldots, y_{Npts} \right\}, \left\{ z_1, z_2, \ldots, z_{Npts} \right\} \right], \tag{4}$$

where the z-coordinates may be taken from the sensor GPS altitude measurements or alternatively an altimeter sensor located on the airframe, using the reference ellipsoid as a datum.

In order to represent the solution grid, a Cartesian grid is constructed encompassing the measurements. Here some amount of buffer space is provided to mitigate difficulties associated with the MLE algorithm. Using UTM coordinates, a simple grid is constructed by slicing the x-coordinate into N_x equal divisions, and subsequently the y-coordinate into N_y equal divisions, thus defining a grid of exactly $N_x N_y$ total cells,

$$\underline{r}^{grid} = [X, Y, Z] = \left[\left\{ X_1, X_2, \ldots, X_{N_x N_y} \right\}, \left\{ Y_1, Y_2, \ldots, Y_{N_x N_y} \right\}, \left\{ Z_1, Z_2, \ldots, Z_{N_x N_y} \right\} \right]. \tag{5}$$

The solution grid lies upon the surface of the ground and thus the z-coordinate represents the height of the local topography at mesh location (X, Y). This value is obtained through use of a digital elevation model, which describes the height of the local topography relative to mean sea level. Such data sets are readily available for most of the world.

Analogous to the Gaussian energy-broadening example, the construction of the operator G for the aerial detection algorithm forms the basis for implementation of the MLE. For the aerial detection problem, the G operator represents the processes of photon transport and detector response. If we choose an indexing scheme whereby i indexes the solution grid and j indexes the measurement location, then the operator G may be discretized into matrix form. In matrix form, the element $G_{i,j}$ represents the detection system response at measurement location j due to the presence of unit source strength at grid cell i. In previous work, an efficient and adequately sophisticated model was implemented and tested for the aerial regime (Reed 2010, 2011). Using this work as a guideline, a general equation may be written for element $G_{i,j}$ as follows:

$$G_{i,j} = \left[\sum_{\substack{\text{detection} \\ \text{window}}} \sum_{\substack{\text{detectors}}} \sum_{\substack{\text{detector} \\ \text{faces}}} \underline{\underline{R}} \left[\underline{\underline{B}} \left(\eta_g \underline{Y} \otimes \underline{p}_s \right) \right] \right]_{i,j}. \tag{6}$$

Here $\underline{\underline{R}}$ is a detector response matrix, $\underline{\underline{B}}$ a photon buildup matrix, η_g is the geometric efficiency, $\underline{Y}$ is a yield vector for the source isotope, and $\underline{p}_s$ is the uncollided survival probability. The summations indicate accrual across each detector face within a system, and the summation over the detection window is necessary to generalize the counting window. Although arguments have been suppressed in this equation, the (i,j) indexing indicates that the equation is evaluated using measurement location i and ground location j. In general, Equation 6 is a function of six spatial variables, the detection system, and the nature of the source.

The MLE procedure requires a starting guess for the deconvolution solution $x^{(0)}$. Typically one employs the raw measurement as an initial guess, but because the measurement and solution grid are not

coexisting, it is necessary to interpolate the raw measurement results and project them onto the solution grid. For this work a simple inverse distance weighted interpolation scheme was employed. The next step of the algorithm involves applying Equation 2 to generate the next deconvolution estimate $x^{(1)}$. In this way, the MLE iteration is performed iteratively to achieve the solution at step k. Though in principle the process can proceed to convergence, significant computational power requirements, slow convergence, and the appearance of undesired artifacts typically limit the iteration to a relatively small number of iterations.

Simulation Testbed

In order to test the performance of the MLE implementation, a test apparatus was set up to exploit an existing spectroscopic aerial detection simulation capability (Reed 2010, 2011). Using existing historical data for flight paths and background, the effects of both point and extended (deposition) sources are artificially inserted to create a simulated data set. The spectral simulator then estimates the spectral response of a detection system, specifically accounting for the effects of detector motion, aircraft altitude, and detector response. In this manner a test data set is generated whereby a collection of geo-referenced spectra taken at 1 Hz is associated with a known ground truth. Such a testbed has significant advantage for conducting performance evaluations, as it allows for testing against arbitrary isotopes, source strengths, and extended deposition footprints against a known ground truth. In this way, both the implementation and performance of the MLE were tested.

Testing and Results

Employing predominantly the simulation testbed to generate high-fidelity benchmarks, a suite of test problems were run to investigate the behavior of the MLE implementation under different regimes. The major parameters investigated were various signal-to-noise environments as well as regions with varying topographic behavior. In addition, some work was performed to investigate the convergence of the method in conjunction with its tendency to produce artifacts with excessive iterations. Here we present results obtained for two particular test problems.

In the first test problem, the simulation testbed was used to generate a data set for a three-detector system flown at 300 m above ground level (AGL) taking 1024-channel spectra at a sampling rate of 1 Hz. The flight path was a parallel line pattern traversing three point sources of ^{137}Cs having activities of 20, 40, and 60 Ci, respectively. The point sources were arranged in a triangle, each separated by approximately 300 m. This test problem examined the ability of the method to dramatically reduce spatial resolution in regimes where the aerial footprint is particularly large.

Figure 2 depicts the results of this test problem. In Figure 2, left, are the results obtained by employing the traditional contouring algorithm to the raw data set. In Figure 2, right, the result of performing a moderate amount of MLE iterations is shown. In order to adequately portray the result, these data have been scaled in order to preserve the integral count rate present in each image. We note that

after a moderate number of iterations the overlapping footprints have been dramatically resolved, the relative source strengths have been preserved, and the background count rates have been sharpened in two regions representing local geological perturbations.
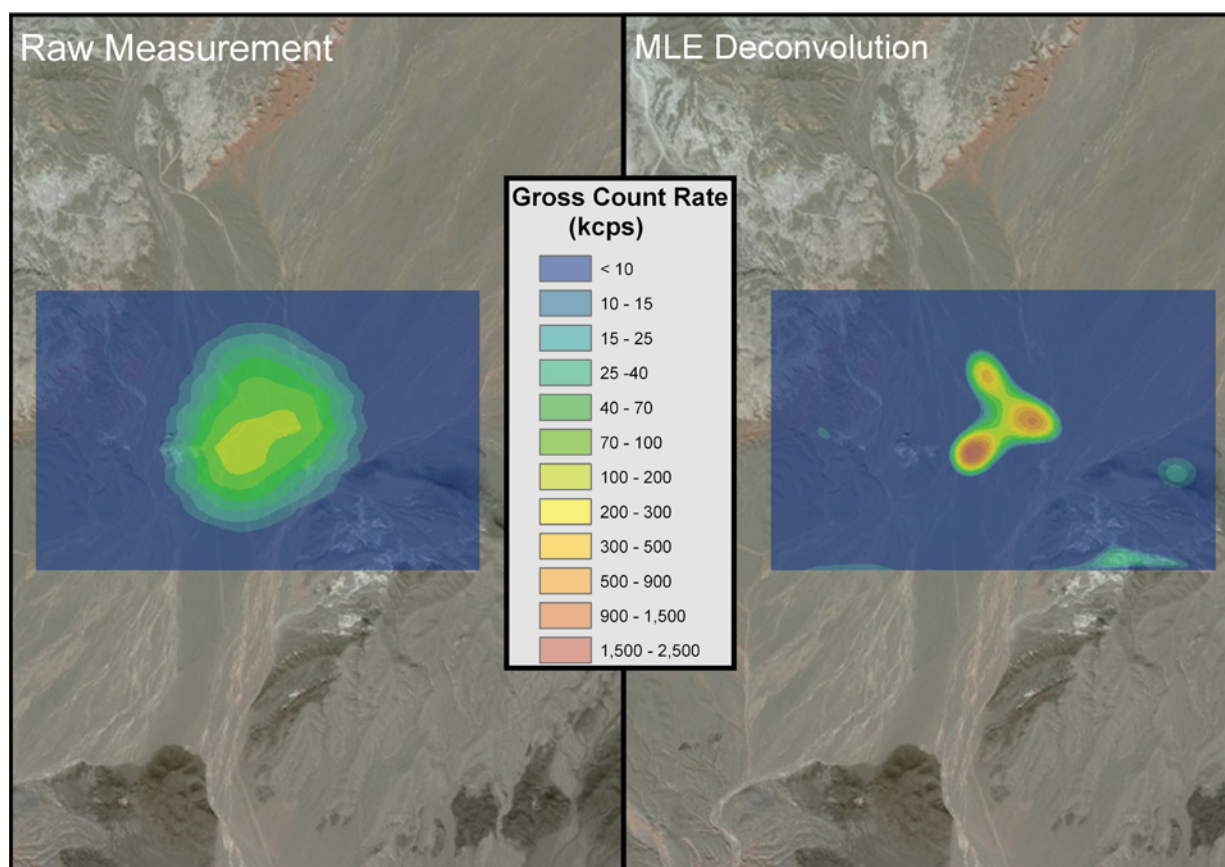

Figure 2. Comparison of standard method versus MLE for simulated three-source response at 300 m AGL. Note the increased spatial resolution and preservation of relative source strengths.

In the second test problem, the method was applied to the results of actual source flights conducted in a rotary wing aircraft over a region of flat terrain. In this experiment a 12-detector NaI:Tl system was flown over two point sources located on the ground in a traditional survey pattern consisting of parallel lines at 30 m AGL, with 30 m between lines. The sources consisted of 27 mCi of ^{137}Cs and 6 mCi of ^{60}Co. Though not standard, these data were collected using a 2 Hz sampling frequency due to the combination of low altitude and relatively significant speed. As was done for the first test problem, these data were scaled appropriately; a comparison plot is shown in Figure 3. In this

problem we note a significant increase in spatial resolution. For each of the point sources, the nominal peak signal to nominal background has increased by a factor of approximately four. Furthermore, for the number of iterations performed, no significant artifacts have been produced by the method.
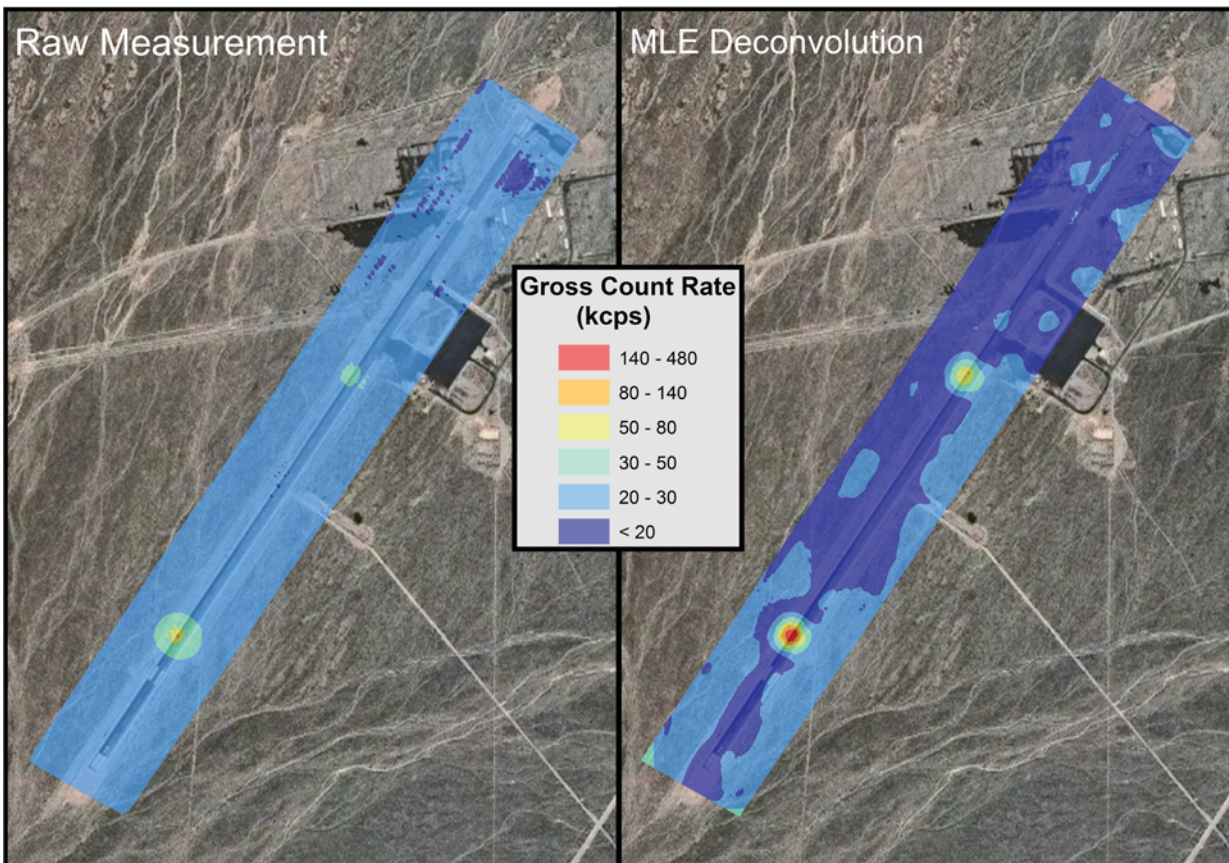
Figure 3. Comparison of standard method versus MLE for source flights performed at 30 m AGL. Note the increased spatial resolution and signal-to-noise response.

Conclusion

Several variants of a deconvolution algorithm for the analysis of aerial measurements have been implemented and tested using the MLE solution. A spectral simulator was used extensively in an attempt to investigate method behavior in a wide parameter space. Finally, the techniques were applied to a collection of experimental data. The methods perform well in the regimes of interest and show immediate promise in advancing the state of the art with respect to AMS data products. These methods exhibit many advantageous properties including (1) significant increase in spatial resolution and thus detection sensitivity, (2) a formal treatment for topological effects, and (3) the promise of

advancing historical analysis techniques that have been predominantly qualitative into the realm of quantitatively defensible products. Future work should focus on modifications to the MLE algorithm to avoid the appearance of boundary effects and other artifacts exhibited in certain scenarios, the acceleration of convergence for the iteration procedure, and also modification of the algorithm to achieve proper scaling in contrast to the preservation of raw measurement integral flux.

Finally, these techniques should be investigated and applied to more general radiation detection problems, such as advanced isotopic identification and ground-based radiation detection, as well as distributed multi-sensor networks.

References

Curry, J. R., K. L. Adair, R. J. Detry, T. Weber, "Improving the quality and spatial resolution of aerially-collected radiation data using spatially-variant deconvolution," INMM 52nd Annual Meeting, Sandia National Laboratories, Albuquerque, New Mexico, 2011.

Kiser, M., M. Reed, "An aerial radiological survey of the Paducah Gaseous Diffusion Plant and surrounding area," Remote Sensing Laboratory, Las Vegas, Nevada, 2010.

Lee, W., D. K. Wehe, "3D position of radiation sources using an automated gamma camera and ML algorithm with energy-dependent response functions," *IEEE Nuclear Science Symposium Conference Record* **2** (2003) 737–741.

Myung, J., "Tutorial on maximum likelihood estimation," *Journal of Mathematical Psychology* **47**, 1 (2003) 90–100.

Reed, M. S., "3-D Aerial Spectral Simulation," NA-42 Technology Integration Program, FY 2010 Final Report, 2010.

Reed, M. S., "Deterministic Transport for Quantification of AMS Data Products," *Nevada National Security Site–Directed Research and Development*, FY 2010, National Security Technologies, LLC, Las Vegas, Nevada, 2011, 177–183.

Photonics

(a)

Input fiber from laser diodes

Seven-fiber bundle to PMTs

Target with LiF window
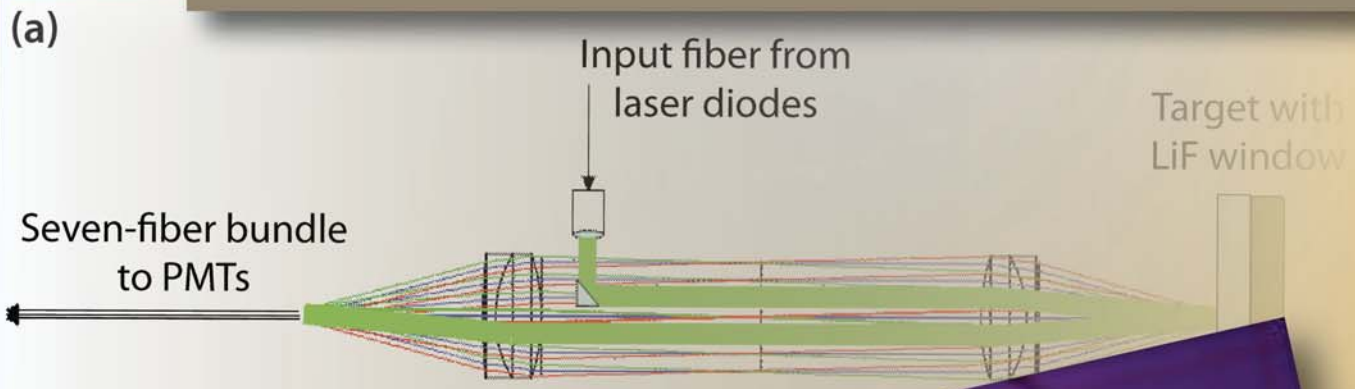
ULTRAFAST MACH-ZEHNDERS WITH CHROMOPHORE POLYMERS

Robert A. Buckles[1,a] and Eric Dutra[a]

This project explored the design, processing, and manufacture of an electro-optically activated (chromophore) polymer-based Mach-Zehnder interferometer, to achieve greater than 100 GHz bandwidth and high sensitivity for the purpose of recording ultrafast analog data through a 1310 nm fiber-optic link. We applied state-of-the-art techniques in electromagnetic design, and developed the in-house polymer processing and wafer coating capabilities. Photolithography, plasma etch, and dicing were subcontracted to a vendor. We present the established process and the measured electro-optic coefficient of the processed test wafers.

Background

In the pursuit of high-bandwidth global communications, fiber-based electro-optic modulator research melded with wideband millimeter-wave and terahertz technologies (Sinyukov 2002). Material dispersion and attenuation properties of crystals, semiconductors, and polymers has been the focus of terahertz research, optimization of which has resulted in chromophores (dyes) exhibiting high electro-optical (EO) coefficients (60 pm/V) superior to zinc-telluride (Boyd 1989). Because nonpolar polymers generally exhibit extremely little dispersion and loss, they make choice materials for wide bandwidth electrical transmission lines. Researchers have demonstrated polymer electro-optic modulators dyed with chromophore (Disperse Red [DR], DR1, DR19) with half-wave voltages less than 1 V and bandwidth in excess of 100 GHz (Shi 2000). Detectable modulation had been demonstrated at 1 THz, and fiber devices built on this technology heralded the next echelon of world-wide communications (Lee 2002). Research and development of 100 Gb/s polymer-based devices and commercial startups were stimulated by the overprescribed demands envisioned by the dot-com boom in the late 1990s. Yet, actual progression of telecommunication demand over the past two decades has been met by wavelength multiplexing capabilities and higher quality photonics. Therefore, polymer devices are still uncommon today, filling niche technologies.

Project

For use as a high-bandwidth, high-sensitivity recorder for high-energy density diagnostics, we intended to fabricate a polymer Mach-Zehnder–style fiber modulator and demonstrate high dynamic range and wideband electrical signals on a streaked recorder. The modulator could record channels simultaneously with greater simplicity and low cost, while achieving ultimate performance. Two

---

[1] bucklera@nv.doe.gov, 925-960-2520
[a] Livermore Operations

such devices have been designed, having similar electrical and optical properties, but varying in chemistry: polyurethane (PUR) with DR19 chromophore, and poly(methyl methacrylate) (PMMA) with DR1 chromophore. The PUR is attractive for its reported high temperature stability through cross-linking (Chen 1992), while the PMMA is a more commonly used material that is easy to process. Presynthesized quantities of the chromophores and polymers are available from chemical supply companies such as Sigma Aldrich, Polyorganix, and Acros, so our processing was somewhat simplified. Figure 1 shows the conceptual layout of our Mach-Zehnder design. An optical waveguide is formed out of an electro-optically active core polymer sandwiched between two clad layers of polymer. These are sequentially spin-coated onto a silicon substrate; a masking and etching process forms the optical channel. The ground plane and transmission line metallizations are likewise patterned. The transmission lines are further embedded in another layer of cladding for wideband performance, although the cross-section of the strip is only marginally trapezoidal (Liu 2006). When diced and coupled to a fiber, the optical signal is split into two paths, and interfere at the fiber receiver. The phase shift through either leg of the Mach-Zehnder is varied by the applied voltage. One leg is typically a low-bandwidth bias control, or phase offset, while the other leg is driven with the signal of interest. The received power signal is an interference sinusoid,

$$U = \tfrac{1}{2} + \tfrac{1}{2} \cdot \sin\left(\pi V / V_\pi + \phi_o\right), \qquad V_\pi = \lambda h / n^3 r L. \tag{1}$$

Full modulation or equal channel split is assumed. V_π is the half-wave switching voltage, which represents the voltage needed to fully modulate the signal from 0 to 1. Optical wavelength is λ, dielectric thickness is h, index of refraction is n, EO coefficient is r, and interaction length is L. For respective values of 1300 nm, 10 μm, 1.4, 60 pm/V, and 4 cm, V_π is 2 V. For large signals (in excess of V_π) this means enhanced signal resolution; however, unwrapping phase to get voltage is complicated by rapid phase shifts. The recording device must have a bandwidth commensurate with the slew rate of the detector, e.g., a 200 V signal could be recorded on a fast 1 V, 8-bit digitizer with effectively 16-bit amplitude resolution; but, if the signal rise time were 10 ns, the recorder would see 100 half cycles in the duration, and require in excess of 10 GHz of bandwidth to capture each "fringe" shift. Conversely, with a typical fast streak camera (16 bits, 400 GHz) the effective signal recording is 24 bits and the signal could be as fast as 250 ps. For small signals (less than V_π) the modulator functions as a typical linear recorder, and the full bandwidth applies.

The main advantages of the polymer devices over crystalline are not so evident in Equation 1; the n^3 factor in the denominator suggests that crystalline devices should be better, since the index is approximately two times greater. Foremost however, in polymers the electrical and optical indices are similar. Therefore, there is negligible phase walk-off between the two signals, which limits the performance of crystalline devices to short lengths and lower bandwidth. Longer, broader traces are allowed in polymer, and the applied field is continuous at the core/clad boundary for polymer, so a lower index is compensated by gains in the other physical terms. The expression does not really favor crystalline vs

polymer over the other, except for the ability to synthesize very large EO coefficients. However, it is challenging to make polymers retain their EO properties. Polymers have to be poled, but poling tends to dissipate over time due to the low glass transition temperatures, under 100°C. Attempts to cross-link the polymer can successfully stabilize the material, but it must be poled before cross-linking occurs. The amount of chromophore in polymer is difficult to maximize, and seems limited to 10% to 20% by weight. These are some reasons why polymer devices have not displaced crystalline devices.
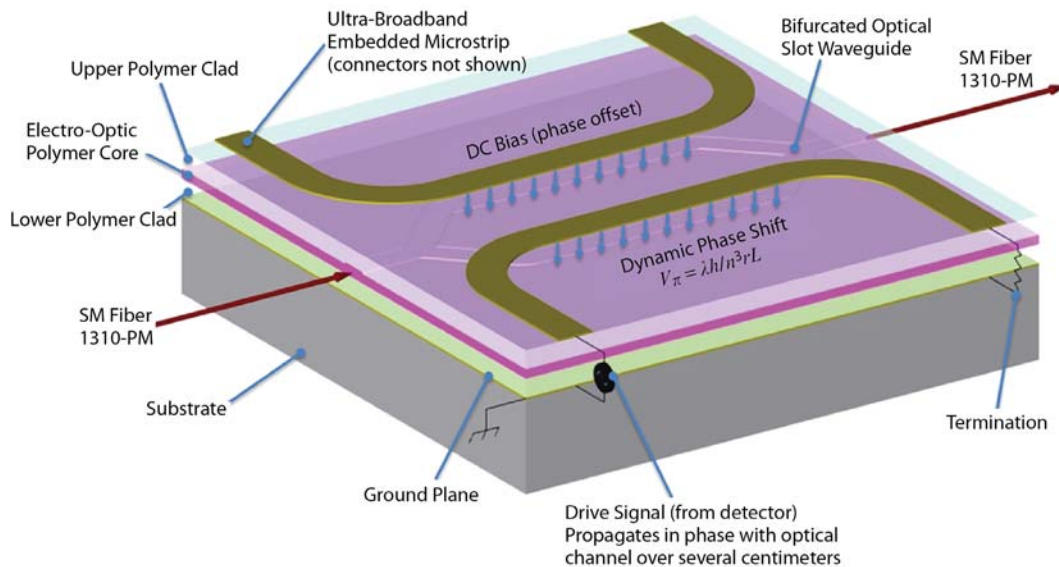
Figure 1. Polymer Mach-Zehnder modulator construction, 1:1000 aspect ratio. Clad and core layers are each 4 μm thick. The optical ridge channel is 6 μm wide by 4 μm thick at the center. Traces are embedded gold microstrip, 1 μm thick and 30 μm wide. The overall embedding layer is not shown for clarity.

Transmission Line Design

We met two challenges with the electrical design. First, because the microstrip is so much smaller than any connector we can apply, we needed to design a customized taper. Most crystalline modulators have an edge-coupled coplanar strip, and tapering is accomplished by simply scaling the width and spacing of the conductors (Burns 1998). We accomplished a similar design (Figure 2a) with a 50 Ω, hybrid coplanar/microstrip transition to an Anritsu W1-102 coaxial connector pin. Electromagnetic calculations were made with 2-D quasi-statics analysis at successive cross sections, first with a method-of-moments code (Trace Analyzer from EE Circle), and then refined with a finite element model using Comsol Multiphysics. Figures 2b and 2c show the electric potential and magnetic energy density of a taper section.
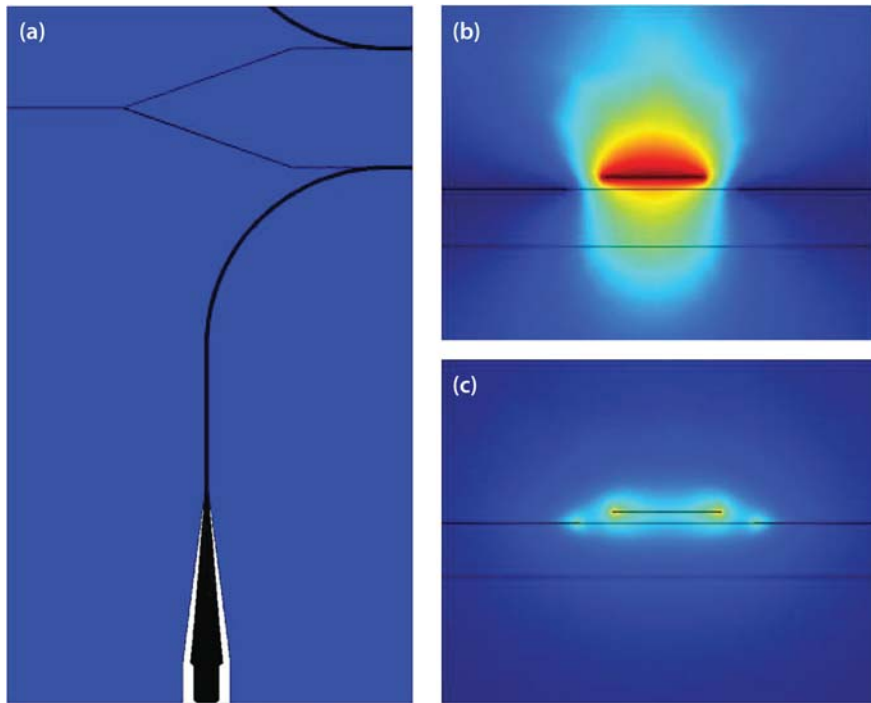
Figure 2. (a) 50 Ω microstrip/hybrid-coplanar transition to connector pin. Black is driven electrode, 12 μm above slotted ground plane (blue). Arc merges over optical channel. (b) Electric potential as shown in a 2-D finite element model. (c) Magnetic energy density around hybrid coplanar transition
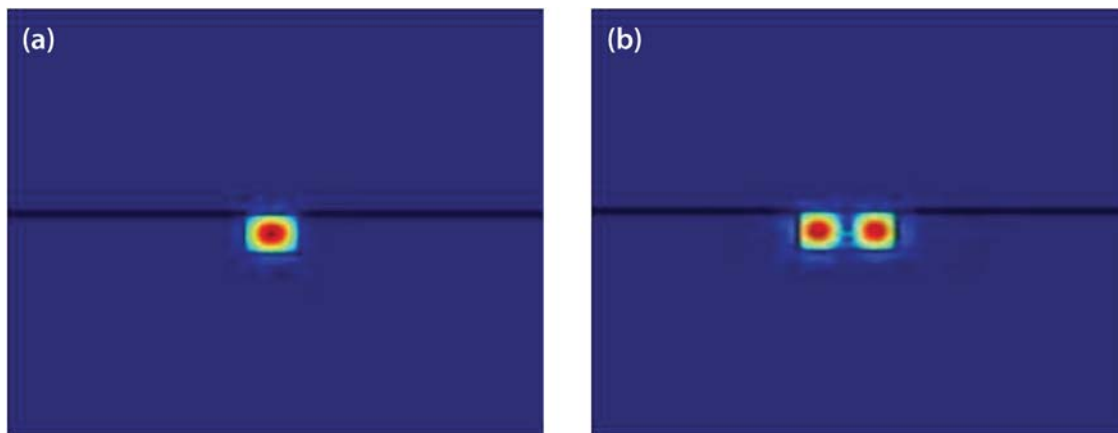

Figure 3. Electric energy density of (a) single-mode optical ridge waveguide, 1310 nm, ncore = 1.5211, nclad = 1.4380, 6 μm wide, 4 μm high; and (b) two-mode optical ridge waveguide just before splitting, 12 μm wide, 4 μm high

The second challenge was to design the optical waveguide channel split. Using Comsol Multiphysics, we performed a boundary mode analysis, iterating the width and height of the channel to achieve a smooth mode transition from a single Eigen mode at the start of the split, to the next higher lateral mode at the end of the split, after which the two channels propagate as independent single modes. Figure 3 shows the electric energy density of the two modes, respectively, at each end of the waveguide transition.

Polymer Chemistry

We set out to link DR1 with PMMA and DR19 with PUR. Some explanation of the molecular chemistry will elucidate our design choices. Figure 4a shows the acrylate ion, the basis of the PMMA matrix, having a strong free oxygen bond. Methyl methacrylate (MMA) (Figure 4b) strongly bonds two of the free ends, leaving the weakest end for polymerization, which occurs by breaking the carbon (π) double bond. This radical polymerization occurs easily at slightly elevated temperatures, and is considered a weak bond. Any length of hydrocarbon chain can be used for forming the PMMA, and each vendor uses this freedom to adjust the molecular weight, viscosity of the polymer solution, and strength of the resulting polymer. Adding DR1 (Figure 4c) substitutes the rightmost methyl group, forming a long side chain (Figure 4d), and produces our desired EO property. The most compact form of PMMA-DR1 is shown in Figure 4e, showing no intermediate methyl chains, but variable mole ratio of DR1. We desired to maximize the amount of DR1, but discovered that a 1:1 mole ratio of DR1 to MMA clumps too easily. Some hydrocarbon chain is necessary to string out the material for layering. The use of a cross-linker, such as di(ethylene glycol) dimethylacrylate (Figure 4f), supplies intervening MMA groups (at the carbon double bonds) while linking opposing polymer chains. This linking not only strengthens the polymer, but also should stabilize the DR1 poling alignment by raising the glass temperature.

We also pursued linking PUR with DR19, as research has shown it to have long-term stability (Shi 1992), and we were uncertain how successful the PMMA matrix alone would be. PUR chains are composed of a core of twin diphenyl and isocyanate groups (methylene diphenyl 4,4'-diisocyanate) (Figure 5a) bonded with diols such as ethylene glycol (1,2-ethanediol) or 1,4-butyldiol (Figure 5b) or any other such hydrocarbon chains, such as diacrylate. These hydrocarbon chains can be quite long as well. Most commercial forms of PUR have huge molecular weights. Figure 5c shows the shortest possible connector (ethylene glycol) between the isocyanate groups. A high concentration of chromophore is desired, so we should be working with a monomer like the ones in Figure 5. DR19 (Figure 5d) is very similar to DR1 but has an additional methanol functional group; therefore, it can substitute for the diols in forming a polymer chain (Figure 5e). Such a linkage, by addition polymerization, is more stable than the case for DR1, but we can make the PUR even more stable with the addition of triethanolamine (Figure 5f), which shares the same functional groups as DR19, diols, and diacrylates. Moreover, the nitrogen triple bond allows two or three different chains to be joined, significantly strengthening the polymer material. The (likely) disadvantage is the need for thermosetting upon mixing, which makes poling difficult. PUR-DR19 is unlikely to lose its poling after thermosetting.
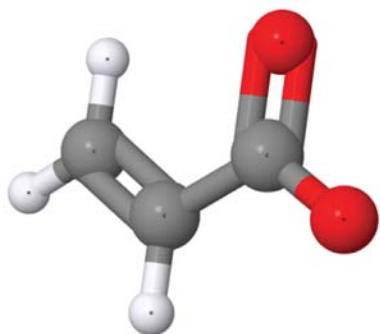
(a) Acrylate ion forms the basis of PMMA matrix, joining at the lone oxygen bond. Polymer chains are made by breaking the double carbon bond.
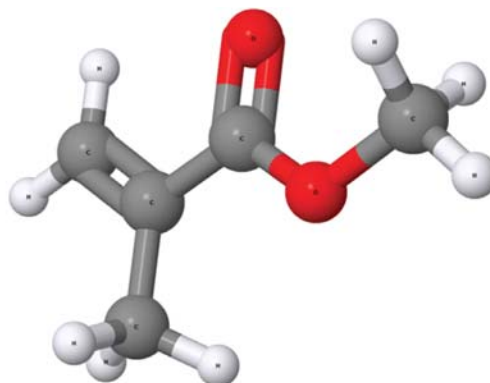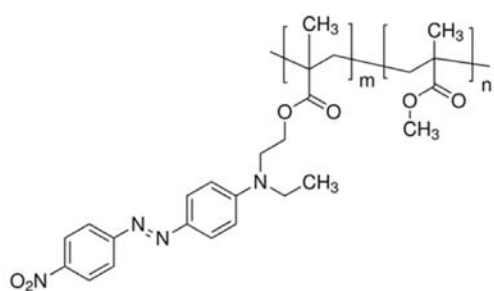
(b) Methyl methacrylate (MMA) is formed with the joining of two methyl groups to acrylate, one at the lone oxygen, and another replacing a hydrogen
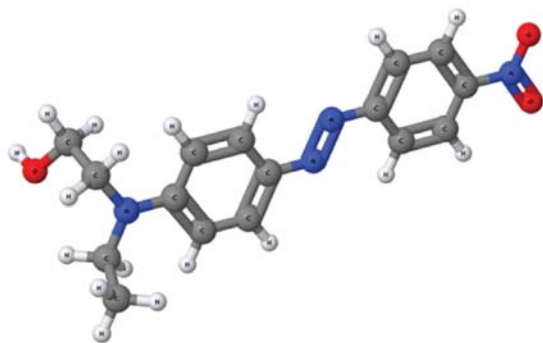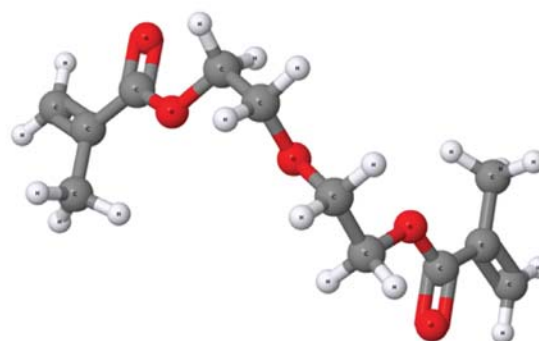
(c) DR1 molecule exhibiting long length and non-centrosymmetric shape, giving rise to large EO coefficient
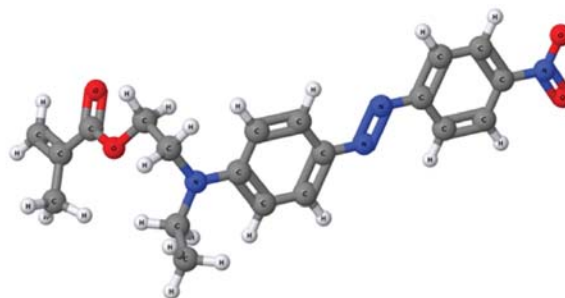
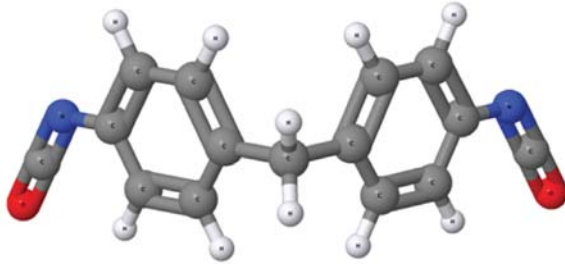(d) DR1 molecule bonded to MMA, substituting the oxygen-bonded methyl group

(e) Polymer chain of the DR1-PMMA. Longer chains of intervening hydrocarbon (not shown) are possible.

(f) Di(ethylene glycol) dimethylacrylate cross-linker. The methylacrylate ends form part of two polymer chains, linking and stabilizing the material.

Figure 4. Linking DR1 to PMMA

(a) Methylene diphenyl diisocyanate (MDI) is a strong symmetric chain that forms the root of urethanes
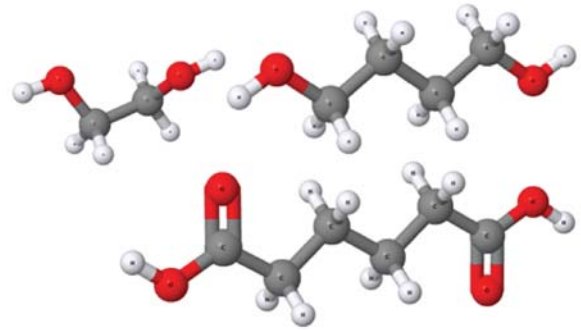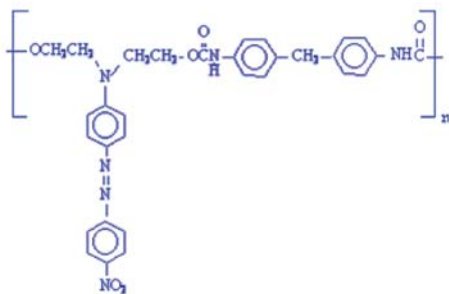

(b) Diols (ethanediol, butanediol, etc.) and diacrylate chains link together MDI roots to form PUR
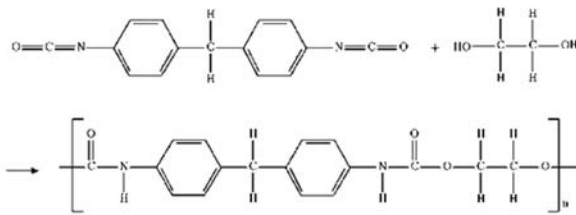
(c) PUR chain formed with ethanediol (ethylene glycol). The hydrocarbon chains can be quite long.
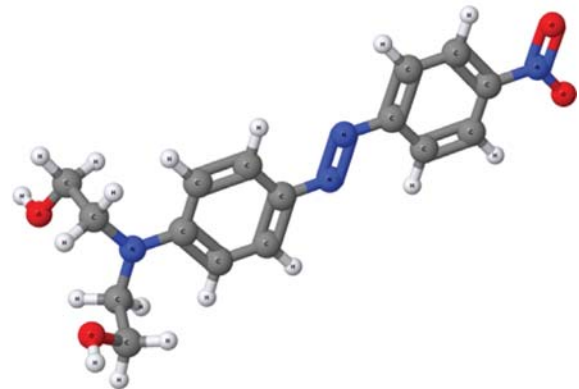
(d) DR19 is much like DR1 except for the dual methanol functional groups. This allows DR19 to directly form part of the PUR chain.

(e) PUR chain wherein DR19 joins the isocyanate groups and yields very stable EO properties
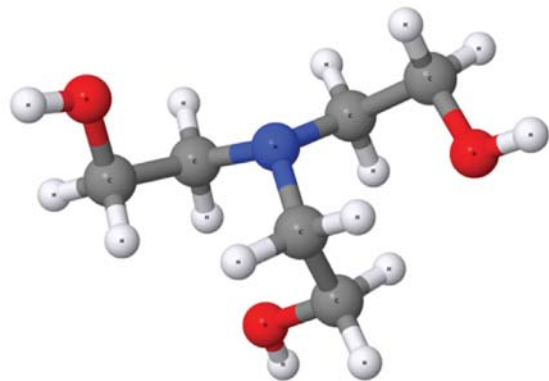
(f) Triethanolamine cross-linker has the same functional group of DR19 and diol/diacrylate connectors, but can also link to adjacent polymer chains. This forms a very strong cross-link.

Figure 5. Linking DR19 to PUR

Processing

We set up a small portable fume hood in the Advanced Sensor Development process lab for mixing chemicals, acquired a heated stir plate, a tenth-milligram weight scale, a reflection-mode ellipsometer for thickness and index measurements, and established a written procedure. We acquired most of the chemicals from Sigma Aldrich and Fischer Scientific (Acros). For dissolving PMMA and DR1, we used a 9:1 mixture of chlorobenzene with methyl ethyl ketone (MEK), and di(ethylene glycol) dimethacrylate as the cross-linker. For dissolving PUR and DR19, we used tetrahydrofuran, and triethanolamine for cross-linker.

First, we characterized spin curves of the polymers on glass slides and decided on a spin rate and solvated concentration that would produce a uniform thickness of ~4 μm over a whole slide. Initial trials produced very thin layers and would require many coatings. Figure 6a shows spin curves by percent weight of Sigma PMMA (3,960 g/mol) on 6-inch silicon wafers. Thicker coatings approaching 4 μm, either by slowing the spin rate or increasing the concentration, were too viscous and produced irregular features. The materials were somewhat expensive, and much of the material was slung off the edge of the wafer, so we had to thicken the material with polymer that had a higher molecular weight. We repeated spin curves with Acros PMMA (44,700 g/mol), but the material was so viscous, we needed high spin rates and could not produce a 4 μm coating without rippling the surface. We settled on applying two coatings, each 2 μm thick, with good uniformity. Figure 6b shows thickness uniformity by speed for the Acros PMMA.
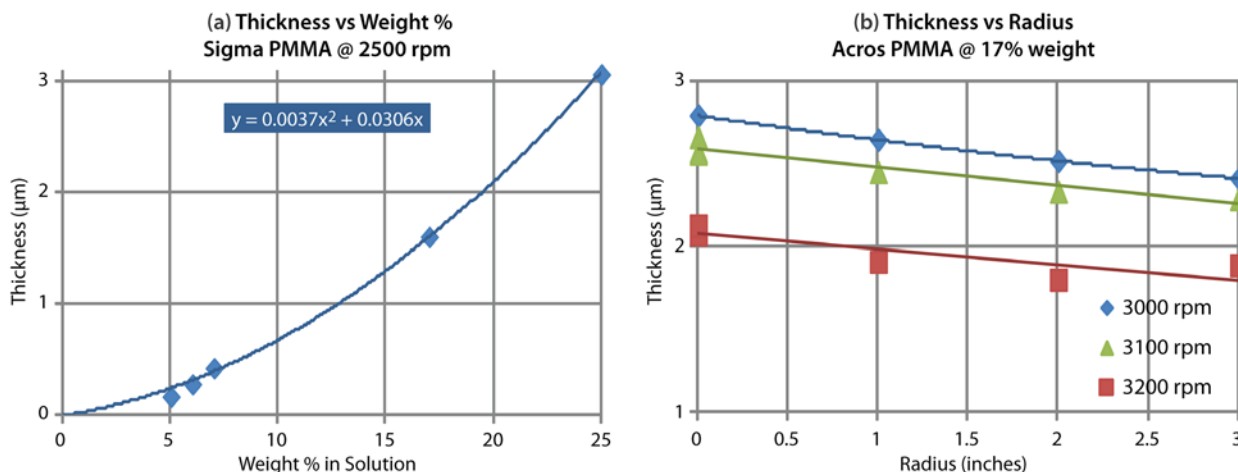

Figure 6. (a) Sigma-Aldrich PMMA spin curve by weight percent. Ideal uniformity occurred around 17 wt %. (b) Acros PMMA spin curve by speed shows good uniformity at 3200 rpm, and reaches our design target with two coatings.

Unfortunately, the spin curve tests for PUR were erratic, producing inconsistent thickness, waviness, and clumps. The only PUR we could acquire (Sigma) had too high a molecular weight (100,000 g/mol), and we apparently could not break it down with the mild temperature and solvents we used (dioxane being prohibited due to its carcinogenic nature). Polyorganix offered customized PUR and PUR-DR19 formulations, but given the late developments we chose to abandon the PUR line.

The second task was to combine chromophore and polymer. The evolved procedure is given as an appendix to this report. Our goal was to maximize the bulk EO coefficient by optimizing the mole ratio of chromophore to monomer (e.g., 1:1), yet only add sufficient polymerization and cross-linker to stabilize the mixture for spin-coating and plasma processing. We discovered that polymers from these vendors are not readily utilized without breaking down into constituents (a more difficult process), so our optimal coatings in terms of uniformity and thickness we set mostly by the average molecular weight, and not by how much chromophore we wanted to add. Despite desiring a 1:1 mole ratio, most of the chromophore precipitated out of solution. This unbound chromophore created problems while spin coating; it produced streaks, clumps, and blemishes. Filtering removed the particulates but produced the same effect with bubbling. Later, we obtained DR1-MMA monomer from Sigma (already synthesized) as we realized the difficulty of synthesis. We also obtained pure PMMA from Acros, in larger, less expensive quantities for cladding layers. Polyorganix offered the PUR-DR19, but did not have any in stock, and could not synthesize in time for our characterizations, so we had to forego the PUR matrix despite its promise for higher temperature stability. By selecting a mole ratio just under 1:1, and carefully mixing, we were able to avoid bubbles and precipitates, producing very smooth, uniform PMMA clad layers, and rich, dark red PMMA/DR1 cores. We controlled viscosity by adding very small amounts of Acros PMMA to the Sigma PMMA/DR1 monomer. Figure 7 shows the cladding thickness measurements with the ellipsometer, and the finished PMMA/DR1 core layer.
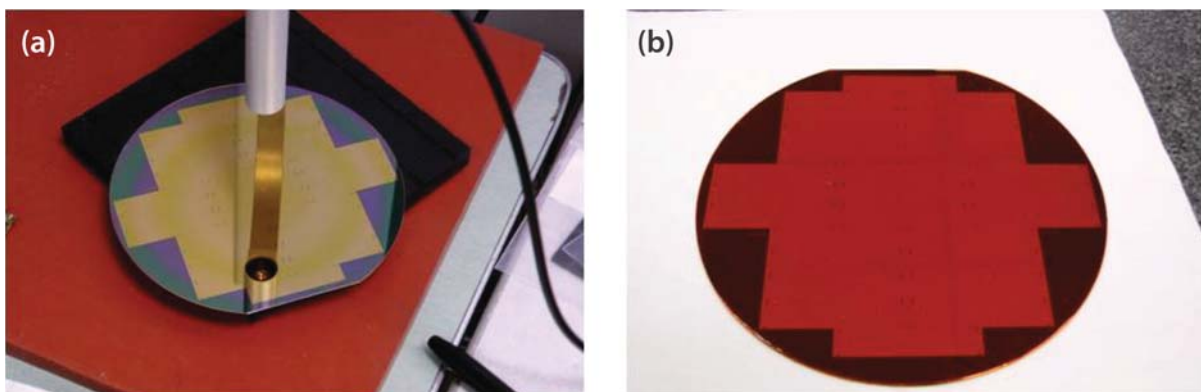

Figure 7. (a) Clad layer thickness measurement of PMMA clad on patterned 6-inch silicon wafer (ground plane). Reflection of ellipsometer is seen in metallization. (b) PMMA/DR1 core layer on top of PMMA clad.

Plasma Poling

We created a plasma chamber (Figure 8a) for applying a poling field to the EO core material while heating and curing (thermosetting) the cross-linker. The coated wafers were slowly heated up to 100°C over 30 minutes, held for 1 hour, and ramped back down to room temperature for another 30 minutes, all the while holding 5000 V/cm field over the wafer. A DC plasma discharge from a fine tungsten tip, 1 cm from the wafer, applied a nearly uniform field across the wafer diameter. Care was taken to condition the system before wafer processing such that no arcs formed, and continuous plasma current (1 mA) was maintained. Initial trials with stainless steel tips produced metallization on the wafers, yet this also revealed nonuniformity. We later spaced four electrodes around the wafer perimeter to make the field uniform, and tungsten tips did not produce any ash. Figure 8b shows the finished processing chamber in action during a high-pressure conditioning cycle.
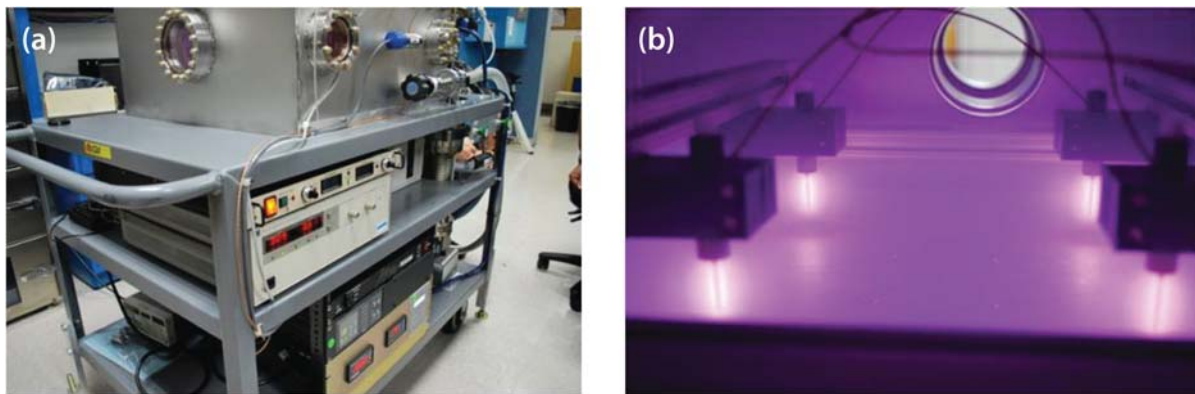

Figure 8. (a) Plasma poling chamber converted from existing diagnostic chamber. Cooling lines and cartridge heaters (not visible) were used for thermal control. (b) DC plasma discharge for poling wafers, 5000 V/cm. Temperature ramp of plate below tips is well controlled.

We measured the core EO coefficient by coating two ITO slides and placing them against each other with a slight overlap for attaching test leads with silver epoxy. Thickness was 2 μm, and voltage was applied across this same dimension (L = d in Equation 1). Figure 9a shows the setup using a crossed polarizer, Wollaston analyzer, quarter waveplate, and balanced photodiodes. The samples were modulated at 100 kHz, 50 V average, and photocurrent modulation of $4 \cdot 10^{-3}$ (1 μA average @ ±125 μA, DC) measured with a Stanford Research SR830 DSP lock-in amplifier. A control sample was used for comparison, and measured negligible feedthrough. Using Equation 1, we calculate an EO coefficient of 18 pm/V. Yet, we believe optimal material composition should improve this figure.

Optical Channel and Electrode Patterning

Two finished wafers, two material sample wafers, and feature mask details were provided to a local processing firm, A.M. Fitzgerald, for reactive ion etching (RIE) and patterning. Due to our low-

temperature requirements, their engineers suggested a wet chemistry masking procedure to imprint an aluminum mask on the wafer, rather than applying a freestanding mask, and relatively high temperature reactive ion etch. Trials on the sample wafers were successful; however, the two Mach-Zehnder wafers were terribly undercut by the wet chemistry used to remove the aluminum mask after etching. The PMMA/DR1 layers and patterned optical waveguide channels were completely obliterated in the final etch and rinse. The only difference between the samples was the lack of cross-linker, but further trials would be required to pinpoint the root cause. Follow-on proposals aim to accomplish the RIE process and regulate the wafer temperature.
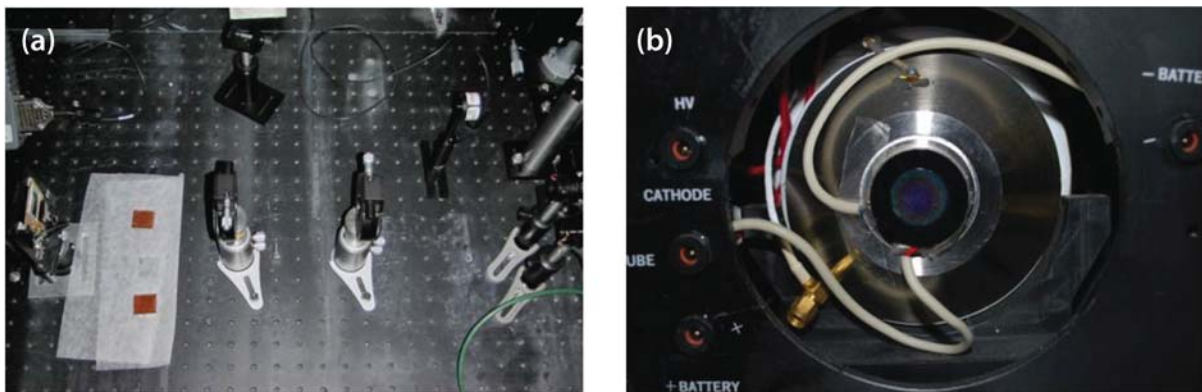
Figure 9. (a) Electro-optical detection setup using modulated samples, polarizer, analyzer, quarter waveplate, and balanced photodiodes with lock-in amplifier; (b) fast IR streak camera prepared for testing the modulators at 1300 nm

Conclusion

We have successfully developed an in-house process for characterizing, applying, and processing EO polymer onto silicon wafers. Much process characterization work revealed the need to obtain inexpensive quantities of the polymer/chromophore monomers, and control the overall molecular weight of the polymer chains for optimal spin coating viscosity and uniformity. Polyorganix offers such tailored services, but the lead-time was longer than our wafer etching and patterning contract could allow. Stripping and reprocessing the wafers with optimal material would be a straightforward, inexpensive task. An untried aluminum masking process (on EO polymer) turned out to be problematic, but we believe the reactive ion etching should not have any chemistry effects. We have designed the wideband transmission line drive structure, for use with 1 mm coaxial connectors, and have prepared for the fiber assembly and testing (Figure 9b) of the diced components. With another batch of materials, we are confident we can complete our prototype Mach-Zehnder modulator testing.

Appendix: PMMA-DR1 Preparation

Used with Acros PMMA (44,700 g/mol) and Sigma DR1+Methylacrylate monomer (382.41 g/mol)

1. Measure out 1.339 g of DR1/PMMA monomer into a 50 mL beaker.

2. Measure out 9 mL of chlorobenzene and 1 mL of MEK; mix together and then add to monomer.

3. Place on top of stirring hot plate and set for 340 rpm.

4. Mix monomer and solvent for 30 minutes.

5. Elevate temperature to 50°C after 30 minutes.

6. Stir for another hour, for a total mixing time of 1 hour and 30 minutes.

7. Add 0.733 g of PMMA; this is just under a 1:1 mole ratio.

8. Stir 30 minutes more at 50°C.

9. Add di(ethylene glycol) dimethacrylate (cross-linker).

10. Stir 30 minutes more at 50°C.

11. Sample is ready. Do not filter. Place inside an airtight storage container. This is a 12% weight mixture of PMMA+DR1 to solvent.

PMMA-DR1 Spin Coating

1. Use 12% weight mixture of PMMA-DR1 to solvent.

2. Set spinner to 800 rpm for 30 seconds, and then 3200 rpm for 3 minutes.

3. Spin.

4. This same procedure is used to coat the PMMA on wafer, as well as mix, only we do not add DR1 or di(ethylene glycol) dimethacrylate (cross-linker).

References

Boyd, G., "Applications requirements for nonlinear-optical devices and the status of organic materials," *J. Opt. Soc. Am. B* **6**, 4 (1989) 685–692.

Burns, W., M. Howerton, R. Moeller, A. Greenblatt, R. McElhanon, "Broad-band reflection traveling-wave LiNbO$_3$ modulator," *IEEE Phot. Tech. Lett.* **10**, 6 (1998) 805–806.

Chen M., L. Dalton, L. Yu, Y. Shi, W. Steier, "Thermosetting polyurethanes with stable and large second-order optical nonlinearity," *Macromolecules* **25**, 15 (1992) 4032–4035.

Lee, M., H. E. Katz, C. Erben, D. M. Gill, P. Gopalan, J. D. Heber, D. J. McGee, "Broadband modulation of light by using an electro-optic polymer," *Science* **298**, 5597 (2002) 1401–1403.

Liu, Z., J. Yu, D. Zhu, "Design of a new type of electro-optic polymer waveguide modulator with ultrahigh bandwidth," *Intl. J. Infrared and Millimeter Waves* **27**, 5 (2006) 707–724.

Shi, Y., W. Steier, M. Chen, L. Yu, L. Dalton, "Thermosetting nonlinear optical polymer: Polyurethane with disperse red 19 side groups," *Appl. Phys. Lett.* **60**, 21 (1992) 2577–2579.

Shi, Y., C. Zhang, H. Zhang, J. H. Bechtel, L. R. Dalton, B. H. Robinson, W. H. Steier, "Low (sub-1-volt) halfwave voltage polymeric electro-optic modulators achieved by controlling chromophore shape," *Science* **288**, 5463 (2000) 119–122.

Sinyukov, A., M. Hayden, "Generation and detection of terahertz radiation with multilayered electro-optic polymer films," *Opt. Lett.* **27**, 1 (2002) 55–57.

this page intentionally left blank

Time-Multiplexed Emissivity and Pyrometry

Bruce Marshall[1,a]

Pyrometric temperature measurements of shocked metal surfaces require knowledge of the surface emissivity to estimate the temperature. We investigated the use of a repetitively pulsed light source to time-multiplex spectrally reflected optical beams onto the pyrometric radiance detectors. By sharing the same detectors and filters, both measurements are inherently made at matching wavelengths and sample locations. We found that detector noise and calibration accuracy make this technique difficult to accomplish around 700 K. Better success may be found at higher temperatures where the radiance is high enough to record data using lower noise detectors.

Background

To measure the pyrometric temperature of a shocked metal sample, it is necessary to calibrate the graybody curve by measuring the sample emissivity, which is equivalent to measuring the reflectance. Simultaneous measurements of the radiance and reflectance have not been possible because the illumination needed for reflectivity interferes with the measurement of the intrinsic shocked-sample radiance. Thus, two measurements are needed, and the experiments must have identical shock and sample conditions, which is not always achievable. We investigated a technique for time-multiplexing pyrometry and spectral reflectivity measurements of shocked surfaces. The basic idea is to illuminate the shocked target surface with diffuse light from a supercontinuum laser or other repetitively pulsed, multispectral source, and to detect the reflected light along with the thermal radiance using a high-speed photomultiplier. The thermal radiance and reflected laser light can be separated in analysis due to their differing time dependence.

Simultaneous radiance and reflectivity measurements could be performed at different wavelengths to avoid cross talk. However, the time-multiplexed system instead makes use of the cross talk to achieve in-band reflectivity measurements. Not only does it allow the two measurements to be made in the same experiment, but it permits use of the same detector and probe system for both reflectance and radiance, thereby achieving precise overlap of the measurement location and exact matching of the detector spectral response.

---

[1] marshabr@nv.doe.gov, 805-681-2266
[a] Special Technologies Laboratory

Project

The proposed system was based on the system described by Poulsen (2006), who presents a method based on normalizing the radiance and reflectance measurements at several wavelengths to those at one wavelength and solving a set of simultaneous equations to obtain the temperature and emissivity at the reference wavelength. Normalization eliminates the dependence on absolute geometric factors in the measurement; this condition is particularly attractive for measurements on shocked surfaces because it allows measurement of emissivity without the need to collect light over 2π, as with an integrating sphere, which is experimentally difficult. It is, however, necessary that the relative geometric factors for the spectral bands be constant during the measurement, so the probe must provide illumination in a manner that will remain constant relative to wavelength while the target travels and possibly tilts. It is also necessary that any changes in the scattering properties of the surface be independent of wavelength. Machined surfaces would present a problem because they can behave like diffraction gratings.

Poulsen (2006) derives an equation for the emissivity in band n as a function of measured reflection and radiance, incident irradiance, and ideal blackbody emission in bands n and i. The blackbody emission F is calculated over a range of temperatures. The multiple estimates of emissivity in band n must agree for measurements in different wavebands, i, so the correct temperature and emissivity are found at the intersection of the curves by

$$\varepsilon_n = \frac{\left(1 - \dfrac{D_i}{E_i}\right)}{\left(\dfrac{A_i}{B_i} - \dfrac{D_i}{E_i}\right)} = \frac{\left(1 - \dfrac{\left(\dfrac{R_i/C_i}{R_n/C_n}\right)}{\dfrac{I_i}{I_n}}\right)}{\left(\dfrac{\left(\dfrac{S_i/C_i}{S_n/C_n}\right)}{\dfrac{F_i}{F_n}} - \dfrac{\left(\dfrac{R_i/C_i}{R_n/C_n}\right)}{\dfrac{I_i}{I_n}}\right)}, \tag{1}$$

where

ε_n = Emissivity in band n,

C_i = Calibration coefficient for band i,

F_i = Blackbody emission in band i, calculated over a range of temperatures,

I_i = Incident light at target for band i,

R_i = Reflected light in band i,

S_i = Radiance in band *i*, and

A_i = $(S_i/C_i) / (S_n/C_n)$ = Calibrated radiance in channel *i*, normalized to the calibrated radiance in channel *n*,

B_i = (F_i/F_n) = Theoretical blackbody emission in channel *i*, normalized to the theoretical blackbody emission in channel *n*,

D_i = $(R_i/C_i) / (R_n/C_n)$ = Calibrated reflected light of channel *i*, normalized to the calibrated reflected light of channel *n*, and

E_i = (I_i/I_n) = Incident light in channel *i*, normalized to the incident light of channel *n*.

A potential problem with this method, which hurt us in this work, is that when the emissivity depends only slightly on wavelength, the uncertainty in ε_n becomes large.

Light Source

Poulsen (2006) used a ~1 μs surface discharge light source. We proposed to make a similar measurement with a 10 ps, 60 MHz repetition-rate, supercontinuum laser source that emits light from 450 to 1800 nm. The broadband laser would provide a bright source that could be efficiently coupled through a fiber and would fill the same spectral bands as the radiance from the target. The narrow pulses should be separable from the radiance light, leaving plenty of unaltered radiance signal between them for analysis. However, the supercontinuum laser proved to be unsuitable because it is increasingly unstable as the wavelength departs from the 1064 nm seed wavelength, as shown in Figure 1.

We assembled a set of pulsed diode lasers that provide a much more stable source. Emission is at 483, 628, 692, and 840 nm. A Highland four-channel delay generator supplies a burst of 90 pulses at 10 MHz repetition rate, which is amplified to drive the laser diodes. The drive circuit goes slightly negative between pulses, ensuring zero light emission except for the desired pulses. The lasers tend to emit very short, high-power pulses because they gain switch when driven without bias. The pulses are broadened to about 4 ns by means of a 60 m step index fiber, which smooths out the spikes and also provides a spatially uniform source. The repetition rate is limited to 10 MHz by the Highland delay generator. A burst of laser diode pulses recorded on an amplified photodiode with 3.5 GHz bandwidth is shown in Figure 2. Pulse-to-pulse variation is small, and there is an overall reduction in amplitude as the laser warms up during the burst.

One concern about the use of spectrally narrow sources is that they do not fill the filter bands; therefore, the reflectivity measurements are not sampling exactly the same spectrum as the radiance measurements. This should not be a significant problem as long as the radiance and ideal blackbody emission do not vary strongly across the width of any of the filters. The integrated transmission of the filter is accounted for when the detector and probe are calibrated.
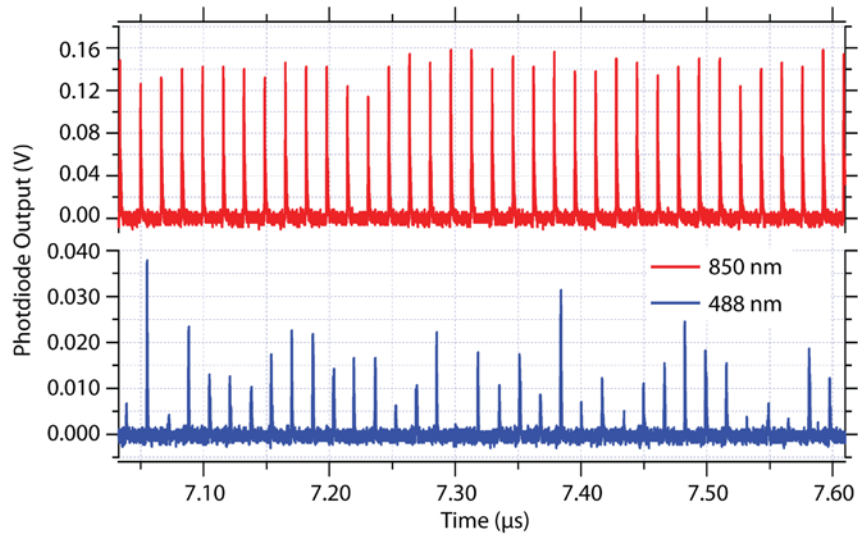
Figure 1. Supercontinuum laser pulses at 488 and 850 nm, as measured using a photodiode. The upper graph shows the relatively stable output at 850 nm. The lower graph shows the output at 488 nm, which is very unstable.
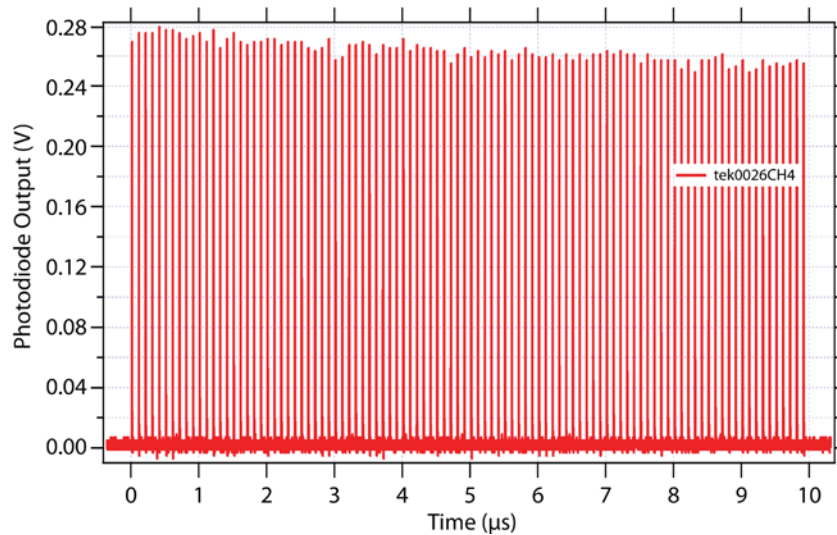

Figure 2. Laser diode burst showing low pulse-to-pulse variation

Photomultiplier Tube (PMT) Response

It is important that the reflectivity signal not degrade the radiance signals that lie between pulses. Radiance signals can vary over many orders of magnitude during a shock measurement, and it is common to use multiple oscilloscope channels to achieve extended coverage. The initially good pulse response of the Hamamatsu R943 photomultipliers was further improved by Brent Davis (NSTec North Las Vegas), who redesigned the housing and circuit (Figure 3). The PMT is fully recovered to less than 0.1% of the peak less than 25 ns after the end of the pulse (Figure 4).
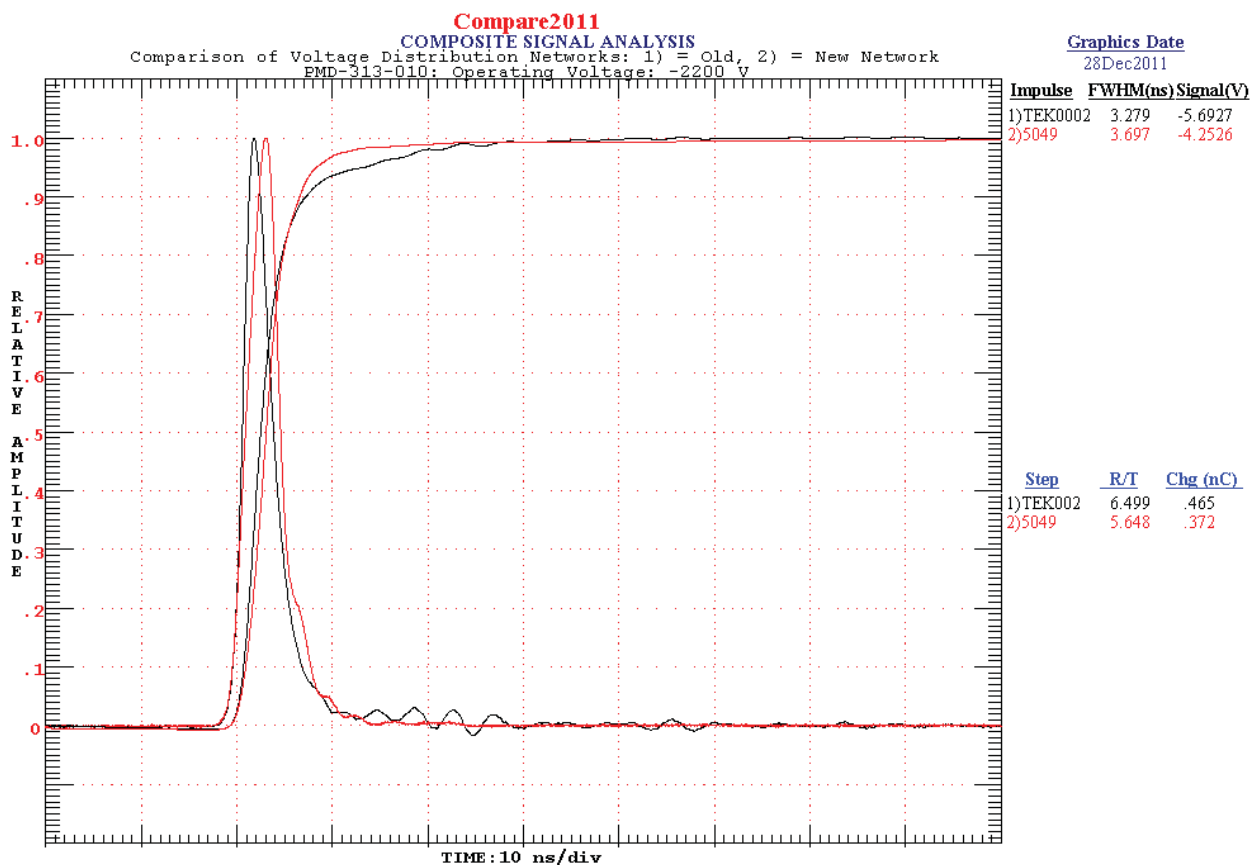
Figure 3. R943 pulse response comparison of new (red) versus old (black) housings

Scope Recovery

Some oscilloscopes do not recover quickly from overloading such as might occur on the most sensitive scale if the reflectivity pulse is large. We tested the Tektronix 6124C oscilloscope using a 2 V pulse generator recorded on a range of scales. Performance was very good, as can be seen in Figure 5. The oscillations in the pulse tail originate in the pulse generator, not in the oscilloscope.
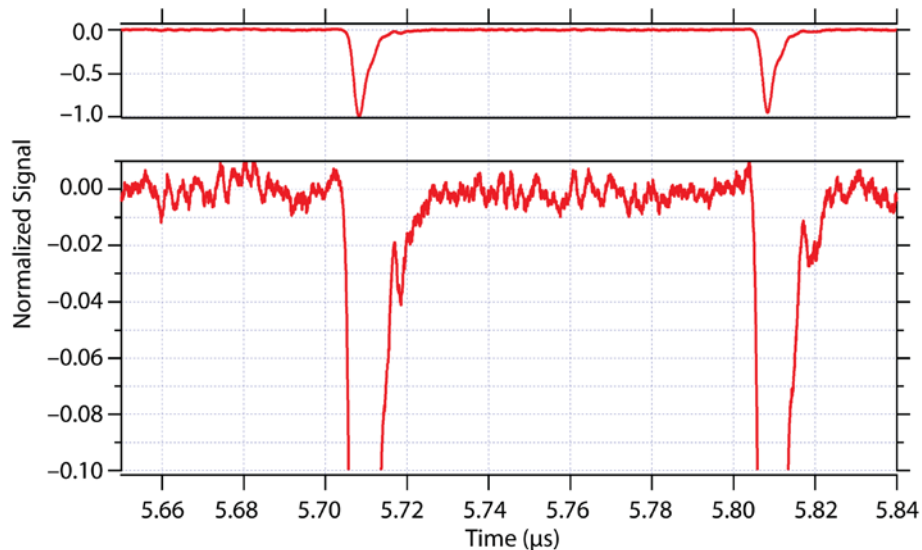
Figure 4. PMT pulse response full scale (upper), expanded scale (lower), showing recovery without artifacts
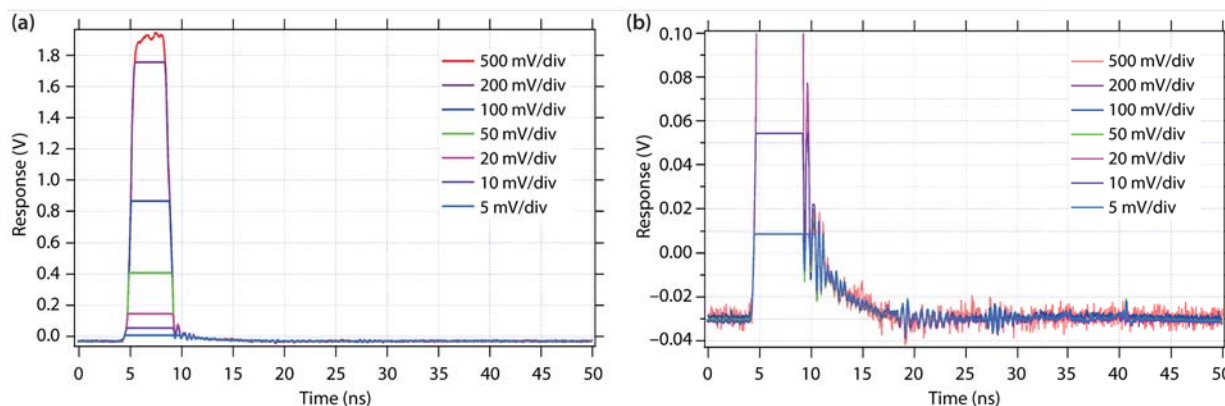
Figure 5. Tektronix 6124C response on different vertical scales to a 2 V pulse. The scope recovers from clipping with minimal distortion.

Probe Design

Several possible optical arrangements were considered for the probe. We wanted it to be substantially similar to the present pyrometry probes that relay an image of the target to a bundle of optical fibers. The reflection measurement requires that we illuminate the target area uniformly so as to tolerate travel and tilt. Our solution was to collimate the light from a 300 μm diameter step-index fiber and inject it into the optical path via an offset 2 mm mirror, as shown in Figure 6. The lenses are 25.4 mm

diameter, 38 mm focal length visible/near infrared achromats. For a specular surface, the reflected light bypasses the mirror and illuminates the fiber bundle uniformly, allowing about 2° of tilt and about 6 mm of travel, which are adequate for most pyrometry experiments.
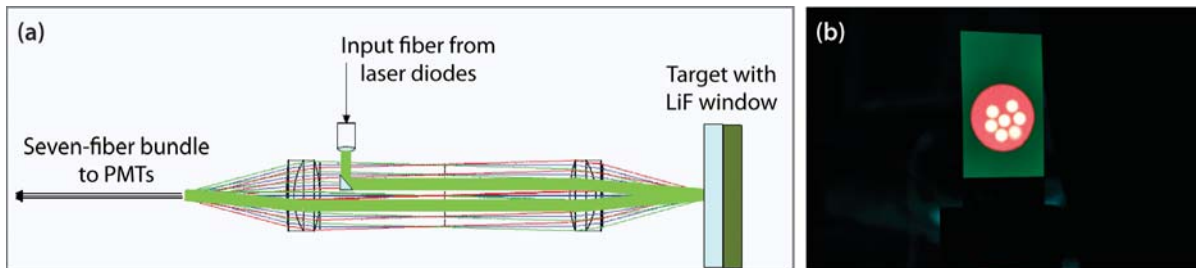
Figure 6. (a) Probe layout and (b) probe illumination spot (red) and collection fiber spots (white)

Experiment

A simple, repeatable test setup was required to evaluate the system performance. Our first attempt to use a modulated thin-film carbon IR emitter was unsuccessful because the protective coatings on the surface dominated the surface emissivity. Instead, we heated a nickel disk to 700°C and incorporated a 10 ms shutter into the probe to protect the PMTs. Although the disk was surrounded with argon to prevent oxidation, its specular surface nevertheless became dull, although no color change was observed. Another heater was obtained that could reach as high as 1200°C, which would have given usable signals on the 488 nm channel, but due to time limitations we did not have the opportunity to use it. PMT signals at 850 nm are shown for 700°C and 77°C in Figure 7.
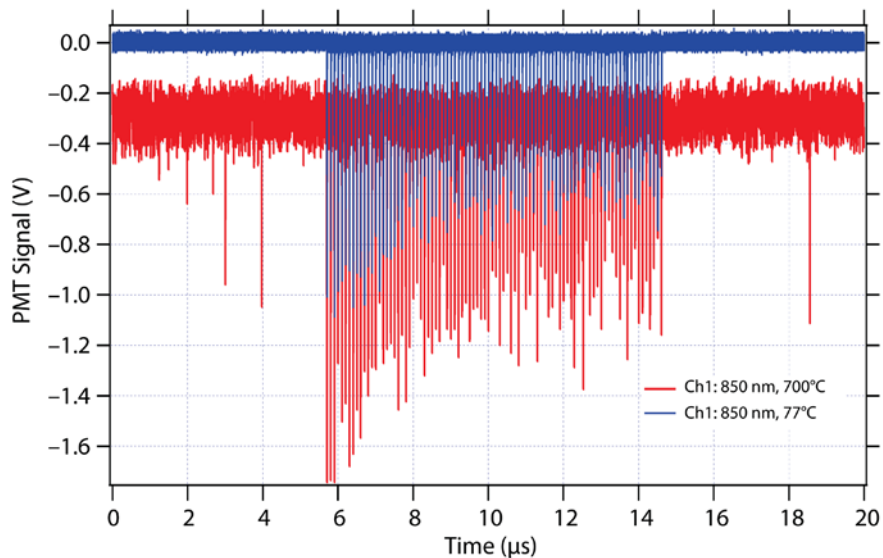
Figure 7. PMT signals at 850 nm: 700°C (red) and 77°C (blue)

Calibration was accomplished using an optical power meter to measure the power at the target surface, and then using a mirror as a target and recording the signals. The data were processed with IGOR software. A time domain filter extracted the pulsed reflectivity data, and the remaining radiance data were smoothed and interpolated to obtain a value at the pulse time (Figure 8). The reflection pulses were each integrated over a 16 ns wide window.
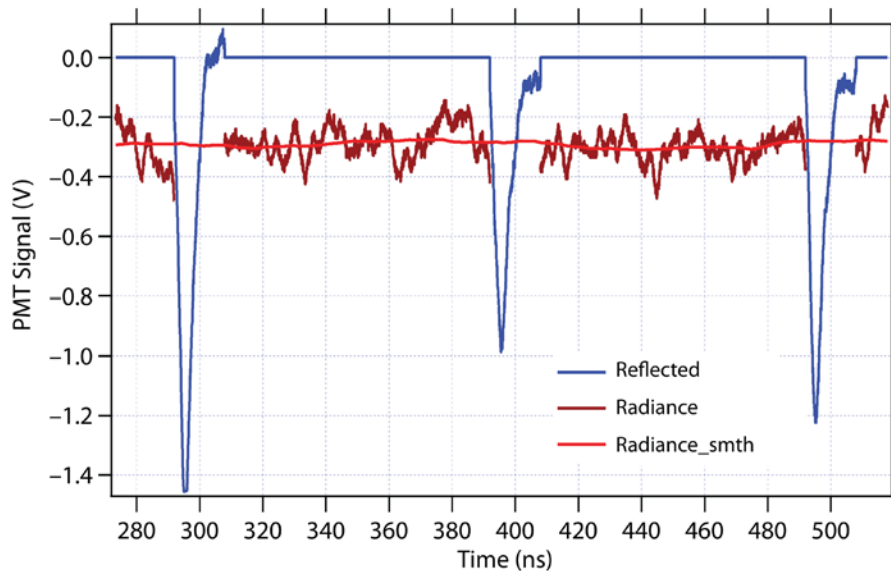

Figure 8. Reflection and radiance signals from the photomultiplier

These data were processed using calibration measurements of the light sources and detector systems, and using Equation 1 to calculate the emissivity. For our initial analysis, we used the average values over the entire pulse burst to reduce noise issues. The three equations for emissivity versus temperature were plotted, and the solution would lie at their intersection. However, the results in Figure 9 were rather discouraging, as the three curves did not intersect. We were unable resolve this problem, but believe that it is the result of a combination of factors: the two usable channels (635 nm and 685 nm) are too close together, over this range the sample resembles a gray body, the radiance signals are small due to the low temperature, and the photomultipliers are very noisy. It is to be expected that the curves for a gray body would be parallel, but it is surprising that these data are so far apart. To understand it, we considered how large an error would be required to account for the situation.

To estimate the error needed to change this result significantly, we varied the calibration factors and found that a 20% change for one of them would produce the result shown in Figure 10. The curves still failed to intersect. The radiance at 488 nm was essentially within the background noise, so it is not surprising that the emissivity curve generated from it diverges widely from the other bands, which did have usable signals.
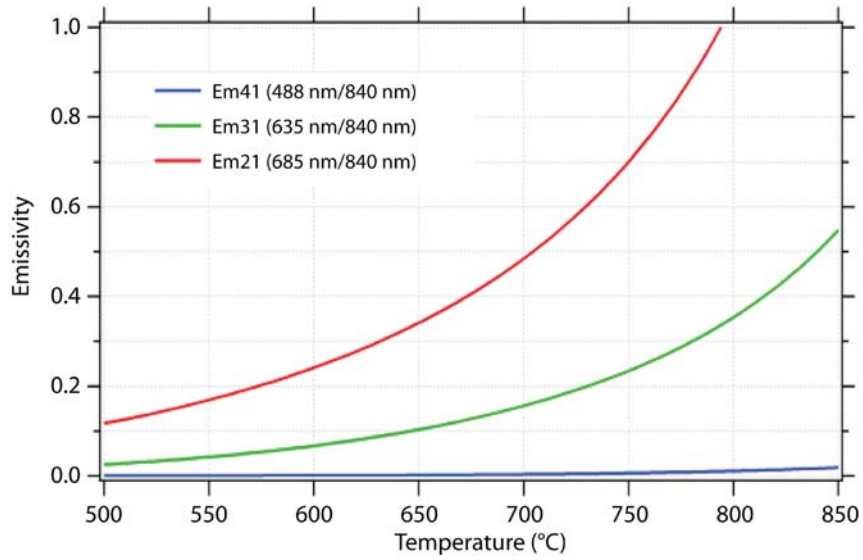
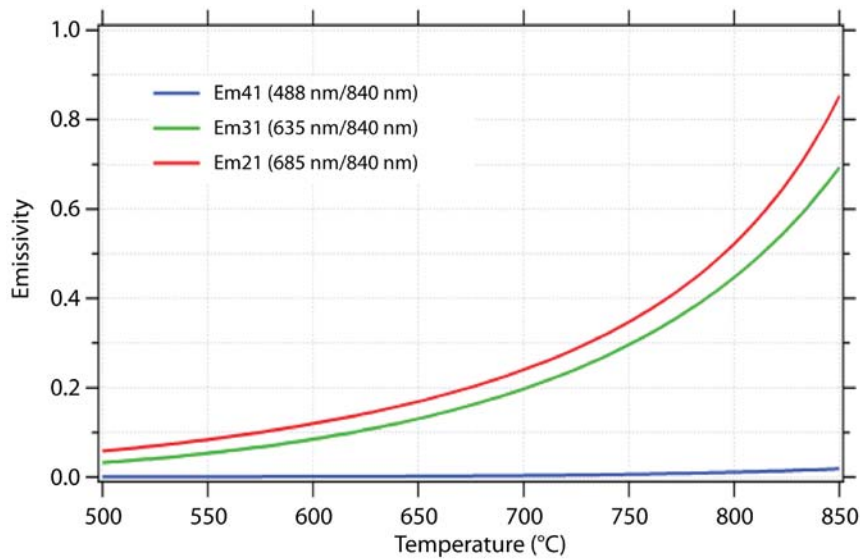**Figure 9. Emissivity plot based on PMT data from nickel surface**

**Figure 10. Emissivity based on adjusted calibration values, with
channel 2 calibration factor reduced by 20%**

We also recorded the spectra on a spectrometer. As can be seen in Figure 11, there was virtually no radiance at 488 nm. Again, the emissivity curves failed to converge (Figure 12). Adjusting the calibration at 635 nm by 5% caused the corresponding curve to intersect the 685 nm curve (Figure 13). However, the 488 nm curve required a 50% adjustment to converge. It should be noted, however, that the 488 nm radiance signal is nearly at background level.
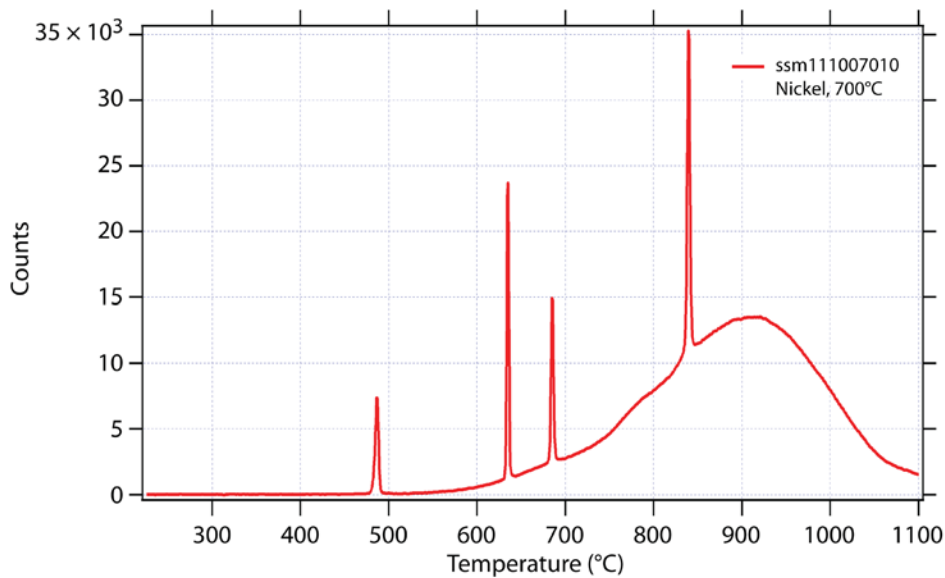
Figure 11. Emission and reflection from nickel target at 700°C, measured on a spectrometer

The failure of the data to converge likely has several causes. One is the selection of nickel as the test piece; it is not very far from a graybody, and, as noted by Poulsen (2006), this method is "problematic when the channel emissivities are nearly equal or are very small." The oxidized nickel surface reflectivity values at 635 nm and 685 nm are very similar.

Another problem was the low temperature we used. At 700°C, radiance at 488 nm is nearly zero. Operation at higher temperatures would have given higher signal levels and possibly even allowed us to use photodiodes instead of photomultipliers.

A third issue was the level of noise in the photomultiplier signals. In the example shown in Figure 13, a 5% adjustment of one calibration factor could produce convergence. At low temperatures, the signals have noise much worse than 5%, so it seems unlikely that we could get useful data there. It may be possible to use this method at higher temperatures and with quieter detectors. Detector linearity may also be an issue in some circumstances.
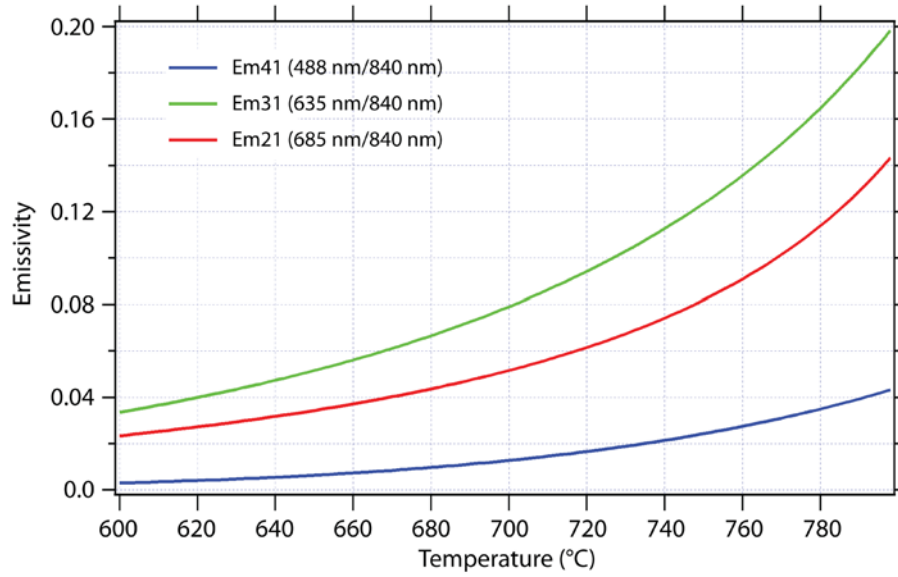
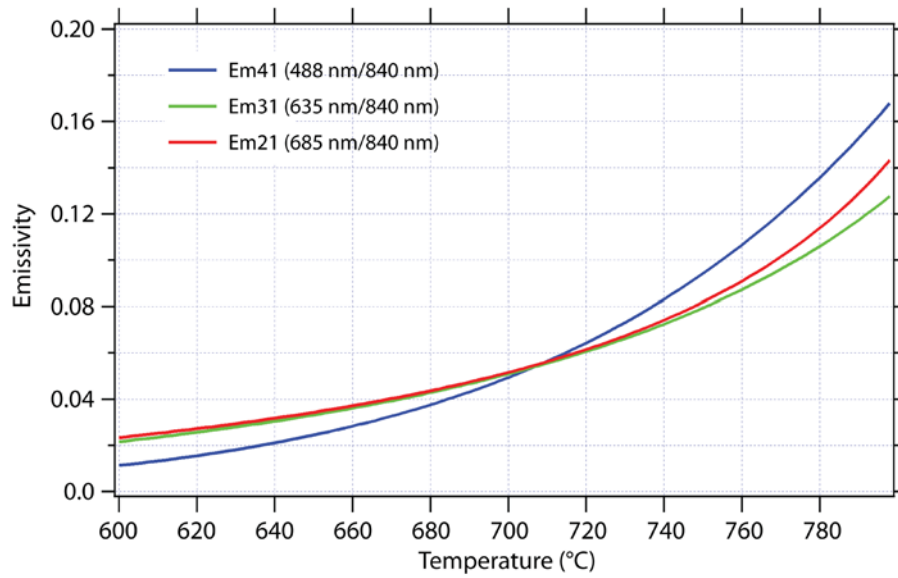Figure 12. Emissivity curves failed to converge

Figure 13. Emissivity curves converged with adjusted calibration data

Conclusions

Our effort to improve upon the time resolution of Poulsen's spectrum method for temperature measurements was largely unsuccessful and points out some pitfalls of the technique. The need for a stable, broadband, bright, pulsed light source proved very challenging. The supercontinuum laser was not stable enough at short wavelengths. The laser diode system was sufficiently stable, but the narrow emission spectra of the lasers did not fill the transmission bands of the filters, requiring additional assumptions to be made about the emissivity of the target. Another problem was the lack of a high temperature target for evaluating the measurement system, which restricted us to low radiance levels at the wavelengths that could be detected by the photomultipliers and resulted in prohibitively high noise levels in the data. The 488 nm band was essentially unusable due to lack of signal. The nickel target too closely resembled a gray body, particularly over the limited range between the two red bands that had sufficient radiance signals to be useful.

In the course of the project, we produced an efficient, unobtrusive probe and were able to generate stable optical pulses for the reflection measurements. We believe that the method would be successful if longer wavelengths were included, higher temperatures were being measured, and the emissivity of the target varied more over the spectrum being measured.

References

Poulsen, P., S. K. Ault, "New method of high-precision thermometry," *Rev. Sci. Instrum.* **77**, 9 (2006) 094901–6.

Three-Dimensional Nanoparticle Enhancement of Scintillations

James Tinsley[1,a] and Larry Franks[b]

The purpose of this project was to test for improved scintillation performance due to the presence of metal nanoparticles distributed throughout a *three-dimensional* scintillator. The concept of nanoparticle enhancement was tried earlier using a two-dimensional nanoparticle matrix, but the interaction dynamics make it extremely difficult to test the concept under such circumstances (Kimblin 2010). In addition, the aluminum nanoparticles of the optimum diameter (100–200 nm) were not available, and the 20 nm particles used were calculated to be considerably less efficient. Our ability to accomplish the project goal was predicated on the recent discovery of sources of "bulk" nanoparticles that could be put in solutions of a liquid scintillator. The use of a liquid scintillator, in this case 1.5 g/L of 2,5-diphenyloxazole in pseudocumene, allowed us to adjust the concentration of nanoparticles in the scintillator.

Background

Although motivations vary over time, the quest for brighter, faster scintillators continues. However, there is always a trade-off between brightness (related to a scintillator's sensitivity) and decay time. Sensitivity is important in situations where low-energy particles are to be detected, and quick response is important when a high flux of radiation may be present: if new particles are detected while the detector is still responding to previous ones, *detector pile-up* will result, which leads to improper, or loss of, function.

Organic (plastic and liquid) scintillators have very quick response, with typical scintillation decay times of a few nanoseconds, but are not efficient; only 2% to 3% of radiation energy deposited is converted to light energy. However, they are inexpensive and rugged and can be produced in large sizes. Inorganic scintillators can be found that have efficiencies of about 10% to 20%, but their response times range from several tens to several hundreds of nanoseconds. They are also significantly more expensive, generally less rugged, and are more limited in the possible sizes. If organic scintillators could be made with higher sensitivity, while maintaining or even improving their decay times, they would be very valuable for applications such as large-scale and/or portable radiation monitoring systems.

Investigators (Geddes 2002) have demonstrated that, for optically stimulated fluorescence, metal nanoparticles in the proper size range lead to greater light emission and faster decay in fluorophores. This led to speculation (Kimblin 2010) that the same metal-enhanced fluorescence (MEF) might apply to scintillation, as it involves some of the same physics as fluorescence. In fluorescence, light is

---

[1] tinslejr@nv.doe.gov, 805-681-2282
[a] Special Technologies Laboratory; [b] Keystone, Inc.

absorbed by the fluorophore and is re-emitted at a longer wavelength. In scintillation, the incident radiation deposits energy in a substance mostly through the interaction of energetic charged particles with the atomic electrons in the material, some of which give rise to the same excited states as fluorescence; these in turn result in light emission. For a given material, the emission spectrum and characteristic exponential decay is essentially the same for both processes. We note that the combination of increased brightness and shorter decay time reported by Geddes with optical excitation of organic solutions (using MEF) is rarely, if ever, achieved with organic scintillators.

The enhancement of fluorescence is due to a surface plasmon resonance in the nanoparticles and has a range of a few tens of nanometers (Glass 1980, Geddes 2002, 2005, Lakowicz 2005, Zang 2006, Chan 2008, Lakowicz 2008). This enhancement is therefore limited to the immediate vicinity of the nanoparticle. In the previous work (Kimblin 2010), only two-dimensional distributions of nanoparticles on a substrate were available, so that any enhancement of scintillation was limited to a few tens of nanometers on one side of the nanoparticle array. This is not an issue in fluorescence studies because the (typically UV) excitation light is entirely absorbed within a few microns of the material. On the other hand, the deposition of radiation energy in a material takes place over a range of several millimeters to several hundred millimeters for the types of radiation of interest in monitoring systems. A very small fraction of the total energy will be deposited in the thin layer where MEF would take place, and so even a significant enhancement of that tiny fraction would be difficult to detect.

By fortuitous circumstance, new sources of nanoparticles that could be put into a colloidal solution, such as a liquid scintillator, were discovered just in the last year (Dutta 2010, Mao 2010), presenting the possibility of studying the effect of nanoparticles on scintillation in a fully three-dimensional system. With nanoparticles dispersed throughout the scintillating material comes the possibility of enhancing a significant fraction of the scintillation light and getting a measurable improvement.

Project

The goal of this work was to demonstrate the effect of nanoparticles dispersed in a volume of liquid scintillator; specifically, whether their presence produces the same enhancement of light emission and emission decay time as is seen in optically stimulated fluorescence. The use of a liquid scintillator was mandated by the desire to vary the concentration of nanoparticles as well as the potential difficulty of polymerizing the base material with uniformly dispersed nanoparticles included.

Recent calculations (Geddes 2005) suggest that the "best" choice for MEF in this context is aluminum particles that are ~100 to 200 nm in diameter (Figure 1). This is in contrast to the ~20 nm particles used by Kimblin (2010). Because these measurements are predicated on the availability of nanoparticles of the desired material size and shape, arrangements were made with both of the sources that had been identified: a group working under Sam Mao at the Lawrence Berkeley National Laboratory, and a group led by Partha Dutta at Rensselaer Polytechnic Institute (RPI). Both researchers have produced aluminum nanoparticles of the desired size range in the past, and were willing to do so again for this work.
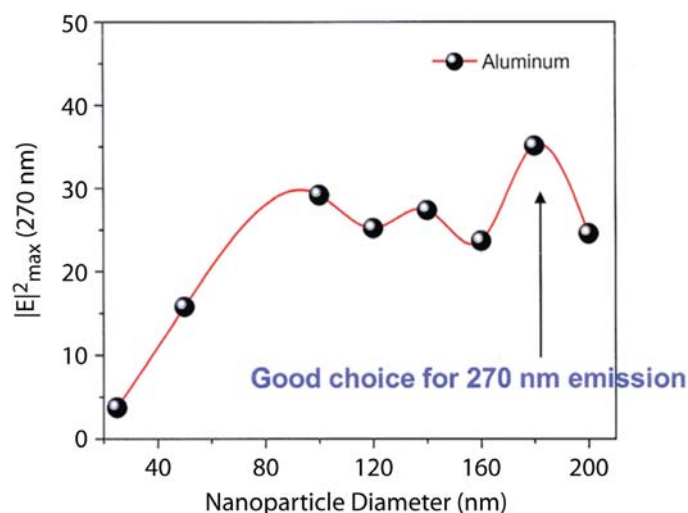
Figure 1. Calculated |E|²$_{max}$ versus nanoparticle diameter where E is the electric field generated by the induced surface plasmon activity on the nanoparticle

Nanoparticles

Unfortunately, due to a number of circumstances, nanoparticles from both sources were not obtained until quite late in the fiscal year. As a consequence, only a limited number of measurements were made using the particles obtained from the RPI group. A scanning electron microscope (SEM) image of these nanoparticles is shown in Figure 2. While most of the particles appear to be between ~100 and 200 nm in size, there are also a number of them that are quite a bit larger. When a small amount of these were added to the liquid scintillator, the largest particles simply dropped to the bottom of the vial (see Figure 5).

Because it was not possible to separate out the very large particles from the smaller ones that would remain in suspension, some fraction of the nanoparticles' mass that was added to the scintillator solution did not contribute to effects measured. Based on an "eyeball" estimate of the size of the sample added to the liquid and the size of the particle mass at the bottom of the vial, it is estimated that about one-quarter to one-third of the initial mass is in this category.

In the preparation of the nanoparticles, care was taken to prevent the aluminum from oxidizing. By the same token, it was necessary to transfer the particles from their original container to the scintillator solution in an oxygen-free glove box. If the particles of this size range (100–200 nm) were exposed to air for any length of time, their conductivity (assumed in the calculations for MEF) would become highly suspect.
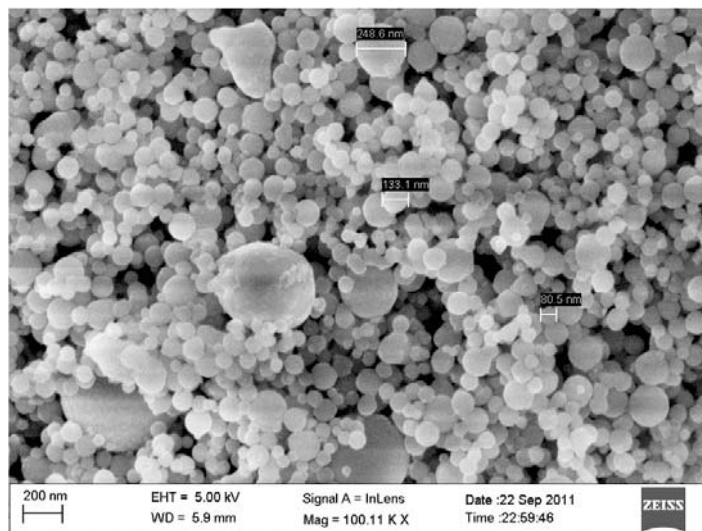
Figure 2. SEM image of the nanoparticles from RPI showing the distribution of particle sizes and their generally spherical shape. The size scale appears on the lower left. Note the occasional very large (>400 nm) particles.

Liquid Scintillator

The scintillator compound chosen for this work was a pseudocumene (1,2,4-trimethylbenzene) base with a 1.5 g/L concentration of 2,5-diphenyloxazole (PPO) as a wavelength shifter. This was chosen because it is easy to make, consists of ingredients that do not have significant health physics issues, and has an emission spectrum that matches well with common photomultiplier tubes (PMTs).

It should be noted that all of the measurements reported here were made with the same batch of liquid scintillator so that the concentration of PPO in pseudocumene was the same throughout.

Experimental Setup for Scintillation Measurements

The apparatus used to measure the scintillation properties is shown schematically in Figure 3. The scintillator solution was contained in cylindrical fused silica vials with stoppered necks on the side of the cylinder. These vials have a capacity of about 3 cm^3. Fused silica is a form of silicon oxide that has a very low concentration of impurities, and is suitable for scintillation measurements because it does not produce any measureable scintillation itself.

A 1-inch diameter Hamamatsu R7899 PMT was chosen to capture the scintillation light on the basis of its low noise and good linearity; the signal from that was digitized using a TRUMP-8k multichannel analyzer (MCA) card installed in an IBM-compatible PC. The radiation source for the measurements reported here was a ^{137}Cs gamma source, a pure gamma source that emits 662 keV gammas. This source has the advantage over a ^{90}Sr beta source used earlier (Kimblin 2010) in that it produces

a recognizable "hump" in the scintillation spectrum, as distinct from the two-component exponential distribution obtained using the latter (Figure 4). The structure of the gamma source distribution makes it easier to see any enhancement of average light output, which would manifest itself by a shift of the hump to higher channels (that is, to the right in the plot shown in Figure 4). In the case of the beta source, it is more difficult to distinguish a shift to the right (higher average light output) from a shift upwards (higher number of events per unit time).
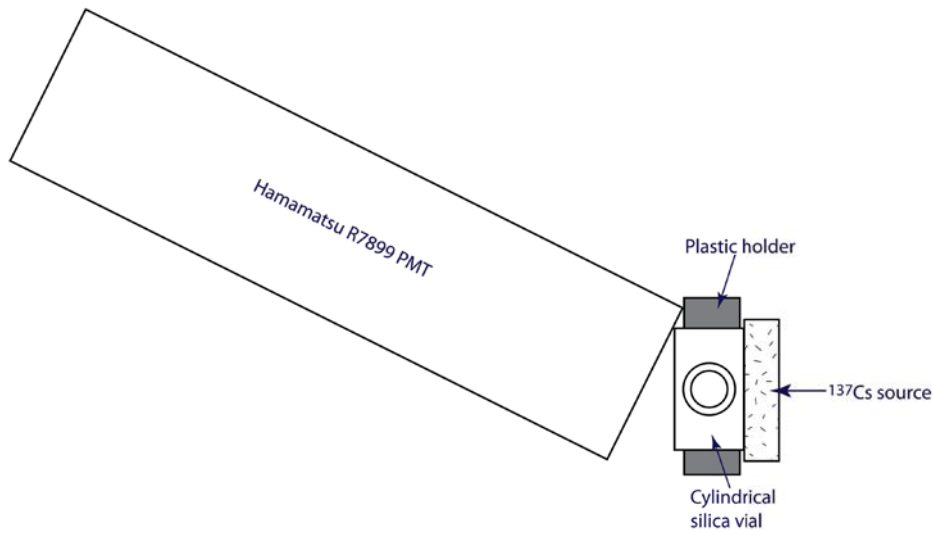
Figure 3. Schematic of the scintillation measurement system. Not shown is the MCA interface and data acquisition PC.
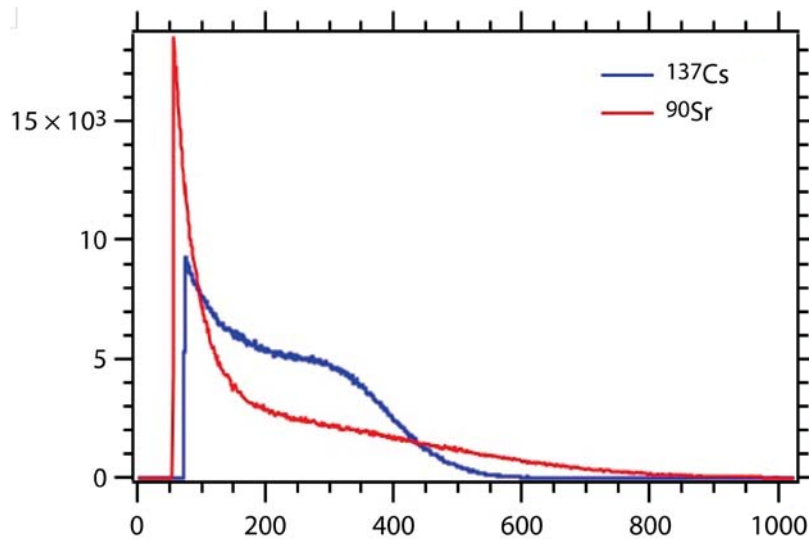
Figure 4. Spectrum of pure PPO in pseudocumene scintillator using a ^{137}Cs source versus a ^{90}Sr source. Both axes are in arbitrary units.

Calculations

Aside from particle size and type, the concentration of nanoparticles dispersed throughout the scintillator is the most relevant parameter. If the concentration is too high, the particles themselves will block most, if not all, of the light from reaching the PMT. Conversely, if the concentration is too dilute, light transmission will be good but the amount of enhancement will be minimal.

The range of nanoparticle-enhanced fluorescence is approximately 50 nm. If we assume an average diameter of 150 nm for our nanoparticles, the active volume for enhancement is a hollow sphere with an outer diameter of 250 nm and inner diameter of 150 nm. This volume is 6.41×10^{-15} cm^3 surrounding a particle with a volume of 1.77×10^{-15} cm^3. If it were possible to set the particles in a close-packed arrangement with each particle 250 nm away from its nearest neighbors, we would have a volume of which 16% was aluminum, 58% was active volume, and the remaining 26% occupied by scintillator that was too distant from the nanoparticles for any enhancement to be expected.

The most extreme case described above corresponds to a nanoparticle mass density of approximately 420 mg/cm^3. Experiments done with some nanoparticles that averaged about 20 nm in diameter, therefore too small to expect any scintillation enhancement, showed that a mass density of even 100 mg/cm^3 in a volume of liquid scintillator would absorb a significant fraction of the light passing though it.

Scintillation Measurements

Based on the above observations, the first sample was made with 30 mg of nanoparticles suspended in 2 cm^3 of a PPO in pseudocumene liquid scintillator. As noted earlier, a significant fraction of the nanoparticle material would not stay in suspension, but collected at the bottom of the vial (see Figure 5); therefore, the *effective* density of nanoparticles was estimated to be 10 mg/cm^3. The 3 cm^3 vials were filled with 2 cm^3 of material to allow the contents to be agitated from time to time so as to preserve the homogeneity of the mixture as much as possible. Some fraction of the nanoparticles that remained in suspension over the short term would eventually settle toward the bottom of the vial over a period of several hours (by contrast, the very heavy particles settled to the bottom within 1 minute or so). To ensure that the measurements were made with a fairly constant density of nanoparticles in solution, all measurements were 1000 seconds in length, made within about 2 minutes of a brief agitation of the vial.

As the images in Figure 5 show, even a nanoparticle concentration of 10 mg/cm^3 results in a marked amount of light absorption. The pulse height spectrum (Figure 6) for this sample showed a marked reduction in average light output (that is, pulse height) compared to a sample of the scintillator with no nanoparticles in it. Also, there were no events that produced as much light as the bare scintillator. This indicates that any nanoparticle enhancement, should it exist, was overwhelmed by the light lost to absorption.
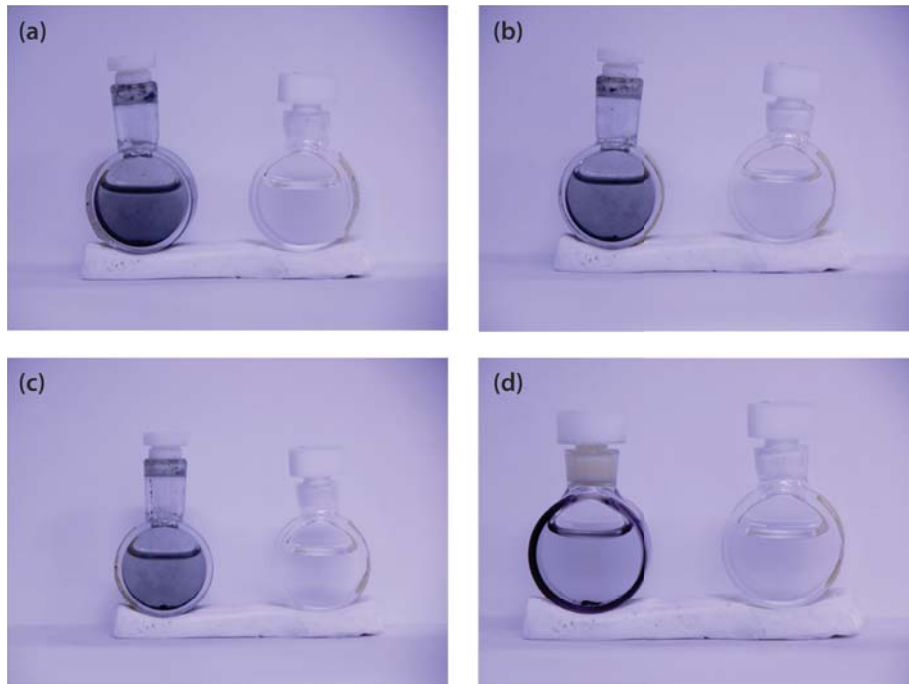
Figure 5. Photographs of liquid scintillator vials (on left) with (a) 10.0, (b) 2.5, (c) 0.63, and (d) 0.156 mg/cm³ nanoparticles. All vials on the right contain pure liquid scintillator (PC+PPO).
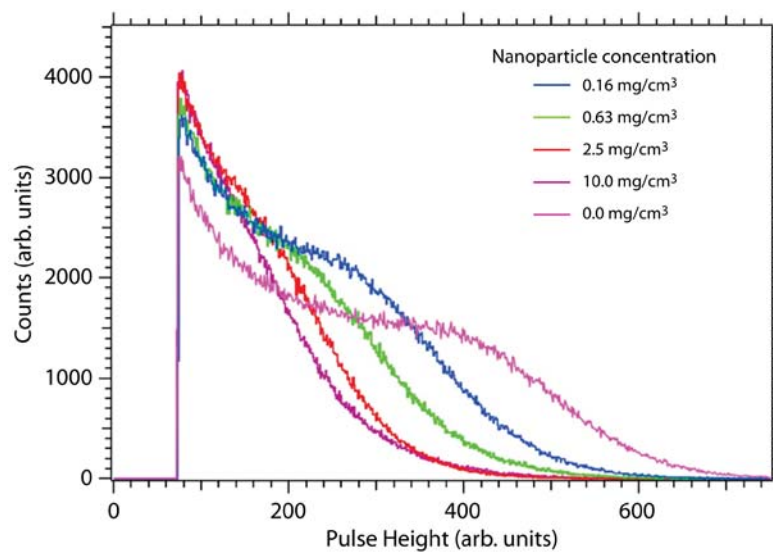

Figure 6. Pulse height spectra for samples of varying nanoparticle concentrations

Several more measurements were made, each with 0.5 cm^3 of the sample containing nanoparticles mixed with 1.5 cm^3 of additional liquid scintillator. Photos of these configurations are also shown in Figure 5, and the resulting data are in Figure 6.

It is clear from these results that diluting the nanoparticle concentration results in better light output through less absorption, but no scintillation enhancement is seen. Each measurement of a sample containing nanoparticles was accompanied by a measurement of the pure scintillator so that any systematic drifts in PMT gain could be accounted for; these corrections were on the order of several percent. A compendium of the results for each sample is given in Table 1. In addition to the relative light output, calculations of the average separation between nanoparticles and an estimation of the fraction of the total volume amenable to MEF are given. For the estimated volume, we use a range of 50 nm from the surface of the particle. We note that in the least concentrated sample, only about 1/5000 of the volume would be close enough to a nanoparticle for enhancement to be expected; even with optimistic levels of enhancement, the gain would be somewhat modest, especially given that there is still some attenuation from the particles themselves to overcome.

Table 1. Summary of results and calculated values for various nanoparticle densities

Nanoparticle Density (mg/cm^3)	Relative Counts (%)	Average Separation (nm)	Relative Volume of Enhancement (%)
0.156	96.5	3508	0.021
0.625	93.3	2210	0.084
2.5	94.1	1392	0.336
10.0	82.4	877	1.34
0.0	100.0	—	—

Conclusion

Clearly, we have seen no evidence for scintillation enhancement due to the presence of nanoparticles. There are two possible explanations: (1) there are enough differences between fluorescence and the scintillation process that the MEF does not extend to the latter, or (2) the minimal enhancement that exists is overshadowed by scattering and/or absorption of the generated light by other nanoparticles on its way out of the cell.

In the case of optically stimulated fluorescence, the absorption of light takes place within a very short distance (on the order of microns) of the surface of the material. Thus, the emitted light does not have to travel some distance through a field of suspended particles before exiting the material. Whether this is the reason for the absence of emission enhancement, or just the difference in methods of excitation that lead to light emission, is not understood.

Acknowledgments

References

Chan, G. H., J. Zhao, G. C. Schatz, R. P. Van Duyne, "Localized surface plasmon resonance spectroscopy of triangular aluminum nanoparticles," *J. Phys. Chem. C* **112**, 36 (2008) 13958–13963.

Dutta, P., private communication, 2010.

Geddes, C. D., J. R. Lakowicz, "Metal-enhanced fluorescence," *J. Fluoresc.* **12**, 2 (2002) 121–129.

Geddes, C. D., K. Aslan, I. Gryczynnski, J. R. Lakowicz, "Metal-enhanced fluorescence sensing," in *Fluorescence Sensors and Biosensors,* ed. Thompson, R., Francis and Taylor Group, Boca Raton, Florida, 2005, 121–181.

Glass, A. M., P. F. Liao, J. G. Bergman, D. H. Olson, "Interaction of metal particles with adsorbed dye molecules: Absorption and luminescence," *Opt. Lett.* **5**, 9 (1980) 368–370.

Kimblin, C. W., C. W. Geddes, L. Franks, "Radiative decay engineering for improved scintillators," *Nevada Test Site–Directed Research and Development*, FY 2009, National Security Technologies, LLC, Las Vegas, Nevada, 2010, 191–200.

Lakowicz, J. R., "Radiative decay engineering 5: Metal-enhanced fluorescence and plasmon emission," *Anal. Biochem.* **337**, 2 (2005) 171–194.

Lakowicz, J. R., K. Ray, M. Chowdhury, H. Szmacinski, Y. Fu, J. Zhang, K. Nowaczyk, "Plasmon-controlled fluorescence: A new paradigm in fluorescence spectroscopy," *The Analyst* **133**, 10 (2008) 1308–1346.

Mao, S., private communication, 2010.

Zang, Y., K. Aslan, M. J. R. Previte, C. D. Geddes, "Metal-enhanced S2 fluorescence from azulene," *Chem. Phys. Lett.* **432** (2006) 528–532.

this page intentionally left blank

NNSA/NA-114

Lucille Gentry (1)   Bob Meisner (1)

NNSA/NA-123.2

Abdul Dasti (1)   Lee Hamilton (1)

NNSA/NSO

Charlotte Carter (2)   Steve Mellington (1)   Laura Tomlinson (1)

NSTec

Dennis Barker	(1)	Howard Bender	(2)	Mike Butchko	(1)
Ken Cooke	(1)	Brian Cox	(1)	Frank Cverna	(1)
Jim Gatling	(1)	Steve Goldstein	(1)	Paul Guss	(2)
E. Chris Hagen	(1)	John Hollabaugh	(1)	A. C. Hollins	(1)
Jim Holt	(1)	Raymond J. Juzaitis	(1)	Ping Lee	(1)
Amy Lewis	(1)	Wil Lewis	(1)	Dana Lindsay	(1)
Eric Machorro	(2)	Michael Martinez	(1)	Michael Mohar	(1)
Eric Moore	(1)	Cheryl Oar	(1)	Raffi Papazian	(1)
PIs	(1 ea)	Dave Post	(1)	Gerald Stevens	(2)
Tom Waltman	(1)	Alan Will	(1)		

Joint Nevada Program Office

Rick Higgs (1)

LANL   *LLNL*   *SNL*

LDRD Office (1)   LDRD Office (1)   LDRD Office (1)
(ATTN: William Priedhorsky)   (ATTN: Bill Craig)   (ATTN: Hank Westrich)

OSTI   *Resource Centers*

Electronic copy (1)   Technical Library (1)
                Public Reading Center (1)